2013

Transient And Distributed Algorithms To Improve Islanding Detection Capability Of Inverter Based Distributed Generation

Mohamed Al Hosani
University of Central Florida

TRANSIENT AND DISTRIBUTED ALGORITHMS TO IMPROVE ISLANDING DETECTION CAPABILITY OF INVERTER BASED DISTRIBUTED GENERATION

by

MOHAMED Y. AL HOSANI
B.S. American University of Sharjah, 2008
M.S. University of Central Florida, 2010

A dissertation submitted in partial fulfillment of the requirements
for the degree of Doctor of Philosophy
in the School of Electrical Engineering and Computer Science
in the College of Engineering and Computer Science
at the University of Central Florida
Orlando, Florida

Fall Term
2013

Major Professor: Zhihua Qu

ABSTRACT

Recently, a lot of research work has been dedicated toward enhancing performance, reliability and integrity of distributed energy resources that are integrated into distribution networks. The problem of islanding detection and islanding prevention (i.e. anti-islanding) has stimulated a lot of research due to its role in severely compromising the safety of working personnel and resulting in equipment damages. Various Islanding Detection Methods (IDMs) have been developed within the last ten years in anticipation of the tremendous increase in the penetration of Distributed Generation (DG) in distribution system. This work proposes new IDMs that rely on transient and distributed behaviors to improve integrity and performance of DGs while maintaining multi-DG islanding detection capability.

In this thesis, the following questions have been addressed: How to utilize the transient behavior arising from an islanding condition to improve detectability and robust performance of IDMs in a distributive manner? How to reduce the negative stability impact of the well-known Sandia Frequency Shift (SFS) IDM while maintaining its islanding detection capability? How to incorporate the perturbations provided by each of DGs in such a way that the negative interference of different IDMs is minimized without the need of any type of communication among the different DGs?

It is shown that the proposed techniques are local, scalable and robust against different loading conditions and topology changes. Also, the proposed techniques can successfully distinguish an islanding condition from other disturbances that may occur in power system networks. This work improves the efficiency, reliability and safety of integrated DGs, which presents a necessary advance toward making electric power grids a smart grid.

This thesis is dedicated to my parents for their endless love, support and encouragement.

This work is also dedicated to everyone who sees the wisdom of sustainability.

ACKNOWLEDGMENTS

First and foremost, praises and thanks to God, the Almighty, for his showers of blessings throughout my research work to complete the research successfully.

I would like to first thank Allah for making all of this possible. This work would not have been possible without the support of many people. I would like to express my gratitude to my supervisor, Prof. Zhihua Qu who was abundantly helpful and offered invaluable assistance, support and guidance. Deepest gratitude are also due to the members of the dissertation committee, Prof. Wasfy Mikhael, Dr. Aman Behal, Dr. Chengying Xu and Dr. Michael Haralambous for their assistance and valuable comments. Special thanks also to my secondary advisor Dr. Hatem Zeineldin for his valuable contribution to my work. I would also like to convey thanks to my sponsor Masdar Institute of Science and Technology (MIST) for their financial and logistic support. This work was also supported in part by the US National Science Foundation under grants ECCS-1308928 and CCF-0956501 as well as by the US Department of Energy (DoE) under award DE-EE0006340 and under the Solar Energy Grid Integration Systems (SEGIS) program (phases I to III).

I must also acknowledge several people inside our robotic Lab for their generous technical assistant. In particular, Dr. Huanhai Xin and Dr. Ali Maknouninejad were always willing to help me when I needed it.

I also want to express my love and gratitude to my beloved family, especially mom and dad, for their understanding and endless love, through the duration of my studies.

Finally, my thanks go to all the people who have supported me to complete the research work directly or indirectly.

TABLE OF CONTENTS

LIST OF FIGURES

LIST OF TABLES

LIST OF ACRONYMS/ABBREVIATIONS

AFD	Active Frequency Drift
CB	Circuit Breaker
DFT	Discrete Fourier Transform
DG	Distributed Generation
IDA	Islanding Detection Algorithm
IDM	Islanding Detection Method
IEEE	Institute of Electrical and Electronic Engineers
IGBT	Insulated Gate Bipolar Transistor
KCL	Kirchhoff Current Law
KVL	Kirchhoff Voltage Law
LS	Least Square
MAE	Maximum Absolute Error
MPPT	Maximum Power Point Tracking
MSE	Mean Squared Error
NDZ	Non-Detection Zone
OUF	Over/Under Frequency Protection
OUV	Over/Under Voltage Protection
PCC	Point of Common Coupling
PI	Proportional-integral
PLL	Phase-Locked Loop
PMS	Power Management Strategy
PWM	Pulse-Width Modulation

RLS	Recursive Least Square
RMS	Root Mean Square
SFS	Sandia Frequency Shift
SIDM	Scheduled Islanding Detection Method
SMS	Slip-Mode Frequency Shift
SNR	Signal-to-Noise Ratio
SVS	Sandia Voltage Shift
THD	Total Harmonic Distortion
UL	Underwriters Laboratories
VSI	Voltage Source Inverter

LIST OF COMMON SYMBOLS

A_{inv}	Magnitude of inverter output current
A_s	Magnitude of grid current
A_v	Magnitude of inverter terminal voltage
C, C_L	*RLC* load capacitance
E	Magnitude of rated grid voltage
I_{base}	Current base value in per-unit system
K, K_f	Sandia Frequency Shift positive feedback gain
K_v	Voltage droop slope
K_ω	Frequency droop slope
L, L_L	*RLC* load inductance
L_f	Inverter series filter inductance
L_g	Distribution line inductance
L_s	PCC level algorithm output
L_v	DG local algorithm output
P, P_{inv}	Inverter output active power
P_o	Initial active power assigned to the DG unit
P_D	Real power term determined by the frequency-droop characteristic
P_L	Load active power
P_N	Network active power

P_{ref}, Q_{ref}	Inverter power regulator power references
P_{RS}	Real power term determined by the frequency-restoration block
Q, Q_{inv}	Inverter output reactive power
Q_o	Initial reactive power assigned to the DG unit at nominal voltage
Q_{CL}	*RLC* load capacitance reactive power
Q_f	*RLC* load quality factor
Q_f^*	Critical quality factor for SFS IDM
Q_f^{**}	Critical quality factor for SIDM
Q_L	Load reactive power
Q_{LL}	*RLC* load inductance reactive power
Q_N	Network reactive power
R, R_L	*RLC* load resistance
R_g	Distribution line resistance
S_{base}	Power base value in per-unit system
S_{TH}	Stiffness IDM threshold
S_ω	Stiffness measure
T_s	Data sampling interval
V	Magnitude of inverter terminal voltage
V_{base}	Voltage base value in per-unit system
$V_{\max}$	Upper threshold of over/under voltage protection

$V_{\min}$	Lower threshold of over/under voltage protection
V_r	RMS rated grid voltage
X_g	Distribution line reactance
Z_{base}	Impedance base value in per-unit system
Z_g	Distribution line impedance
Z_L	Equivalent impedance of *RLC* load
cf, cf_o	Initial chopping fraction
f_o	Resonant frequency of *RLC* load
f_o^*	Resonant frequency corresponding to Q_f^*
f_o^{**}	Resonant frequency corresponding to Q_f^{**}
f_g	Utility grid base frequency
f_{is}	Island steady-state frequency
$f_{\max}$	Upper threshold of over/under frequency protection
$f_{\min}$	Lower threshold of over/under frequency protection
f_p	Inverter terminal voltage frequency acquired by PLL
f_s	Data sampling frequency
i_a, i_b, i_c	Three-phase inverter output currents
i_C	Capacitance branch current of *RLC* load
i_d, i_q	Inverter output currents on *dq*-axis
i_{DG}, i_{inv}	DG output current

i_{dref}, i_{qref}	Inverter current regulator current references
i^*_{dref}, i^*_{qref}	Inverter distorted current references
i_L	Inductance branch current of *RLC* load
i_{load}	*RLC* load total current
i_N, i_s	Network current
i_R	Resistance branch current of *RLC* load
k_{ii}	Integral gain of inverter current regulator
k_{ip}	Integral gain of inverter power regulator
k_{iPLL}	Integral gain of PLL controller
k_{iRS}	Integral gain of the frequency-restoration block
k_{pi}	Proportional gain of inverter current regulator
k_{pp}	Proportional gain of inverter power regulator
k_{pPLL}	Proportional gain of PLL controller
k_{pRS}	Proportional gain of the frequency-restoration block
p	Derivative operator
s	Laplace operator
u_d, u_q	Inverter current regulator output voltages
v_1, v_{PCC}	Bus voltage at the PCC
v_a, v_b, v_c	Three-phase inverter terminal voltages
v_d, v_q	Inverter terminal voltages on *dq*-axis

v_{DG}	DG terminal voltage
v_{sa}, v_{sb}, v_{sc}	Three-phase supply power system voltages
v_{sd}, v_{sq}	Supply power system voltages on *dq*-axis
Δ	Small-signal variables
$\Delta\mathbf{u}$	Small-signal input vector
$\Delta\mathbf{x}$	Small-signal state variable vector
ΔP	Active power mismatch
ΔQ	Reactive power mismatch
δ_0	Initial phase angle of inverter terminal voltage
θ	Phase angle of inverter terminal voltage
θ_f	Equivalent phase shift angle introduced by SFS
θ_p	Inverter terminal voltage phase angle acquired by PLL
φ_i	Phase angle of inverter output current
φ_L	Phase angle of total *RLC* load current
φ_s	Phase angle of grid current
ω	Angular frequency of inverter terminal voltage
ω_o	Resonant angular frequency of *RLC* load
ω_g	Utility grid base angular frequency
ω_{is}	Angular frequency of islanded DG system
ω_p	Inverter terminal voltage angular frequency acquired by PLL

CHAPTER 1: INTRODUCTION

A lot of work has been conducted recently to facilitate the idea of smart grid into existing distribution systems. Many different definitions can be found for the term “Smart grid”, but the closest one seems to be introduced by the US Department of Energy website as follows: “A smart grid is an electrical grid that uses information and communications technology to gather and act on information, such as information about the behaviors of suppliers and consumers, in an automated fashion to improve the efficiency, reliability, economics, and sustainability of the production and distribution of electricity” [1]. From this definition, availability of information and two-way communication seems to be the key behind the future concept of smart grid. Additionally, the “smart” utilization of these information toward an autonomous behavior is essential to improve efficiency, reliability, safety and sustainability of existing distribution networks.

The tremendous increase in the number of employed Distributed Generations (DGs) in today’s grid has stimulated further research to improve performance and reliability of those newly added components. The concepts of macro- and micro-grid came into place where a localized group of energy sources and loads operate while connected to a traditional grid (macro-grid) or autonomously when traditional grid is disconnected (micro-grid). The distributed resources could include photovoltaics or solar cells, wind turbines, fuel cells and other energy sources. Both macro- and micro-grids are intended to be part of the so called smart grid structure. Figure 1-1 shows a visionary diagram of future smart grid structure where micro-grid structure is illustrated [2].

In Figure 1-1, it can be seen that protection schemes, in addition to smart behavior and demand management, will play a major role in improving future grid reliability.

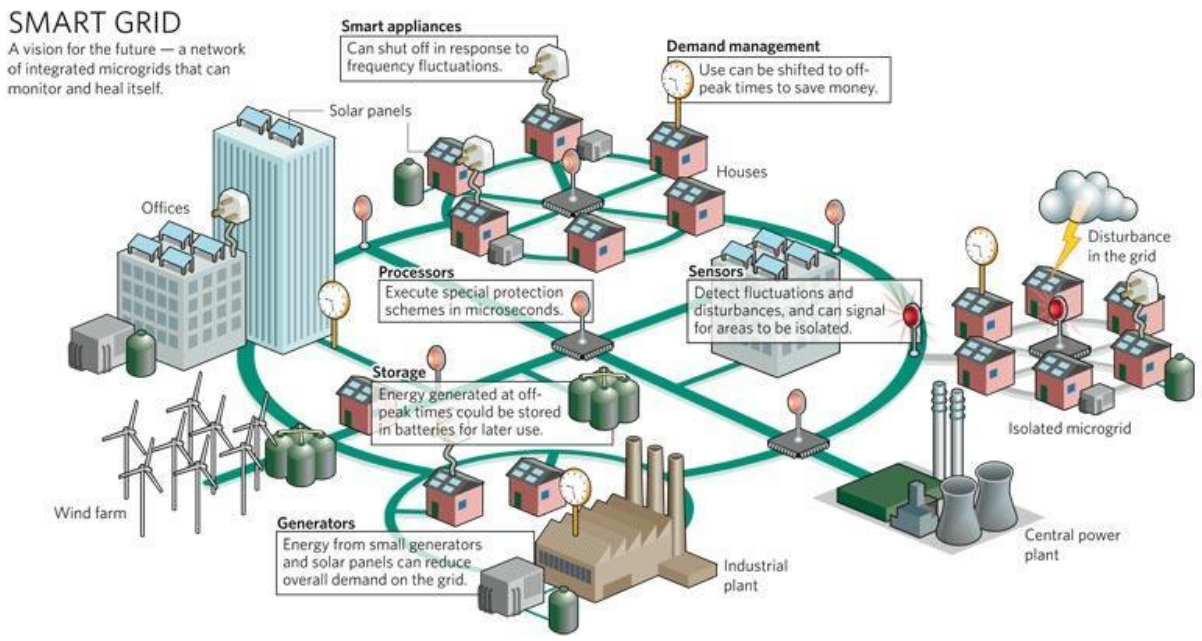

Figure 1-1: Future smart grid diagram illustrating micro-grid structure.

The focus of this work will be toward development of new techniques that can efficiently detect the formation of a micro-grid or the so called islanding detection problem. Islanding is the case where part of the grid including a load and a DG is separated from the rest of the grid and continues to operate. Many standards and detailed reports have been issued to address the requirements for grid-connected DGs as well as anti-islanding requirements and testing requirements for islanding detection [3]-[15]. It is important for grid-connected inverters to be able to detect an islanding condition and to be equipped with a reliable anti-islanding algorithm that will efficiently disconnect the DG when islanding is detected in a timely manner [3]-[5]. There are many reasons behind disconnecting unintentional islanding DGs. An important reason is the safety of maintenance utility workers. For example, if a line that is scheduled for maintenance is disconnected by a network operator, then the confusion, resulted from a maintenance personnel trying to work on a line that is assumed to be de-energized while it is

actually still energized by an unmonitored DG unit, is not tolerated. This scenario posses a severe threat to the safety of workers and might result in severe injury or even death. Another reason is the safety of equipments where reclosing the switch by utility on an out-of-phase island might destroy inverter components for inverter-based DGs [12]. Also, utility as well as distributed resource owner will be found liable in case of any electrical damage to customer equipment caused by either voltage or frequency operating outside acceptable ranges [15].

Islanding Detection Methods (IDMs) are divided into three categories: local passive IDMs [15]-[22], local active IDMs [15]-[19], [23]-[25], and remote or communication based techniques [15]-[17].

Passive methods basically monitor selected parameters such as voltage and/or frequency where no perturbation or disturbance is injected by the inverter. The decision on existence of an islanding condition will be based upon the behavior of these parameters. Some of the commonly known passive IDMs are Over/Under Frequency protection (OUF), Over/Under Voltage protection (OUV), voltage phase jump, and detection of voltage or current harmonics [15]. The OUF, for example, monitors frequency of voltage at the point of couple coupling (PCC) between the DG-inverter and utility where islanding is detected if frequency exceeds pre-specified threshold values for a specific amount of time (delay time). The delay time is proposed to avoid excessive nuisance tripping due to short-term disturbances [3].

Active techniques, in addition to monitoring certain parameters, inject small perturbation to enhance the drifting behavior caused by losing grid-connectivity. Active Frequency drift (AFD), Sandia Frequency Shift (SFS), Slip-Mode phase Shift (SMS), and Sandia Voltage Shift (SVS) methods are examples of commonly used active IDMs. SFS can be implemented in inverter controller where the DG output current is injected at a biased angle, in relative to PCC

voltage, with a constant known as initial chopping fraction (cf_o) and a frequency error multiplied by a gain known as the SFS gain (K). Other active IDMs rely on injecting negative sequence current or disturbances in either the direct axis (*d*-axis) or the quadrature axis (*q*-axis) current controllers to detect islanding [26], [27].

Remote or communication-based techniques are usually implemented at utility level where some sorts of communication are provided between utility side and customer side. Examples of those techniques are impedance insertion, power line carrier communications (PLCC), and supervisory control and data acquisitions (SCADA) [15]. In PLCC, a transmitter and receiver are installed at utility and customer sides, respectively. The detection of the transmitted signal by the receiver will indicate that the grid is connected while the absence or interruption of this signal corresponds to islanding condition. Then, a signal will be sent to DG-inverter to cease operation.

Conventionally, IDMs are evaluated using the concept of Non-Detection Zone (NDZ) which was developed and implemented using different methods such as power mismatch and phase criteria [28]-[38]. NDZs are regions in an appropriately defined space in which the islanding detection scheme under test fails to detect islanding in a timely manner [29], [37]. *RLC* load resonant frequency−quality factor ($f_o - Q_f$) space has been proven to be more representative for AFD and SFS NDZs [30].

To compare among those techniques, passive techniques are generally simple to implement at a low cost where no power quality degradation or interference with maximum power point tracking (MPPT) operation are presented by those techniques. However, passive techniques suffer from relatively large NDZs and relatively larger time is required by passive IDMs to detect islanding condition. On the other hand, active IDMs are highly effective with

smaller NDZ compared to passive methods. Also, faster response or detection time is provided by those techniques in comparison to passive ones. Nevertheless, active IDMs require output power quality of inverter-based DG to be reduced slightly due to the injected perturbation. Also, for systems with high DG penetration, active techniques raise stability concerns since the injected disturbance is a destabilizing force in general. Another important issue with active IDMs is scalability where different active IDMs might degrade the performance of each other in multi-DG system. Furthermore, the interaction between active IDMs and different interface controls has been of concern for protection engineers and researchers [37]-[40]. In [38] and [40], it is shown that SFS is more effective for constant current-controlled inverter in comparison to constant power-controlled inverter where the later controller counter effect perturbation introduced by SFS. In contrast, communication-based techniques have zero NDZ if implemented properly with no degradation to inverter power quality. However, those techniques are relatively expensive and it would be economical for systems with high DG penetration only.

Recently, hybrid IDMs that combine advantages of both passive and active techniques are proposed in [41]-[43]. In [41], a hybrid technique, that combines SFS and voltage unbalance and total harmonic distortion, is proposed. It is shown that the new technique overcomes the drawbacks resulted from using each technique separately and hence provides a better performance.

The main idea behind this thesis is to combine advantages of multiple techniques where limited-communication or synchronization is required to enhance overall islanding detection capability for the multi-DG system. Also, dynamics resulting from an islanding condition will be utilized to develop a distributed two-level algorithm that can successfully detect islanding condition for both single and multi-DG systems. Furthermore, the concept of dispersed

frequency perturbation is used to develop a new active IDM that eliminate the need of communication among different DGs in the multi-DG system.

The main results of this thesis are presented in Chapters 2 and 3. In the first section of Chapter 2, a new IDM is proposed to dynamically estimate islanding occurrence. The proposed dynamic estimators estimate both amplitudes and phase angles of the current injected by the grid at the Point of Common Coupling (PCC) with the DG in addition to the DG's bus voltage. A distributed two-level algorithm is proposed to detect an islanding condition for both single and multi-DG configurations. Analytical design and transient analysis are carried out for the islanding detection problem to determine the Non-Detection Zone (NDZ) of the proposed Islanding Detection Algorithm (IDA). The IEEE 34-bus network is used to demonstrate the effectiveness of proposed technique. A local low-frequency meshed communication network is sufficient to achieve distributed islanding detection capability for a general multi-DG network with negligible NDZ. It is shown through simulations that the proposed IDM can successfully distinguish an islanding condition from other disturbances that may occur in power system networks. One issue with the dynamic estimator is that no analytical proof of robustness and convergence can be obtained for the RLS estimator. Hence, a robust non-linear observer is proposed in the next section as an alternative to the RLS algorithm.

The second section of Chapter 2 provides the design of a robust non-linear adaptive observer for the purpose of islanding detection of inverter based Distributed Generation (DG). The non-linear observer provides simultaneous online estimates for the amplitude and frequency of a noisy sinusoidal signal where amplitude estimation values of grid current will be used to determine the existence of islanding condition or not at PCC level. The main goal of this section is to provide analytical derivations and proofs of robustness and convergence for the proposed

non-linear observer and to utilize results of proposed observer for the islanding detection problem. The IEEE 34-bus system with inverter-based DGs is used to demonstrate the effectiveness of the proposed observer. Simulations are carried out for both sections to verify analysis. It is shown through simulation that the proposed non-linear observer provides better robust performance against harmonics and noise than the dynamic estimator.

Lately, the Sandia Frequency Shift (SFS) IDM has been a hot research topic for protection engineers due to its high performance to cost ratio. It is known that the choice of gain (K) in the SFS scheme has direct impact on stability of a system with grid-connected DGs. In the first section of Chapter 3, a scheduled perturbation technique is proposed to reduce such stability impact of K and its role in eliminating the Non-Detection Zone (NDZ). In the proposed technique, initial chopping fraction (cf) is used to compensate for reduction in K, and zero NDZ is achieved under a zero gain K through increasing cf. It is shown by analysis that theoretical NDZ reduction can be achieved by increasing cf beyond certain thresholds. Simulations for single and multi-DG systems are carried out to verify the analytical analysis. It is shown that an appropriate design of scheduled signal duty cycle (d) is of critical importance to realize the proposed reduction in NDZ. Synchronization of perturbation signals for multi-DG system is required, and a delay of 0.33s is shown to be tolerated for a two-DG system. Synchronization can be achieved either through locally synchronized timers or by limited communication among DGs. The proposed technique is desired for systems with high DG penetration in order to reduce the negative impact on stability by K. The proposed scheduled perturbation is limited to DG systems with constant current controllers. Also, for systems with very large number of DGs, implementing this technique will be too involved and it might be

extremely difficult to synchronize their performances. Hence, a new active IDM is proposed for multi-DG systems in the second section of Chapter 3.

In the second section of Chapter 3, a new active IDM is proposed, and it depends on estimating an overall transient stiffness-measure for the multi-DG system such that a clear separation between prior- and post-islanding stiffness is established. For the multi-DG system, the concept of dispersed frequency perturbation is utilized where each DG is required to perturb at distinct frequencies to avoid spectrum overlapping. By doing so, the proposed technique can be applied to a large number of DG systems with no type of communication required among different DGs. Simulation results show that the proposed technique is scalable and robust against different loading conditions, variation in grid stiffness level, number of connected DGs, and different types of DG controllers. It is also shown that the proposed technique can successfully distinguish islanding condition from other disturbances that may occur in power system networks.

The rest of the thesis is organized as follows. Chapter 2 presents two techniques for designing estimators for both the grid current and the DG bus voltage for the purpose of detecting islanding condition in a distributive manner. Techniques to improve performance and multi-DG islanding detection capability are introduced in Chapter 3. Conclusions are drawn in Chapter 4. Thesis limitations and some possible directions for future research are pointed out in Chapter 5.

CHAPTER 2: DESIGN OF GRID CURRENT AND BUS VOLTAGE ESTIMATORS FOR DISTRIBUTED ISLANDING DETECTION

This chapter presents two main problems. The first problem, in section 2.1, is to design a dynamic estimator to estimate the amplitudes and phase angles of both the grid current and the DG bus voltage for the purpose of islanding detection. Section 2.2 illustrates the design of a robust non-linear observer that estimates grid current amplitude and frequency and the results are used to determine the existence of islanding condition.

2.1 Dynamic Estimation for Amplitude and Phase of Grid Current and DG Bus Voltage

2.1.1 Introduction

Islanding detection schemes has been of great interest to enhance reliability and safety of growing green energy. Many schemes have been developed to detect islanding where locally utilized ones have been widely used such as Over/Under Voltage Protection (OUV) and Over/Under Frequency Protection (OUF) [15], [16]. Those schemes utilize Root Mean Square (RMS) measurements to detect islanding condition and they suffer from large Non-Detection Zone (NDZ) regions. As shown in [29]-[32], most of the IDMs are analyzed in the steady state, and thus not taking into account the transient analysis. According to the NDZ graphs in [30] and [37], the performance of active IDMs deteriorate as the load quality factor (Q_f) increases; while passive IDMs typically have very large NDZ regions.

In this section, the dynamics induced from an islanding condition are modeled and used to detect an islanding situation. A distributed two-level algorithm is proposed to detect islanding condition for single and multi-DG networks. The proposed algorithm is implemented both

locally at each DG and at the Point of Common Coupling (PCC) with the grid. A dynamic version of OUV is implemented locally at each DG to reduce communication requirement while achieving distributed multi-DG islanding detection capability. As such, the resulting IDA is improved to ensure wide applicability and robust performance. The proposed technique is shown to have negligible NDZ, and it can estimate both the grid current amplitude and phase angle. This new IDM belongs to the class of local passive methods since no disturbance is applied to drift either frequency or voltage amplitude. In addition, analysis is carried out in this section to quantify the NDZ for the proposed IDM, and a three-dimensional NDZ subspace is explicitly found. For a general multi-DG structure, a local low-frequency meshed communication topology is sufficient to achieve robust islanding detection with negligible NDZ. It is also shown that the proposed distributed algorithm is robust against different types of disturbances and power network events such as three-phase short circuit, startup of induction motors, switching of capacitor, and load variations.

This section is organized as follows. A DG interface model and its testing conditions are introduced in subsection 2.1.2. Analyses of islanding conditions are carried out in subsection 2.1.3. The proposed dynamic estimators are designed in subsection 2.1.4, and the islanding detection algorithm is presented in subsection 2.1.5. The NDZ of the proposed algorithm is investigated with respect to load parameter spaces in subsection 2.1.6. A distributed multi-DG algorithm is proposed in subsection 2.1.7. Performance of the proposed algorithm is tested through simulations in subsection 2.1.8. Finally, discussions are presented in subsection 2.1.9.

2.1.2 Islanding Testing Conditions

A generic model for the transient anti-islanding study is shown in Figure 2-1. The circuit used resembles the anti-islanding testing diagram defined in UL 1741 and IEEE 929-2000 [3], [4].

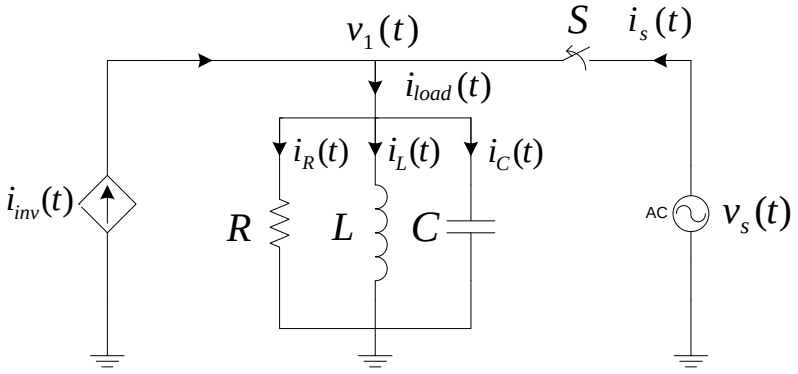

Figure 2-1: A generic model for the transient islanding study.

The following assumptions will be used to simplify analysis and calculations:

1) The utility or grid frequency and amplitude are assumed to be constant, and the reference angle is assumed to be the grid voltage angle. That is, the grid voltage can be represented as $v_s(t) = E\sin(\omega_g t + 0^o)$, where E is the amplitude of instantaneous grid voltage, and $\omega_g = 2\pi f_g$ is the grid frequency in rad/sec.

2) The steady-state form of the grid current is expressed as $i_s(t) = A_s \sin(\omega_g t + \varphi_s)$.

3) The dynamics of Phase Locked Loop (PLL) are fast and hence are considered negligible. The PLL input is $v_1(t)$, which is the voltage at the point of common coupling (PCC), and the steady-state PLL output can be given by the following form:

$$\omega_p(t) = \begin{cases} \omega_g(t), & \text{grid is connected} \\ \omega_{is}(t), & \text{grid is disconnected} \end{cases},$$

where ω_{is} is the PLL output frequency after islanding in rad/sec.

4) The inverter employs a constant current controller to supply active power and, if required, reactive power. In addition, the controller dynamics are ignored. That is, $i_{inv}(t) = A_{inv}\sin(\omega_p t + \varphi_i)$, where ω_p is the frequency output of the PLL in rad/sec.

5) The load is assumed to be a parallel *RLC* load (and it meets both islanding and nominal operation requirements).

6) The grid impedance is neglected.

2.1.3 Steady State and Transient Analysis

For a parallel *RLC* load, its quality factor (Q_f) is defined as:

$$Q_f = \omega_o RC = \frac{R}{\omega_o L} = R\sqrt{\frac{C}{L}}\ , \tag{2.1}$$

where $\omega_o = 2\pi f_o = 1/\sqrt{LC}$ is the resonance frequency of the *RLC* load in rad/sec.

2.1.3.1 Mode 1, Switch (*S*) is Closed

Let us assume that the steady-state form of $v_1(t)$ is given by:

$$v_1(t) = A_v \sin(\omega_g t + \varphi_v),$$

where A_v and φ_v are the amplitude and phase angle of inverter terminal voltage, respectively. Then, the circuit dynamic equations before islanding occurs are:

$$v_1(t) = v_s(t) = L\frac{di_L(t)}{dt},\ \ i_C(t) = C\frac{dv_1(t)}{dt},\ i_R(t) = \frac{v_1(t)}{R}\ . \tag{2.2}$$

It follows from the first assumption in subsection 2.1.2 that the inductor current can be represented in the steady state as follows

$$i_L(t) = \int \frac{v_1(t)}{L} dt = -\frac{A_v}{\omega_g L} \cos(\omega_g t) + i_L(t_o), \tag{2.3}$$

where t_o is the initial time in seconds and $i_L(t_o)$ is the initial inductor current. Similarly, the capacitor current in the steady state can be represented as follows

$$i_C(t) = C \frac{dv_1(t)}{dt} = \omega_g C A_v \cos(\omega_g t). \tag{2.4}$$

A PLL will be used to track the frequency of the Point of Common Coupling (PCC) voltage, $v_1(t)$, and that frequency will be used by the inverter to inject its current in phase with the voltage across the load to yield unity power factor operation (φ_i is zero). In other words, the PLL frequency before islanding is equal to the grid frequency ($\omega_p = \omega_g$). This technique of operating the inverter is categorized as a constant current controlled inverter [39]. It is worth mentioning that high frequency components and distortion caused by inverter's switching can be considered by improving the aforementioned model.

According to [37], the *RLC* circuit parameters for islanding condition are calculated as

$$\begin{aligned} R &= \frac{V_r^{\,2}}{P_L},\ L = \frac{V_r^{\,2}}{2\pi\, f_o Q_f P_L},\ C = \frac{Q_f P_L}{2\pi\, f_o V_r^{\,2}}, \\ A_{inv} &= \frac{\sqrt{2}}{V_r}\sqrt{P_{inv}^{\,2} + Q_{inv}^{\,2}},\ \varphi_i = -\text{atan2}(Q_{inv}, P_{inv}), \end{aligned} \tag{2.5}$$

where

atan2(.): is a Matlab command used to find the four-quadrant inverse tangent (arctangent),

P_{inv}: is the active power (in Watt) supplied by the inverter before islanding,

Q_{inv}: is the reactive power (in VAR) supplied by the inverter before islanding,

P_L: is the active power (in Watt) absorbed by the *RLC* load before islanding,

V_r: is the Root Mean Square (RMS) value of grid voltage,

f_o: is the resonance frequency (in Hz) of the *RLC* load.

Under zero initial conditions and upon neglecting PLL and controller dynamics, the steady-state grid current becomes:

$$\bar{i}_s(t) = \bar{A}_s \sin(\omega_p t + \bar{\varphi}_s), \tag{2.6}$$

where

$$\begin{aligned} \bar{A}_s &= \frac{\sqrt{2}}{V_r}\sqrt{\Delta P^2 + \Delta Q^2}, \\ \bar{\varphi}_s &= -\text{atan2}(\Delta Q, \Delta P), \end{aligned} \tag{2.7}$$

ΔP: (which equals to $P_L - P_{inv}$) is the active power mismatch between the load and inverter (i.e., the active power injected by the grid), and ΔQ is the reactive power mismatch (i.e., the reactive power injected by the grid). Also, ΔQ can be written in terms of load's resonant frequency (f_o) and quality factor (Q_f) as follows

$$\Delta Q = P_L Q_f \left(\frac{f_o}{f_g} - \frac{f_g}{f_o} \right) - Q_{inv}, \tag{2.8}$$

By applying Kirchhoff Current Law (KCL) and Kirchhoff Voltage Law (KVL) to the circuit shown in Figure 2-1, the following differential equation is obtained

$$\dot{v}_1(t) = -a\, v_1(t) + b[i_s(t) + i_{inv}(t) - i_L(t)], \tag{2.9}$$

where $a = \frac{1}{RC}$ and $b = \frac{1}{C}$.

The solution to the differential equation in (2.9) is

$$v_1(t) = z_1(t) + z_2(t), \tag{2.10}$$

where

$$\begin{aligned} z_1(t) &= e^{-a(t-t_o)} z_1(t_o) + \int_{t_o}^{t} e^{-a(t-\tau)} b\, i_s(\tau)\, d\tau, \\ z_2(t) &= e^{-a(t-t_o)} z_2(t_o) + \int_{t_o}^{t} e^{-a(t-\tau)} b[i_{inv}(\tau) - i_L(\tau)]\, d\tau. \end{aligned} \tag{2.11}$$

2.1.3.2 Mode 2, Switch (*S*) is Open

An islanding condition is simulated by opening the switch (*S*) in Figure 2-1. The circuit dynamic equations after islanding are:

$$v_1'(t) = L\frac{di_L'}{dt} \neq v_s(t),\ i_C'(t) = C\frac{dv_1'}{dt},\ i_R'(t) = \frac{v_1'(t)}{R}. \tag{2.12}$$

The PLL frequency after islanding is equal to the load resonant frequency ($\omega_p = \omega_o$) if Q_{inv} is equal to zero. In case Q_{inv} is not equal to zero, the steady-state value of the PLL frequency after islanding is given by

$$f_{is} = -\frac{f_o Q_{inv}}{2P_{inv}Q_f} + f_o\sqrt{\left(\frac{Q_{inv}}{2P_{inv}Q_f}\right)^2 + 1}\ . \tag{2.13}$$

Furthermore, the RMS value of PCC voltage after islanding is obtained by balancing active power equation after islanding and the result is as follows:

$$V_{is} = V_r\frac{P_{inv}}{P_L}\ . \tag{2.14}$$

In addition, similar to mode 1, the system dynamics can be described by the following differential equation:

$$\dot{v}_1'(t) = -a\, v_1'(t) + b[i_{inv}'(t) - i_L'(t)]. \tag{2.15}$$

And, the solution to (2.15) can be written as follows:

$$v_1'(t) \equiv z_2'(t) = e^{-a(t-t_o)} v_1'(t_o) + \int_{t_o}^{t} e^{-a(t-\tau)} b[i_{inv}'(\tau) - i_L'(\tau)] d\tau . \quad (2.16)$$

2.1.4 Design Procedure

The main concept behind the proposed technique is to detect the transient behavior of grid current during different types of disturbances. The grid current estimation is conducted at the PCC level and is expected to converge to zero when islanding occurs. Additionally, the change in system dynamics from (2.9) to (2.15) will result in voltage variation if i_s is significant. Hence, by estimating the DG bus voltage amplitude, a transient behavior could be detected locally due to islanding. Therefore, the main goal of this paper is to estimate both grid current and DG bus voltage amplitudes such that those estimates are used to distinguish between islanding and other disturbances in power system networks.

In addition to the DG's local current measurement, the proposed design requires either load current measurement or PCC voltage measurement with the knowledge of the load or its estimate. In what follows, PCC voltage (v_1), PLL frequency output (ω_p), and DG current (i_{inv}) are available measurements to the estimator. From both Modes (1 and 2), the estimated version of the PCC voltage can be represented as:

$$\hat{v}_1(t) = \hat{z}_1(t) + z_2(t), \quad (2.17)$$

where

$$\hat{z}_1(t) = e^{-a(t-t_o)} \hat{z}_1(t_o) + \int_{t_o}^{t} e^{-a(t-\tau)} b \hat{i}_s(\tau) d\tau , \quad (2.18)$$

and $\hat{i}_s(t) = \hat{A}_s \sin(\omega_p t + \hat{\varphi}_s)$ is the estimate of the current injected by the grid.

As shown in (2.17), the estimate of $v_1(t)$ includes two parts: one being reconstructed through known measurements (z_2), and the other part being based on the estimate of the grid current ($\hat{z}_1$). Since the solution of $\hat{z}_1$ contains an integration term as shown in (2.18), a sliding integration window will be used to implement the integration of the proposed estimator. Figure 2-2 illustrates how the sliding window works.

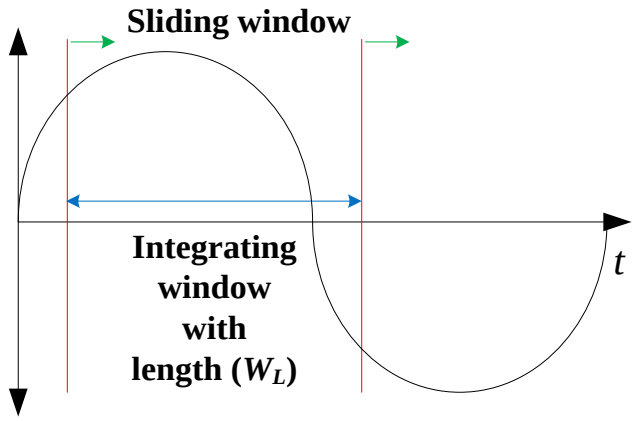

Figure 2-2: A sliding window used in the estimation.

The proposed dynamic estimator utilizes the recursive least square algorithm. In particular, we re-write (2.17) as

$$y_k(i) = \theta_k^{\,T} w_k(i), \tag{2.19}$$

where

$$\begin{aligned}
&w_1(i) = \begin{bmatrix} \int_{t_{i-1}}^{t_{M+i-1}} e^{-a(t_{M+i-1}-\tau)} b \sin(\omega_p \tau) d\tau \\ \int_{t_{i-1}}^{t_{M+i-1}} e^{-a(t_{M+i-1}-\tau)} b \cos(\omega_p \tau) d\tau \end{bmatrix}, \quad w_2(i) = \begin{bmatrix} \sin(\omega_p t_{M+i-1}) \\ \cos(\omega_p t_{M+i-1}) \end{bmatrix}, \\
&\theta_1 = \begin{bmatrix} A_s \cos(\varphi_s) & A_s \sin(\varphi_s) \end{bmatrix}^T, \ \theta_2 = \begin{bmatrix} A_v \cos(\varphi_v) & A_v \sin(\varphi_v) \end{bmatrix}^T, \\
&y_1(i) = v_1(t_{M+i-1}) - v_1(t_{i-1}) - \int_{t_{i-1}}^{t_{M+i-1}} e^{-a(t_{M+i-1}-\tau)} b \left[i_{inv}(\tau) - i_L(\tau) \right] d\tau, \\
&y_2(i) = v_1(t_{M+i-1}),
\end{aligned} \tag{2.20}$$

and

$i = 1,2,3,\ldots,\infty,\ k = 1,2$,

$M = \text{floor}(W_L\, f_s)$: is the number of data points in a window of length W_L and floor is a Matlab command to round the number between brackets toward the nearest lower integer,

$t_{M+i-1} = t_o + (M + i - 1)\times T_s$, $t_{i-1} = t_o + (i-1)\times T_s$,

f_s : is the data sampling frequency in Hz where f_s is assumed to be high enough in order not to lose any transient information,

T_s: is the data sampling interval in seconds ($T_s = 1/f_s$).

In essence, θ_k is the parameter vector to be estimated, $w_k(i)$ is the regression vector, and $y_k(i)$ is the measured signal. Equation (2.19) is obtained by expanding both the estimated grid current and DG bus voltage forms into sine and cosine, by expressing both the grid current and DG bus voltage amplitudes and phases in linearly parameterized forms, and by utilizing the sliding window of integration. Equation (2.20) shows that generating the first estimates of $w_1(i)$ and $y_1(i)$ takes $t_o + M \times T_s$ seconds.

Alternatively, the Laplace domain can be used to obtain formulas for $w_1(i)$ and $y_1(i)$ where there is no need to use an integration window. The details for using the Laplace domain technique can be found in Appendix A.

Given the linearly parameterized expression in (2.19), standard algorithms can be applied to estimate the parameter vector θ_k. The discrete RLS algorithm with forgetting factor is chosen to estimate both the amplitudes and phase angles of the grid current and DG bus voltage. The RLS algorithm relies on the following equations [44]:

$$P_k(i+1) = \frac{1}{\lambda_k}\left(P_k(i) - \frac{P_k(i) w_k(i) w_k^T(i) P_k(i)}{\lambda_k + w_k^T(i) P_k(i) w_k(i)} \right), \tag{2.21}$$

$$\hat{\theta}_k(i+1) = \hat{\theta}_k(i) - P_k(i+1) w_k(i) \left[w_k^T(i) \hat{\theta}_k(i) - y_k(i) \right], \tag{2.22}$$

where

$\hat{\theta}_k(i) = \begin{bmatrix} \hat{\theta}_{k1} & \hat{\theta}_{k2} \end{bmatrix}^T$: is the RLS estimated parameter vector for $\theta_k \in \Re^2$ at the i^{th} instant,

$e_k(i) = w_k^T(i)\hat{\theta}_k(i) - y_k(i)$: is the error signal,

$P_k(i)$: is the covariance matrix $\in \Re^{2\times 2}$,

$0 < \lambda_k \le 1$: is the forgetting factor which determines the discount or length of memory being used. $\lambda_k = 1$ stands for zero forgetting factor or infinite memory case.

Convergence of the algorithm is guaranteed since the regression vectors $w_k(i)$ defined in (2.20) are persistently excited [44]. It follows from the RLS results that the estimates of both grid current and DG bus voltage amplitudes (in per-unit) and phases (in degree) can be calculated as follows:

$$\begin{aligned} \hat{A}_s &= \frac{1}{I_{base}} \sqrt{\hat{\theta}_{11}^{\,2} + \hat{\theta}_{12}^{\,2}}, \quad \hat{\varphi}_s = \frac{180}{\pi} \operatorname{atan2}\left(\hat{\theta}_{12}, \hat{\theta}_{11}\right), \\ \hat{A}_v &= \frac{1}{V_{base}} \sqrt{\hat{\theta}_{21}^{\,2} + \hat{\theta}_{22}^{\,2}}, \quad \hat{\varphi}_v = \frac{180}{\pi} \operatorname{atan2}\left(\hat{\theta}_{22}, \hat{\theta}_{21}\right). \end{aligned} \tag{2.23}$$

where V_{base} and I_{base} are the single-phase base voltage and current, respectively.

2.1.5 Islanding Detection Algorithm

The algorithm of detecting an islanding condition employs a sliding rectangular test region of a time length T_d and with width of $2\zeta_d$, as shown in Figure 2-3.

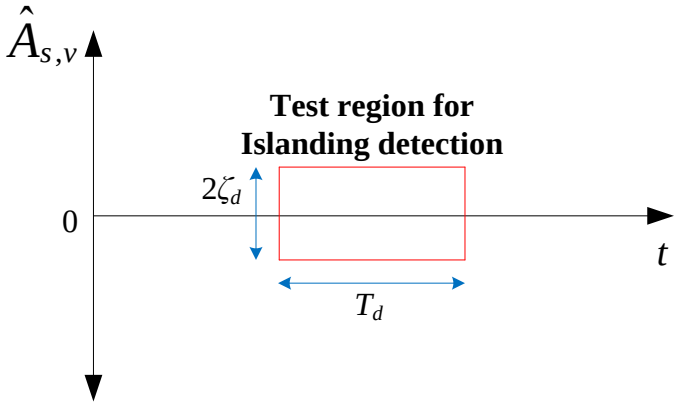

Figure 2-3: The test region for achieving robust islanding detection.

The same testing region, but with a width of $2\zeta_\varphi$, is used in phase estimation. The following quantities can be defined as follows:

$$\begin{aligned} A_{err}^{s,v}(j) &= A_{\max}^{s,v}(j) - A_{\min}^{s,v}(j) \\ &= \max\left(\hat{A}_{s,v}(j - N_d : j)\right) - \min\left(\hat{A}_{s,v}(j - N_d : j)\right), \\ \varphi_{err}^{s}(j) &= \max\left(|\hat{\varphi}_s(j - N_d : j)|\right) - \min\left(|\hat{\varphi}_s(j - N_d : j)|\right), \end{aligned} \tag{2.24}$$

where $j = N_d + 1, N_d + 2, \ldots$ and $N_d = \text{floor}(T_d f_s)$.

Figure 2-4 shows the flowchart of the proposed IDAs. The parameters $V_{\max}$ and $V_{\min}$ are the upper and lower thresholds for Over/Under Voltage Protection (OUV), respectively. The outcomes of both algorithms' outputs can be interpreted as follow:

$$L_{s,v}(j) = \begin{cases} 0 & \text{Islanding is detected} \\ 1 & \text{Normal operation} \\ 2 & \text{Oscillation or transition} \end{cases}. \tag{2.25}$$

It can be seen from Figure 2-4 (b) that a dynamic version of OUV is implemented locally at the DG side. The proposed DG level algorithm provides local detection of both grid oscillation and islanding condition. Hence, the DG level algorithm will play a major role in reducing

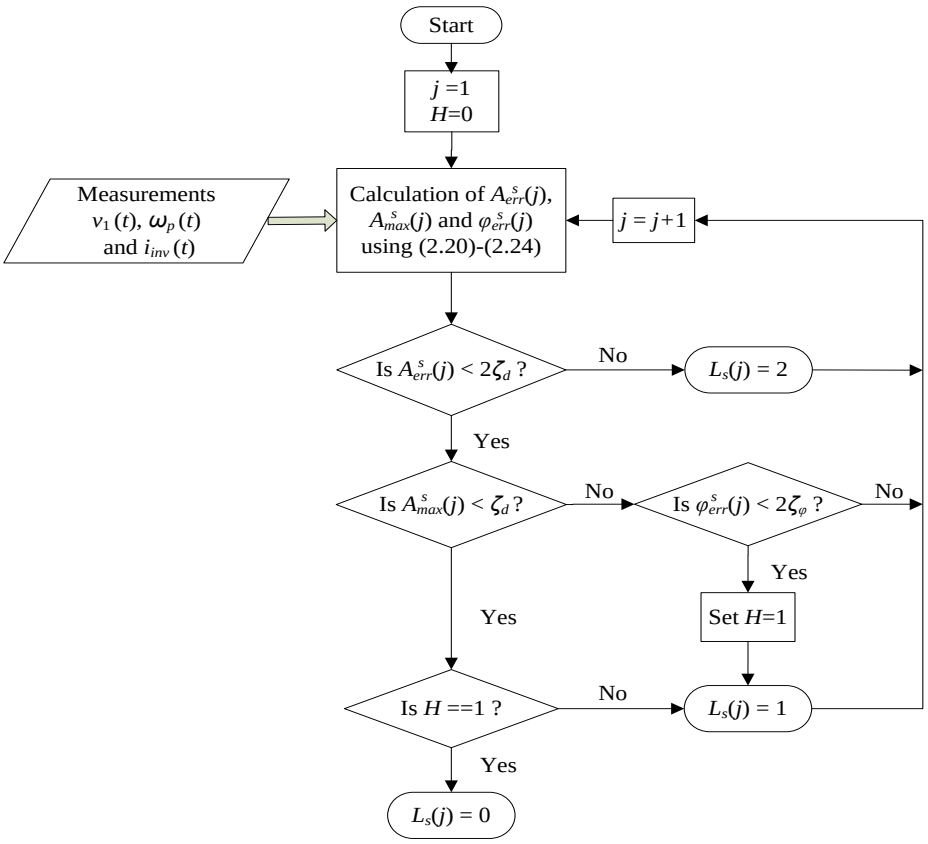

Figure 2-4: Flowchart of the proposed IDAs: (a) PCC level algorithm. (b) DG local algorithm.

communication requirement while achieving distributed islanding detection capability for a general multi-DG structure as will be shown in subsection 2.1.7. However, the NDZ of the proposed DG level algorithm is similar to OUV NDZ and is considered to be a very large NDZ [37]. Therefore, a PCC level algorithm is proposed in Figure 2-4 (a) to significantly reduce the overall NDZ. A triggering variable H is used in the PCC level algorithm to prevent premature islanding detection. Hence, the above logic distinguishes islanding from other transition cases, which prevents false islanding detection, improves islanding confirmation decision, and enhances robustness of the proposed islanding detection algorithm. For the simple case shown in Figure 2-1, the PCC level algorithm in Figure 2-4 (a) is also implemented locally at the DG side since the DG is assumed to have access to PCC information. As a result, both algorithms in Figure 2-4 can detect islanding condition while negligible NDZ can be achieved only by the PCC level algorithm as will shown in subsection 2.1.6.

Standards such as IEEE 929-2000 require disconnection of inverter when islanding is confirmed for safety reasons [3]. The DG is required to cease operation (unless micro-grid operation is permitted) if either one of the algorithms presented in Figure 2-4 detected islanding condition. It is recommended for an inverter to maintain its normal operation under grid oscillation cases in order to support loads and suppress grid oscillations. It is shown in Figure 2-3 that threshold value ζ_d (or ζ_φ) and window length T_d are standard parameters to achieve robust identification. In practice, the value of ζ_d should be chosen to be larger than the noise level such that steady-state normal operation ($L_v = L_s = 1$) can be achieved for both algorithms in Figure 2-4 during normal DG operations. Also, the window length should not be too small or too large because a very short window would be insufficient for islanding detection while a long window would confirm an islanding condition but introduce an unnecessary delay. Different ζ_d values

could be used for each algorithm in Figure 2-4 if necessary and a single value is used for the rest of this section for simplicity.

2.1.6 Non-Detection Zone of PCC Level IDA

The NDZ for the DG local algorithm in Figure 2-4 (b) is similar to OUV NDZ which has been studied in [32] and [37]. However, the proposed algorithm will provide higher sensitivity to detect oscillation since it depends on instantaneous estimation of bus voltage amplitude rather than RMS values. On the other hand, a theoretical NDZ can be found for the PCC level algorithm in Figure 2-4 (a) by studying the grid current steady state behavior.

In order to develop a theoretical boundary condition for the non-detection zone of the PCC level algorithm presented in Figure 2-4 (a), the following assumptions are used:

1) The grid frequency and voltage are assumed to be constant.
2) The algorithm used for estimating the grid current amplitude should provide a small consistent excitation such that it responds to an error signal caused by a step change in amplitude from the steady-state value defined in (2.7) to zero. The time needed for convergence of estimated grid current amplitude to zero after islanding occurrence is not considered when estimating NDZ region.
3) The algorithm has operated in a normal operating condition, with a steady-state angle error less than $2\zeta_{\varphi}$, at least once during the whole time interval of estimation before islanding occurrence. In other words, the variable H was set to one before islanding occurrence for load cases lying outside the NDZ of the proposed algorithm.
4) The sensitivity parameters ζ_d and ζ_{φ} are properly designed to tolerate measurement noise where ζ_d is in per-unit system.

5) The load doesn't change significantly during islanding.

Then, the non-detection zone for the PCC level algorithm in Figure 2-4 (a) is determined by the loading cases that will not trigger H when the estimated grid current amplitude converges to a value less than half of the test region width as shown in Figure 2-3. That is, the NDZ for the proposed algorithm is bounded by the following region:

$$\overline{A}_{spu}{}^2 \le \zeta_d{}^2$$

where $\overline{A}_{spu} = \overline{A}_s / I_{base}$ is the per-unit value of the grid current steady-state amplitude defined in (2.7).

The equilibrium condition, which can be used to plot the boundaries of the NDZ region, is given as follows:

$$\overline{A}_{spu}{}^2 - \zeta_d{}^2 = 0 \tag{2.26}$$

2.1.6.1 NDZ in Reactive Vs. Active Power Mismatch Space

The reactive-active power mismatch space is one of the commonly used load spaces to evaluate the performance of anti-islanding detection algorithms [37]. In order to develop the equilibrium condition in this space, let us assume a 1kW inverter that can supply reactive power with an active power mismatch not necessarily equal to zero (i.e. $Q_{inv} \neq 0$ and $\Delta P \neq 0$). Then, the equilibrium condition can be written as follows:

$$\Delta Q_n{}^2 + \Delta P_n{}^2 - \zeta_d{}^2 = 0 \tag{2.27}$$

where $\Delta P_n = \dfrac{\Delta P}{S_{base}}$, $\Delta Q_n = \dfrac{\Delta Q}{S_{base}}$, and $S_{base} = P_{base} = Q_{base}$.

Figure 2-5 shows the NDZ for the proposed IDM for different values of ζ_d in the power mismatch space.

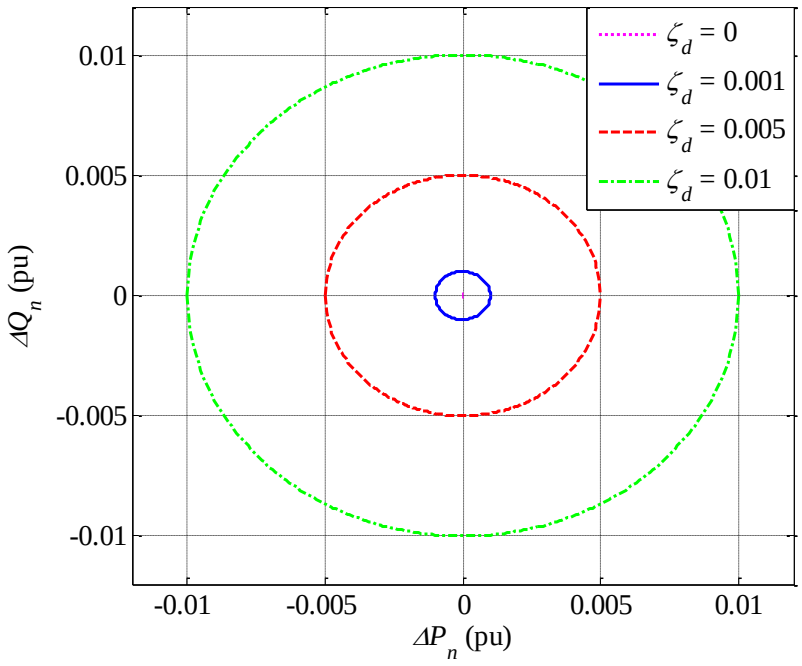

Figure 2-5: NDZ of the proposed PCC level algorithm in power mismatch space for different values of ζ_d.

It can be seen from Figure 2-5 that, as ζ_d becomes smaller, the theoretical circular NDZ for the PCC level algorithm converges to a single point at (0,0). The problem with the power mismatch space is that it doesn't represent all possible *RLC* loading conditions. Also, it is known that active IDMs' performances depend upon the load's Q_f and hence the power mismatch space is inadequate to assess the performance of active IDMs [29].

2.1.6.2 NDZ in Load Resonant Frequency Vs. Quality Factor Space

The load resonant frequency−quality factor ($f_o - Q_f$) space is proposed in [30] to address the drawbacks of the power mismatch space. Let us assume that we have a 1kW inverter that supplies only active power to the full load (i.e. $\Delta P = Q_{inv} = 0$). Then, by substituting (2.8) into (2.27), one can obtain the following equilibrium condition:

$$f_o^{\,4} - f_g^{\,2}\left(2+\frac{\zeta_d^{\,2}}{Q_f^{\,2}}\right)f_o^{\,2} + f_g^{\,4} = 0 \tag{2.28}$$

The two positive roots of equation (2.28) determine the theoretical NDZ boundaries for the proposed IDM. Figure 2-6 shows the NDZ for the proposed IDM for different values of ζ_d in $f_o - Q_f$ space. Result shows that as ζ_d value is increased, the NDZ becomes larger at low Q_f values while the two NDZ lines converge to 60 Hz as Q_f value becomes larger. The increase in NDZ width at low Q_f values is a result of small values of grid current amplitude as will be shown later by simulation. On the other hand, the NDZ collapses to a single line at 60 Hz as ζ_d value converges to zero. Therefore, the single point in $\Delta Q_n - \Delta P_n$ space corresponds to a single line at 60 Hz in $f_o - Q_f$ space. For design purposes, the value of ζ_d is set equal to 0.001pu in the simulations and a window of width 0.002pu and length 35ms (i.e., 2 cycles in 60Hz) is shown to provide robust performance against disturbances and to successfully distinguish islanding from other disturbances that may occurs in power system networks (as will be shown in subsection 2.1.8). In Figure 2-7, the NDZ for the proposed dynamic estimator IDM is compared to the Over/Under Frequency Protection (OUF) NDZ and the NDZ of the SFS (with $cf_o = 0$ and $K = 0.15$) [45].

The NDZs plot in Figure 2-7 show a small NDZ width at low Q_f for the PCC level algorithm NDZ which can be considered negligible and the overall size of NDZ for proposed technique is much smaller than OUF or SFS NDZs. Therefore, the NDZ for the proposed PCC level algorithm can be approximated by a single line at 60 Hz in $f_o - Q_f$ space or a single point at (0,0) in $\Delta Q_n - \Delta P_n$ space. However, the $f_o - Q_f$ space doesn't entirely represent the overall NDZ for the proposed algorithm since the condition of ΔP being equal to zero is not always the

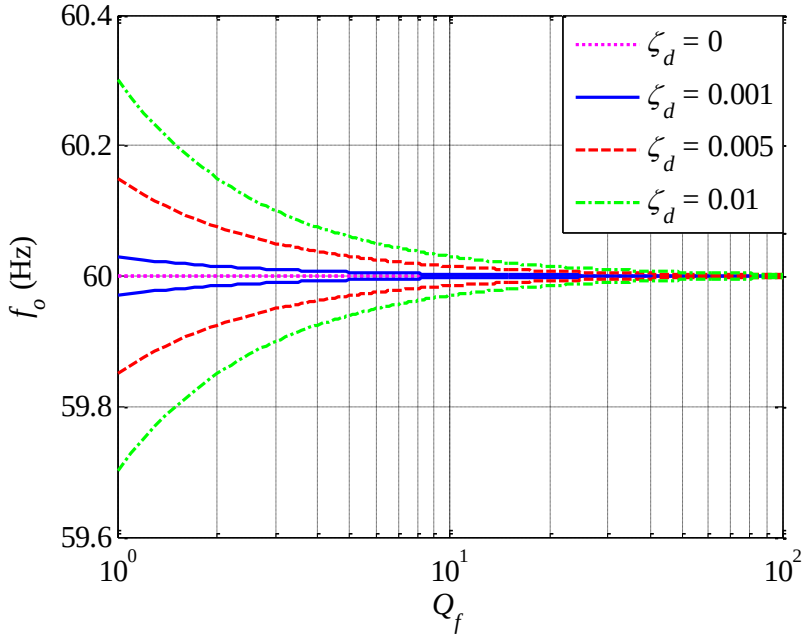

Figure 2-6: NDZ of the proposed PCC level algorithm in $f_o - Q_f$ space for different values of ζ_d.

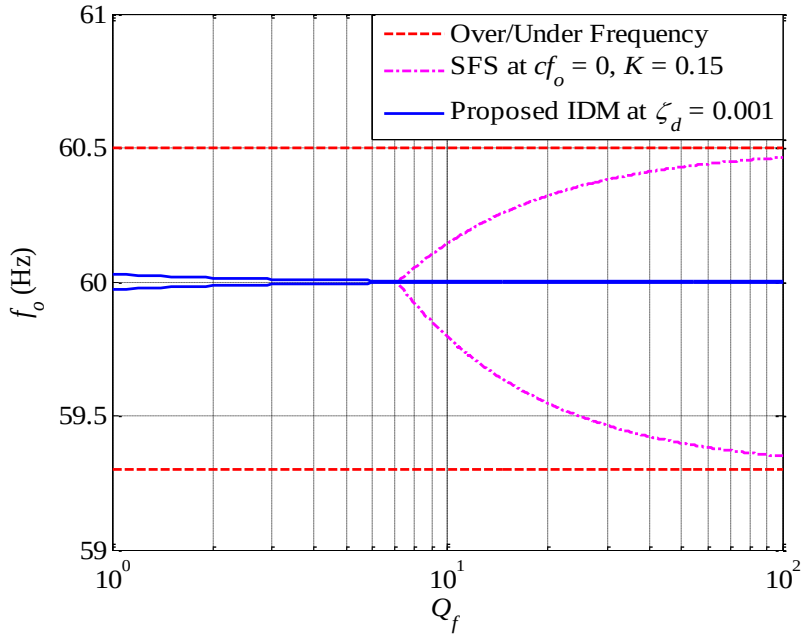

Figure 2-7: Comparison of NDZs between different IDMs and the proposed PCC level algorithm.

case. In [30], a modified Q_f value is proposed when ΔP is not equal to zero. This technique might be suitable for active IDMs where NDZ is dependent on loading condition after islanding. However, the NDZ for the proposed technique depends on small estimated amplitude values that cannot be considered as an islanding condition. Therefore, a 3-D NDZ space is needed to reveal all the possible load cases for the proposed IDM as will be seen in the next subsection.

2.1.6.3 NDZ in 3-D Space

In order to combine the advantages of both previously presented spaces, a 3-D NDZ space is proposed to represent all possible load cases for the proposed IDM. The proposed 3-D space contains Q_f, f_o, and ΔP_n. If the inverter supplies zero reactive power ($Q_{inv} = 0$), the following equilibrium condition is obtained by substituting (2.8) into (2.27):

$$Q_f{}^2 = \left(\frac{f_o f_g}{(1+\Delta P_n)(f_g{}^2 - f_o{}^2)} \right)^2 \left[\zeta_d{}^2 - \Delta P_n{}^2 \right] \tag{2.29}$$

The negative root of (2.29) is ignored since Q_f is positive. Figure 2-8 shows the theoretical 3-D NDZ for proposed technique with ζ_d = 0.001pu. As seen in Figure 2-8, the proposed PCC algorithm has a small NDZ at low Q_f values and negligible NDZ at high Q_f values. Therefore, the overall NDZ of the proposed PCC level algorithm is much smaller than the available IDMs. It is worth mentioning that all the derivations for NDZ assume a proper choice of ζ_φ in order to properly trigger H to indicate that both estimates of the grid current parameters converge to their steady-state values under the normal operation (before islanding occurrence). Also, a constant VAR compensation can be considered in the derivation of (2.29) and Q_{inv} being equal to zero is used to simplify the formula.

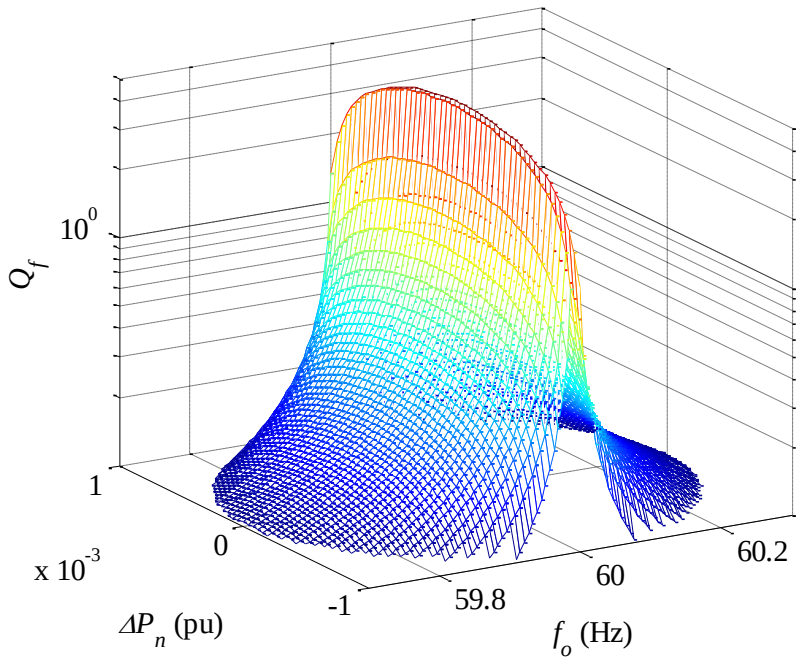

Figure 2-8: The 3-D NDZ for the proposed PCC level algorithm with ζ_d = 0.001pu.

2.1.7 Distributed Multi-DG Islanding Detection Algorithm

The algorithm developed in subsection 2.1.5 assumes that the DG has access to the PCC information and hence both the DG bus voltage and grid current estimations are carried out locally at the DG side. In general, this is not always true since the PCC could be far away from the DG unit. Let us assume the general multi-DG structure shown in Figure 2-9. Z_{line}^{j} and Z_L^j are the line and the local load impedances for the j^{th} DG, respectively. Then, the following distributed algorithm is proposed. First, each DG estimates its own bus voltage (v_{DG}) and produces L_v using the algorithm in Figure 2-4 (b), while the grid current estimation is carried out at PCC level only and the algorithm in Figure 2-4 (a) is applied to determine the status of the grid. Then, there are several cases:

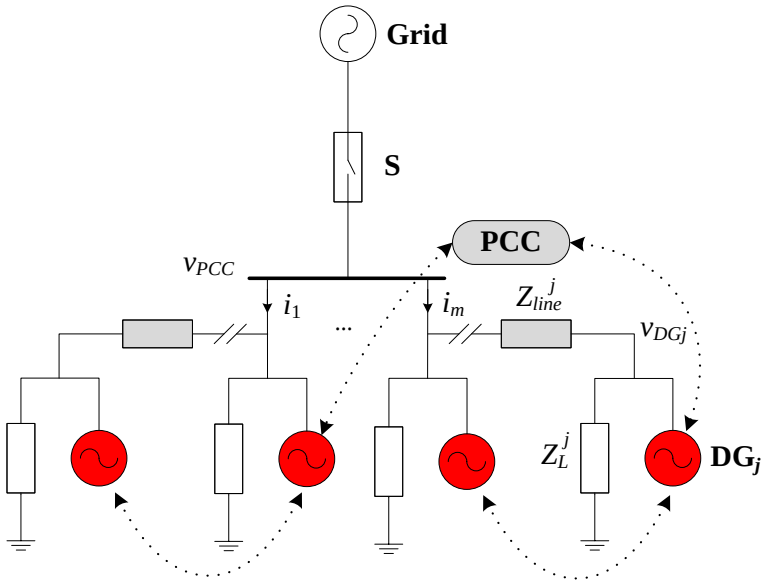

Figure 2-9: General multi-DG structure for distributed multi-DG algorithm.

(i) If the j^{th} DG detected a local islanding condition ($L_v^j = 0$), a signal is sent to PCC to check the status of the grid. While waiting for a response from PCC, the specific DG temporarily ceases its operation in order to protect its own equipment and maintain safety.

a) In case that PCC confirms islanding, a signal is sent through a meshed communication network so that all DGs can take appropriate action (e.g., de-energizing unless islanding operation is permitted).

b) If the PCC only detected grid oscillation, the DG shall receive this information from the PCC and in turn restore its operation, and the rest of DGs would maintain normal operation. If the j^{th} DG couldn't restore normal operation and the local islanding condition is detected again, then the j^{th} DG should cease its restoration and report its status to PCC.

(ii) If the j^{th} DG detected oscillation ($L_v^j = 2$), a signal is sent to PCC to check the status of the grid. The DG needs to check the status of grid with PCC when either an islanding condition or oscillation behavior is locally detected. While waiting for a response from PCC, the specific DG should maintain normal operation.

a) In case that PCC confirms islanding, a signal is sent through a meshed communication network to all DGs within the micro-grid to take an action.

b) If the PCC only detected grid oscillation, then no action is taken by the j^{th} DG and it would maintain normal operation.

(iii) If the PCC first detects islanding, it shall send the information through a meshed communication network to all the DGs within the micro-grid.

Robustness has been considered in the design of the proposed distributed algorithm. For example, a specific DG, that is unable to maintain its steady-state operation within the pre-specified voltage range, would temporarily cease its operation until it hears back from PCC. However, the proposed algorithm provides an autonomous recovery procedure to restore normal operation of the specific DG when confirmation of a non-islanding condition is received from PCC. Additionally, the information from the DG-level algorithm is only for the DG's own use (as to whether temporarily cease its own operation or maintain its normal operation) while waiting for a confirmation from PCC and hence avoiding unnecessary tripping of other DGs. Furthermore, in the case that PCC detects an islanding condition but it didn't receive any information (due to loss of communication, delays, and etc.) from other DGs, the PCC would send the information of the islanding condition in order to avoid any further delay.

At PCC level, the information required are the currents of all branches that are directly connected to PCC ($i_1, \cdots, i_m$) in addition to the PCC voltage frequency. Individually, each DG

will require its own bus voltage information. The PCC voltage frequency tracked by PLL is utilized in the grid current estimator while the frequency of local DG bus voltage is used for local voltage estimator. Hence, the regression vector $w_1(i)$ defined in (2.20) becomes similar to $w_2(i)$ while $y_1(i)$ is replaced by the summation of PCC branch currents ($\sum_{n=1}^{m} i_n$). Then, the overall NDZ of the proposed algorithm is similar to the PCC algorithm NDZ provided that the network has a proper communication topology with PCC.

- Communication Network Requirement for Multi-DG System

The proposed distributed islanding detection scheme (with negligible NDZ) can be implemented if the micro-grid has a secure low-bandwidth meshed communication network (illustrated by Figure 2-9). It is sufficient that DGs have low-frequency communication capability among the neighbors. It is worth noting that the meshed network only requires neighboring communication and that the more DGs there are in the micro-grid, the more connected their communication network becomes. Any delay or loss of communication will only affect the detection time. The requirement of the communication system in terms of design is that each DG should be able to identify the source of the originated signal (whether it is PCC or other DGs). This can be easily done through appending a simple source designation to communication signals.

Furthermore, the requirement for the communication system in terms of speed is the maximum 2 second detection time specified by IEEE 929-2000 in [3] for the worst case scenario. For design purposes, the following condition can be used to choose the right frequency for the required meshed communication network:

$$\max_j \left(t_{DG}^j + t_d^j + t_{PCC}^j \right) \leq 2 , \tag{2.30}$$

where t_{DG}^{j} is the time required for the j^{th} DG to detect transient behavior locally, t_{d}^{j} is the total propagation time of a communication signal transferred from the j^{th} DG to PCC and back to the j^{th} DG, and t_{PCC}^{j} is the required time for PCC to confirm islanding condition. The total propagation time t_{d}^{j} includes the frame serialization time, link delay, queuing delay, and node processing delay for tranferring a signal from the j^{th} DG to PCC and back to the j^{th} DG. Any communication topology that satisfies condition (2.30) is sufficient to achieve distributed islanding detection capability with negligible NDZ for the general multi-DG structure shown in Figure 2-9. Further details on communication requirement for such distributed algorithms can be found in [46].

2.1.8 Results

The system under study for the first three subsections consists of a 1kW inverter based DG connected to an *RLC* load and a grid as illustrated in Figure 2-1. The system is simulated in MATLAB/Simulink. The performance of the developed dynamic estimators during islanding transients is studied under three loading conditions. The three loading conditions are:

1. *RLC* load that approximately resonates at 60 Hz with Q_f = 2.5 and absorbs approximately 1kW.
2. *RLC* load that approximately resonates at 59.6 Hz with Q_f = 2.5 and absorbs approximately 1kW.
3. *RLC* load that approximately resonates at 60 Hz with Q_f = 2.5 and absorbs approximately 0.95kW.

The loads chosen represent cases where other IDMs might fail to detect an islanding situation as will be seen in the coming subsections. For simulation purposes, micro-grid operation is permitted and the forgetting factor (λ_k) is set to 0.9 for all simulation cases. This value was chosen in order to make the estimator more sensitive to fast dynamics and to reduce the amount of memory required by both algorithms. Table 2-1 shows the rest of the parameters used for simulation. A sampling frequency of 7.68 kHz is used which corresponds to 128 samples/cycle at 60 Hz.

Table 2-1
Simulation Parameters for Dynamic Estimator IDM

Parameters	*Value*
S_{base}	1 kW
V_{base}	169.7 V
I_{base}	11.79 A
A_v	169.7
V_r	120 V
$V_{\max}$	1.1 pu
$V_{\min}$	0.88 pu
f_g	60 Hz
f_s	7.68 kHz
W_L	8.333 ms
T_d	35 ms
$P(0)$	100
ζ_d	0.001 pu
ζ_φ	1^o

2.1.8.1 Detectability and Convergence under Load Cases

At t = 2 seconds, the grid switch was opened to examine the response of the dynamic estimators during islanding. Figure 2-10 shows the responses of estimated DG bus voltage amplitude ($\hat{A}_v$), estimated grid current amplitude ($\hat{A}_s$), DG local algorithm output (L_v), and the

PCC algorithm output (L_s) for all the load cases. As seen in Figure 2-10, case 1 is theoretically undetectable by both algorithms but practically inconsequential due to the perfect match in power, voltage and frequency between load and inverter. Therefore, the grid will not supply any active or reactive power and the amplitude of current injected by the grid is almost zero. Hence, no significant variation is detected in the DG bus voltage (L_v = 1) during islanding. Cases 2 and 3 are detectable by the PCC algorithm although they lie within the NDZs of OUF method and OUV method, respectively. The NDZ of OUF is shown in Figure 2-7, and it can be seen that case 2 lies within its NDZ. The NDZ for OUV is given in Fig. 3 in [37] and it can be seen that the point of ΔP = -5% and ΔQ = 0 (i.e., case 3) is obviously located inside the NDZ of OUV. When the grid is disconnected, $\hat{A}_s$ converged to zero within approximately 20 and 30ms for cases 2 and 3, respectively. The required time to confirm islanding conditions by PCC algorithm for cases 2 and 3 are 56.6 and 65.2ms, respectively. Also, there is an initial delay of 43.2ms or 2.6 cycle (W_L plus T_d) to produce the first value of L_s. On the other hand, the DG local algorithm detected oscillation (L_v = 2) for cases 2 and 3. The oscillation detected for case 2 is a result of dynamic changes of voltage frequency from 60Hz to 59.6Hz. For case 3, $\hat{A}_v$ converged to a value of 1.05pu after islanding and hence a transient behavior is detected for this case as well. It is worth mentioning that the designed high sensitivity of the DG local algorithm to detect transient behavior is critically important for islanding detection of more complicated multi-DG structures as mentioned in subsection 2.1.7. Furthermore, the proposed estimators provide good amplitude estimation with maximum steady-state errors at the level of 0.5e-3 for all the cases studied.

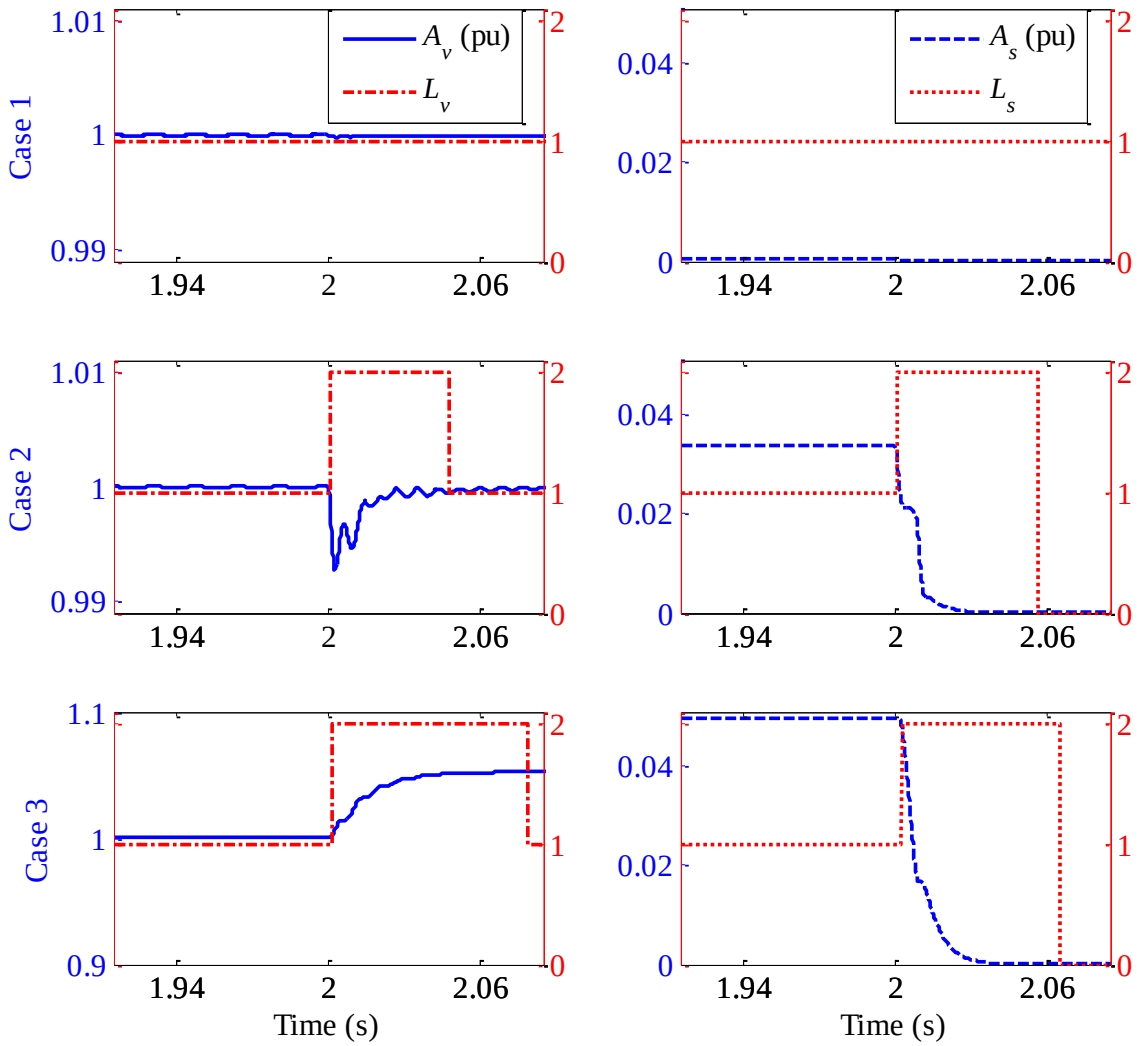

Figure 2-10: Responses of both estimated amplitudes and algorithms' outputs for different load cases.

In addition to islanding detection, the flow direction of grid active and reactive power can be determined through the following steady-state relation:

$$\begin{aligned} sign(\Delta Q) &= sign(-\hat{\theta}_{12}), \\ sign(\Delta P) &= sign(\hat{\theta}_{11}). \end{aligned} \tag{2.31}$$

The relation in (2.31) might produce incorrect results at steady state when ΔP or ΔQ is equal to zero. Therefore, a small threshold area around zero can be used to eliminate this

problem. The grid in case 2 (capacitive load case) absorbs reactive power only, whereas it absorbs active power only for case 3.

2.1.8.2 Effect of Q_f on Estimator Response

The *RLC* load condition of case 2 will be used to study the effect of Q_f on both estimators and algorithm outputs responses. Figure 2-11 shows the effect of different Q_f values on $\hat{A}_v$, $\hat{A}_s$, L_v, and L_s. From Figure 2-11, it is noticed that high quality factor values resulted in higher $\hat{A}_s$ values since loads with high Q_f value will require more support from the grid (i.e., absorbing higher reactive power) than loads with low Q_f value. This explains the reduction in NDZ size under high Q_f values as shown in Figure 2-6 and Figure 2-8. However, larger $\hat{A}_s$ value will require a slightly larger time to converge to zero since the decaying speed, when grid is disconnected, is mainly determined by the forgetting factor of the RLS algorithm. Hence, the required time for the PCC level algorithm to confirm islanding is 52.6, 56.6, and 63.7ms for Q_f values equal to 1, 2.5, and 10, respectively. In contrast, the frequency for high-Q_f loads slowly drifts after islanding and hence a larger period of oscillation is detected for loads with higher Q_f values.

2.1.8.3 Effect of Forgetting Factor on Estimator Response

The *RLC* load condition of case 2 will be used to study the effect of algorithms' forgetting factor (λ_k) on both estimators and algorithms' outputs responses during islanding condition. The effect of different λ_1 values on $\hat{A}_s$ and L_s is shown in Figure 2-12 while the

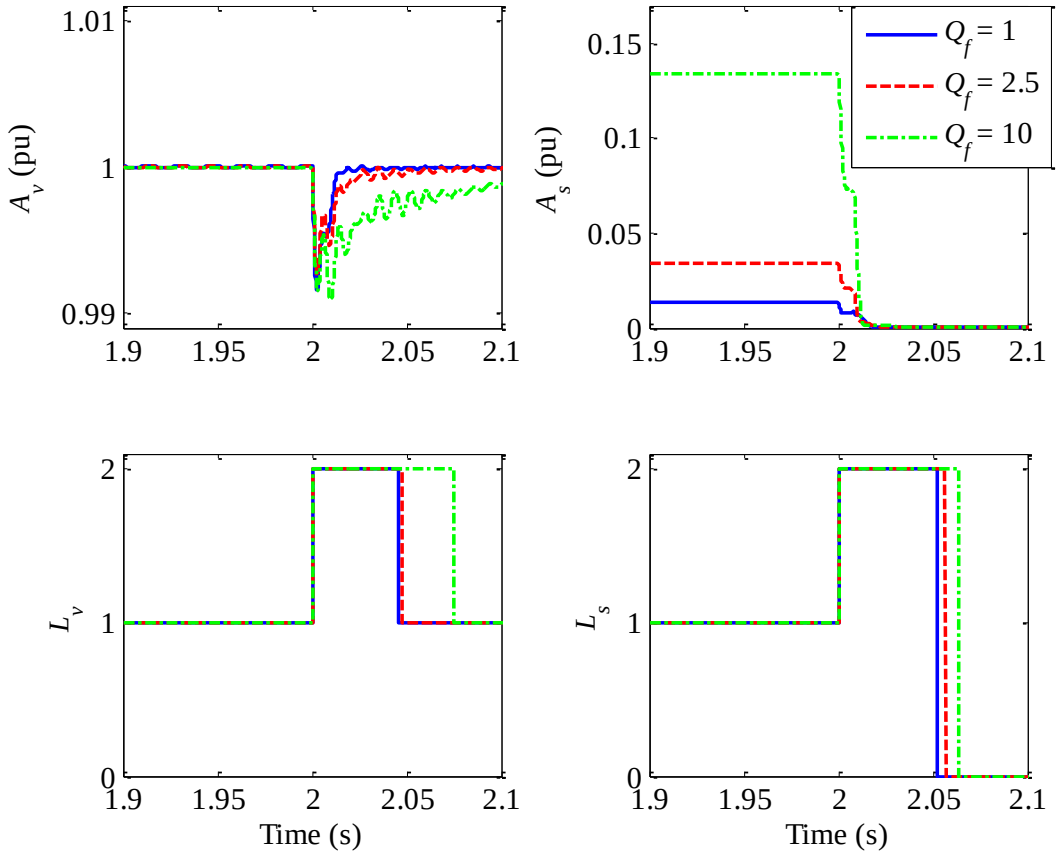

Figure 2-11: Effect of different Q_f values on estimated amplitudes and algorithms' outputs responses: Q_f = 1 (solid), Q_f = 2.5 (dashed) and Q_f = 10 (dash-dotted).

effect of different λ_2 values on $\hat{A}_v$ and L_v is shown in Figure 2-13.

It can be noticed from Figure 2-12 that higher λ_1 values result in slower decaying $\hat{A}_s$ values to zero which will increase the required time for the PCC level algorithm to confirm islanding condition. The required time for the PCC level algorithm to detect islanding (at T_d = 35ms) is 55.2, 56.6, 57.2, 63.7, and 87.2ms for λ_1 values equal to 0.8, 0.9, 0.95, 0.98, and 0.99, respectively. On the other hand, results from Figure 2-13 show that as the value of λ_2 is increased, the response of $\hat{A}_v$ becomes less sensitive to islanding switching and hence smaller

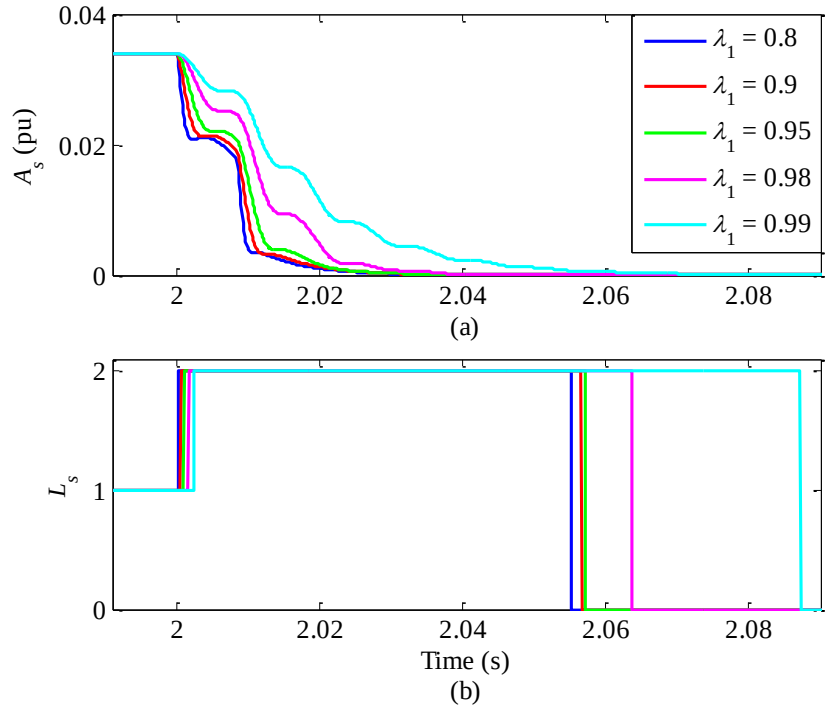

Figure 2-12: Responses of $\hat{A}_s$ and L_s during islanding for different λ_1 values: (a) $\hat{A}_s$, (b) L_s.

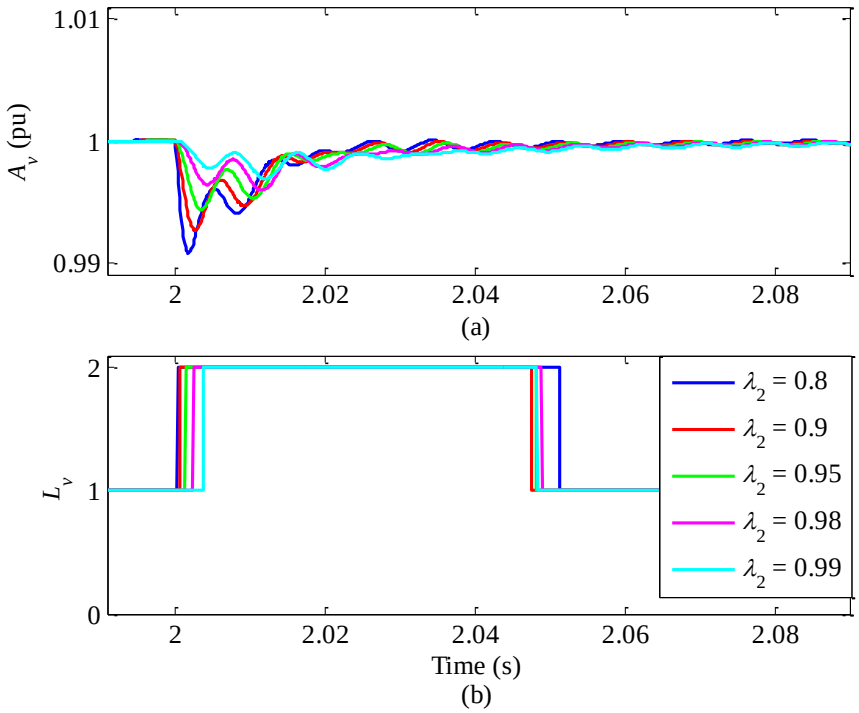

Figure 2-13: Responses of $\hat{A}_v$ and L_v during islanding for different λ_2 values: (a) $\hat{A}_v$, (b) L_v.

variation in $\hat{A}_v$ is obtained. As a result, the detected transient ($L_v = 2$) period by the DG local algorithm is slightly decreased.

In order to illustrate the effect of forgetting factor (λ_1) on the PCC level algorithm islanding detection time, let us assume that the expected apparent power injected by the grid before islanding is between 1% and 20%. Then, the islanding detection time is found with respect to λ_1 changes for different per-unit grid current amplitude values as shown in Figure 2-14. It can be seen from Figure 2-14 that the difference in detection time for the previously assigned power range increases as λ_1 increases. From Figure 2-14, a time difference of 5.21ms is obtained for $\lambda_1 = 0.9$ while $\lambda_1 = 0.97$ resulted in 10.81ms detection time difference.

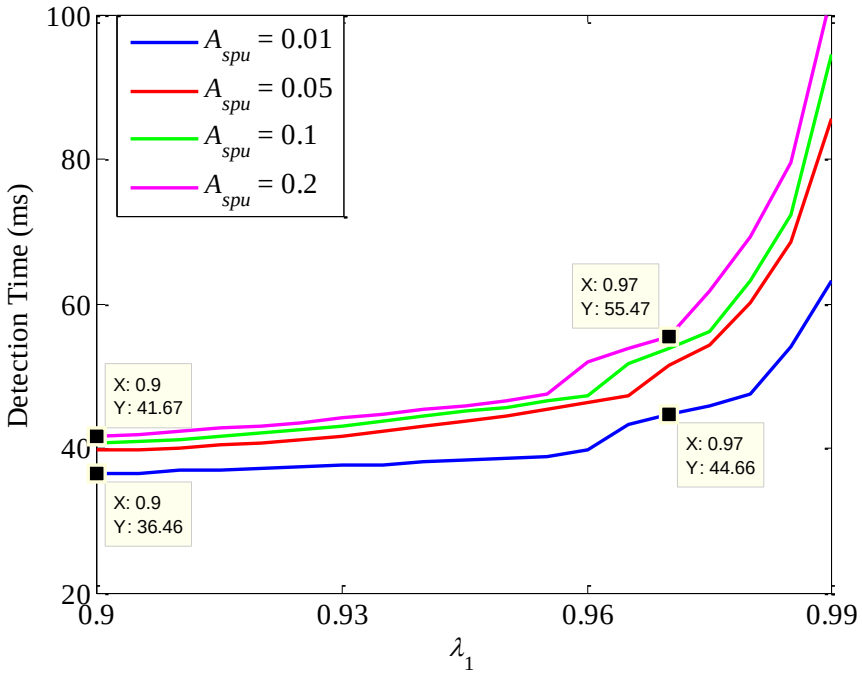

Figure 2-14: Islanding detection time Vs. forgetting factor for different per-unit grid current amplitude values.

For design purposes, it is recommended that the forgetting factor value, resulting in a smaller time difference range, is chosen. However, there is a tradeoff between the islanding

detection time for the PCC level algorithm and the robust performance against disturbances when designing for its forgetting factor. In order to illustrate the tradeoff, a third and fifth order harmonics are added to the measured signal $y_1(i)$ obtained from case 2 *RLC* loading condition. The third harmonic is assumed to have twice the amplitude of the fifth harmonic. The maximum Total Harmonic Distortion (THD) level that maintains a normal operation in the PCC level algorithm output (L_s = 1) is found for each λ_1 value as shown in Figure 2-15 (a). Similarly, a normally distributed white noise is added to $y_1(i)$. The average Signal-to-Noise Ratio (SNR) of 10 experiments with normal operation output is calculated for different λ_1 values as shown in Figure 2-15 (b). From Figure 2-15, normal algorithm output is maintained for distortions up to THD = 2% or SNR = 30dB for λ_1 = 0.9 and ζ_d = 0.001 p.u. Therefore, given the expected THD or SNR level along with the range of apparent power imbalance, one can use both curves in Figure 2-14 and Figure 2-15 to design for λ_1.

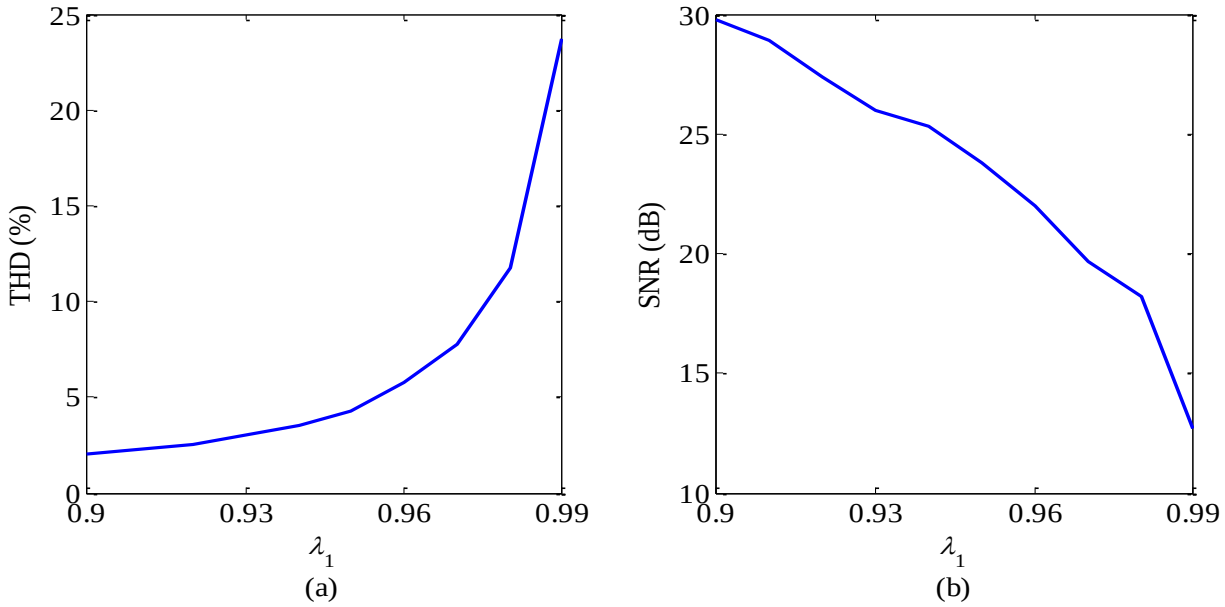

Figure 2-15: Design curves for forgetting factor to achieve robust performance against (a) harmonics and (b) noise distortions.

2.1.8.4 Effect of Special Case Loading Conditions

The problem of special loading condition other than a parallel *RLC* load is addressed in this subsection. The corresponding *R*, *L* and/or *C* parameters are designed as follows:

$$R = \frac{V_r^{\,2}}{P_L},\ L = \frac{V_r^{\,2}}{2\pi f_g Q_{LL}},\ C = \frac{Q_{CL}}{2\pi f_g V_r^{\,2}}, \tag{2.32}$$

where Q_{LL} is the reactive power (in VAR) absorbed by inductance at nominal voltage and frequency, and Q_{CL} is the reactive power (in VAR) injected by capacitance at nominal voltage and frequency. Three special load cases are considered in this subsection: *R* load, *RL* load, and *RC* load. The load active power (P_L) is set to 0.95 pu. Q_{LL} is set to 0.05 pu while Q_{CL} is set to 0.1 pu. In order to avoid singularity in the proposed PCC level algorithm, *L* is set to a very large number (10^{12} for example) when Q_{LL} is equal to zero while *C* is set to a very small number (10^{-12} for example) when Q_{CL} is equal to zero. Responses of $\hat{A}_s$ and L_s are shown in Figure 2-16 while responses of $\hat{A}_v$ and L_v are shown in Figure 2-17 for different loading conditions. For the *R* loading case, the grid supplies the active power imbalance (ΔP) between the load and inverter before islanding and islanding condition is detected within 48.0ms of occurrence. For the *RL* and *RC* loading conditions, in addition to supplying ΔP, the grid supplies/absorbs the reactive power required by both *L* and *C*, respectively. The steady-state grid current amplitude before islanding can be found by (2.7). Islanding condition is detected for both the *RL* and *RC* loading conditions with a detection time of 47.5 and 50.3ms, respectively. The NDZ for the special loading conditions is the one described in subsection 2.1.6.1. On the other hand, Figure 2-17 shows that different loading conditions resulted in different settling time for $\hat{A}_v$ responses. The *RL* load

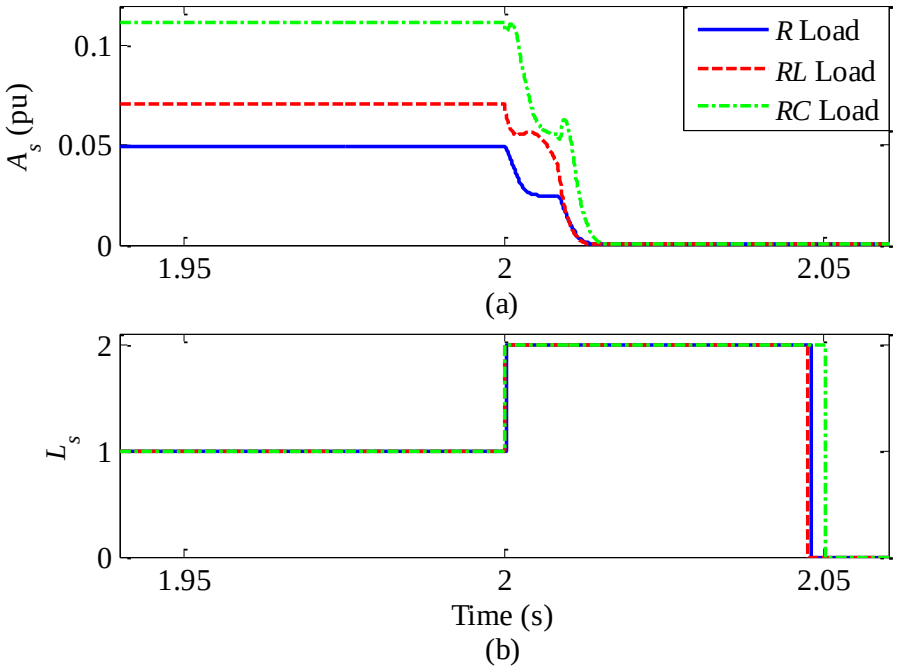

Figure 2-16: Responses of $\hat{A}_s$ and L_s during islanding for special loading conditions: (a) $\hat{A}_s$, (b) L_s.

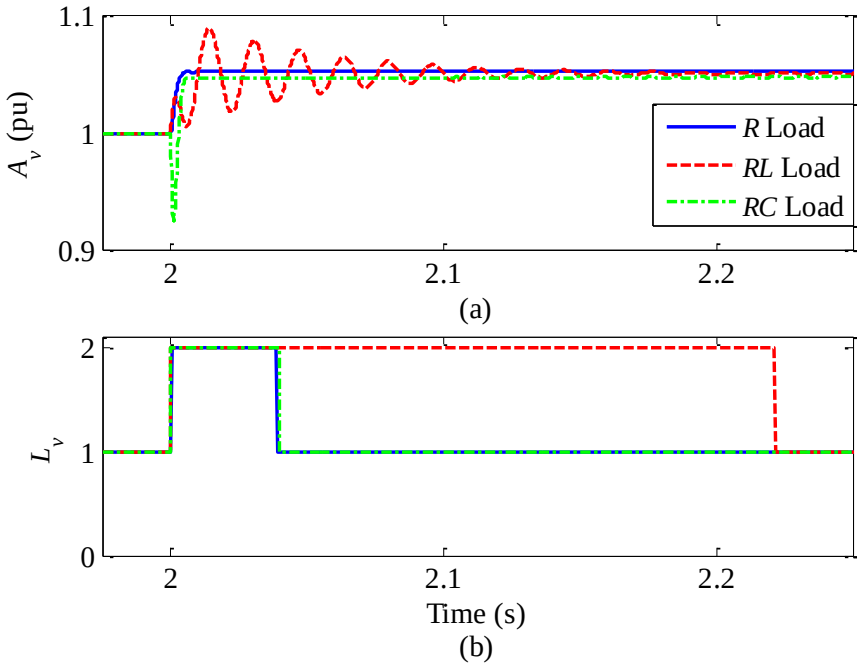

Figure 2-17: Responses of $\hat{A}_v$ and L_v during islanding for special loading conditions: (a) $\hat{A}_v$, (b) L_v.

settling time is higher than the *R* or *RC* loads settling times and hence a larger transient period is obtained for the *RL* load.

2.1.8.5 IEEE 34-Bus Network

The standard IEEE 34-bus distribution network, which is shown in Figure 2-18, will be used to test the effectiveness of the proposed multi-DG algorithm. DigSilent, which is a very powerful program for studying and integrating power system networks, will be used for simulation. The detail of the parameters used in this network can be found in [46] and [47]. Sixteen Photovoltaic DGs are integrated at different buses in the IEEE 34-bus network as illustrated in Figure 2-18. The three-phase base power is 1MVA and the line-to-line RMS base voltage is 24.9kV. Measurements are taken at both buses (**B**) and (**C**) where the load and DG power at these two buses are as follows:

$$S_L^B = 0.21\text{MW} + j0.01\text{MVAR},\ \ S_L^C = S_{inv}^B = S_{inv}^C = 0.2\text{MW}.$$

It follows that the power mismatch (i.e., the power injected by the grid to the island) is 0.01MW and 0.01MVAR. The following cases are simulated:

1. A micro-grid formation or islanding condition taking place at bus (**C**) by disconnecting line **d** at t = 2s.
2. A three-phase-to-ground short circuit fault taking place at point (**A**) at t = 2s and clears out within 0.03s.
3. A 0.5MW induction motor switching on at t = 2s and off at t = 8s at bus (**D**).
4. A 1.0MVAR capacitor switching on at t = 2s and off at t = 5s at bus (**C**). Also, a 1MW + j 1MVAR load switching on at t = 8s and off at t = 11s at bus (**B**).

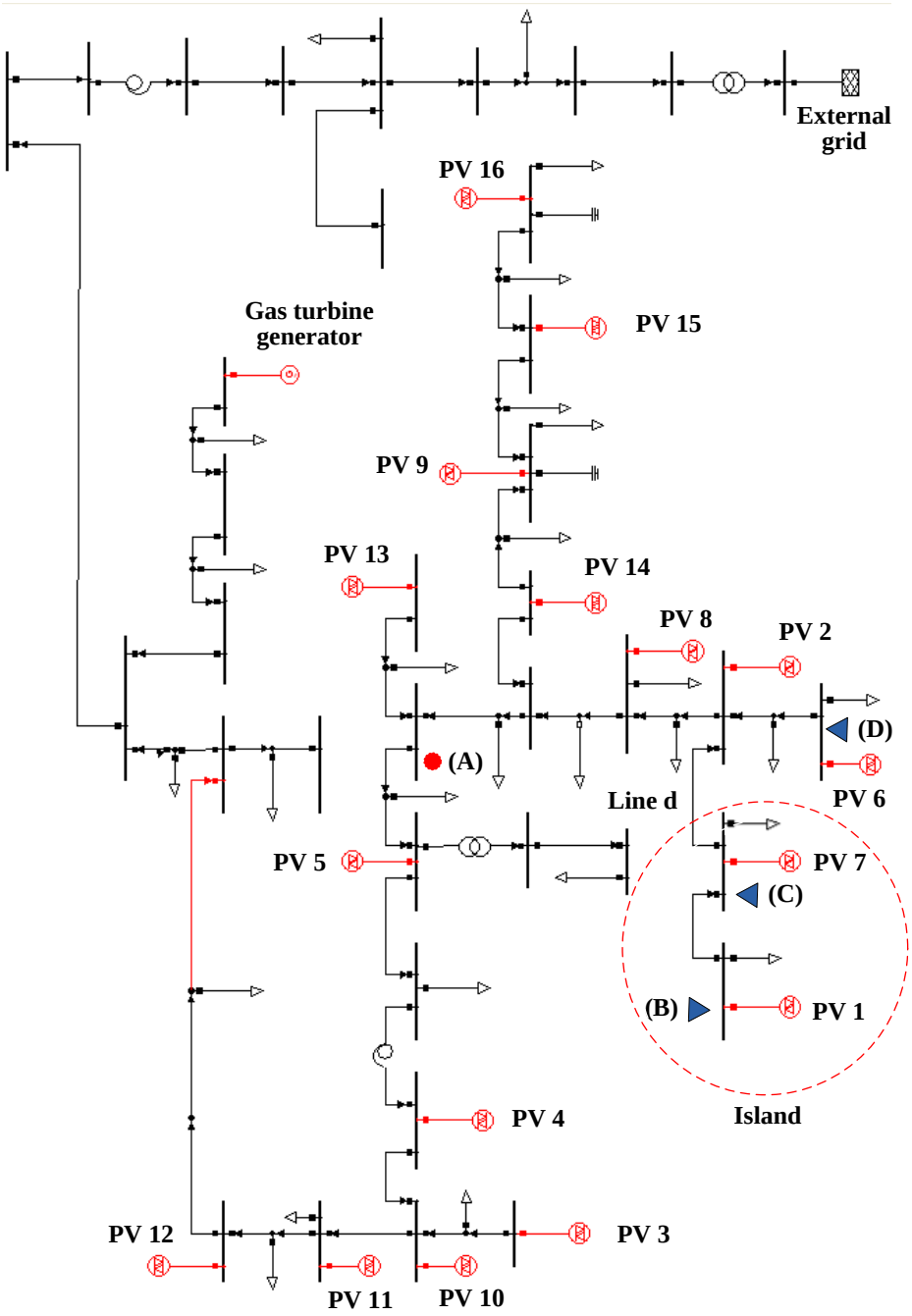

Figure 2-18: Diagram of the IEEE 34-bus network.

The added induction motor, capacitor, and load in cases 3 and 4 are not shown in Figure 2-18. Since the capacitor switching in case 4 is applied to PCC bus (**C**), the switching capacitance information should be adapted in the PCC level algorithm to provide correct

estimation for the grid current amplitude injected at PCC. Figure 2-19, Figure 2-20, and Figure 2-21 show the responses of estimated DG bus voltages ($\hat{A}_v^{B,C}$) with its local algorithms' outputs ($L_v^{B,C}$) for buses (**B**) and (**C**) in addition to $\hat{A}_s$ and L_s for all simulated cases.

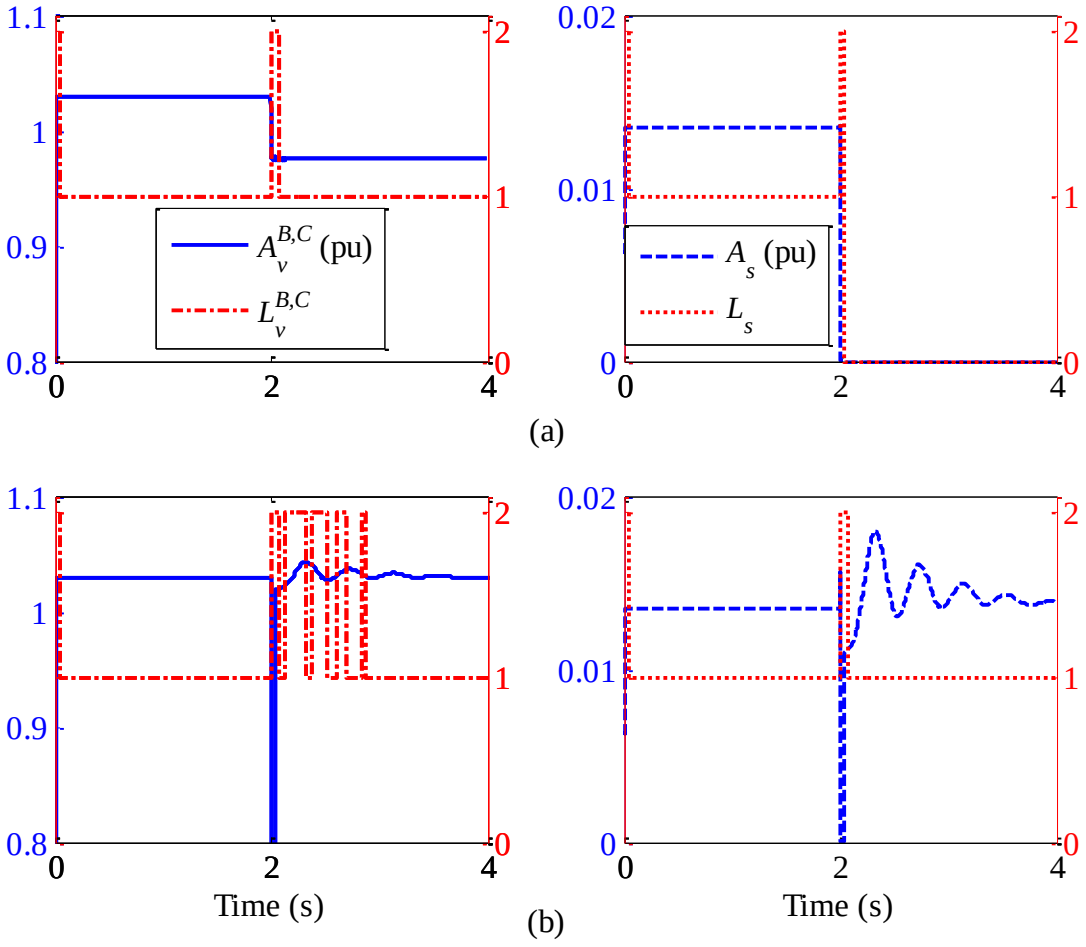

Figure 2-19: Responses of estimated amplitudes and algorithms' outputs during: (a) islanding, (b) three-phase short circuit.

The DGs' local voltages at buses (**B**) and (**C**) are almost similar and hence are plotted using a single legend. Results show that the PCC level algorithm distinguishes islanding condition ($L_s = 0$) from three-phase short circuit, startup of induction motor, switching of capacitor, and load variations. In Figure 2-19 (a), an islanding condition is detected subsequent

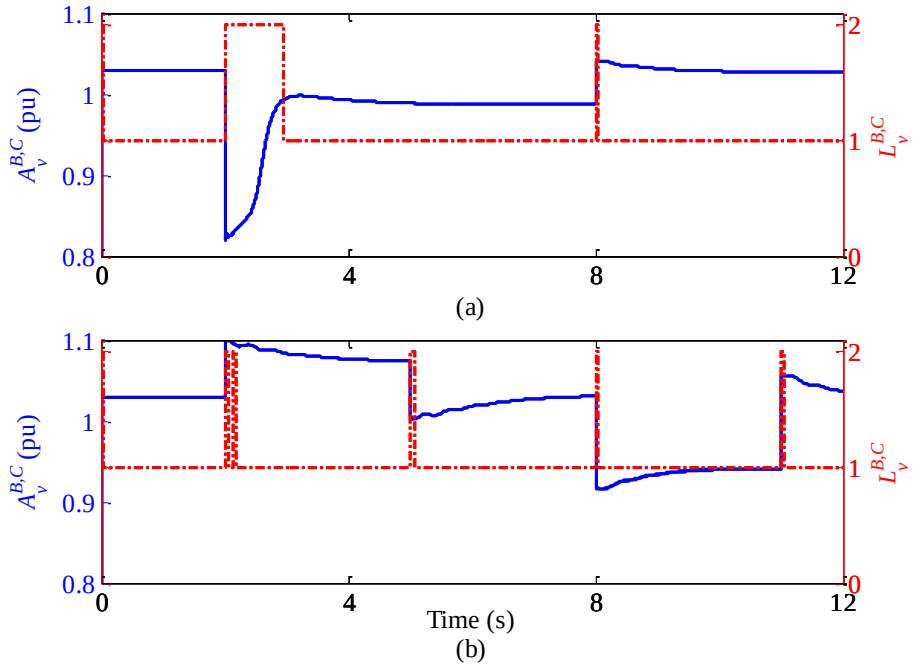

Figure 2-20: Responses of $\hat{A}_v^{B,C}$ (solid) and $L_v^{B,C}$ (dash-dotted) during: (a) startup of induction motor, (b) capacitor and load switching.

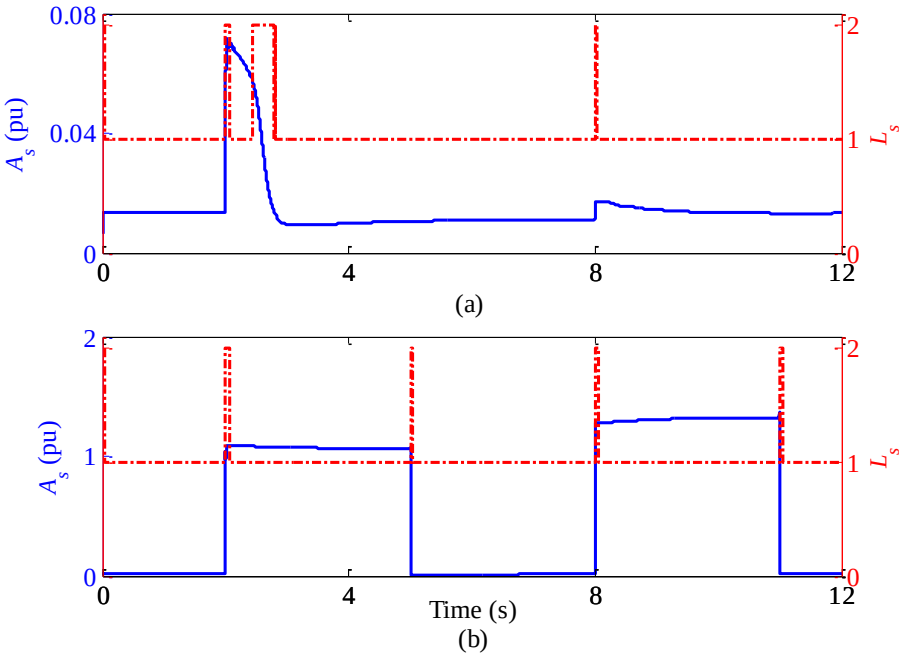

Figure 2-21: Responses of $\hat{A}_s$ (solid) and L_s (dash-dotted) during: (a) startup of induction motor, (b) capacitor and load switching.

to a transient behavior caused by grid disconnection. The transient behavior is detected locally as well by both DGs ($L_v^{B,C}$ = 2) and hence a signal is sent to PCC to check the status of grid. The islanding is detected by PCC within 39.5ms of occurrence. Also, a transient behavior ($L_s = L_v^{B,C}$ = 2) caused by a three-phase short circuit is detected both at PCC and locally by each DG as shown in Figure 2-19 (b). Since the test region in Figure 2-3 is designed to detect fast or switching transient behavior only, the slowly varying grid amplitude afterward is considered as normal operation (L_s = 1) as seen in Figure 2-19 (b). In contrast, a larger period of oscillation is detected locally at both DGs but the PCC level algorithm declares this case as non-islanding condition. From Figure 2-20, a transient behavior is detected locally by both DGs during both on and off switching of induction motor, capacitor, and load. In Figure 2-20 (a), a sudden drop in voltage is noticed followed by a recovery behavior when the grid reacts by supplying higher current to suppress the voltage drop caused by the startup of induction motor as seen in Figure 2-21 (a). Both transients caused by induction motor on and off switching are detected locally and similarly the PCC level algorithm is capable of classifying this case as a non-islanding condition. Similar behavior is noticed for capacitor and load switching. However, a higher $\hat{A}_s$ value is observed in Figure 2-21 (b) for both capacitor and load switching. The reason for the high $\hat{A}_s$ value is that both switching takes place inside the island and hence the grid reacts by absorbing/injecting the power mismatch to support both bus voltages in the island. Therefore, the proposed technique is robust against power system disturbances such as three-phase short circuit, induction motor switching, capacitor switching, and load switching.

2.1.9 Discussion

Table 2-2 shows a comparison between the proposed dynamic estimator IDM and OUF or OUV IDMs.

Table 2-2
Comparison between Dynamic Estimator IDM and OUF/OUV IDMs

	Dynamic Estimator IDM	*OUF and OUV IDMs*
Type of data required	Instantaneous values.	RMS values.
Data required	Amplitude, frequency and phase of $v_1(t)$ and inverter current ($i_{inv}(t)$) Also, knowledge of load or its estimate.	Amplitude and/or frequency of $v_1(t)$.
NDZ	Close to one line at f_o = 60 Hz for all values of Q_f.	Refer to [15], [29], [30], [32], [37].
Detection time	Less than 4 cycles (39.5 – 65.2ms) is achieved for all simulated cases.	six cycles + time required to drift beyond triggering limits (>100ms) [3], [6], [32].
Tradeoff	More data, smaller NDZ and smaller detection time.	Less data, larger NDZ and larger detection time.

As seen from Table 2-2, the additional requirement in terms of highly sampled data paid its price and resulted in reducing both NDZ and required detection time significantly. Also, the proposed technique showed robust behavior against different power system disturbances. In section 2.1.8.5, the PLL dynamics during fault is not considered. In practice, the tracking performance of PLL during disturbances could significantly degrade the performance of the proposed dynamic estimator. The tracking performance of PLL depends on proper design of PI controller gains (k_{pPLL} and k_{iPLL}) [48]. According to [48], even when PLL controller gains are properly designed, the PLL output can tolerate small amplitude frequency variations. Also, there

is a lack of analytical proof of robustness and convergence for the RLS estimator. The way we propose to avoid utilizing PLL output and not to go through all design requirements of PLL parameters is to parameterize grid current frequency as well. Hence, the theory of non-linear estimators and observers come into place. In the next section, a robust non-linear observer is proposed as an alternative of the RLS algorithm to estimate both the amplitude and frequency of grid current.

2.2 Non-Linear Observer for Grid Current Amplitude and Frequency

2.2.1 Introduction

In the last decade, a lot of work has been conducted to improve observers' algorithms performance and robustness in order to meet new requirements of developing high technologies and new practical applications. One of the common problems in this field is parameter identification of distorted sinusoidal signals. Most of the power system applications depend on sinusoidal signals and this is why sinusoidal observation has a great attention from people who works in power system and communication. Many techniques with local convergence property have been employed for the purpose of estimating sinusoidal amplitude such as Least Square (LS) [49], and extended Kalman filter [50]. These statistical methods can be effective but no prove of global convergence can be provided. Also, LS is very sensitive to frequency deviation [49], [51]. Recently, globally convergent frequency estimation techniques such as adaptive notch filter [52]-[54], adaptive identifier [55], and adaptive observer [51], [56]-[59] have stimulated further research in control and power system applications. The problem of simultaneous reconstruction of amplitude and frequency of a sinusoid were not clearly addressed except at [51], [59] and [60]. Many of these techniques have been adapted to power system applications as

seen in [50] and [54] where modifications have been applied to the original design in order to enhance robust performance.

Two non-linear adaptive observers are presented in [59] to estimate amplitude and frequency of a pure sinusoidal signal for arbitrary phase values. Results in [59] showed global convergence of those two estimators where they allow simultaneous online reconstruction of amplitude and frequency of a pure sinusoidal signal at low percentage error. The observers presented in [59] assumed pure sinusoidal signal where no clue was provided on the robust performance of those observers under different types of disturbances.

This section aims to propose a new observer based on observers presented in [59] for the purpose of detecting islanding condition at PCC. The design procedure is extended from estimating amplitude and frequency of an ideal sinusoidal waveform to those of a noisy sinusoidal waveform with piecewise-constant amplitude. The main contribution of the section is to provide the robust observer design with detailed analytical derivations and proofs of robustness and convergence. The proposed observer provides better performance for the purpose of detecting islanding condition for inverter based Distributed Generation (DG). The IDA with sliding window presented in subsection 2.1.5 will be used in conjunction with the proposed non-linear observer to provide more reliable islanding detection at PCC and to distinguish between islanding and other operating condition for the DG inverter.

This section is organized as follows. Subsection 2.2.2 presents the formulation for the problem to be studied. The proposed non-linear observer is introduced in subsection 2.2.3. Comparison to other observers in literature is presented in subsection 2.2.4. The algorithm to detect islanding condition is illustrated in subsection 2.2.5. The performance of the proposed

non-linear observer is tested through simulation in subsection 2.2.6. Finally, discussions are presented in subsection 2.2.7.

2.2.2 Problem Formulation

The same system defined in subsection 2.1.2 will be used here. Figure 2-22 shows the generic model for transient islanding study. This circuit is the same as the anti-islanding testing diagram defined in the standards of UL 1741 and IEEE 929-2000 [3], [4].

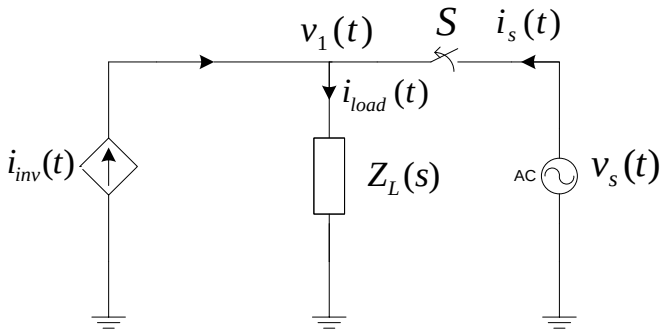

Figure 2-22: A generic model for the transient islanding study.

Applying Kirchhoff Current Law (KCL) to the circuit shown in Figure 2-22 yields

$$\begin{aligned} i_s(t) &= i_{load}(t) - i_{inv}(t) \\ &= A_s \sin(\omega t + \varphi_s) u(\tau - t) + \delta(t), \end{aligned} \tag{2.33}$$

where $u(..)$ is a step function, $\tau > 0$ is the unknown instant at which islanding condition would occur (otherwise $\tau = \infty$) and $\delta(t)$ is a bounded disturbance that may include measurement noises, grid transient and its harmonics.

When islanding occurs (if τ is finite), the transition caused by switching action will force the amplitude of grid current (A_s) to experience the transient behavior from its prior-switch steady state value to zero. Therefore, it is important to detect this transition by employing an

observer that can real-time estimate the signal amplitude under disturbances. Such observer-based technique will have a superior advantage over regular Islanding Detection Methods (IDMs) which are based on RMS values, and this is because considering dynamic behavior of the system will allow faster detection with negligible NDZ as seen in section 2.1.

Let us assume that load current (i_{load}) and DG inverter current (i_{inv}) are available measurements at PCC. Then, the objective of this problem is to use available disturbed instantaneous measurements to provide online estimation of grid amplitude ($\hat{A}_s$) whose value is expected to settle down to zero within a small period of time Δt after islanding occurs. From an application point of view, the main requirements of the observer design are to ensure robustness (against disturbances) and to minimize Δt such that islanding is detected within less than 2 seconds of occurrence [3]. The maximum two seconds detection time was proposed for techniques that are based on RMS measurements and no standards are available for techniques that employ instantaneous measurement. Hence, the total time required for islanding confirmation using proposed observer is within 67ms which corresponds to four cycles in 60 Hz.

2.2.3 Design Procedure

Technically, the main purpose of this section is to design robust observers that estimate amplitude and frequency of a noisy sinusoidal signal. While the proposed results are based on the ideal designs in [59], the main contribution is to make the observer robust against the effects of lumped disturbance $\delta(t)$ on the estimates. Let us begin with the following measurement of a sinusoidal signal:

$$y(t) = A\sin(\omega t + \phi) + \delta(t), \tag{2.34}$$

where A is the amplitude in per unit that may have piecewise-constant changes, ω is the frequency in rad/sec., ϕ is the phase and $\delta(t)$ is a bounded disturbance.

In power systems, the second derivative of lumped disturbance $\delta(t)$ might go unbounded due to disturbance behavior. Hence, following similar design procedure as in [59], where the second derivative of y^2 is taken to derive state equation, will lead to losing the boundedness property for observer error due to the term $\ddot{\delta}$. Therefore, a pre-filtering stage is proposed to avoid this problem such that the filtered version of state error produced by δ is bounded provided that both $\delta(t)$ and $y(t)$ are bounded. By ignoring non-persistent initial conditions, one can define the following states

$$\begin{cases} \eta_1 = L^{-1}\left(H(s)\, L\left(y^2/2\right)\right) \\ \eta_2 = L^{-1}\left(s\, L\left(\eta_1\right)\right) \end{cases}$$

where $L(.)$ is the Laplace operator, $L^{-1}(.)$ is the inverse Laplace operator and $H(s)$ is the transfer function of the pre-filter. Then, the following state equation can be obtained:

$$\begin{cases} \dot{\eta}_1 = \eta_2 \\ \dot{\eta}_2 = \theta^T \beta_F - \upsilon_F \end{cases}, \tag{2.35}$$

where $\theta_1 = A^2\omega^2$, $\theta_2 = \omega^2$, $\theta = \begin{bmatrix} \theta_1 & \theta_2 \end{bmatrix}^T$, $\beta_{F2} = -4\eta_1$, $\beta_F = \begin{bmatrix} 1 & \beta_{F2} \end{bmatrix}^T$, $\upsilon = y\delta + \delta^2/2$, $\upsilon_F = L^{-1}\left(s^2 H(s)\, L(\upsilon)\right)$.

The pre-filtering stage is designed such that $sH(s)$ has a relative order greater than or equal zero, i.e. the signal η_2 is observable. Therefore, a second order Low Pass Filter (LPF) will be used. The applied LPF has the following form

$$H(s) = \frac{B_0}{B_2 s^2 + B_1 s + B_0}, \qquad B_2 = 1.$$

The LPF coefficients (B_0 and B_1) will be designed according to the following equations:

$$B_0 = \omega_c^2, \quad B_1 = 2\zeta_d \omega_c,$$

where ω_c is the cutoff frequency of the LPF in rad/sec. and ζ_d is the damping factor.

Since the frequency in power systems is a bounded parameter, the projection scheme in [61] will be utilized on $\hat{\theta}_2$ in conjunction with the sigma-modification scheme [61] on $\hat{\theta}_1$ and $\hat{\theta}_2$ which will reduce transient rippling and enhance robust performance. Define a new estimation parameter vector as

$$\hat{\varphi} = \hat{\theta} - aN = \begin{bmatrix} \hat{\theta}_1 & \hat{\varphi}_2 \end{bmatrix}^T \in \Re^2 ,$$

where $\bar{\theta}_{2\min} \le \hat{\theta}_2 \le \bar{\theta}_{2\max}$ or $|\hat{\varphi}_2| \le \bar{\varphi}_{2\max}$,

$N = \begin{bmatrix} 0 & 1 \end{bmatrix}^T$, $a = \left(\bar{\theta}_{2\max} + \bar{\theta}_{2\min}\right)/2$ and $\bar{\varphi}_{2\max} = \left(\bar{\theta}_{2\max} - \bar{\theta}_{2\min}\right)/2$.

Then, the proposed fifth-order robust observer for the islanding detection problem can be represented as follows:

$$\begin{cases} \dot{\eta}_1 = \eta_2 \\ \dot{\eta}_2 = -B_0\eta_1 - B_1\eta_2 + B_0\, y^2/2 \\ \dot{\hat{\eta}}_2 = -\alpha\, e_\eta + (\hat{\varphi}^T + aN^T)\beta_F \\ \dot{\hat{\varphi}} = -\Gamma\beta_F\, e_\eta - \sigma\hat{\varphi} - k_a[m_a{}^2 + e_\eta{}^2]M\hat{\varphi} \end{cases}, \tag{2.36}$$

where $m_a = \left(\dfrac{\max\{\| \hat{\varphi}_2 \|^2, \bar{\varphi}_{2\max}{}^2\}}{\bar{\varphi}_{2\max}{}^2} - 1 \right)$, $M = diag(0,1)$, $e_\eta = \hat{\eta}_2 - \eta_2$, $\Gamma = diag(\gamma_1, \gamma_2)$ and $\alpha, \gamma_i, k_a, \sigma > 0$ are design constants. The last term in (2.36) which contains e_η^2 is used to enhance the robustness of frequency estimation [62].

The overall system in (2.36) contains two linear differential equations coming from the pre-filtering stage and three non-linear differential equations representing the proposed robust

adaptive observer. Figure 2-23 shows a diagram of the proposed overall system to detect islanding condition.

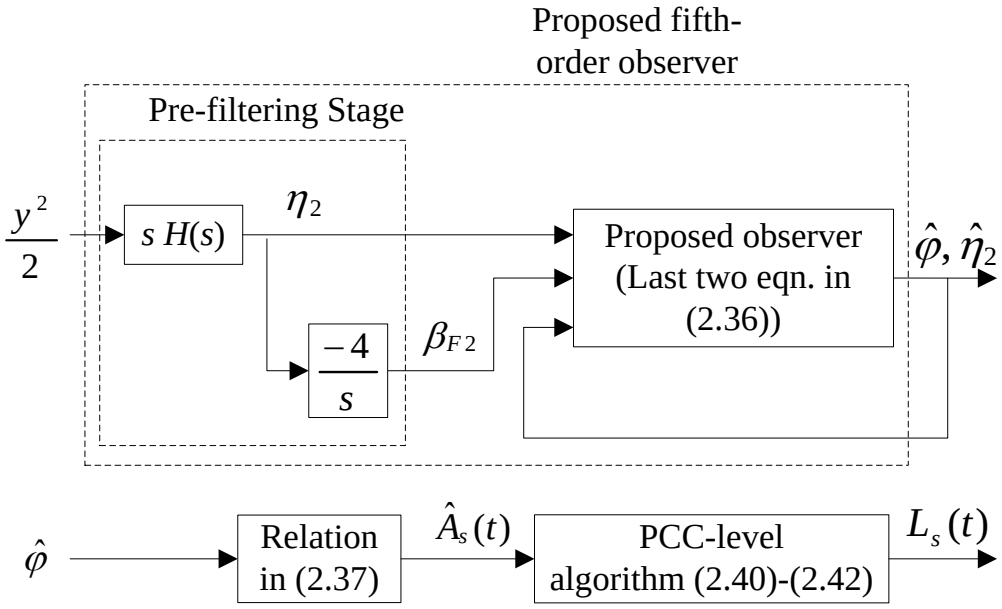

Figure 2-23: Diagram of the overall system to detect islanding using non-linear observer.

This technique is more suitable for power systems application in which dc components are to be neglected or filtered out. Also, a pre-filtering stage might be necessary when current measurements are used instead of voltage ones since the later is already filtered out by the load components. The proof of the following lemma can be found in Appendix B.

Lemma 1*:* The proposed robust observer in (2.36) will provide uniformly bounded state error $(\hat{\eta}_2 - \eta_2)$ and estimation parameter error $(\hat{\varphi} - \varphi)$ for all uniformly bounded disturbance $\delta(t)$.

The estimated values of grid current amplitude and frequency can be calculated as follow

$$\hat{f}(t) = \frac{1}{2\pi}\sqrt{\hat{\varphi}_2(t) + a}, \quad \hat{A}_s(t) = \sqrt{\frac{\hat{\theta}_1(t)}{\hat{\varphi}_2(t) + a}}. \tag{2.37}$$

2.2.4 Comparison to Other Observers

For an ideal sinusoidal waveform (that is, in equation (2.33), $\tau = \infty$ and $\delta(t) = 0$), nonlinear observer designs have been studied to estimate amplitude A_s and frequency ω for arbitrary phase shift φ_s. In particular, the following third-order observer is proposed in [59]:

$$\begin{cases} \dot{\hat{x}} = -\alpha(\hat{x} - x) + \hat{\theta}^T \beta \\ \dot{\hat{\theta}} = -\Gamma \beta(\hat{x} - x) \end{cases}, \tag{2.38}$$

where $\beta = \begin{bmatrix} 1 & -2y^2 \end{bmatrix}^T$ and $\hat{x}$ is the estimate of state variable $y\dot{y}$. In parallel, the following fifth-order observer is also presented in [59]. This observer introduces a filtered version (ζ) of signal $\beta(t)$ in the estimation:

$$\begin{cases} \dot{\zeta}_2 = -\lambda'(\zeta_2 + 2y^2) \\ \dot{\hat{z}}_1 = -(1 + \alpha'\lambda')e_{z1} + \hat{z}_2 + \hat{\theta}^T \zeta \\ \dot{\hat{z}}_2 = -\alpha' e_{z1} + \lambda' \hat{\theta}^T \zeta \\ \dot{\hat{\theta}} = -\Gamma \zeta e_{z1} \end{cases}, \tag{2.39}$$

where $\hat{z}_1$ and $\hat{z}_2$ are estimates of state variables y^2 and $y\dot{y}$, respectively, $e_{z1} = (\hat{z}_1 - z_1)$, $\zeta = \begin{bmatrix} 1 & \zeta_2 \end{bmatrix}^T$, and $\lambda' > 0$ is the filter design constant.

The observer defined in (2.36) reduces to the observer in (2.38) when k_a, σ, B_1 and B_2 are zeros. The main difference between the proposed observer in (2.36) and the observer in (2.39), other than the second-order pre-filtering stage, is that a filtered version of the signal y^2 is used in (2.36) to drive the negative definite error into steady state. Also, two states are estimated for the observer in (2.39) in comparison to one state only for (2.36).

In comparison to adaptive observers presented in [51] and [60] where amplitude estimation depends on estimated frequency and estimated first derivative of signal (i.e. two stage

estimation process), the use of square signal in proposed observer provided a clear linearly parameterized form to estimate both frequency and amplitude simultaneously.

2.2.5 Islanding Detection Algorithm

The robust PCC level algorithm presented in subsection 2.1.5 will be used to detect islanding. The algorithm employs a sliding rectangular window to test convergence. Let us define the following

$$\begin{aligned} A_{err}(t) &= \max_{0\le\tau'\le T_d} |\hat{A}_s(t-\tau')| - \min_{0\le\tau'\le T_d} |\hat{A}_s(t-\tau')|, \\ A_{\max}(t) &= \max_{0\le\tau'\le T_d} |\hat{A}_s(t-\tau')|, \end{aligned} \tag{2.40}$$

where T_d is the designed time length for the window. A triggering memory variable μ is used to prevent false islanding detection under ambiguous cases. The variable μ is set to 1 if and only if the following condition is true:

$$(A_{err} < 2\varepsilon) \bigcap (A_{\max} \ge \varepsilon) \tag{2.41}$$

where ε is half the window width. Then, the following logical output (L_s) can be used to distinguish islanding condition from other conditions:

$$L_s(t) = \begin{cases} 0\ , & (A_{err} < 2\varepsilon) \bigcap (A_{\max} < \varepsilon) \bigcap (\mu == 1) \\ 1\ , & (A_{err} < 2\varepsilon) \bigcap (A_{\max} \ge \varepsilon) \\ 1\ , & (A_{err} < 2\varepsilon) \bigcap (A_{\max} < \varepsilon) \bigcap (\mu == 0) \\ 2\ , & (A_{err} \ge 2\varepsilon) \end{cases} \tag{2.42}$$

where the outcomes of L_s can be interpreted as follows:

$$L_s = \begin{cases} 0 & \text{Islanding is detected} \\ 1 & \text{Normal operation} \\ 2 & \text{Oscillation or transition} \end{cases}$$

As mentioned in subsection 2.1.5, this algorithm distinguishes islanding from other transition cases, prevents fault islanding detection, improves islanding confirmation decision, and enhances robustness of employed observer data. The value of ε should be chosen according to the maximum possible oscillation in per-unit amplitude during the steady state operation. The NDZ for the PCC level algorithm, as seen in subsection 2.1.6, is proportional to the test region parameter ε. The estimated NDZ is close to one line for a small value of ε where points at this line represent cases of perfect match between load demands and inverter outputs. This islanding detection technique provides smaller NDZ and faster detection time but requires more data compared to other existing islanding detection techniques.

2.2.6 Results

The same assumptions in subsection 2.1.2 are used in the MATLAB/Simulink model. Since current measurements will be utilized, the third and fifth assumptions in subsection 2.1.2 are conditions under which the MATLAB model is designed and the technique presented in this work can be generalized for other types of load and inverter controller as long as current measurements are available and currents maintain sinusoidal shape. The MATLAB/Simulink model consists of a 1kW inverter based DG connected to an *RLC* load and a grid as illustrated in Figure 2-22. The performance of the proposed observer during islanding transient was studied for three loading conditions. The three loading conditions are:

1. *RLC* load that approximately resonates at 60 Hz with Q_f = 2.5 and absorbs approximately 1kW.
2. *RLC* load that approximately resonates at 59.6 Hz with Q_f = 2.5 and absorbs approximately 1kW.

3. *RLC* load that approximately resonates at 60 Hz with Q_f = 2.5 and absorbs approximately 0.95kW.

The loads chosen represent cases where other IDMs might fail to detect an islanding situation. Table 2-3 shows some of the parameters used for simulation.

Table 2-3
Simulation Parameters for Non-Linear Observer IDM

Parameters	*Value*
V_r	120 V
f_g	60 Hz
$f_{\min}$	59.3 Hz
$f_{\max}$	60.5 Hz
ω_c	240π rad/s
ζ_d	0.707
ε	0.001 pu
T_d	35 ms
α	10^3
γ_1	10^6
γ_2	10^4
k_a	0.01
σ	0.1

2.2.6.1 Detectability and Convergence under Load Cases

At t = 2 seconds, the grid switch was opened to examine the proposed observer response during islanding. Figure 2-24 shows responses of grid current estimated amplitude ($\hat{A}_s$) in per-unit and PCC algorithm output (L_s) during islanding transition for different load cases. As seen in Figure 2-24, case 1 is theoretically undetectable by the proposed observer but practically inconsequential due to the perfect match in power, voltage and frequency between load and

inverter where the amplitude of current injected by the grid is zero. Cases 2 and 3 are detectable by the proposed observer where the estimated amplitude response settles down to zero within almost 20ms. The required time to confirm islanding conditions for cases 2 and 3 are 50.5 and 49.2ms, respectively. The observer responses during islanding can be modified by manipulating their parameters but that will degrade the convergence time Δt as will be shown in the next subsection.

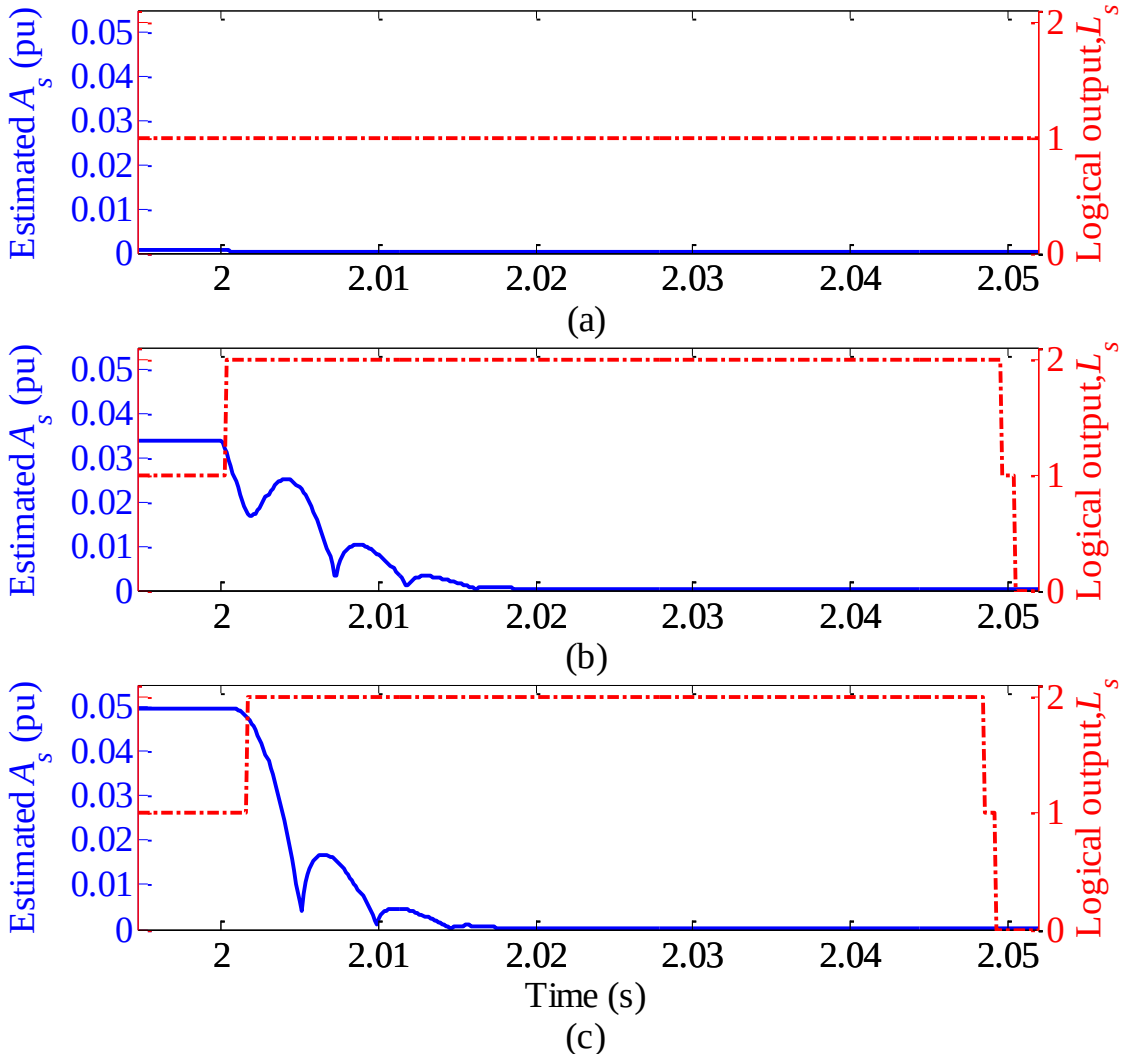

Figure 2-24: Responses of estimated amplitude (solid) and algorithm output (dashed) during islanding for different load cases: (a) Case 1. (b) Case 2. (c) Case 3.

2.2.6.2 Parameter Effect during Islanding Condition

The signals produced from case 2 loading condition will be used to study the effect of different parameter changes on proposed observer. Figure 2-25 shows the effect of α and γ_1 parameters on estimated amplitude and PCC algorithm output responses for proposed observer during islanding transition. From Figure 2-25, both α and γ_1 parameters affect both convergence speed and rippling of estimated amplitude when islanding occurs. Therefore, those two parameters should be optimized to obtain faster convergence to zero when islanding occurs in order to provide faster islanding detection. Also, other parameters such as k_a and γ_2 should be designed properly where limitations are imposed on observed frequency and that led to faster amplitude convergence and also minimizing steady-state rippling of amplitude. Moreover, k_a and γ_2 parameters will help in reducing the test region parameter ε which will reduce the NDZ of the proposed PCC level algorithm. It was noticed through simulation that steady-state rippling in amplitude response depends on frequency error where it increases/decreases as frequency error increases/decreases. Furthermore, proper design for pre-filtering parameters (ω_c and ζ_d) is necessary to allow y^2 frequency component to pass through with minimum attenuation. The σ parameter helps in attenuating both amplitude and frequency transition but it increases steady-state parameter error.

2.2.6.3 Robustness against Harmonics and Noise

The same $y(t)$ produced from case 2 loading condition will be used to study and compare robust performances of proposed observer and observers introduced in [59] against noise or harmonic distortion. For harmonic distortion, third and fifth order harmonics are added

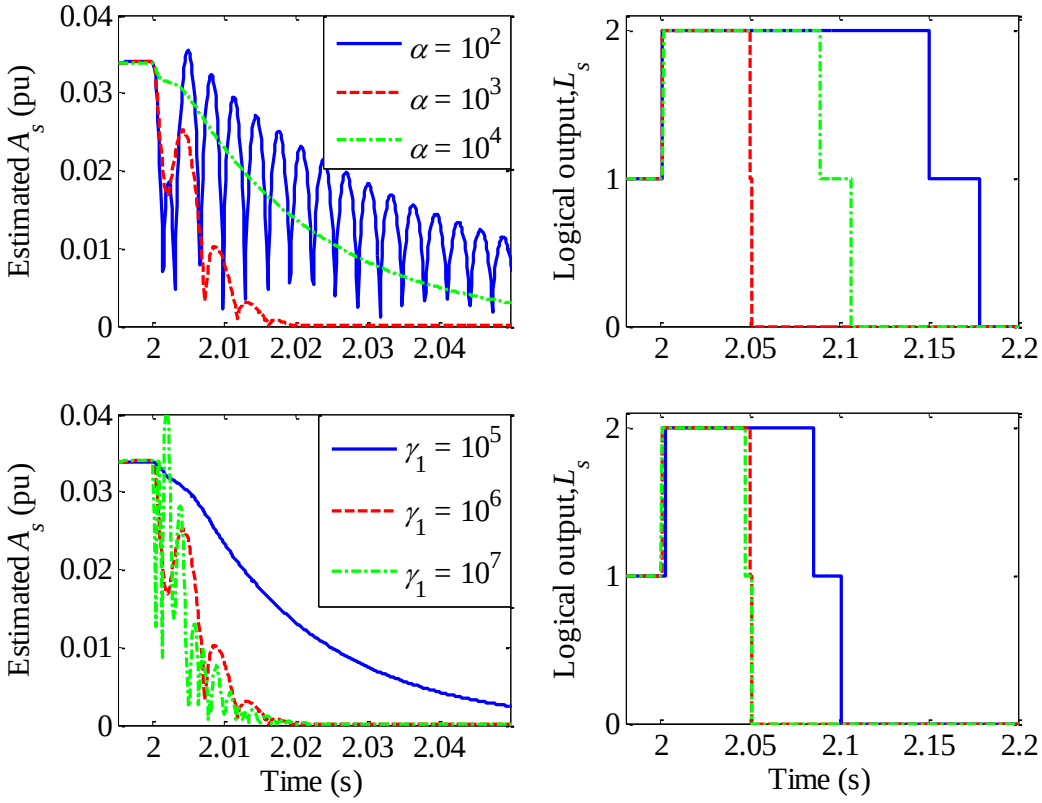

Figure 2-25: Effect of different α (upper) and γ_1 (lower) values on $\hat{A}_s$ (left) and L_s (right) responses during islanding.

to y where the Total Harmonic Distortion (THD) level is 5% and the third harmonic is assumed to have twice the amplitude of the fifth harmonic. A normally distributed white noise is used for the second scenario with a Signal-to-Noise Ratio (SNR) of 30dB. Both distortions are added at t = 2 seconds. The responses of $\hat{A}_s$ and L_s for third and fifth order observers presented in (2.38) and (2.39) are compared to proposed observer under harmonics and noise distortions as shown in Figure 2-26. The fifth-order observer parameters are set as follows:

$$\lambda' = \omega_c, \quad \alpha' = (\alpha - 1)/\omega_c$$

Simulation results in Figure 2-26 show that the proposed observer robust performance is superior against harmonics and noise compared to observers in [59]. This is mainly due to the

introduced second-order pre-filtering stage. The fifth-order observer shows better performance than third-order observer as a result of the first-order LPF applied to β only. For ε = 0.001 p.u., the proposed observer maintains similar algorithm output (L_s = 1) for distortions up to THD= 8% or SNR=25dB.

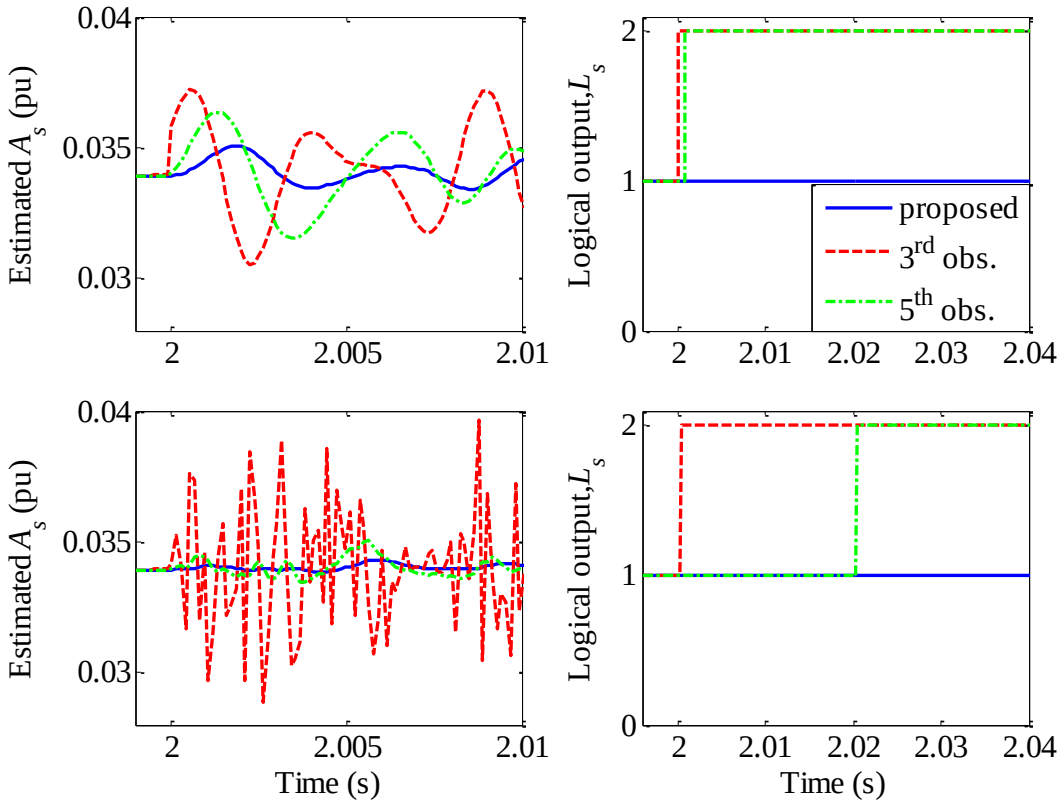

Figure 2-26: Comparison responses of $\hat{A}_s$ (left) and L_s (right) under harmonics (upper) and noise (lower) distortions.

2.2.6.4 IEEE 34-Bus Network

The standard IEEE 34-bus distribution network, which is shown in Figure 2-18, will be used to test the effectiveness and performance of the proposed observer scheme. The model is simulated in DigSilent. The detail of the parameters used in this network can be found in [47].

For illustrative purposes, two cases will be studied. The first case is an islanding situation at t = 2sec. which takes place at Bus (**C**) in Figure 2-18. The second case is a three-phase short circuit fault that takes place at point (**A**) at t = 2sec. and clears out within 0.03sec. Figure 2-27 shows comparison responses of $\hat{A}_s$ and L_g for both study cases.

It can be noticed from Figure 2-27 that the proposed observer significantly reduced rippling during both islanding and fault transition. Results in Figure 2-27 imply that the proposed observer is more robust against fault disturbances than observers proposed in [59].

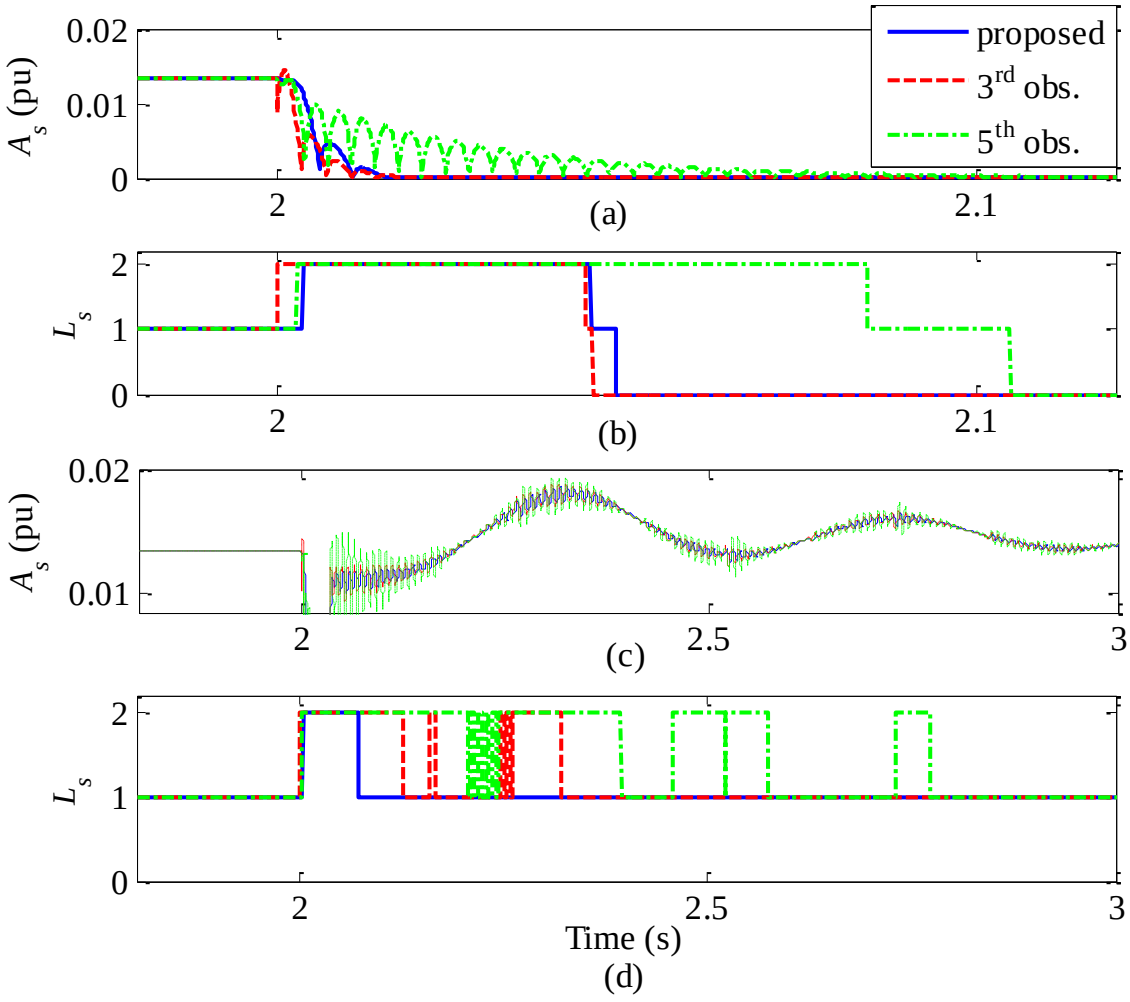

Figure 2-27: Responses during islanding and three phase short circuit fault: (a) $\hat{A}_s$ and (b) L_s during islanding. (c) $\hat{A}_s$ and (d) L_s during fault.

2.2.7 Discussion

Detailed analytical derivation and proof of robustness and convergence have been presented for the proposed fifth-order robust non-linear observer that estimates both amplitude and frequency of a noisy sinusoidal signal. The observer was designed to ensure robustness and to provide better performance for the islanding detection problem. Analytical and simulation results show that the performance of proposed observer is superior in comparison to observers presented in [59]. The time required to detect islanding condition is within four nominal cycles for all implemented cases. The proposed observer showed robust performances against noise, harmonics and disturbances. To compare with previous section results, the case presented in subsection 2.2.6.3 will be used. The responses of $\hat{A}_s$ and L_s for the dynamic estimator presented in section 2.1 are compared to the proposed non-linear observer under THD= 8% and SNR =25dB as shown in Figure 2-28.

In Figure 2-28 (b), the PCC algorithm output for observer went through a transition state as a result of observer pre-filtering response behavior. The forgetting factor, introduced in the RLS algorithm in (2.21), plays a major role in enhancing the robust performance of dynamic estimator. It can be seen from Figure 2-28 that the proposed non-linear observer shows better robust performance against harmonics and noise in comparison to the dynamic estimator presented in section 2.1. Also, a solid theoretical proof of robustness and convergence for proposed observer can be obtained through Lyapunov function analysis as can be seen in Appendix B where no similar results can be found for dynamic estimator. The problem of improving both performance and islanding detection capability for single and multi-DG systems will be studied in the next chapter.

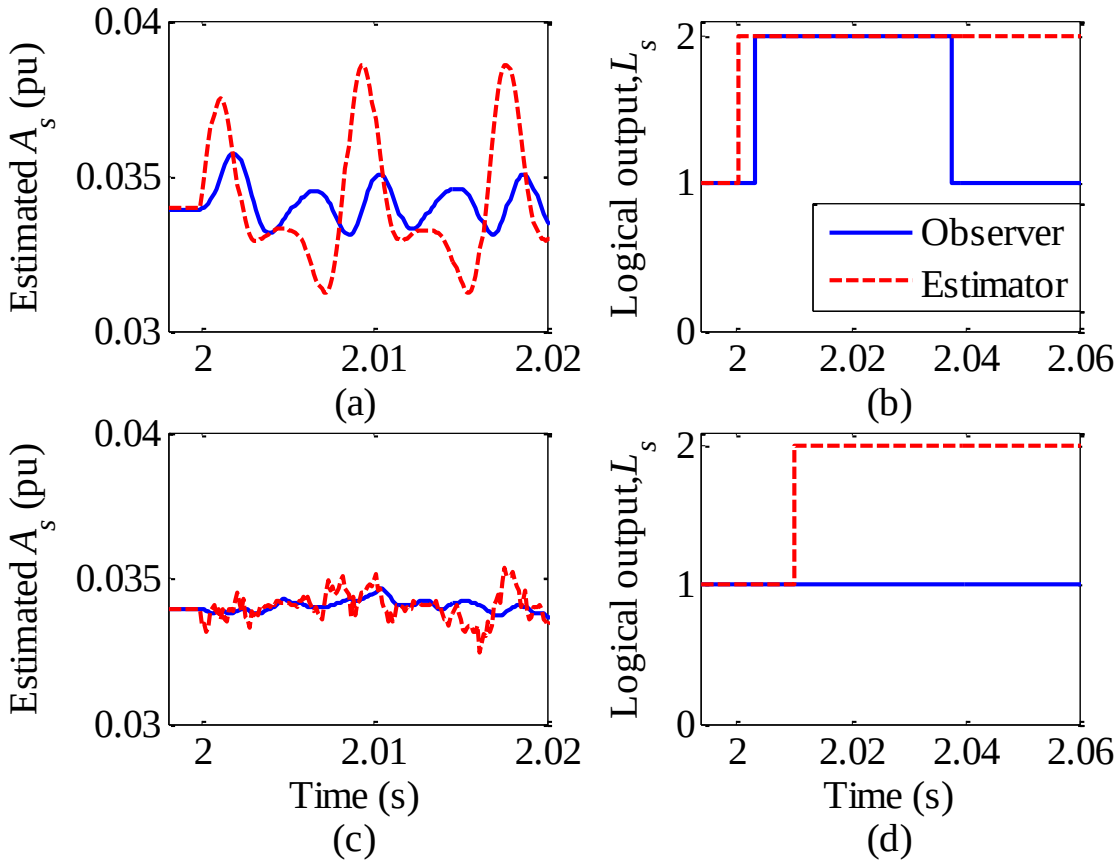

Figure 2-28: Comparison between observer (solid) and estimator (dashed) responses for $\hat{A}_s$ (left) and L_s (right) under THD= 8% (upper) and SNR= 25dB (lower).

CHAPTER 3: TECHNIQUES TO IMPROVE MULTI-DGS ISLANDING DETECTION CAPABILITY

Two main techniques to improve both the performance and islanding detection capability for single- and multi-DG systems are presented in this chapter. The first technique, in section 3.1, is the use of scheduled perturbation where two IDMs can be used consecutively to enhance single- and multi-DGs overall IDMs performance. Section 3.2 illustrates the development of a new active IDM that is based on transient stiffness measurement for the multi-DG system.

3.1 Scheduled Perturbation to Reduce NDZ for Low Gain SFS Method

3.1.1 Introduction

Typically, the performance of IDMs is evaluated based on the Non-Detection Zone (NDZ) concept. NDZ is a region in appropriately defined load space in which the IDM under test fails to detect islanding condition in a timely manner [29]. *RLC* load resonant frequency−quality factor ($f_o - Q_f$) space has been proven to be more representative for AFD and SFS NDZs [30]. In [38], small-signal stability analysis is used to determine critical Q_f value (Q_f^*) where any operating point with smaller Q_f than Q_f^* is destabilized by SFS during islanding operation. However, this technique is time consuming and an analytical expression for Q_f^* is required. Moreover, the impact of SFS on system stability has been studied in [63] and results showed that high SFS gain (K) might destabilize grid-connected DG system when grid is weak or DG size is large. Hence, it is important to develop a technique that reduces the dependency on gain K to eliminate NDZ. Recently, few studies have considered the problem of applying active IDMs for multi-DG system [63]-[70]. For two DGs case, it has been shown in [67] that the use of AFD in

one DG will degrade the SFS or SMS performance for the other DG and the NDZ will increase significantly compared to single DG case.

The objective of this section is to propose a scheduled perturbation IDM (SIDM) where the overall NDZ of this technique is represented by the intersection area between two NDZs of two different IDMs. Two interesting cases are considered in this section. The first case is to apply scheduling between SFS and OUF (SFS/OUF) IDMs. The second case is to use two SFS (SFS/SFS) with alternating sign of initial chopping fraction. The provided concept could be expanded to other combination of IDMs. The initial chopping fraction (cf) in SFS plays a major role in eliminating NDZ for this technique. Hence, this technique will reduce the dependency on K to eliminate NDZ where zero NDZ, up to certain Q_f value, can be obtained through proper design of cf at $K = 0$. Also, analytical expressions will be provided to find critical Q_f values for both scheduled perturbation and conventional IDMs.

The rest of this section is organized as follows. Subsection 3.1.2 presents the DG interface model under study. The design concept is introduced in subsection 3.1.3. Effect of scheduled perturbation IDM on critical quality factor and resonant frequency values (Q_f^* and f_o^*) is studied in subsection 3.1.4. The theoretical reduction in NDZ size obtained from utilizing scheduled perturbation is analyzed in subsection 3.1.5. The performance and synchronization requirements for proposed technique are tested through simulation for single and two DGs systems in subsection 3.1.6. At last, discussions are presented in subsection 3.1.7.

3.1.2 System Under Study

A single-line diagram of a general *N*-DG system is shown in Figure 3-1 where *N* is the number of connected DGs. The detail of this model can be found in [38]. In Figure 3-1, L_g and R_g corresponds to the inductance and resistance of the utility line, respectively. Utility or grid voltage is $E\angle 0$ and the voltage at the point of common coupling (PCC) is $V\angle\delta$. For the i^{th} DG, the output power is $P^i - jQ^i$ and the output current is $m_i I\angle\delta+\theta_i$ where I is the load current magnitude, m_i is the fraction of load power supplied by the i^{th} DG and θ_i is the positive feedback signal for the i^{th} DG unit. The negative sign in the reactive power indicates that Q^i is the reactive power absorbed by the i^{th} DG. The inductance of inverter filter is represented by L_f and is assumed to be the same for all DGs. $\Delta P + j\Delta Q$ is the power imbalance between the parallel *RLC* load and the total power output supplied by all DGs. A circuit breaker (CB) is used to simulate an islanding situation by disconnecting the grid. In this model, an average model for three-phase inverter is employed where the pulse width-modulated (PWM) signal generator, the dc source, and the switching power electronics devices, such as insulated gate bipolar transistors (IGBTs), are replaced by a three-phase controlled voltage source [13], [38], [63]. A three-phase PLL is used to measure the frequency of PCC voltage. The interface control used for each inverter is a constant current controller. Details of DG controller, scheduled IDM and PLL blocks are shown in Figure 3-2.

The constant current controller implemented for DG system is shown in Figure 3-2 (a). i_{dref} and i_{qref} are the *d*- and *q*-axis DG output current references, respectively. A phase angle transformation is applied to obtain new current references i^*_{dref} and i^*_{qref}. The angles θ' or θ''

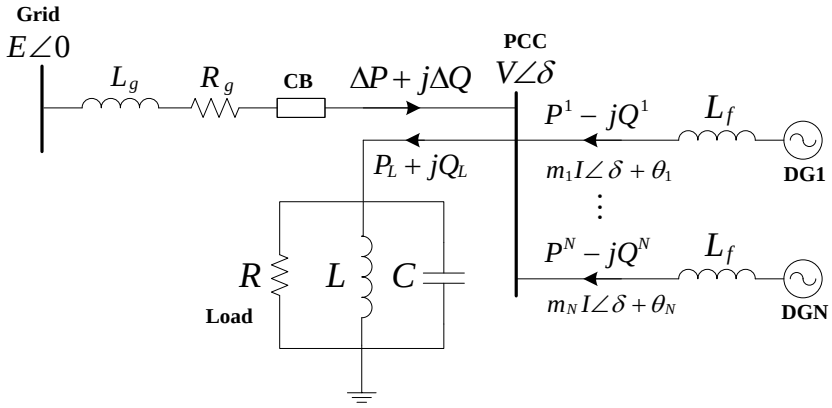

Figure 3-1: Single-line schematic diagram of multi-DG system.

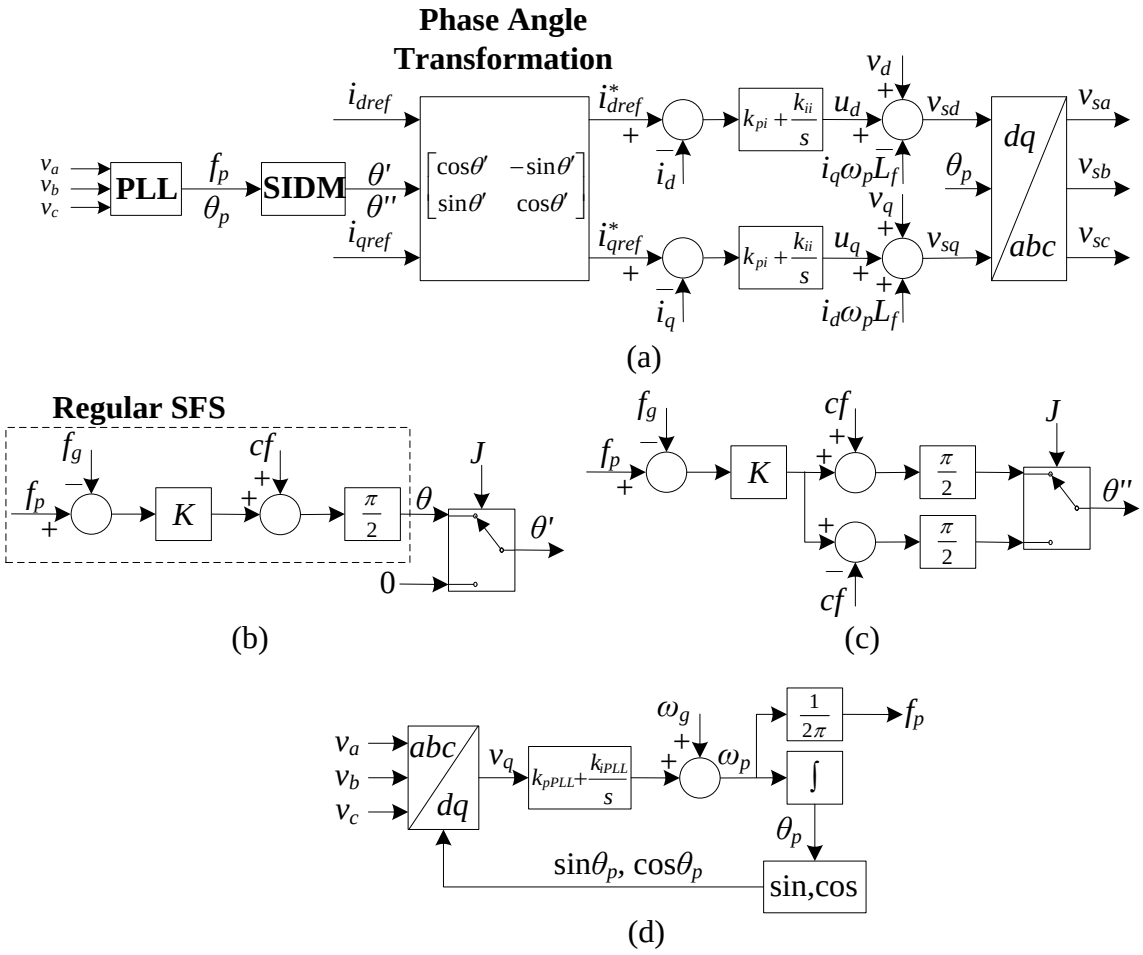

Figure 3-2: Block diagrams of controller and islanding detection circuits of DG system. (a) Constant current controller. (b) Scheduled SFS/OUF IDM. (c) Scheduled SFS/SFS IDM. (d) Three-phase PLL.

used in transformation are the outputs of scheduled SFS/OUF and SFS/SFS IDMs introduced in Figure 3-2 (b) and Figure 3-2 (c), respectively. In Figure 3-2 (b), the regular SFS output is applied to a multi-input single-output switch, which is driven by a scheduled signal J, to obtain θ'. The difference between block (b) and (c) in Figure 3-2 is that zero is used for the other input to the multi-input single output switch for case (b) while an SFS output with negative chopping fraction is used for case (c). The input frequency to both Scheduled IDMs (SIDMs) is measured by a three-phase PLL presented in Figure 3-2 (d). Then, the new references are subtracted from measured output currents (i_d and i_q) and applied to proportional-integral (PI) controllers with gains k_{pi} and k_{ii}, respectively. The *d*- and *q*-axis outputs of PI controller are u_d and u_q, respectively. Adding $v_d - i_q \omega_p L_f$ term to u_d and $v_q + i_d \omega_p L_f$ term to u_q is known as cross-coupling which is used to match control design equation such that the *dq* currents are decoupled from each other in terms of control equations, and also to substitute for voltage drop caused by DG inductance filter (L_f). Finally, a *dq-abc* transformation is applied to construct three-phase voltage signals (v_{sa}, v_{sb} and v_{sc}) which will be used to drive controlled voltage sources as seen in Figure 3-1.

3.1.3 Design Concept

For conventional SFS, the positive feedback signal for the i^{th} DG is defined as

$$\theta_i = \frac{\pi}{2}\left(cf_i + K_i(f_p - f_g)\right), \tag{3.1}$$

where $i = 1,2,\ldots,N$, cf_i is the initial chopping fraction, K_i is the positive feedback gain, f_p is the measured frequency of PCC voltage in Hz, and f_g is the grid base frequency in Hz.

The design objective behind switching perturbation is to obtain an overall NDZ as the intersection area between two different IDMs. Two interesting cases are considered in this work. The first case is to apply scheduling between SFS and OUF (SFS/OUF) IDMs. The second case is to use two SFS (SFS/SFS) with alternating sign of initial chopping fractions.

3.1.3.1 Scheduled SFS/OUF IDM

Let us assume that J_i is a periodic scheduled signal with period T_i that will be used to re-define the positive feedback signal for the i^{th} DG as follows:

$$\theta_i'(t) = \begin{cases} \theta_i, & 0 < t \le d_i T_i \\ 0, & d_i T_i < t \le T_i \end{cases} \tag{3.2}$$

where d_i is the duty cycle for the periodic perturbation signal J_i. For simplicity, let us assume that similar design parameters (cf, K, d, and T) will be used for all DGs and hence $\theta_i' = \theta'$. In case of a multi-DG system ($N \ge 2$), synchronization of scheduled perturbation signals is required. The synchronization can be achieved through either one of these two methods. The first method is to provide a local timer to each DG system where all timers have to be set in advance to provide the required perturbation signal (J). The synchronicity requirement is quite flexible as will be seen later where a loss of synchronism study will be conducted in subsection 3.1.5.2. Also, the scheduled signal parameters (d and T) will be chosen in a way to simplify implementation. The other method is to achieve synchronization through limited communication where d_i information are exchanged among DGs. This method is more expensive but might be more feasible if some type of communication already exist among DGs [46].

For conventional SFS, the phase criterion to obtain NDZ for a single DG system is given as follows [30]:

$$f_o^{\,2} + f_p \frac{\tan(\theta)}{Q_f} f_o - f_p^{\,2} = 0, \tag{3.3}$$

where f_p are substituted by upper ($f_{\max}$) and lower ($f_{\min}$) threshold values of OUF to determine upper and lower bounding functions of NDZ, respectively. Figure 3-3 shows NDZs of OUF and conventional SFS with cf = 0.1 and K = 0.05. The OUF technique can be considered as a special case of regular SFS with $cf = K = 0$. The NDZ for OUF technique is represented by areas **A** and **B**. On the other hand, areas **A** and **C** are the corresponding NDZ for conventional SFS IDM. The SFS critical point, under which any point to the left of this point is unstable, is indicated by point **E** with corresponding coordinate values of Q_f^* and f_o^*.

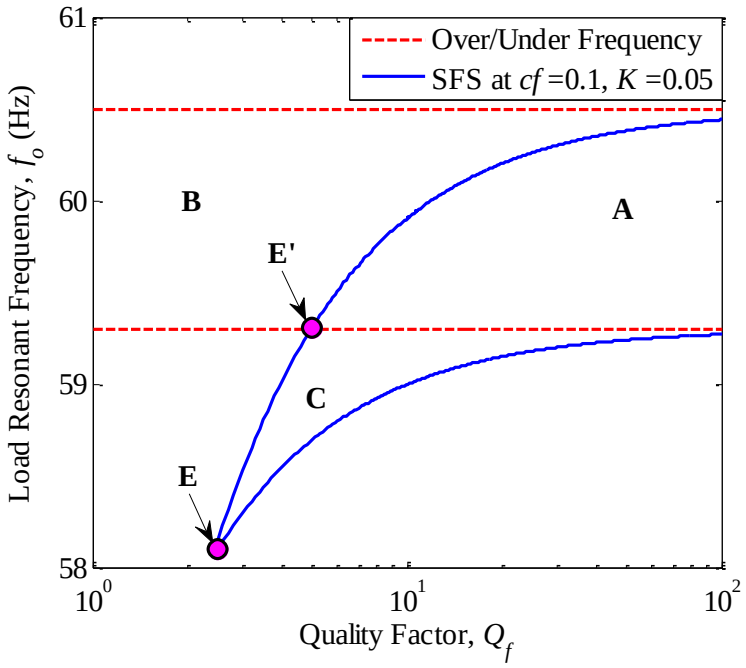

Figure 3-3: NDZ for OUF (dashed) compared to regular SFS (solid) at cf = 0.1 and K = 0.05.

Let us assume that both d and T are properly designed such that enough time is provided for both SFS and OUF output frequency to converge to steady-state value such that points lying in Areas **B** and **C** are considered detectable. Then, area **A** which corresponds to the

intersection between the two NDZs can be obtained by employing the scheduled perturbation algorithm in (3.2). Hence, the critical point **E** will be shifted to point **E'** which will lead into significant reduction in NDZ size through eliminating area **C** from the NDZ of conventional SFS IDM. The coordinates of point **E'** are Q_f^{**} and f_o^{**} where Q_f^{**} has a higher value than Q_f^*. The change in NDZ will be studied further in subsections 3.1.4 and 3.1.5.

3.1.3.2 Scheduled SFS/SFS IDM

Similarly, the periodic scheduled signal J_i is used to re-define the positive feedback signal for the i^{th} DG as follows:

$$\theta_i''(t) = \begin{cases} \theta_i^+ , & 0 < t \le d_i T_i \\ \theta_i^- , & d_i T_i < t \le T_i \end{cases} \tag{3.4}$$

where $\theta_i^+ = \frac{\pi}{2}\left(cf_i + K_i(f_p - f_g)\right)$ and $\theta_i^- = \frac{\pi}{2}\left(-cf_i + K_i(f_p - f_g)\right)$.

For simplicity, let us assume that similar design parameters (cf, K, d, and T) will be used for all DGs and hence $\theta_i'' = \theta''$. Figure 3-4 shows NDZs of two SFS, one at $cf = -0.05$ and $K = 0.05$ and the other one is at $cf = 0.05$ and $K = 0.05$. The NDZ for SFS at positive cf is represented by areas **A** and **C** while areas **A** and **B** are the corresponding NDZ for SFS at the negative cf value. The SFS critical point is indicated by point **E** for positive cf or point **E'** for negative cf with corresponding coordinate values of Q_f^* and f_o^* for each.

Assuming that both d and T are properly designed to provide enough time for both SFSs output frequency to converge to steady-state value such that points lying in Areas **B** and **C** are considered detectable. Then, area **A** which corresponds to the intersection between the two NDZs can be obtained by employing the scheduled perturbation algorithm in (3.4). Hence, the

critical point **E** or **E'** will be shifted to point **E''** which will lead into significant reduction in NDZ size through eliminating areas **C** and **B** from conventional SFS at positive and negative cf values, respectively. The coordinates of point **E''** are Q_f^{**} and f_o^{**} where Q_f^{**} is always greater than or equal to Q_f^* as will be seen in subsection 3.1.4.

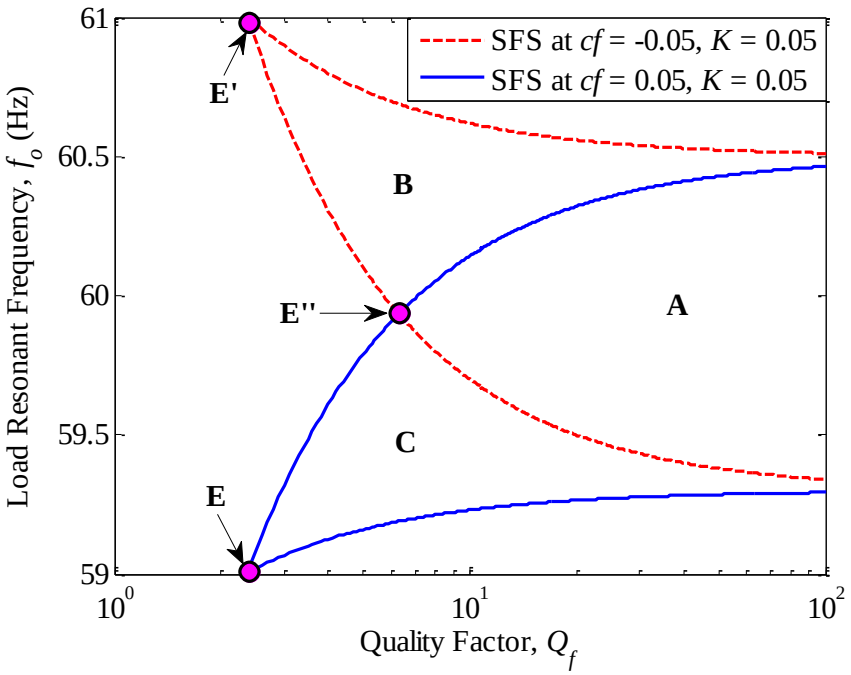

Figure 3-4: NDZ for SFS at $cf = -0.05$ and $K = 0.05$ (dashed) and SFS at $cf = 0.1$ and $K = 0.05$ (solid).

3.1.4 Scheduled Perturbation Effect on Q_f^* and f_o^*

For conventional SFS, the equivalent angle for *N*-DGs can be found as:

$$\theta_{eq} = \tan^{-1}\left(\frac{\sum_{i=1}^{N} m_i \sin\theta_i}{\sum_{i=1}^{N} m_i \cos\theta_i}\right), \tag{3.5}$$

where θ_{eq} reduces down to θ if similar design parameters (i.e. cf and K) are used for all *N*-DGs. Let us assume that upper and lower frequency thresholds are $f_{\max}$ and $f_{\min}$, respectively. Then, the coordinates of critical points for conventional IDMs can be approximated by

$$\begin{aligned} Q_f^* &\cong \frac{f_g\left(\tan(\theta|_{f_p=f_{\max}}) - \tan(\theta|_{f_p=f_{\min}})\right)}{2(f_{\max} - f_{\min})}, \\ f_o^* &\cong \frac{f_{\max}\,\tan(\theta|_{f_p=f_{\max}})}{2Q_f^*}\left[-1+\sqrt{1+\left(\frac{2Q_f^*}{\tan(\theta|_{f_p=f_{\max}})}\right)^2}\right], \end{aligned} \tag{3.6}$$

where the upper NDZ bounding line is used to calculate the corresponding f_o^*. The lower bounding line of NDZ can be used alternatively to calculate f_o^* where similar results will be obtained. The result of Q_f^* in (3.6) was obtained by equating the two NDZ lines equations obtained from phase criteria where *RLC* load current phase (φ_L) behavior was approximated by Taylor series expansion around $f_p = f_g$ as follows:

$$\tan(\varphi_L) \cong \alpha_0 + \alpha_1(f_p - f_g), \tag{3.7}$$

where

$$\begin{aligned} \alpha_0 &= Q_f(f_g/f_o - f_o/f_g), \\ \alpha_1 &= Q_f(1/f_o - f_o/f_g^2) \approx 2Q_f/f_g. \end{aligned}$$

3.1.4.1 Scheduled SFS/OUF IDM

In a similar way used to obtain (3.6), the formula for Q_f^{**} and f_o^{**}, resulting from scheduled SFS/OUF IDM, can be calculated. Assuming that both d and T are designed properly, the coordinates of **E'** in Figure 3-3 can be calculated by equating the two NDZs intersected lines equations where the following results are obtained:

$$Q_f^{**} \cong \frac{f_g\left(\max(\tan(\theta|_{f_p=f_{\max}}),0)-\min(\tan(\theta|_{f_p=f_{\min}}),0)\right)}{2(f_{\max}-f_{\min})},$$
$$f_o^{**} \cong \frac{f_{\max}\,\max(\tan(\theta|_{f_p=f_{\max}},0)}{2Q_f^{**}}\left[-1+\sqrt{1+\left(\frac{2Q_f^{**}}{\max(\tan(\theta|_{f_p=f_{\max}}),0)}\right)^2}\right]. \quad (3.8)$$

In Figure 3-5, the values of both Q_f^* and Q_f^{**} and their corresponding resonant frequencies (f_o^* and f_o^{**}) for scheduled SFS/OUF IDM are shown with respect to cf changes for different K values. For each value of K, scheduled SFS/OUF technique produces similar Q_f^* values as conventional SFS from cf equal zero up to certain critical cf values (cf_+ or cf_-) after which the value of Q_f^{**} increases linearly as a function of cf and no significant change is noticed for Q_f^*. In other words, there is a specific interval in cf values at which no significant improvement can be achieved from the use of properly designed scheduled SFS/OUF technique, and this interval depends on the gain (K) value. On the other hand, the value of f_o^{**} decreases/increases linearly as cf value is increased/decreased until it reaches $f_{\min}$ or $f_{\max}$ where it stays constant afterwards while f_o^* keeps changing linearly. Hence, proper design for scheduled SFS/OUF technique requires that critical cf values are completely known.

The critical cf values can be approximated through studying the behavior of Q_f^{**}. By using Taylor series expansion on $\tan(\theta)$, the design condition for linearly increased Q_f^{**} is:

$$cf > K(f_g - f_{\min}) \text{ or } cf < -K(f_{\max} - f_g). \quad (3.9)$$

The interval defined in (3.9) is symmetric around zero if the threshold area of OUF is symmetric around f_g which is not typically the case for 60 Hz. Therefore, the critical cf values depend on both the SFS gain and frequency threshold values compared to nominal.

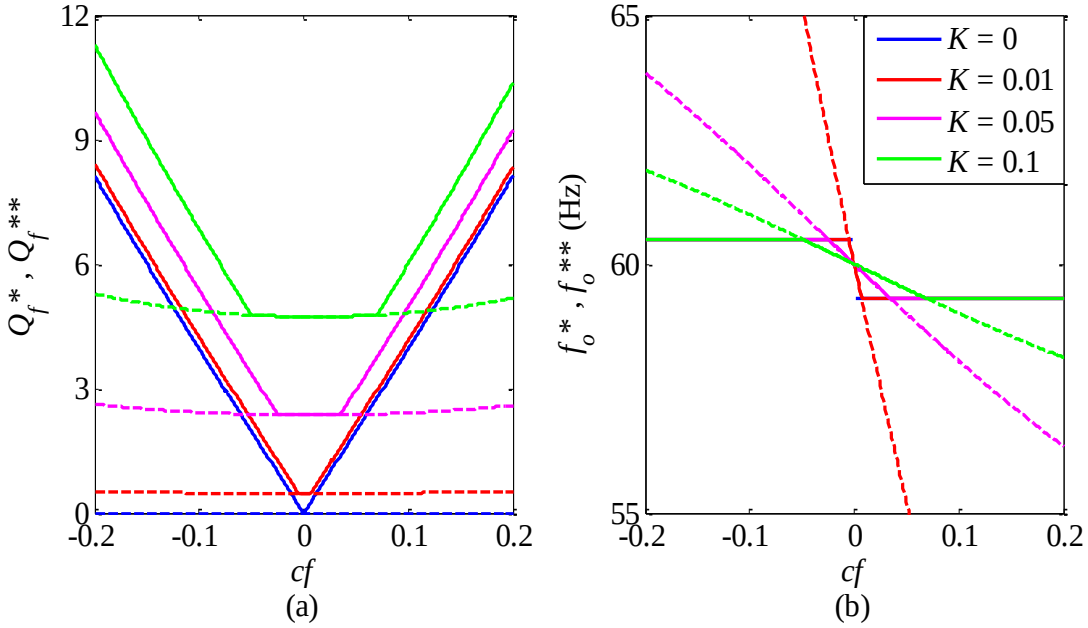

Figure 3-5: Effect of cf on (a) Q_f^* (solid) and Q_f^{**} (dashed) (b) f_o^* (solid) and f_o^{**} (dashed) at different K's for scheduled SFS/OUF IDM.

3.1.4.2 Scheduled SFS/SFS IDM

Similarly, the formula for Q_f^{**} and f_o^{**} achieved through scheduled SFS/SFS IDM can be obtained. Assuming that both d and T are designed properly, the coordinates of **E''** in Figure 3-4 can be calculated as follows:

$$Q_f^{**} \cong \frac{f_g\left(\max(\tan(\theta^+\big|_{f_p=f_{\max}}),\tan(\theta^-\big|_{f_p=f_{\max}})) - \min(\tan(\theta^+\big|_{f_p=f_{\min}}),\tan(\theta^-\big|_{f_p=f_{\min}}))\right)}{2(f_{\max}-f_{\min})},$$

$$f_o^{**} \cong \frac{f_{\max}\,\max(\tan(\theta^+\big|_{f_p=f_{\max}}),\tan(\theta^-\big|_{f_p=f_{\max}}))}{2Q_f^{**}}\left[-1+\sqrt{1+\left(\frac{2Q_f^{**}}{\max(\tan(\theta^+\big|_{f_p=f_{\max}}),\tan(\theta^-\big|_{f_p=f_{\max}}))}\right)^2}\right]. \quad (3.10)$$

In Figure 3-6, the values of both Q_f^* and Q_f^{**} and their corresponding resonant frequencies (f_o^* and f_o^{**}) for scheduled SFS/SFS IDM are shown with respect to cf changes for different K values. For each value of K, Q_f^{**} of scheduled SFS/SFS technique increases linearly as a function of cf while no significant change is noticed for Q_f^*. In other words, the use of cf for scheduled SFS/SFS technique always improves critical Q_f values and hence NDZ is reduced. On the other hand, the value of f_o^{**} decreases exponentially as cf value is increased where the value of K determines the convergence speed and higher K value corresponds to slower convergence. As cf is increased to infinity, f_o^{**} converges to the middle point of OUF (f_{mid}) which can be obtained as follows:

$$f_{mid} = \frac{f_{\max} + f_{\min}}{2}.$$

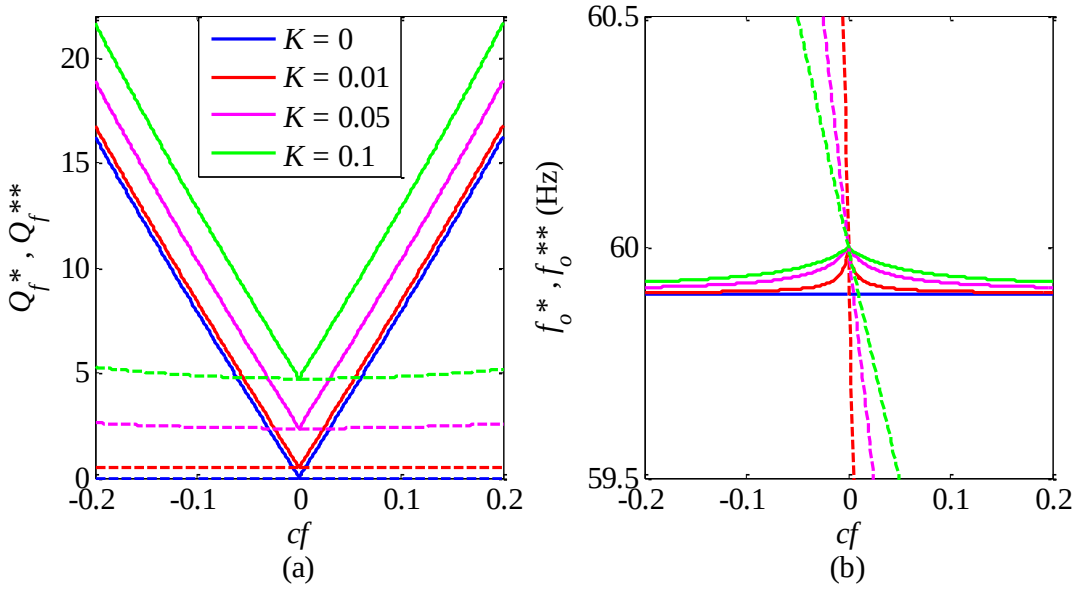

Figure 3-6: Effect of cf on (a) Q_f^* (solid) and Q_f^{**} (dashed) (b) f_o^* (solid) and f_o^{**} (dashed) at different K's for scheduled SFS/SFS IDM.

In this case, the design condition defined in (3.9) for linearly increased Q_f^{**} collapses to the following interval:

$$cf > 0 \text{ or } cf < 0. \tag{3.11}$$

Also, by comparing Figure 3-5 to Figure 3-6, it can be noticed that the slope of Q_f^{**} is twice higher for scheduled SFS/SFS compared to SFS/OUF IDM. Therefore, the Q_f^{**} value, obtained at certain cf and K values for scheduled SFS/SFS IDM, is at least twice the Q_f^{**} value obtained at similar cf and K values for scheduled SFS/OUF IDM. The Q_f^{**} value for scheduled SFS/SFS is exactly twice the value obtained from scheduled SFS/OUF for cases with $K = 0$. Hence, the requirement on cf to achieve a certain Q_f^{**} value for scheduled SFS/OUF IDM is at least twice as much as the requirement on cf to achieve similar Q_f^{**} for scheduled SFS/SFS IDM.

3.1.5 Improvement in NDZ

In order to quantify NDZ improvement, the size of NDZ is considered. The middle point Riemann sum can be used to calculate the NDZ size and is given by [67]:

$$S = \sum_{j \in NDZ} \left(\frac{u(j+1) - u(j)}{2} - \frac{l(j+1) - l(j)}{2} \right) \cdot \left(\log Q_f(j+1) - \log Q_f(j) \right), \tag{3.12}$$

where u and l are the upper and lower bounding function of NDZ, respectively. The log of Q_f is used to emphasize on NDZ size for small Q_f values which are of more interest for protection engineers to eliminate. The relative change of NDZ size can be calculated as follows:

$$\Delta S = \frac{S_j - S_k}{S_k} \times 100\% \ , \tag{3.13}$$

where S_j is the NDZ size of scheduled IDM and S_k is the NDZ size for conventional IDM.

3.1.5.1 Scheduled SFS/OUF IDM

Let us assume that the considered NDZ area for simulation is from Q_f equal 0.1 to 100 with a step of 0.1. Figure 3-7 shows the size of NDZs of scheduled SFS/OUF and conventional SFS as a function of cf and the relative change of size at different K values. Similar conclusions can be obtained from Figure 3-7 where no size reduction can be achieved if cf is outside the interval defined in (3.9). Also, higher size reduction can be achieved at smaller K where up to 82.5% reduction in NDZ size is acquired at $cf = -0.2$ and $K = 0$.

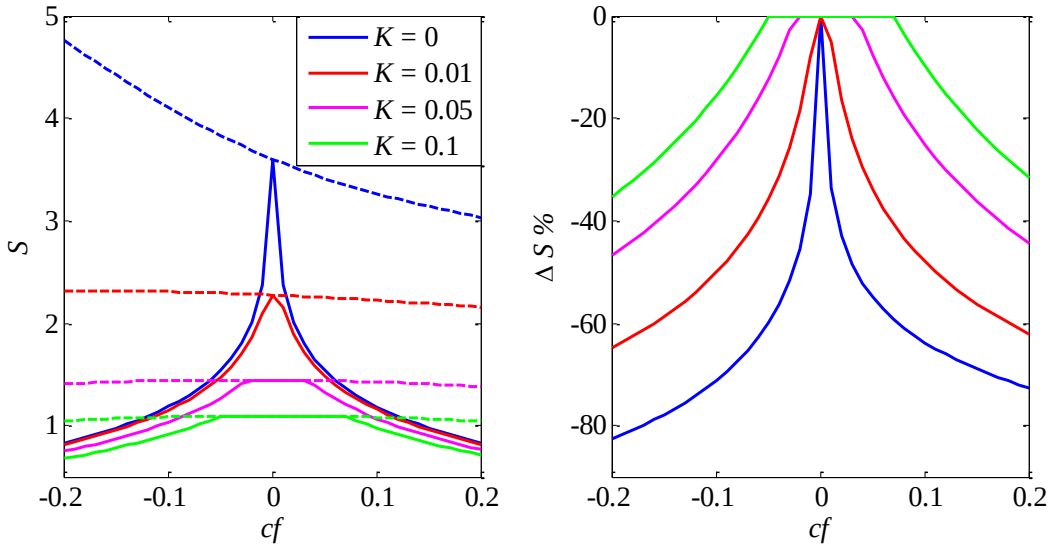

Figure 3-7: Size of NDZ for single DG scheduled SFS/OUF (solid) compared to regular SFS (dashed) for different K's.

3.1.5.2 Scheduled SFS/SFS IDM

Figure 3-8 shows the size of NDZs of scheduled SFS/SFS and conventional SFS as a function of cf and the relative change of size at different K values. The size of NDZ for

scheduled SFS/SFS is always smaller than regular SFS for non-zero cf . Also, higher reduction can be achieved in comparison to scheduled SFS/OUF technique even at large K where a NDZ reduction of 62.76% is achieved at $cf = -0.2$ and $K = 0.1$ in comparison to 35.32% for scheduled SFS/OUF IDM.

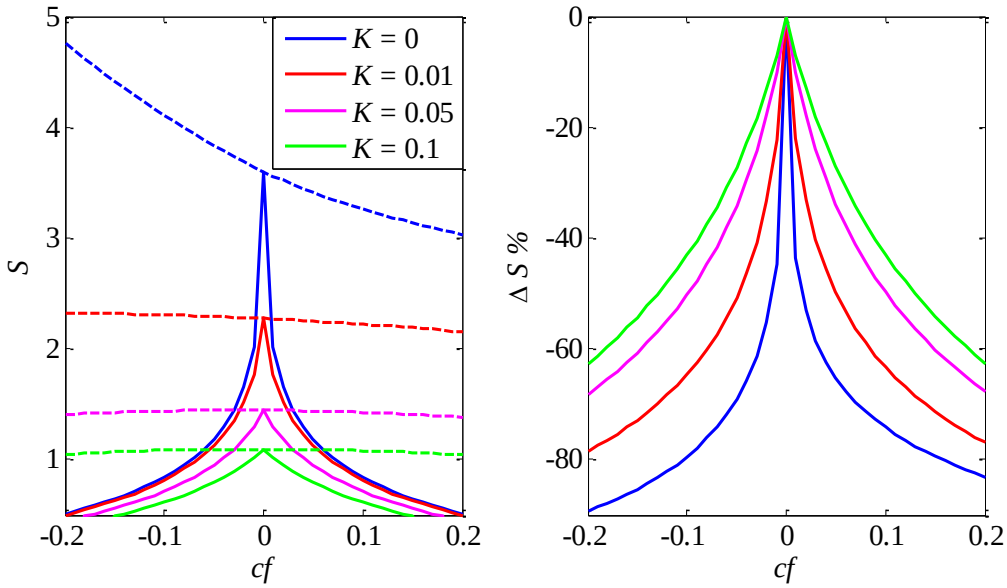

Figure 3-8: Size of NDZ for single DG scheduled SFS/SFS (solid) compared to regular SFS (dashed) for different K's.

3.1.6 Results

The system, shown in Figure 3-1, was modeled in MATLAB Simulink to verify theoretical analysis provided in earlier subsections. For illustration purposes, the results for single and multiple ($N = 2$) 10kW DGs are considered and the concept can be easily extended to N-DG system. Unless mentioned otherwise, the model parameters in Table 3-1 are used for simulation. The parallel *RLC* load parameters provided in Table 3-1 correspond to a 10kW load

with f_o = 60Hz and Q_f = 2.5. For all cases except subsection 3.1.6.3, the simulation is stopped if islanding condition is confirmed where measured frequency exceeds threshold values for more than six consecutive cycles [3]. The six cycle delay was proposed to avoid nuisance tripping due to short-term disturbances. This stopping criterion assumes that NDZ bounding lines are part of the NDZ where loading points lying on these lines are considered undetectable.

Table 3-1
Simulation Parameters for Scheduled Perturbation IDM

Parameters	*Value*	*Parameters*	*Value*
$V_{(phase\text{-}to\text{-}ground)}$	120 V	L	4.5837 mH
V_{base}	170 V	C	1.5351 mF
S_{base}	10 kVA	k_{pi}	0.5
f_g	60 Hz	k_{ii}	500
$f_{\max}$	60.5 Hz	k_{pPLL}	50
$f_{\min}$	59.3 Hz	k_{iPLL}	500
R_g	0.2 Ω	K	0
L_g	0.796 mH	d	1 s
L_f	1 mH	T	2 s
R	4.32 Ω		

3.1.6.1 Effect of Duty Cycle (d)

Let us assume that $d_i = \mu_i T_g$ where $T_g = 1/f_g$ is the nominal frequency period and μ_i is the number of cycles perturbed by the i^{th} DG. Standards such as IEEE929-2000 and IEEE1547 require islanding to be detected within less than 2 seconds of occurrence [3], [6]. Hence, the perturbation signal period for all DGs is assumed to be fixed and equal 2 seconds (T = 2s) which correspond to 120 cycles in 60Hz. For a single DG case with scheduled SFS/OUF IDM, cf = 0.06345 and K = 0 corresponds to $Q_f^{**} = 2.5$ from Figure 3-5 where SFS technique reduces to

AFD in cases with $K = 0$. This is a very interesting case to study since AFD always have NDZ and is relatively large compared to regular SFS with K greater than zero. The reference values used for constant current controller are i_{dref} = 1pu and i_{qref} = 0. The circuit breaker (CB) is opened at t = 0.5s to simulate islanding behavior. For simulation purposes, the perturbation signal is triggered at t = 0.5s. Figure 3-9 (a) shows frequency responses for scheduled SFS/OUF technique at f_o = 59.2Hz and Q_f = 2.5 for different μ values.

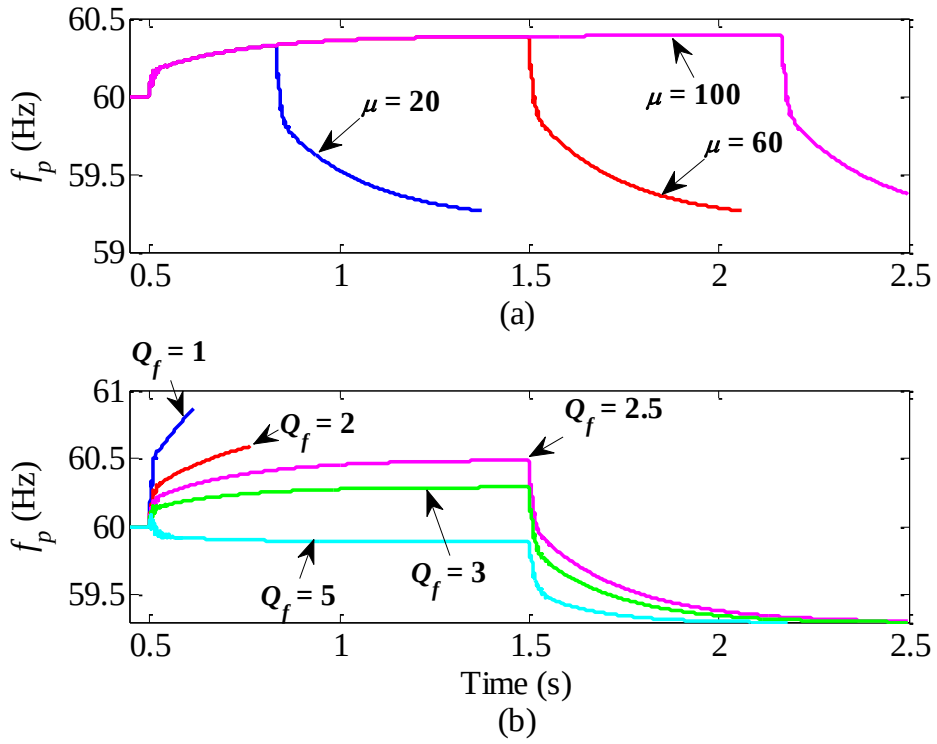

Figure 3-9: Frequency responses for scheduled SFS/OUF IDM. (a) f_o = 59.2Hz, Q_f = 2.5, μ changes. (b) f_o = 59.3Hz, μ = 60, Q_f changes.

This loading point lies inside AFD NDZ and outside OUF NDZ and is considered to be theoretically detectable by proposed method. It can be seen that the frequency started drifting upward by cf and then converged to load resonant frequency (59.2Hz) when perturbation is set

to zero for the rest of the cycle. Both cases (μ = 20 and μ = 60) detect islanding condition where enough time is allowed for frequency to converge to resonant frequency and trigger islanding condition. On the other hand, no sufficient time was allowed for μ = 100 to detect islanding within 2 seconds due to large duty cycle. Hence, proper design of μ is critically important to achieve NDZ reduction as close to results introduced in Figure 3-7. The choice of μ equal 60, which corresponds to a duty cycle of 1 second, will be used for the rest of simulations since it provides equivalent time for both SFS and OUF techniques to drift the frequency outside threshold values. Figure 3-9 (b) shows frequency responses for scheduled SFS/OUF technique at f_o = 59.3Hz, μ = 60 and different Q_f values. Cases with Q_f < 2.5 are detected since they lie outside NDZ of proposed technique. Case Q_f = 2.5 corresponds to point **E'** in Figure 3-3 and is undetectable since frequency converges to both upper and lower frequency threshold values without exceeding them. It is noticed that as Q_f value is increased, the ability of cf term to drift frequency becomes less and less. Points with Q_f > 2.5 are undetectable since they lie on the lower bounding line of proposed NDZ. It is important to notice that the use of cf shifts the critical point toward the upper/lower bound of OUF. Hence, the Q_f loading value that can be detected at f_o = 60Hz is higher than Q_f^{***} and can be obtained from (3.3) to be 6.025 for this case. Figure 3-10 shows the simulated NDZs of proposed scheduled SFS/OUF technique at different μ values. The simulation steps have been selected as 0.05Hz for f_o and 0.05 for $\log Q_f$.

It can be seen from Figure 3-10 that small duty cycle (μ = 20) resulted in a NDZ with slower drifting at low Q_f values compared to theoretical NDZ for proposed technique. Therefore, as duty cycle gets smaller than 20 nominal cycles, NDZ of proposed scheduled

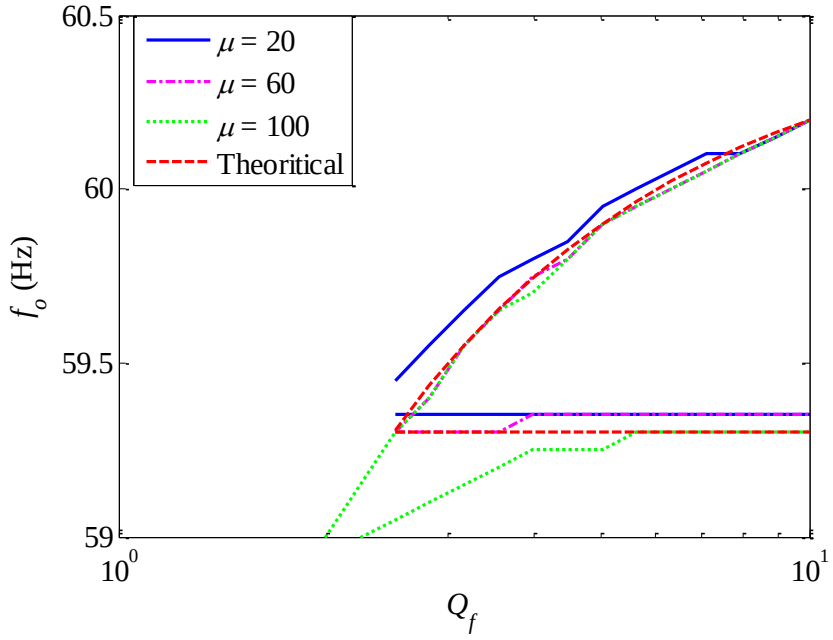

Figure 3-10: NDZ of scheduled SFS/OUF IDM for different duty cycle (μ) values.

SFS/OUF technique converges to OUF NDZ. In comparison, for a large duty cycle (μ = 100), NDZ converges to regular SFS NDZ as μ increases further. The closest result to theoretical was obtained for μ = 60, which corresponds to a duty cycle of half of T, and this result shows why proper duty cycle design is critically important.

Similarly, for a single DG case with scheduled SFS/SFS IDM, cf = 0.03181 and K = 0 correspond to $Q_f^{**} = 2.5$ from Figure 3-6. It is noticed that the required cf value is almost half the value used for scheduled SFS/OUF technique which is considered as an advantage for this technique. Similarly, the reference values used for constant current controller are i_{dref} = 1pu and i_{qref} = 0. The circuit breaker (CB) is opened at t = 0.5s to simulate islanding behavior. Figure 3-11 (a) shows frequency responses for scheduled SFS/SFS technique at f_o = 59.8Hz and Q_f = 2.5 for different μ values.

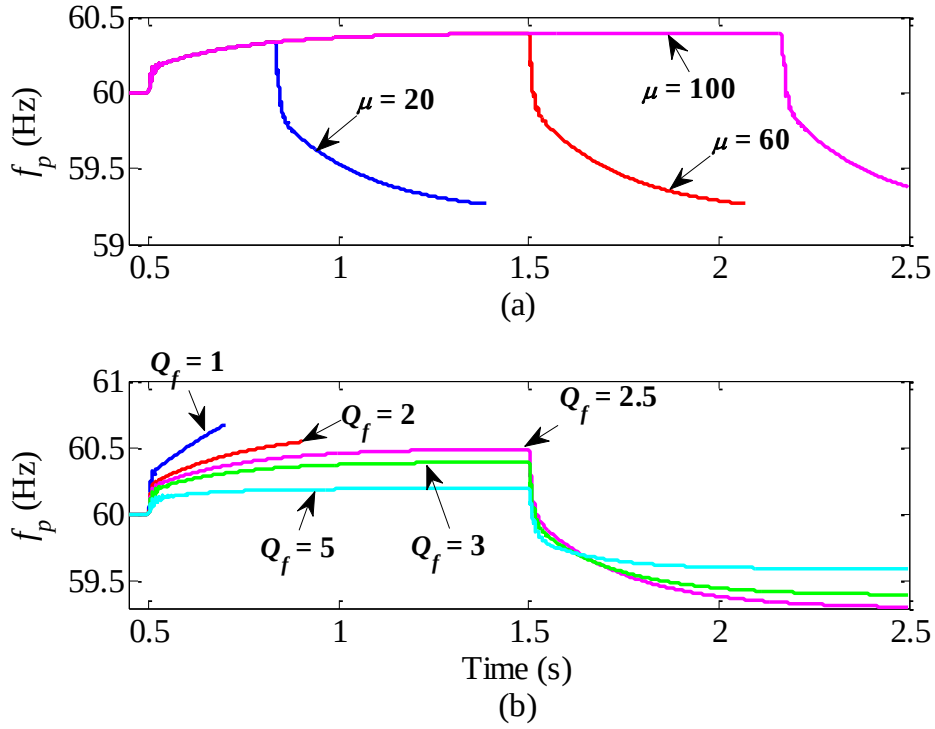

Figure 3-11: Frequency responses for scheduled SFS/SFS IDM. (a) f_o = 59.8Hz, Q_f = 2.5, μ changes. (b) f_o = 59.9Hz, μ = 60, Q_f changes.

It can be seen from Figure 3-11 that similar behavior is achieved although the tested resonant frequency value has been shifted from lower bound of OUF to middle point of OUF as seen in Figure 3-6. The loading point, f_o = 59.8Hz and Q_f = 2.5, lies inside NDZ of SFS with positive cf and outside NDZ of SFS with negative cf and is considered to be theoretically detectable by the proposed scheduled SFS/SFS technique. It can be seen from Figure 3-11 (a) that the frequency started drifting upward by cf in the first interval and then drifted downward by $-cf$ for the rest of cycle. Both cases (μ = 20 and μ = 60) detect islanding condition where enough time is allowed for SFS with negative cf to drift the frequency below $f_{\min}$ and trigger islanding condition. In contrast, no sufficient time was allowed for μ = 100 to detect islanding

within 2 seconds due to large duty cycle. Hence, proper design of μ for scheduled SFS/SFS technique is also important to achieve NDZ reduction as close to results introduced in Figure 3-8. The choice of μ equal to 60 seems to be the optimal choice for this case as well and μ = 60 will be used for the rest of simulations. If different positive and negative values of cf are used for scheduled SFS/SFS technique, then the value of optimal μ could be shifted toward allowing more time to the interval with lower drifting power (i.e. lower cf value). Figure 3-11 (b) shows frequency responses for scheduled SFS/SFS technique at f_o = 59.9Hz, μ = 60 and different Q_f values. Similarly, cases with Q_f < 2.5 are detected since they lie outside NDZ of scheduled SFS/SFS technique. Case Q_f = 2.5 corresponds to point **E''** in Figure 3-4 and is undetectable since frequency converges under the influence of positive and negative cf to both upper and lower frequency threshold values, respectively, without exceeding them. It is noticed that as Q_f value is increased, the ability of cf term to drift frequency becomes less and less. Points with Q_f > 2.5 are undetectable since they lie inside the NDZ of proposed scheduled SFS/SFS technique. It is important to notice that the use of cf shifts the critical point toward the middle point of OUF which happens to be at 59.9 Hz. Therefore, the Q_f loading value that can be detected at f_o = 60Hz is slightly higher than Q_f^{**} for this case and can be obtained from (3.3) to be equal to 3.013. This value is almost half the value obtained by SFS/OUF since SFS/SFS technique uses a cf value equal to half the value required by SFS/OUF to obtain similar Q_f^{**} value. Figure 3-12 shows simulated NDZs of proposed scheduled SFS/SFS technique at different μ values. The simulation steps have been also selected as 0.05Hz for f_o and 0.05 for $\log Q_f$.

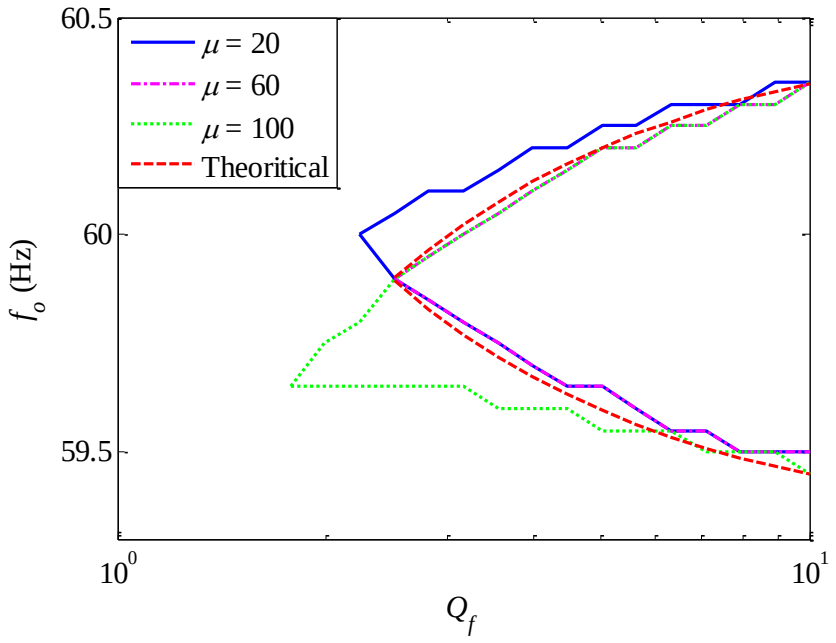

Figure 3-12: NDZ of scheduled SFS/SFS IDM for different duty cycle (μ) values.

It can be seen from Figure 3-12 that small duty cycle (μ = 20) resulted in a NDZ with slower drifting at low Q_f values compared to theoretical NDZ for proposed technique. Therefore, as duty cycle gets smaller than 20 nominal cycles, NDZ of proposed scheduled SFS/SFS technique converges to NDZ of SFS with negative cf . In comparison, for a large duty cycle (μ = 100), NDZ converges to NDZ of SFS with positive cf as μ increases further. The closest result to theoretical was obtained for μ = 60. The small difference in NDZ lines between theoretical and simulated one at μ = 60 is caused by the resolution used for simulation.

3.1.6.2 Loss of Synchronism Study for 2-DG System

Let us assume that we have a 2-DG system (N = 2) where J_1 is the perturbation signal applied to DG1 and J_2 is the perturbation signal applied to DG2. Assume that J_2 is delayed

from J_1 by $L_d T_g$ seconds where L_d is the number of nominal cycles representing the delay. Figure 3-13 shows the two perturbation signals J_1 and J_2. Assume that similar design parameters (K, d, and T) as in Table 3-1 are used for both DGs. Similar chopping fraction values of 0.06345 are used for both DGs (i.e., $cf_1 = cf_2 = 0.06345$). Also, the load is equivalently shared by the two DGs such that $i_{dref1} = i_{dref2} = 0.5\,\text{pu}$ and $i_{qref1} = i_{qref2} = 0$. Figure 3-14 shows the effect of selected number of delayed cycles (L_d) on simulated NDZ of scheduled SFS/OUF technique.

For small L_d values ($L_d \leq 20$), there is no significant change on NDZ and therefore, the synchronization requirement for multi-DGs scheduled SFS technique is flexible where a delay of 0.33s can be tolerated for T = 2s without significant degradation on NDZ for a two-DG system. As L_d is increased further, the Q_f^{**} value started degrading significantly until no zero NDZ area can be achieved and simulated NDZ converges to a typical 2-DGs NDZ for SFS at $cf_1 = cf_2 = 0.06345$ and $K_1 = K_2 = 0$ where load is equivalently shared between the two DGs (i.e., $m_1 = m_2 = 0.5$). The NDZ when J_1 and J_2 are totally out of synchronism ($L_d = 60$) can detect a Q_f value of approximately half the value detected by a single DG ($Q_f \approx 3$ in this case) at f_o = 60Hz. Therefore, the performance for properly designed two DGs scheduled SFS/OUF will degrade to conventional SFS if both DGs were completely out of synchronism. This result shows the advantage of using simultaneous perturbation technique for a multi-DG system rather than alternating one where the later will degrade to OUF NDZ in case of a complete loss of synchronization as will be seen below.

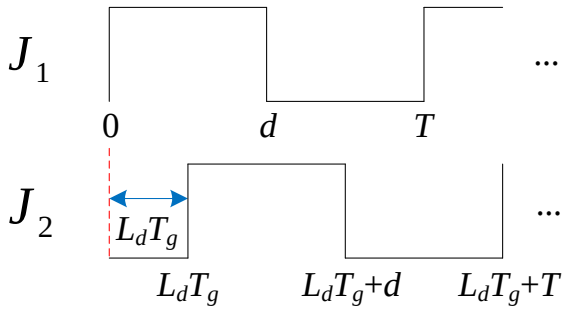

Figure 3-13: Delayed perturbation signals applied to DG1 and DG2.

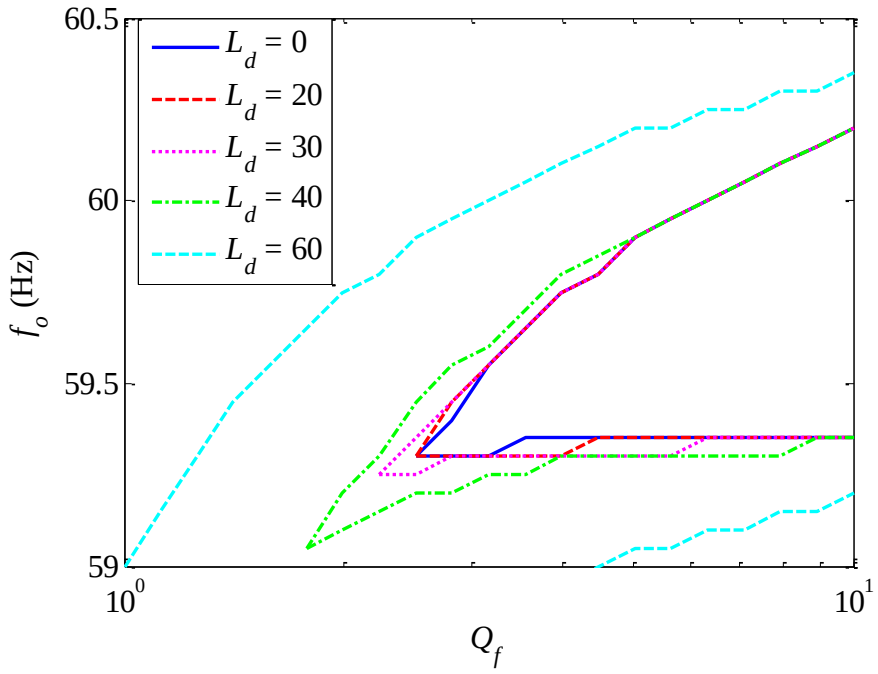

Figure 3-14: Effect of introduced delay parameter L_d on NDZ of scheduled SFS/OUF IDM.

Similarly, for scheduled SFS/SFS technique, equivalent chopping fraction values of 0.03181 are set for both DGs (i.e., $cf_1 = cf_2 = 0.03181$). The load is also assumed to be equivalently shared by the two DGs such that $i_{dref1} = i_{dref2} = 0.5\,\text{pu}$ and $i_{qref1} = i_{qref2} = 0$. Figure 3-15 shows the effect of number of delayed cycles (L_d) on simulated NDZ of scheduled SFS/SFS technique.

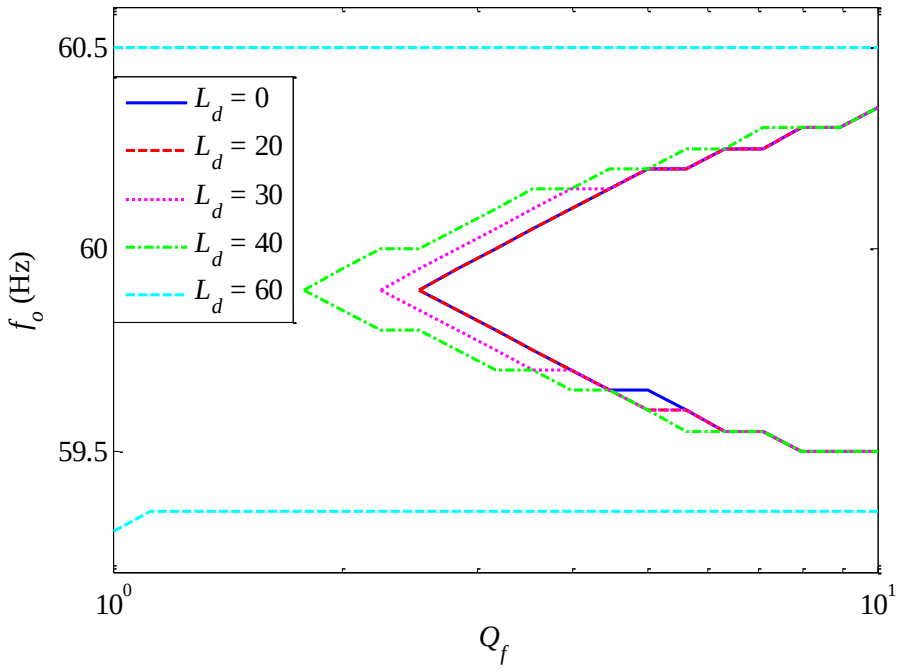

Figure 3-15: Effect of introduced delay parameter L_d on NDZ of scheduled SFS/SFS IDM.

For small L_d values ($L_d \leq 20$), there is no significant change on NDZ and therefore, a delay of 0.33s can be tolerated for a two-DG system without significant degradation on NDZ. As L_d is increased further, the Q_f^{**} value started decreasing significantly on the same line of f_o = 59.9 Hz until simulated NDZ converges to NDZ of OUF when both DG1 and DG2 are completely out of synchronism ($L_d = 60$). This result is considered as one of the major disadvantages of this technique since scheduled SFS/OUF technique performs much better when both DGs are completely out of synchronism as seen earlier in Figure 3-14.

For both techniques, it is important to note that for a multi-DG system, all cf_i's should be designed to have the same sign for all DGs in order to avoid counter effect cancellation where one DG tries to cancel out the perturbation introduced by the other DG [67]. Also, if different design parameters (cf or K) are chosen for each DG, then the equivalent angle (θ_{eq}) presented

in (3.5) does not reduce down to θ and the overall NDZ will be dependent on output ratios (m_i) of each DG in addition to SFS parameters [65]. Therefore, it is recommended for a multi-DG system that all design parameters (cf, K, d, and T) are chosen to be the same for all DGs such that the overall NDZ is insensitive of ratios between different m_i's. The proposed design condition will make the *N*-DG system robust against disturbances where no degradation in overall NDZ will be caused from losing one or two DGs outputs as long as the rest of DGs can support the active power of the islanding load. However, there is a stability concern related to total DGs-load share limit as seen in [63] and [66], and this issue will be studied in the next subsection along with switching effect.

3.1.6.3 Sensitivity Parameters

In order to study the effect of switching on frequency response when grid is connected, the infinity-norm of frequency error square is chosen to show these effects. Let us define frequency error as $f_e = f_p - f_g$ where the $\|.\|_\infty$ of its square corresponds to the maximum square error value obtained by switching transition. $\| f_e^2 \|_\infty$ versus total DGs-load power share (m_t) will be used to study the effect of different parameters on single and multiple (*N*=2) DGs cases for scheduled SFS/OUF technique as shown in Figure 3-16. For a single DG case, m_t corresponds to m_1. The simulation step for m_t is chosen to be 0.05. The load power is assumed to be fixed for the two-DG case where both DGs are assumed to supply similar power (i.e. $m_1 = m_2 = m_t / 2$). The scheduled SFS/OUF parameters are set to $cf_1 = cf_2 = 0.06345$ and $K_1 = K_2 = 0$ where cf_1 and K_1 are used for the single DG case. The distribution system line impedance is an important factor that will significantly affect f_e. Stronger grid can be

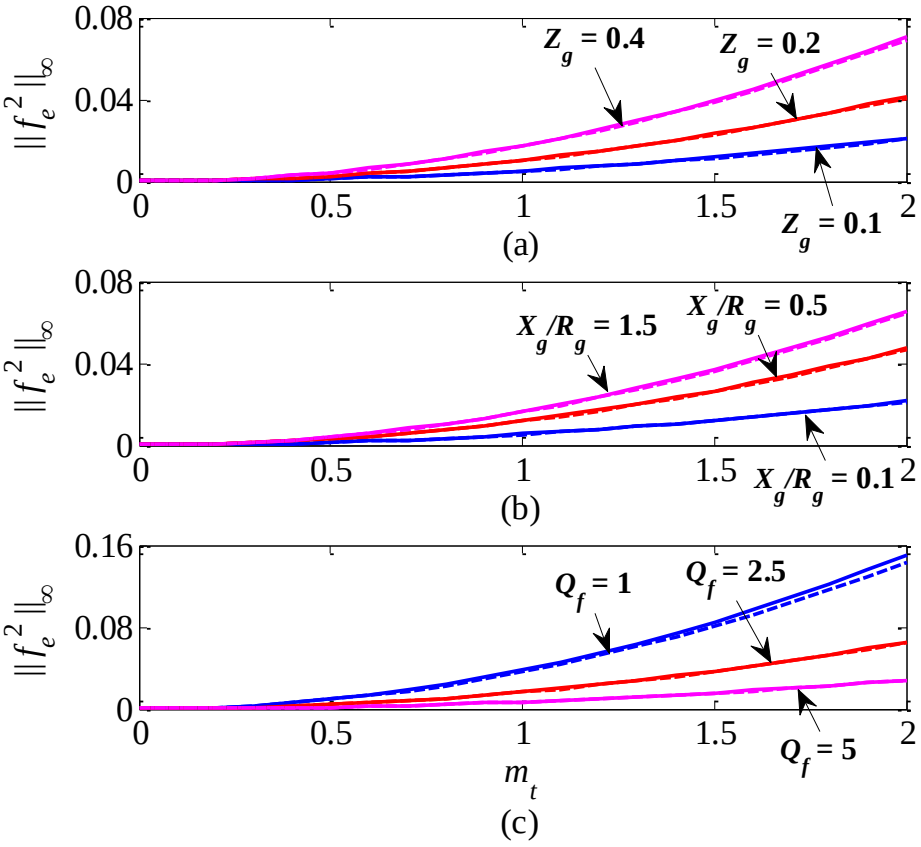

Figure 3-16: $\| f_e^2 \|_\infty$ Vs. m for single DG (solid) and two DGs (dashed) cases with scheduled SFS/OUF technique. (a) Z_g changes. (b) X_g / R_g changes. (c) Q_f changes.

represented either by lower impedance magnitude (Z_g) or lower X_g / R_g ratio. The parameters in Table 3-1 corresponds to Z_g = 0.36, X_g / R_g = 1.5 and Q_f = 2.5. Parameters are changed one at a time while others are kept constant and the corresponding values of R_g and L_g can be calculated by:

$$R_g = \frac{Z_g}{\sqrt{1+(X_g/R_g)^2}}, \quad L_g = \frac{Z_g(X_g/R_g)}{2\pi f_g \sqrt{1+(X_g/R_g)^2}}. \tag{3.14}$$

As seen in Figure 3-16, $\| f_e^2 \|_\infty$ increases quadratically as m_t increases where higher norm value is obtained as Z_g or X_g / R_g ratio increases which indicates weaker grid. Also,

higher Q_f value compresses frequency transition caused by switching and resulted in lower norm values. The results for a two-DG case are slightly smaller than single DG and the difference is negligible. Furthermore, other parameters could influence frequency error norm such as PLL proportional gain (k_{pPLL}) where $\| f_e^2 \|_\infty$ decreases as k_{pPLL} is decreased. Another parameter is load active power (P_L) where higher P_L value corresponds to lower load resistance (R) value which results in lower $\| f_e^2 \|_\infty$. Figure 3-17 shows $\| f_e^2 \|_\infty$ versus m for a single DG case at different cf and K values. The *RLC* load was set to f_o = 60Hz and Q_f = 1.

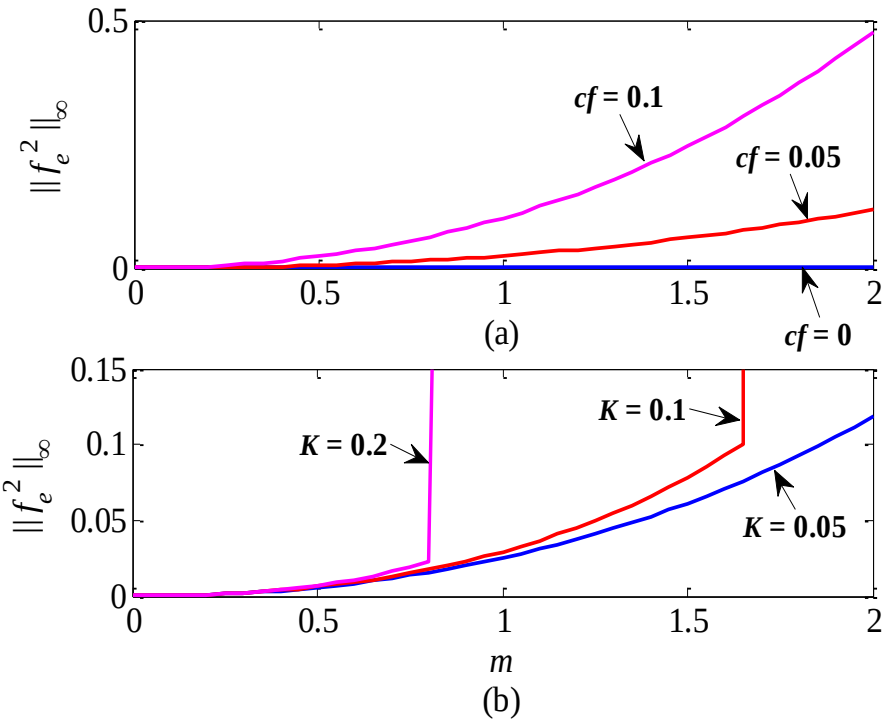

Figure 3-17: $\| f_e^2 \|_\infty$ Vs. m for single DG scheduled SFS/OUF IDM at Q_f = 1. (a) K = 0.05, cf changes. (b) cf = 0.05, K changes.

Figure 3-17 (a) shows that as K is kept at 0.05 and cf increases, $\| f_e^2 \|_\infty$ increases quadratically as m increases where higher norm value is obtained at higher cf. On the other hand, Figure

3-17 (b) shows that for high K values, there is an upper limit on m after which the system become unstable while grid is connected. For K = 0.1 and 0.2 the system becomes unstable for m higher than 1.65 and 0.8, respectively.

Similarly, for scheduled SFS/SFS technique, $\| f_e^2 \|_\infty$ versus total DGs-load power share (m_t) will be used to study the effect of different parameters on single and multiple (N=2) DGs cases as shown in Figure 3-18. The scheduled SFS/SFS parameters are set to $cf_1 = cf_2 = 0.03181$ and $K_1 = K_2 = 0$ where cf_1 and K_1 are used for the single DG case.

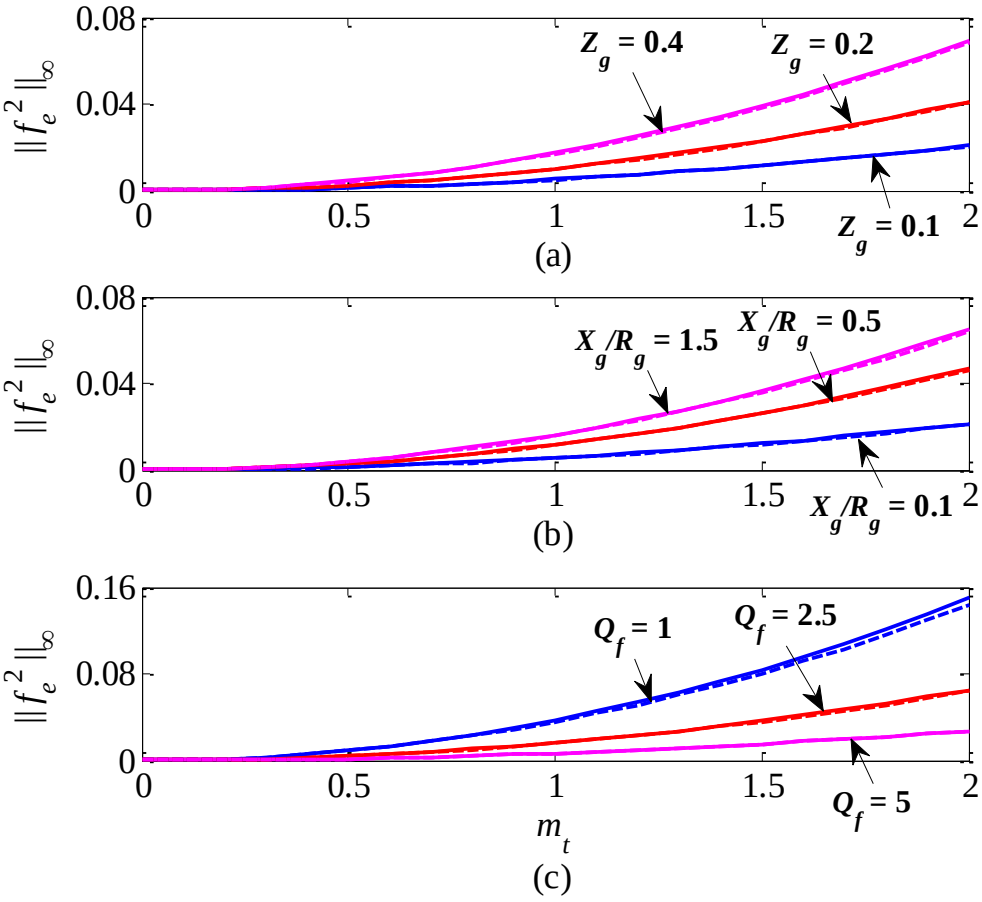

Figure 3-18: $\| f_e^2 \|_\infty$ Vs. m for single DG (solid) and two DGs (dashed) cases with scheduled SFS/SFS technique. (a) Z_g changes. (b) X_g / R_g changes. (c) Q_f changes.

As seen in Figure 3-18, $\| f_e^2 \|_\infty$ increases quadratically as m_t increases where higher norm value is obtained as Z_g or X_g / R_g ratio increases which indicates weaker grid. Also, higher Q_f value resulted in lower norm values. Similarly, results for the two-DG case are slightly smaller than the single DG case. It is noticed that results in Figure 3-18 are similar to the results obtained in Figure 3-16 although the value of cf used in scheduled SFS/SFS technique is almost half the value used for SFS/OUF. Therefore, one can conclude that similar $\| f_e^2 \|_\infty$ values are obtained for both techniques to achieve a certain Q_f^{**} at $K = 0$.

Figure 3-19 shows $\| f_e^2 \|_\infty$ versus m for a single DG with scheduled SFS/SFS technique at different cf and K values. The *RLC* load was set to $f_o = 60$Hz and $Q_f = 1$.

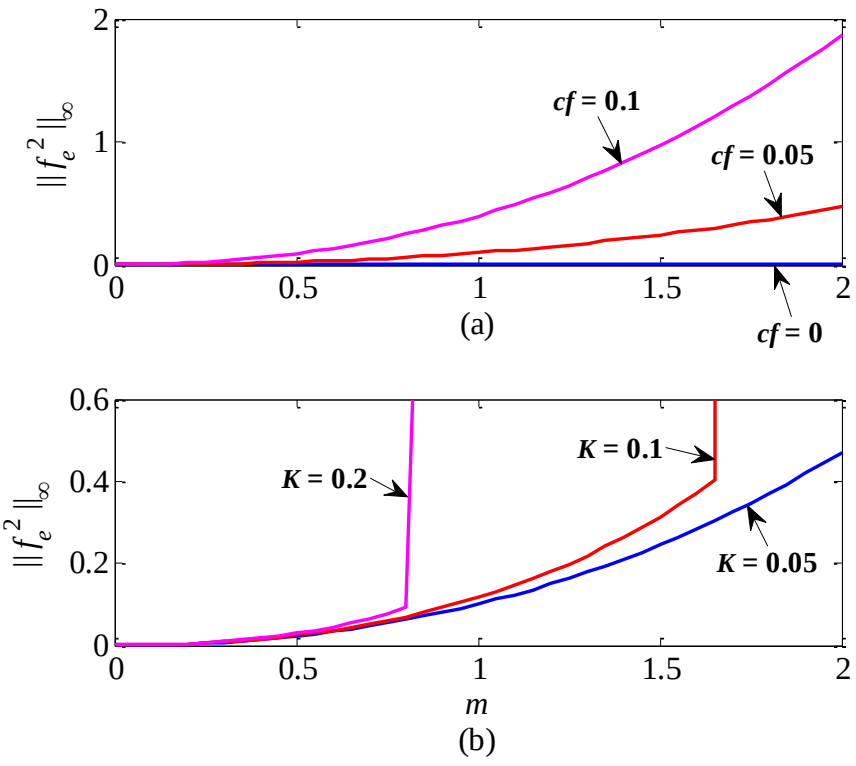

Figure 3-19: $\| f_e^2 \|_\infty$ Vs. m for single DG scheduled SFS/SFS IDM at $Q_f = 1$. (a) $K = 0.05$, cf changes. (b) $cf = 0.05$, K changes.

Figure 3-19 (a) shows that as K is kept at 0.05 and cf increases, $\| f_e^2 \|_\infty$ increases quadratically as m increases where higher norm value is obtained at higher cf. The $\| f_e^2 \|_\infty$ values obtained for each cf value is almost four times the value obtained by scheduled SFS/OUF at similar cf values. Similarly, Figure 3-19 (b) shows that for K = 0.1 and 0.2 the system becomes unstable for m higher than 1.65 and 0.8, respectively.

3.1.7 Discussion

Results from Figure 3-17 and Figure 3-19 confirm the outcomes in [63] where high K reduces the maximum allowable share of load power from DG (m) while cf has no impact on maximum allowed m. Consequently, there is a tradeoff design problem when choosing scheduled SFS parameters (cf and K) and the tradeoff is between maximum allowable $\| f_e^2 \|_\infty$ and required DG-load power share (m). $\| f_e^2 \|_\infty$ is proportional to the value of cf which in turns degrade DG power quality [45]. Therefore, the proposed scheduled techniques are very useful for systems with high penetration of DGs since they reduce the requirements of K which will lead to lower negative impact on system stability while grid is connected.

For design purposes, the $\| f_e^2 \|_\infty - K$ curve and the $cf - K$ curve are proposed for both techniques to meet a certain Q_f^{**} value as seen in Figure 3-20 and Figure 3-21. Let us assume that the load operating point of interest lies inside $Q_f \geq 1$ region. Hence, the *RLC* load is set to Q_f = 1. The rest of parameters are as shown in Table 3-1.

For example, if Q_f^{**} = 2.5 and $\| f_e^2 \|_\infty \leq 0.02$ are requirements to be met for scheduled SFS/OUF technique, then the range of K can be found from Figure 3-20 (a) to be between

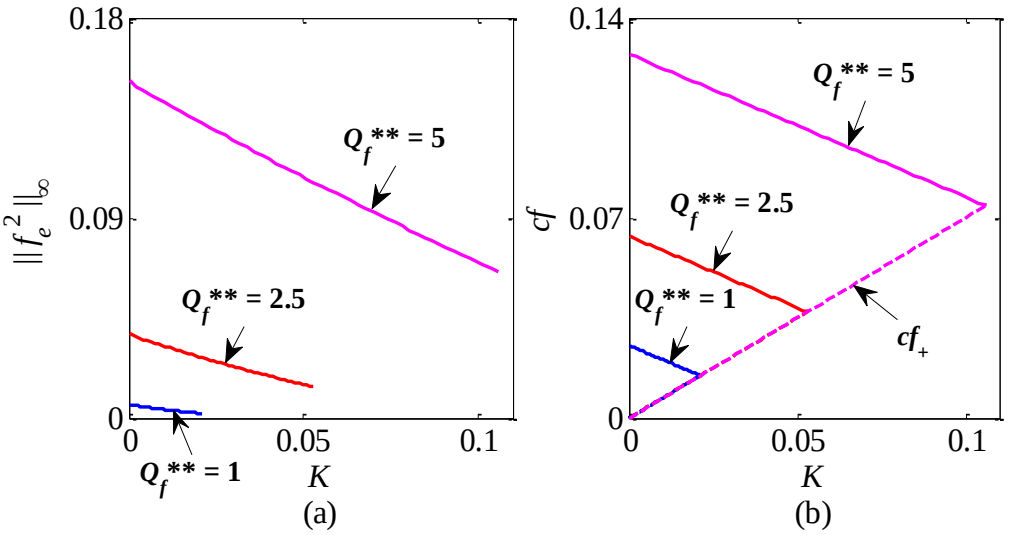

Figure 3-20: (a) $\| f_e^2 \|_\infty - K$ curve (b) $cf - K$ curve for scheduled SFS/OUF technique at different Q_f^{**}'s at $Q_f = 1$.

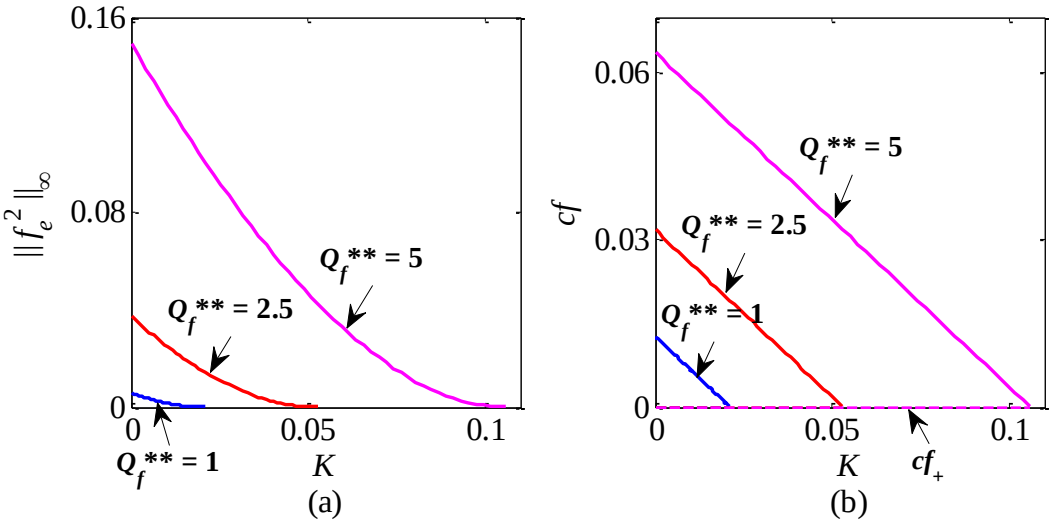

Figure 3-21: (a) $\| f_e^2 \|_\infty - K$ curve (b) $cf - K$ curve for scheduled SFS/SFS technique at different Q_f^{**}'s at $Q_f = 1$.

0.0375 and 0.053 which corresponds to cf values between 0.0449 and 0.0372, respectively. This range is limited from the right, as shown in Figure 3-20 (b), by positive critical cf (cf_+) value defined in (3.9) after which no improvement will be obtained from using scheduled SFS/OUF in

comparison to regular SFS technique. It is proposed that cf = 0.0449 and K = 0.0375 to be chosen since stability degradation will be minimum in this case while other objectives are achieved. Other combinations of cf and K in the linear range determined above could be chosen depending on other introduced requirements you might have but the further you increase K, the less improvement is obtained from using scheduled SFS/OUF in comparison to regular SFS. On the other hand, if Q_f^{**} = 2.5 and $\| f_e^2 \|_\infty \leq 0.02$ are requirements to be met for scheduled SFS/SFS technique, then the range of K can be found from Figure 3-21 (a) to be between 0.0149 and 0.053 which corresponds to cf values between 0.0229 and 0.00003, respectively. This range is limited from the bottom, as shown in Figure 3-21 (b), by cf = 0 line at which no improvement will be obtained from using scheduled SFS/SFS in comparison to regular SFS technique. It can be noticed that a larger range of K values are obtained for scheduled SFS/SFS technique in comparison to SFS/OUF while same requirements are met and this counts as an advantage for scheduled SFS/SFS IDM where dependency on K can be reduced further to eliminate NDZ. It is suggested that cf = 0.0229 and K = 0.0149 to be chosen for scheduled SFS/SFS technique where the required K value is less than half the value required for scheduled SFS/OUF.

It is important to note that proposed techniques were studied for DG systems with constant current controller. In [40], it is shown that SFS is more effective for constant current-controlled inverter in comparison to constant power-controlled inverter where the later controller counter effect perturbation introduced by SFS. Also, the steady-state frequency after islanding (f_{is}) for constant power controller is given by [38]:

$$f_{is}^{\,2} + f_o \frac{Q}{PQ_f} f_{is} - f_o^{\,2} = 0, \tag{3.15}$$

where P and Q are the active and reactive powers injected by the DG system, respectively. The scheduled perturbation technique relies on the drifting action introduced by cf to trigger the OUF relay. It is clearly seen from (3.15) that the islanding frequency is independent of cf value and hence the scheduled perturbation technique is not suitable for DG systems with constant power controller. Also, the detection time for the scheduled perturbation technique is inconsistent since it depends on the load operating point falling outside the NDZ of the switched IDM in addition to the load characteristic. Moreover, for systems with a very large number of DGs, implementing this technique will be too involved and it might be extremely difficult to synchronize their performances. As a result, a new active IDM is proposed for multi-DG systems where no communications are needed among different DGs. The proposed technique is shown to be scalable and robust against different loading conditions, variation in grid stiffness level, and different types of power system disturbances as will be seen in the next section.

3.2 Transient Stiffness-Measure for Islanding Detection of Multi-DG System

3.2.1 Introduction

Small-signal stability analysis has been used to study the effect of adding inverter-based DGs on distribution networks stability in addition to the contribution of implemented control and IDM schemes in single and multi-DG system stability [71]-[75]. In [75], a detailed small-signal analysis is used to study the effect of different IDMs on the stability of single and multi-DG systems under constant current and constant power controllers. Constant current/power controllers are useful for DGs working in the grid-connected mode while stand alone or micro-grid operation is considered as a major drawback for aforementioned control schemes. This is mainly because both the constant current and constant power controllers do not provide

appropriate Power Management Strategy (PMS) that is required to support both the voltage and the frequency within the micro-grid. In [76]-[78], switching control strategies are proposed to support the voltage of the micro-grid in the stand alone mode. The problem with these techniques is that a large transient/oscillation is introduced as a result of switching between different modes of control. The switching process between different control modes is typically triggered by an IDM that detects an islanding condition, which mostly depends on the island voltage or frequency drifting outside pre-specified thresholds. Hence, the recovery process of both the frequency and voltage of the micro-grid becomes more difficult and introduces large transients. Alternatively, droop controllers, which replicate the droop characteristic of synchronous generators, are proposed for micro-grid power management strategies or power sharing mechanism [71], [79]-[89]. In [81], an integral-derivative power terms are added to the traditional droop controller in order to enhance the transient performance of droop controllers. In [82] and [89], a virtual output impedance is used to improve the active and reactive power decoupling performance. In [71], an active/reactive PMS is proposed, and it includes a frequency restoration term, and frequency/voltage droop blocks in addition to the typical power regulator. The detail of this strategy is shown in Appendix C.

The objective of this section is to propose a new active IDM for a multi-DG system such that no communications are required among different DGs. The proposed technique is based on the idea of transient stiffness measurement for the multi-DG system where a clear separation is established between prior- and post-islanding stiffness measures. The idea was inspired from the simple mass-spring-damper system and is expanded to be applied to the multi-DG system. Small-signal models for both the single and multi-DG systems are developed and used for simulations along with equivalent average Simulink models. The proposed technique is suitable

for different types of DG controllers and is shown to be robust against different types of power system disturbances.

The rest of this section is organized as follows. Subsection 3.2.2 presents the multi-DG system under study. The design concept for the proposed multi-DG IDM is introduced in subsection 3.2.3. The proposed IDM are tested for single and two-DG systems in subsection 3.2.4. Finally, discussions are presented in subsection 3.2.5.

3.2.2 System Under Study

A single-line diagram for the general *N*-DG system is shown in Figure 3-22 where *N* is the number of connected DGs. The detail of this model can be found in Appendix C. In Figure 3-22, L_g and R_g corresponds to the inductance and resistance of the utility line, respectively. The utility or grid voltage is v_{sabc} and the voltage at the point of common coupling (PCC) is v_{abc}. For the i^{th} DG, the output power is $P^i - jQ^i$ and the output current is i^i_{abc}. The negative sign in the reactive power indicates that Q^i is the reactive power absorbed by the i^{th} DG. The inductance of the i^{th} inverter filter is represented by L^i_f. $P_N + jQ_N$ is the power imbalance between the parallel *RLC* load ($P_L + jQ_L$) and the total power output supplied by all DGs ($\sum_{i=1}^{N} P^i - jQ^i$). The current absorbed by the grid is i_{Nabc}. For the parallel *RLC* load, i_{Rabc}, i_{Labc}, and i_{Cabc} are the resistance, inductance, and capacitance currents, respectively. A circuit breaker (CB) is used to simulate an islanding situation by disconnecting the grid. In this model, an average model for the three-phase Voltage Source Inverter (VSI) is employed where the pulse width-modulated (PWM) signal generator, the dc source, and the switching power electronics devices are replaced

by a three-phase controlled voltage source [13], [38], [63]. A three-phase PLL is used to measure the frequency of the PCC voltage. The interface control used for each DG includes a current regulator in addition to the PMS introduced in [71]. The details for deriving small-signal models for single and multi-DG systems can be found in Appendix C.

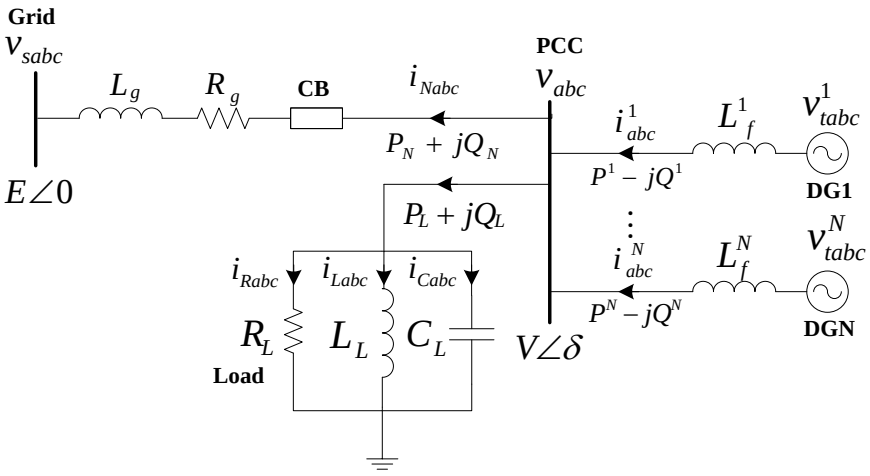

Figure 3-22: Single-line schematic diagram of multi-DG system.

3.2.3 Design Concept

The idea behind the proposed technique is to introduce a measure for the transient stiffness of the multi-DG system such that a clear separation is obtained for stiffness measures prior- and post-islanding condition. First, the concept of system stiffness is introduced in subsection 3.2.3.1. Then, the idea is expanded to the multi-DG system in subsection 3.2.3.2.

3.2.3.1 Introduction to Stiffness Measure

In order to understand the concept of system stiffness, the typical mass-spring-damper system shown in Figure 3-23 is studied.

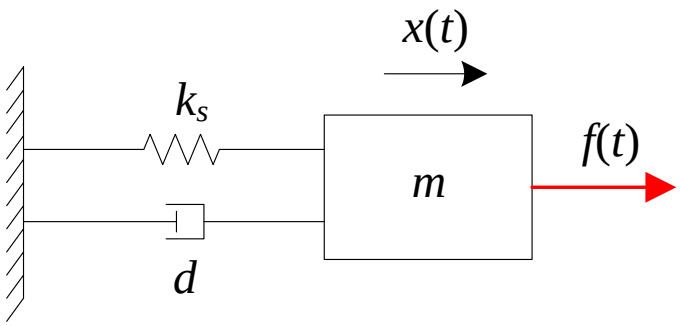

Figure 3-23: Diagram of mass-spring-damper system.

In Figure 3-23, m is the body mass, k_s is the spring constant, d is the damping coefficient, and $f(t)$ is the applied force. The spring constant k_s is also known as the stiffness measure of the spring characteristics. By applying Newton's second law on Figure 3-23, the spring damper model can be represented by the following equation:

$$m\ddot{x} = -k_s x - d\dot{x} + f(t), \tag{3.16}$$

where x is the displacement. Let us define the following state:

$$z = \begin{bmatrix} z_1 & z_2 \end{bmatrix}^T = \begin{bmatrix} x & \dot{x} \end{bmatrix}^T.$$

Then, (3.16) can be rewritten in the state space form as follows:

$$\dot{z}(t) = \begin{bmatrix} 0 & 1 \\ -k_s/m & -d/m \end{bmatrix} z(t) + \begin{bmatrix} 0 \\ 1/m \end{bmatrix} f(t). \tag{3.17}$$

Assuming unity mass ($m = 1$), the state-to-input transfer functions are obtained as follows:

$$\frac{Z_1(s)}{F(s)} = \frac{X(s)}{F(s)} = \frac{1}{s^2 + ds + k_s} = \frac{1}{s^2 + 2\zeta\omega_n s + \omega_n^2}, \tag{3.18}$$

$$\frac{Z_2(s)}{F(s)} = \frac{sX(s)}{F(s)} = \frac{s}{s^2 + ds + k_s} = \frac{s}{s^2 + 2\zeta\omega_n s + \omega_n^2}, \tag{3.19}$$

where s is the Laplace operator, $\omega_n = \sqrt{k_s}$ is the radian resonance frequency, and $\zeta = \dfrac{d}{2\sqrt{k_s}}$ is the damping factor. The peak frequency, which is the frequency that corresponds to the maximum magnitude of the frequency response, for (3.18) is given by:

$$\omega_r = \begin{cases} 0 & , \quad \zeta \geq 1/\sqrt{2} \\ \omega_n \sqrt{1-2\zeta^2} & , \quad \zeta < 1/\sqrt{2} \end{cases} \tag{3.20}$$

On the other hand, the peak frequency for (3.19) is ω_n. Then, the infinity-norm of (3.18) and (3.19) can be obtained as follows:

$$\begin{aligned} \left\| \frac{X(s)}{F(s)} \right\|_\infty &= \max\left\{ \frac{1}{k_s}, \frac{2}{d\sqrt{4k_s - d^2}} \right\} = \begin{cases} 1/k_s, & d \geq \sqrt{2k_s} \\ \dfrac{2}{d\sqrt{4k_s - d^2}}, & d < \sqrt{2k_s} \end{cases} \\ &= \max\left\{ \frac{1}{\omega_n^2}, \frac{1}{2\zeta\omega_n^2\sqrt{1-\zeta^2}} \right\} = \begin{cases} \dfrac{1}{\omega_n^2}, & \zeta \geq 1/\sqrt{2} \\ \dfrac{1}{2\zeta\omega_n^2\sqrt{1-\zeta^2}}, & \zeta < 1/\sqrt{2} \end{cases}, \\ \left\| \frac{sX(s)}{F(s)} \right\|_\infty &= \frac{1}{d} = \frac{1}{2\zeta\omega_n}. \end{aligned} \tag{3.21}$$

Let us define $H(s) = \dfrac{X(s)}{F(s)}$. Then, the stiffness measure k_s is initially calculated from (3.21) as follows:

$$k_s = \left(\frac{\|sH(s)\|_\infty}{\|H(s)\|_\infty} \right)^2 + \frac{1}{4\|sH(s)\|_\infty^2} \approx \left(\frac{\|sH(s)\|_\infty}{\|H(s)\|_\infty} \right)^2 \tag{3.22}$$

The damping condition is then tested to reset k_s to $1/\|H(s)\|_\infty$ if $d \geq \sqrt{2k_s}$ where $d = 1/\|sH(s)\|_\infty$, and k_s is calculated by (3.22).

3.2.3.2 Stiffness Measure for the Multi-DG System

Now, let us look at the multi-DG system in Figure 3-22 for which a small-signal model is derived in Appendix C. From the basic principle of power flow, the following transfer function is considered:

$$H_{\omega}^{i}(s)=\frac{\Delta\omega_{p}'(s)}{\Delta P_{o}'^{i}(s)}, \tag{3.23}$$

where $\omega_{p}'=\omega_{p}/\omega_{g}$, ω_{p} is the inverter terminal voltage angular frequency acquired by PLL, Δ is the small-signal variable, and $\Delta P_{o}'^{i}$ is the i^{th} DG variation in input active power. For a single DG system, one can easily design for $\Delta P_{o}'$ such that the measured ω_{p} is used to identify H_{ω}. Then, the stiffness of the single DG system can be approximated by (3.22) assuming that the second order terms in the transfer function H_{ω} are dominant. However, for a multi-DG system, the problem becomes more complicated due to spectral overlapping in ω_{p} as a result of disturbing each DG separately. Hence, the problem that should be addressed is how to design for $\Delta P_{o}'^{i}$ such that an overall measure of stiffness can be obtained from measuring ω_{p} with no communication needed among different DGs. The proposed idea in this work relies on the concept of dispersed frequencies in the Discrete Fourier Transform (DFT) to define for an overall stiffness measure for the multi-DG system.

The input disturbance $\Delta P_{o}'^{i}[n]$ for the i^{th} DG is designed as follows:

$$\Delta P_{o}'^{i}[n]=\frac{A}{M}\sum_{l=1}^{M}\cos\left(\omega_{l}^{i}(n-1)T_{s}\right), \tag{3.24}$$

where $n=1,2,\cdots,N_{T}$, $\omega_{l}^{i}=2\pi f_{l}^{i}$, $f_{l}^{i}=[k_{1}+M_{1}(Nk_{2}+i-1)]f_{step}$, $T_{s}=1/f_{s}$: is the data sampling interval, A is the disturbance amplitude, $k_{1}=0,1,\cdots,M_{1}-1$, $k_{2}=0,1,\cdots,M_{2}-1$, M_{1} is the

number of consecutive frequencies disturbed by the i^{th} DG, $M_2 = \text{floor}\left(\frac{f_u + f_{step}}{NM_1 f_{step}}\right)$, f_u is the maximum frequency injected by the input, and $M = M_1 M_2$. The distribution for the DFT of input frequency components for each DG is shown in Figure 3-24. It can be seen from Figure 3-24 that the first M_1 frequency components are injected by DG1, the second M_1 frequency components are injected by DG2, and so on up to the N^{th} DG. The disturbed bands for each DG are separated by f_{step} in order to avoid overlapping between different DGs' spectral components. Then, the sequence is repeated M_2 times to cover the whole region between 0 and f_u.

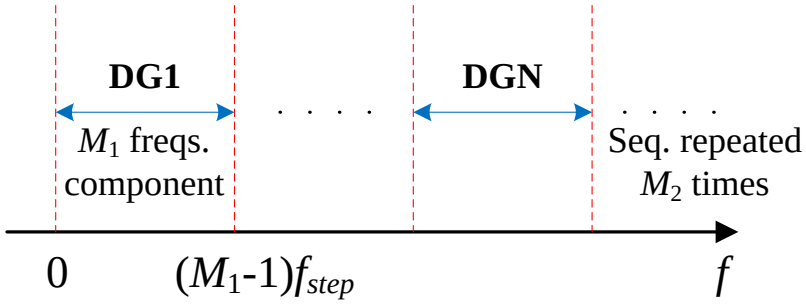

Figure 3-24: Distribution of frequency components for disturbed inputs.

The design parameters in (3.24) are f_u, f_{step}, f_s, N_T, A, and M_1. The relation between some of those design parameters and design conditions can be obtained from DFT properties, practical considerations, and the uniform band-pass sampling theorem [90]. According to [90], the minimum sampling frequency to avoid aliasing for a single band-pass signal, with a center frequency located at $0.5 f_u$, is the Nyquist sampling rate. Hence, f_s should be chosen to be greater than or equal to $2 f_u$. For convenience, f_s is chosen to be 7.68 kHz which corresponds to 128 samples/cycle at 60 Hz. Let us assume that the time interval for collecting data (T) is fixed

to 0.1s. Then, N_T is equal to $f_s T$ = 768 points. By fixing the value of T, the minimum frequency resolution of input DFT is also fixed to $1/T$ = 10 Hz. Thus, f_{step} is set to 10 Hz. In addition, let us assume that the frequency region of interest for calculating the infinity norm is $[f_0, f_c]$ where f_0 is set to 60 Hz and f_c is equal to 0.5 kHz. Then, f_u is chosen to be equal to $5f_c$ = 2.5 kHz to allow for more frequency components to be considered into the DFT and hence a higher accuracy is obtained for $\hat{H}_\omega$. The choice of f_0 and f_c values are based on the physical knowledge of the system and is verified by simulation. The choice of M_1 value is critically important for multi-DG system and hence it will be studied further in subsection 3.2.4.2. The disturbance amplitude is set to one (A = 1).

For design purposes, the protection engineer needs to know the total number of DGs (*N*) within the micro-grid of interest and hence an index should be assigned to each DG. Also, similar design parameters for (3.24) are used for each DG system. Then, the following procedure can be used to estimate an overall stiffness measure for a multi-DG system with *N* DGs:

1) The disturbance input $\Delta P_o'^i[n]$, defined in (3.24), is injected by the i^{th} DG where $n = 1,2,\cdots,N_T$, and $i = 1,2,\cdots,N$.
2) For the i^{th} DG, measure $\omega_p[n]$ where $n = 1,2,\cdots,N_T$.
3) $\omega_p[n]$ is normalized by ω_g and then the dc component is removed by subtracting one to obtain $\Delta\omega_p'[n]$.
4) Apply Discrete Fourier Transform (DFT) on $\Delta\omega_p'[n]$ to get $\Delta W_p(j\omega_k)$ where $k = 1,2,\cdots,N_T$. The DFT is defined as follows:

$$\Delta W_p(j\omega_k) = \frac{1}{N_T}\sum_{n=1}^{N_T}\Delta\omega_p'[n]e^{-j\frac{2\pi}{N_T}(n-1)(k-1)}, \tag{3.25}$$

where $\omega_k = \frac{2\pi}{N_T}(k-1)f_s$ and $f_k = \frac{\omega_k}{2\pi} \in [0, f_s - f_s/N_T]$.

5) The estimated overall frequency-response over the region of interest is given by the following equation:

$$\hat{H}_\omega(j\omega_i) = \frac{2M}{A}\Delta W_p(j\omega_i), \tag{3.26}$$

where $\omega_i = 2\pi f_i$ and $f_i \in [f_0, f_c]$.

6) The estimated stiffness for the overall multi-DG system in dB is calculated as follows:

$$\hat{S}_\omega(\text{dB}) = 20\log_{10}\left(\frac{\max\limits_{\omega_i}\omega_i\left|\hat{H}_\omega(j\omega_i)\right|}{\max\limits_{\omega_i}\left|\hat{H}_\omega(j\omega_i)\right|}\right), \tag{3.27}$$

In practice, an additional low-pass filtering stage could be applied to $\omega_p[n]$ at step 3 of the aforementioned procedure to remove high-frequency harmonics and noise. Then, the filter response should be accounted for in (3.26) to calculate the right $\hat{H}_\omega$. The previous process is repeated every T second. Then, the proposed stiffness-measure IDM is defined as follows:

$$\begin{cases}\hat{S}_\omega \le S_{TH}, & \text{Islanding is detected}\\ \hat{S}_\omega > S_{TH}, & \text{Normal operation}\end{cases} \tag{3.28}$$

where S_{TH} is the stiffness threshold value in dB that separates islanding from non-islanding conditions. S_{TH} is designed such that the proposed IDM is robust against different loading conditions, variation in grid stiffness level, number of connected DGs, and different types of power system disturbances. S_{TH} is set equal to 59 dB. The theoretical stiffness-measure for the *N*-DG system is defined as follows:

$$S_{\omega}(\text{dB}) = \frac{1}{N}\sum_{i=1}^{N} 20\log_{10}\left(\frac{\max\limits_{\omega\in[\omega_0,\omega_c]}\omega\left|H_{\omega}^{i}(j\omega)\right|}{\max\limits_{\omega\in[\omega_0,\omega_c]}\left|H_{\omega}^{i}(j\omega)\right|}\right), \tag{3.29}$$

where $\omega_0 = 2\pi f_0$ and $\omega_c = 2\pi f_c$.

3.2.4 Results

The proposed stiffness-measure IDM in subsection 3.2.3.2 is verified using an average model implemented in MATLAB Simulink. The detail of the model can be found in Appendix C. For illustration purposes, the results for single and two-DG systems are considered and the concept can be easily extended to the general *N*-DG system. Unless mentioned otherwise, the single and multi-DG model parameters, introduced in Table C-1 and Table C-2 in Appendix C, respectively, are used for simulation. The three-phase base power is 10kVA. The parallel *RLC* load parameters provided in Table C-1 correspond to a 10kW load with f_o = 60Hz and Q_f = 2.5.

3.2.4.1 Sensitivity Study for a Single DG System with Parallel *RLC* Load

The purpose of this study is to understand the effect of important parameters on the stiffness measure for a single DG system. The small-signal model for a single DG system, developed in Appendix C, is used for sensitivity analysis. The stiffness measure obtained from an ideal H_{ω} is compared with the estimated one obtained from $\hat{H}_{\omega}$. Five factors are investigated in this section and they are: the load parameters, the distribution line impedance, the SFS parameters, the maximum levels of power, and the proportional gains of different PI controllers. The range of variation for each parameter is chosen such that the stability of the single DG system is maintained before and after islanding condition.

- Load Parameters

The *RLC* load parameters include load power level (P_L), load quality factor (Q_f), and load resonant frequency (f_o). These parameters are changed one at a time while others are kept constant and the corresponding values of the three-phase *RLC* load are calculated as follows:

$$R_L = \frac{{V_{LL}}^2}{P_L},\ L_L = \frac{{V_{LL}}^2}{2\pi f_o Q_f P_L},\ C_L = \frac{Q_f P_L}{2\pi f_o {V_{LL}}^2}, \tag{3.30}$$

where $V_{LL} = \sqrt{3}V_r$ is the line-to-line RMS grid voltage. Figure 3-25, Figure 3-26, and Figure 3-27 show both the actual (S_ω) and estimated ($\hat{S}_\omega$) stiffness measure before and after islanding for different P_L, Q_f, and f_o values, respectively.

It can be seen from Figure 3-25 that as P_L increases, the stiffness measure before islanding decreases while it increases after islanding. As the value of P_L increases, the reactive power of both the capacitance and inductance increases accordingly to maintain a constant load Q_f value. The stiffness measure before islanding depends on the exchange of power between the load and the grid as well as the reactive power exchange between the capacitive and inductive parts of the load. When P_L increases, the grid will respond by injecting more active power and hence a higher stiffness measure should be obtained. However, the exchange of higher reactive power within the load will have a higher negative impact on the stiffness and hence the overall stiffness of the system will decrease. On the other hand, the stiffness measure after islanding depends on both the interaction between the PMS and the load, and the characteristics of the parallel *RLC* load. Therefore, as the value of P_L increases after islanding, the DG will respond by injecting higher active power and hence the overall stiffness will increase. The stiffness gab, between $\hat{S}_\omega$ values for prior- and post-islanding condition, changes from 6.94 to 3.74 dB as P_L

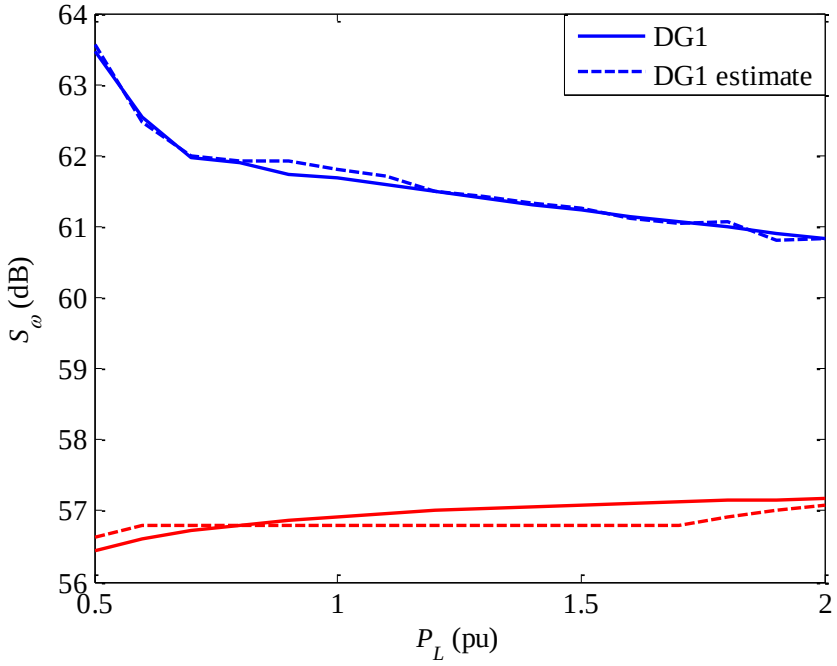

Figure 3-25: S_ω (solid) and $\hat{S}_\omega$ (dashed) before (blue) and after (red) islanding for different P_L values.

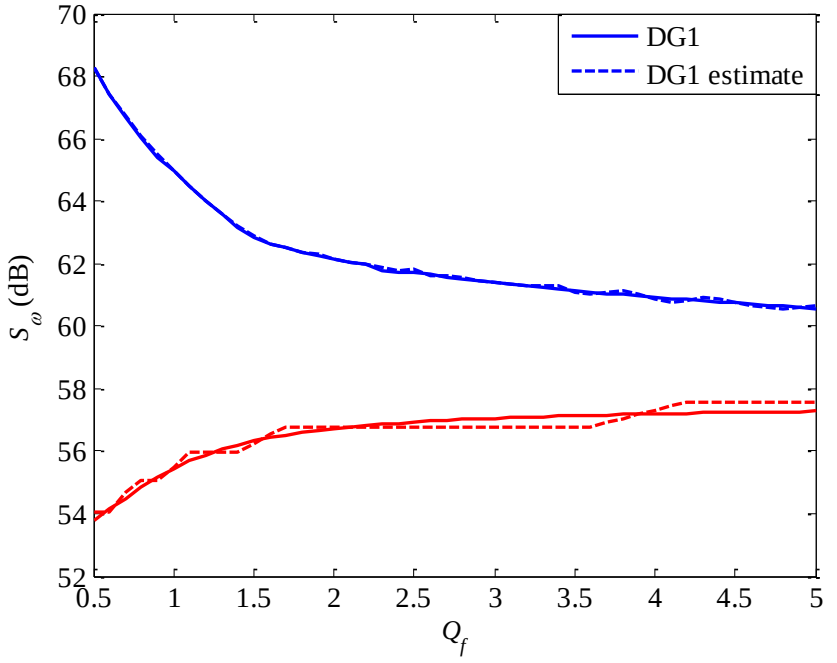

Figure 3-26: S_ω (solid) and $\hat{S}_\omega$ (dashed) before (blue) and after (red) islanding for different Q_f values.

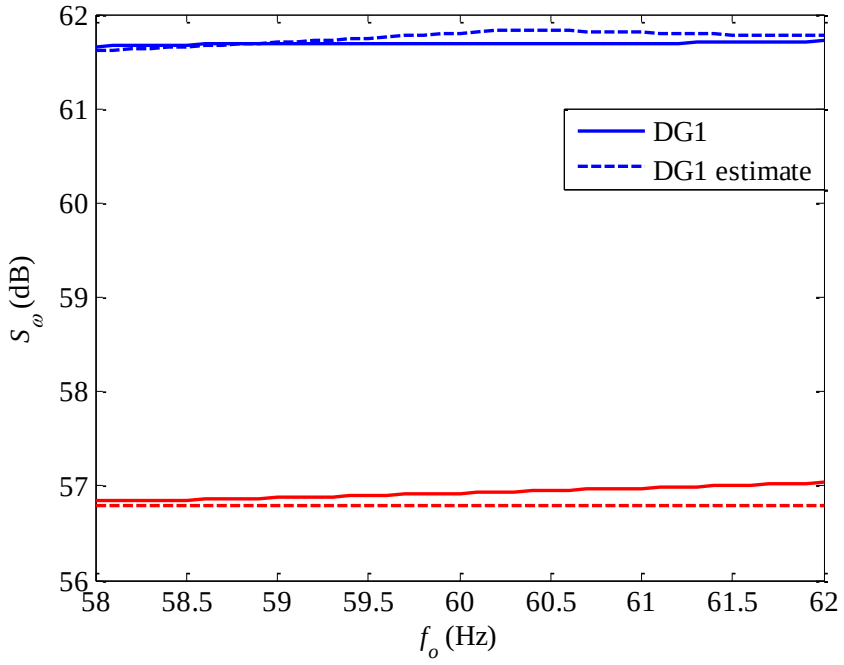

Figure 3-27: S_ω (solid) and $\hat{S}_\omega$ (dashed) before (blue) and after (red) islanding for different f_o values.

is increased from 0.5 to 2 pu, respectively. From Figure 3-25, a threshold value of 59 dB provides a clear separation between prior- and post-islanding regions and hence the value of S_{TH} is set to 59 dB. The 59 dB threshold provides appropriate classification of islanding condition for P_L values up to 3 pu at Q_f = 2.5 and f_o = 60 Hz. The difference between estimated and actual stiffness is a result of the 10Hz resolution used for calculating $\| \hat{H}_\omega \|_\infty$ where a Maximum Absolute Error (MAE) of 0.33 dB is obtained for this case. Figure 3-26 shows that as the load Q_f increases, the stiffness measure before islanding decreases while it decreases after islanding. As the load Q_f value increase, the load capacitive and inductive parts exchange higher reactive power and hence lower S_ω value is obtained before islanding. For the parallel *RLC* load, a

higher Q_f value corresponds to lower bandwidth or lower damping ratio. The increase in stiffness measure after islanding, for high Q_f value, is a result of a higher resonance frequency for H_ω and hence lower $\| H_\omega \|_\infty$ value is obtained. At Q_f values equal to 0.5 and 5, the stiffness gab is 14.22 and 3.11 dB, respectively. The MAE for this case is 0.36 dB and the 59 dB threshold provides appropriate classification of islanding condition for Q_f values up to 8.5 at P_L = 1 pu and f_o = 60 Hz. Figure 3-27 shows that for f_o values below 60Hz (capacitive load), a lower S_ω is obtained while f_o values above 60Hz (inductive load) resulted into a higher S_ω value. In the capacitive load case, the grid responds by absorbing a higher reactive power and hence the value of S_ω decreases as the load becomes more capacitive. On the other hand, the grid injects more reactive power as the load becomes more inductive and the value of S_ω increases accordingly. The change of S_ω values, within the tested range of f_o, is slight and a larger range of f_o could result into unstable operating point after islanding due to the inability of PMS to support the micro-grid frequency. The MAE obtained for this case is 0.24 dB.

- Distribution Line Impedance

The distribution system line impedance is an important factor that will significantly affect S_ω value. Stronger grid can be represented either by lower grid impedance magnitude (Z_g) or lower X_g / R_g ratio. The parameters in Table C-1 corresponds to Z_g = 0.2 Ω, and X_g / R_g = 1.5. Parameters are changed one at a time while others are kept constant and the corresponding values of R_g and L_g can be calculated by:

$$R_g = \frac{Z_g}{\sqrt{1+(X_g / R_g)^2}}, \quad L_g = \frac{Z_g (X_g / R_g)}{2\pi f_g \sqrt{1+(X_g / R_g)^2}}. \tag{3.31}$$

Figure 3-28 shows the effect of X_g / R_g ratio and Z_g value on both the actual and estimated stiffness measure before and after islanding.

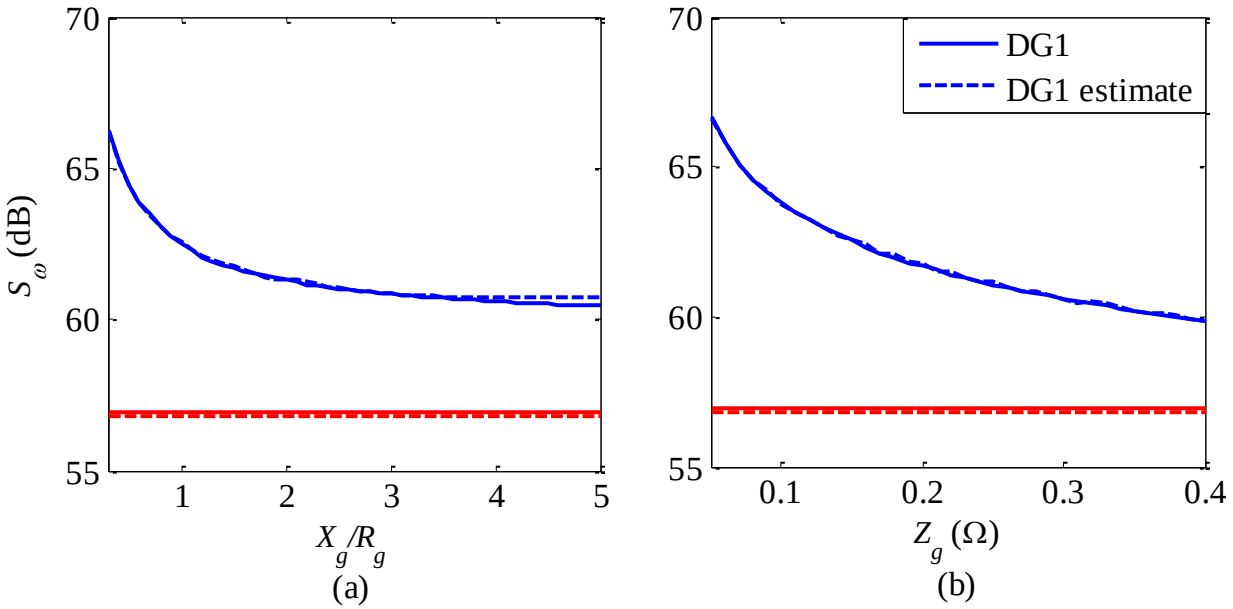

Figure 3-28: S_ω (solid) and $\hat{S}_\omega$ (dashed) before (blue) and after (red) islanding. (a) Z_g = 0.2, X_g / R_g changes. (b) X_g / R_g = 1.5, Z_g changes.

Results in Figure 3-28 show that a weaker grid, which corresponds to higher X_g / R_g ratio or higher Z_g value, resulted in a lower stiffness measure and hence reducing the separation gab between prior- and post-islanding stiffness measures. The gab shrinks from 9.43 to 3.93 dB as X_g / R_g ratio changes from 0.3 to 5, respectively. Also, as Z_g value changes from 0.05 to 0.4 Ω, the corresponding gab changes from 9.8 to 3.07 dB. The MAE from Figure 3-28 (a) is 0.27 dB while MAE of 0.15 dB is obtained from Figure 3-28 (b). The 59 dB threshold provides appropriate classification of islanding condition for Z_g values up to 0.54 Ω at X_g / R_g = 1.5 or

any practical range of X_g / R_g ratio at Z_g = 0.2 Ω. Hence, the proposed technique provides robust performance for a very wide range of Z_g values and X_g / R_g ratio.

- The SFS Parameters

In [63], it is shown that the SFS gain (K_f) has significant impact on the stability of a single DG system. Since the proposed IDM is an active technique, the existence of other active IDMs such as SFS could degrade the performance of the proposed technique. Figure 3-29 shows the effect of cf_o and K_f on the stiffness measure before and after islanding. It is shown that cf_o has negligible effect on the stiffness measure and hence a constant S_ω is obtained. On the other hand, the SFS gain has a negative impact on the system stability and hence a lower S_ω value is obtained when the grid is connected to the DG system. The stiffness gab reduces from 5.01 to 3.78 dB as the value of K_f changes from 0 to 0.02, respectively.

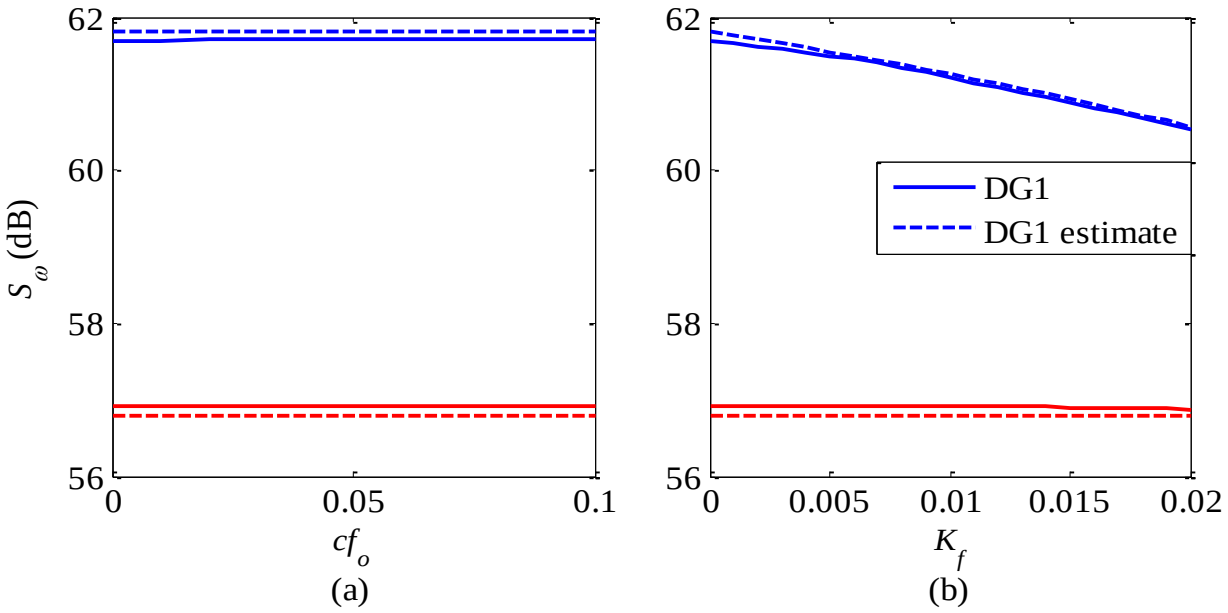

Figure 3-29: S_ω (solid) and $\hat{S}_\omega$ (dashed) before (blue) and after (red) islanding. (a) K_f = 0, cf_o changes. (b) cf_o = 0, K_f changes.

- Maximum Levels of Power

The maximum levels of allowed power in the DG system are used for calculating droop gains ($1/K_v$ and $1/K_\omega$) in the utilized PMS. Hence, the effect of using different droop gains is studied accordingly. Figure 3-30 shows the effect of different $P_{\max}$ and $Q_{\max}$ values on the stiffness measure before and after islanding condition.

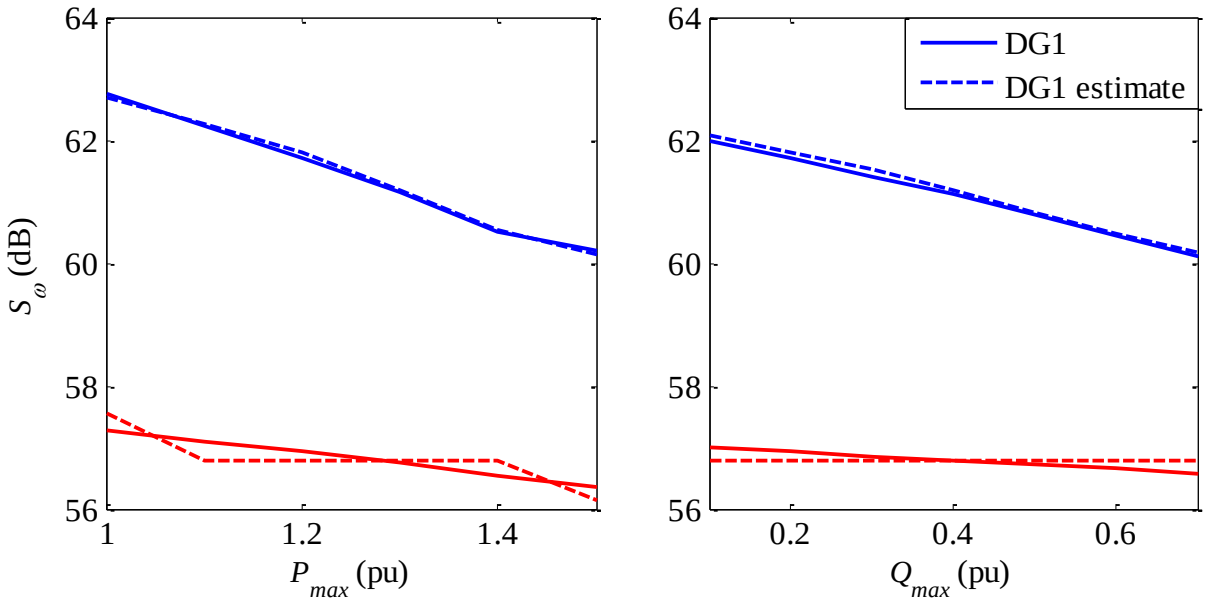

Figure 3-30: S_ω (solid) and $\hat{S}_\omega$ (dashed) before (blue) and after (red) islanding. (a) $Q_{\max}$ = 0.2, $P_{\max}$ changes. (b) $P_{\max}$ = 1.2, $Q_{\max}$ changes.

Figure 3-30 shows that as the per-unit value of $P_{\max}$ or $Q_{\max}$ is increased, the value of S_ω decreases accordingly. The increase in maximum level of power results into lower droop slope or higher droop gains. Hence, a larger weight is applied to the frequency/voltage error which negatively affects the stiffness measure and a smaller S_ω value is obtained. The gab shrinks from 5.14 to 4 dB as $P_{\max}$ changes from 1 to 1.5 pu, respectively. Also, as the value of $Q_{\max}$ changes from 0.1 to 0.7 pu, the corresponding gab changes from 5.28 to 3.37 dB, respectively.

The MAE obtained from Figure 3-30 (a) and (b) are 0.31 dB and 0.21 dB, respectively. A large value of droop gains could significantly degrade the system stability after islanding and the system could become unstable. Therefore, the droop gains should be designed carefully such that high system stiffness is maintained.

- Proportional Gains

There are four types of different PI controllers in the single DG system derived in Appendix C. The controllers are constant current controller, constant power controller, PLL controller, and frequency restoration controller. The PLL and frequency restoration controllers affect frequency directly and hence are expected to have significant influence on the stiffness measure. Figure 3-31 and Figure 3-32 show the effect of different proportional gains on the stiffness measure.

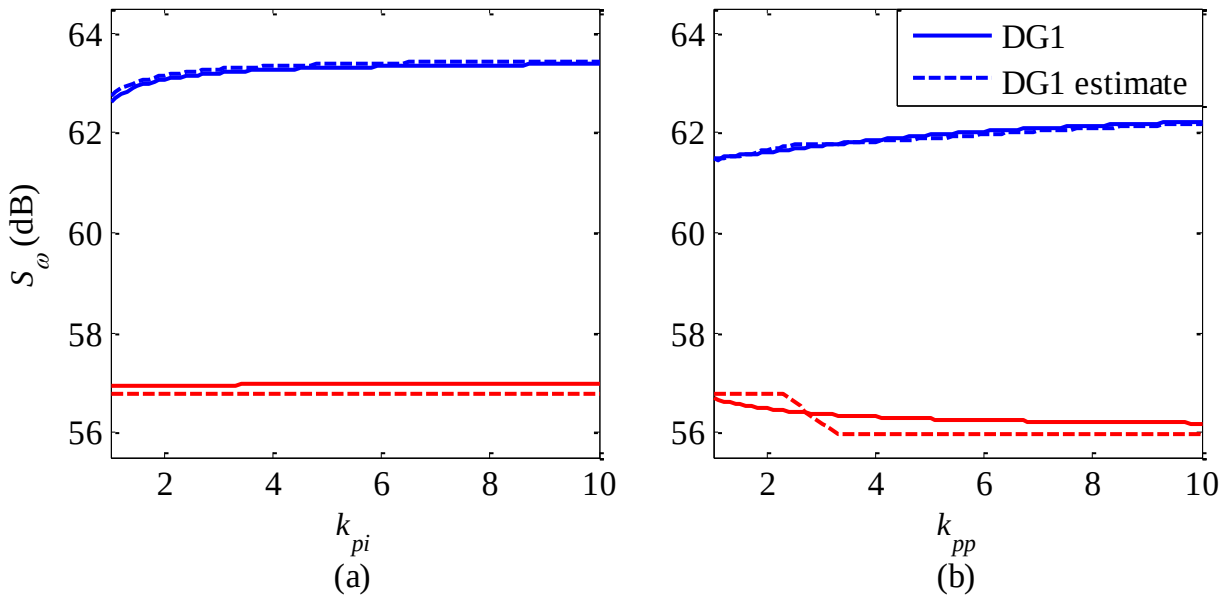

Figure 3-31: S_ω (solid) and $\hat{S}_\omega$ (dashed) before (blue) and after (red) islanding. (a) $k_{pp} = 0.5$, k_{pi} changes. (b) $k_{pi} = 0.5$, k_{pp} changes.

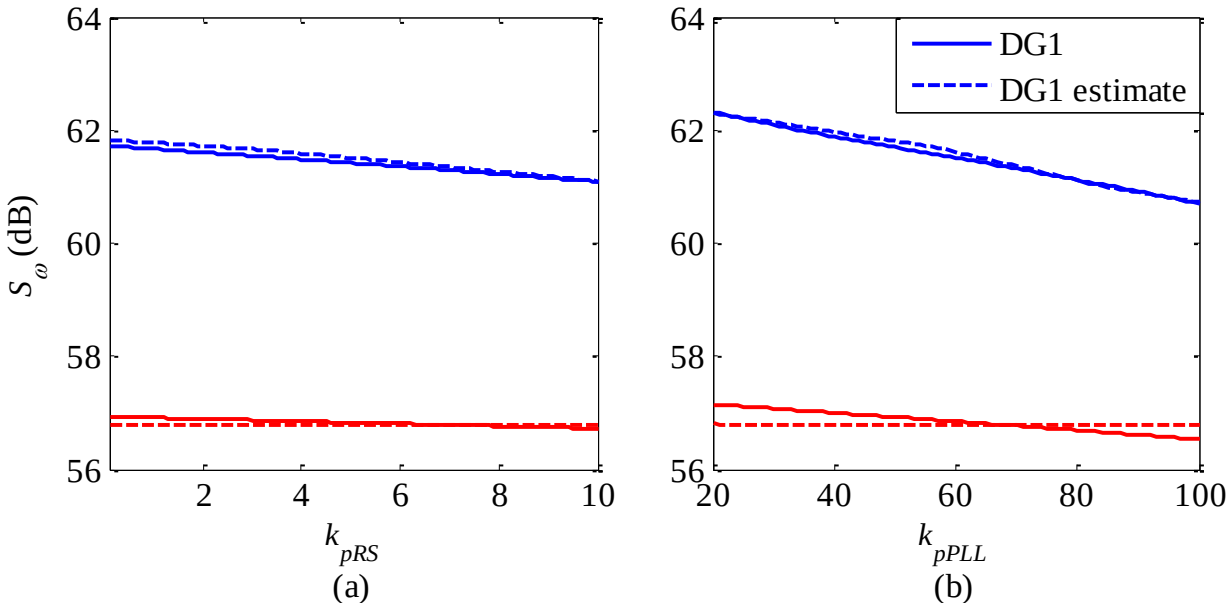

Figure 3-32: S_ω (solid) and $\hat{S}_\omega$ (dashed) before (blue) and after (red) islanding. (a) k_{pPLL} = 50, k_{pRS} changes. (b) k_{pRS} =0.5, k_{pPLL} changes.

Results in Figure 3-31 show that as k_{pp} or k_{pi} value increases, the value of S_ω before islanding increases since a higher proportional gain will result into a higher infinity-norm value for sH_ω. On the other side, the increase in k_{pp} value after islanding resulted into a slightly lower S_ω value due to the small decrease in the resonance frequency of H_ω, while the increase in k_{pi} value has a negligible effect on S_ω value after islanding. The slight decrease in S_ω was undetected by $\hat{S}_\omega$ due to the 10Hz frequency resolution used. Figure 3-32 shows that as k_{pRS} or k_{pPLL} value increases, the value of S_ω decreases accordingly. This is a result of the larger weight applied to the frequency error which negatively affect the stiffness measure obtained from frequency variation. The MAE for all these cases is 0.38 dB. For design purposes, the values of k_{pRS} and k_{pPLL} should be chosen carefully such that a sufficient gab in stiffness is maintained. A k_{pRS} = 0.5 and k_{pPLL} =50 is chosen and will be used for the rest of simulations.

3.2.4.2 Effect of Load Share Ratio on Stiffness for Multi-DG System

First of all, the input design parameter M_1, presented in (3.24), should be optimized for the multi-DG system. As mentioned in subsection 3.2.3.2, M_1 corresponds to the number of consecutive frequencies disturbed by the i^{th} DG. The Mean Squared Error (MSE) of stiffness measure is used for optimization and the load Q_f value is changed from 1 to 5 at a step of 0.2. The MSE is defined as follows:

$$\text{MSE} = \frac{1}{N_Q}\sum_{j=1}^{N_Q}\left(\hat{S}_\omega(j) - S_\omega(j)\right)^2, \tag{3.32}$$

where N_Q is the number of different Q_f values used for calculating the MSE. For the two-DG system, the parameters given by Table C-2 in Appendix C are used. Similar parameters are used for the 3-DG and 4-DG systems with $k_{pp}^3 = 5$ and $k_{pp}^4 = 1$. Also, the load is assumed to be equally shared by all DGs and hence $P_o'^i$ is set equal to $1/N$ per-unit where N is the number of connected DGs, and i is the DG index. The maximum power is normalized by the number of DGs to avoid system instability and hence $P_{\max}'^i = 1.2/N$ and $Q_{\max}'^i = 0.2/N$ in per-unit system. Figure 3-33 shows the effect of different M_1 values on the MSE for different number of connected DGs. It can be seen from Figure 3-33 that a minimum MSE is obtained for all simulated cases at $M_1 = 1$ and hence M_1 is set equal to 1 for the rest of simulations. At $M_1 = 1$, the Maximum Absolute Error (MAE) is 0.67, 1.02, and 1.37 dB for 2-DG, 3-DG, and 4-DG systems, respectively.

For the two-DG system, let us define the load share ratio to be $m' = P_o'^2 / P_o'^1$ where $P_o'^1 + P_o'^2 = 1$ pu. The maximum powers for the two-DG system are set as follows: $P_{\max}'^1 = 0.6$,

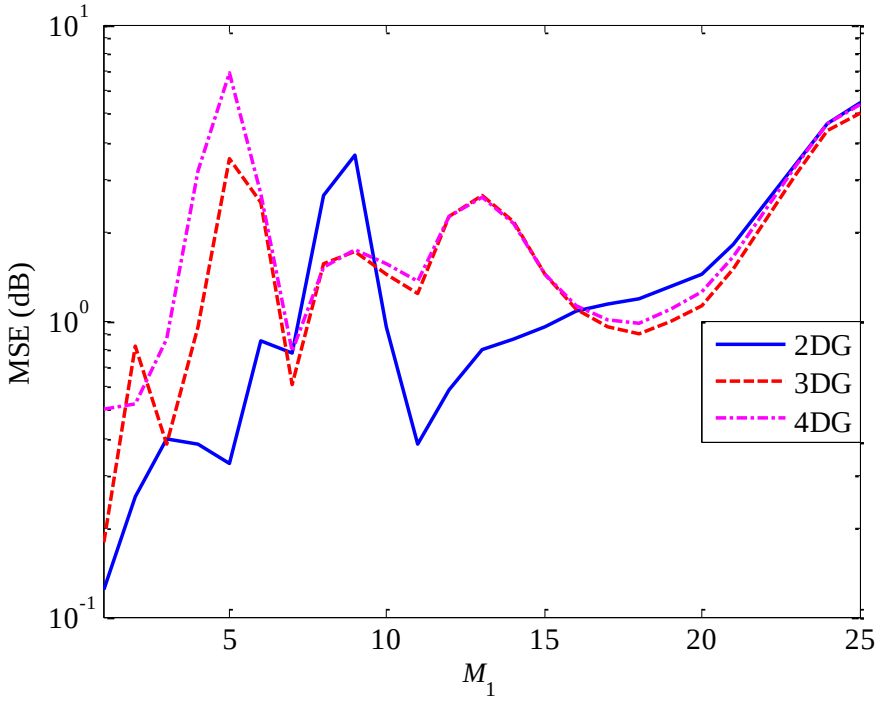

Figure 3-33: MSE versus M_1 for different number of connected DGs.

$P'^{2}_{\max}$ = 0.7, $Q'^{1}_{\max}$ = 0.1, and $Q'^{2}_{\max}$ = 0.2 pu. The rest of parameters are similar to Table C-2 introduced in Appendix C and the proportional gains of constant power controllers are initially set to $k^{1}_{pp} = k^{2}_{pp}$ = 0.5. Two cases are considered for simulation. For the first case, the Power Management Strategy (PMS), described in section C.2 in Appendix C, are employed for both DGs. On the other hand, the PMS is implemented for DG1 only while DG2 employs a constant power controller in the second case. Figure 3-34 and Figure 3-35 show the effect of m' on $\hat{S}_{\omega}$ for a two-DG system with different parameters for cases 1 and 2, respectively.

In Figure 3-34 (a), it can be seen that no significant change in $\hat{S}_{\omega}$ value is noticed as m' changes for a two-DG system with slightly different droop gains. The gab is reduced from 9.92 to 3.26 dB for Q_f values of 1 and 5, respectively. Also, Figure 3-34 (b) shows that as m'

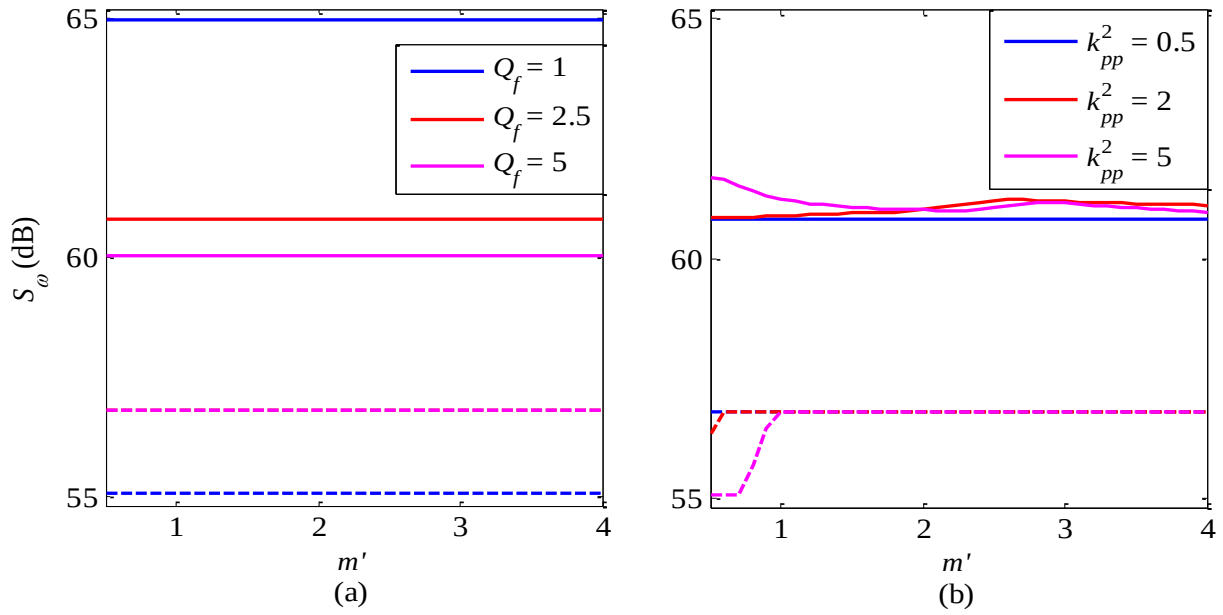

Figure 3-34: $\hat{S}_\omega$ versus m' for a 2-DG system before (solid) and after (dashed) islanding with PMS employed at both DGs. (a) $k_{pp}^2 = 0.5$, Q_f changes. (b) $Q_f = 2.5$, k_{pp}^2 changes.

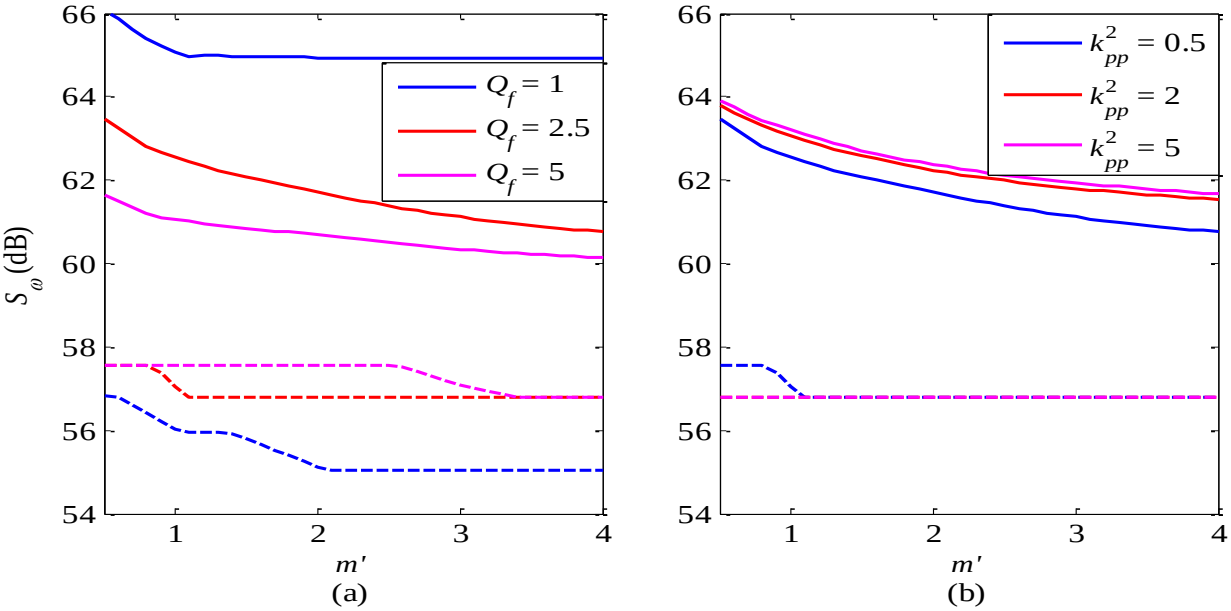

Figure 3-35: $\hat{S}_\omega$ versus m' for a 2-DG system before (solid) and after (dashed) islanding with PMS employed at DG1 only. (a) $k_{pp}^2 = 0.5$, Q_f changes. (b) $Q_f = 2.5$, k_{pp}^2 changes.

increases, the value of $\hat{S}_\omega$ before islanding decreases more for higher k_{pp}^2 value while $\hat{S}_\omega$ converges to the case k_{pp}^2 = 0.5 after islanding. On the other hand, results from Figure 3-35 (a) show that as the value of m' increases, the value of $\hat{S}_\omega$ decreases and a lower/higher value of $\hat{S}_\omega$ is obtained for larger Q_f value during before/after islanding condition. At m' = 1, the stiffness gab is 9.07, 5.49, and 3.51 dB for Q_f value 1, 2.5 and 5, respectively, while at m' = 4, the gab is 9.86, 3.97, and 3.34 dB for Q_f value 1, 2.5 and 5, respectively. Figure 3-35 (b) shows that as the value of m' increases, the value of $\hat{S}_\omega$ decreases where a higher $\hat{S}_\omega$ value is obtained for larger k_{pp}^2 value. Hence, the PMS provides a higher $\hat{S}_\omega$ value and the use of different control schemes can significantly degrade the system overall stiffness when DGs with lower stiffness provides higher power ratio. However, the 59 dB threshold maintains a robust islanding detection performance for all simulated cases.

3.2.4.3 Robustness against Other Power System Disturbances

In this subsection, the performance of the proposed IDM during different types of power system disturbances is verified. In addition to islanding condition, the proposed IDM is validated during load variation, capacitance switching, and three-phase-to-ground fault. An average Simulink model of a two-DG system, shown in Figure 3-22, is used for simulation. The switching load and capacitance are connected in parallel to the *RLC* load. The parameters used for the two-DG average model are given by Table C-2 presented in Appendix C. The *RLC* load power is assumed to be equally shared by both DGs (i.e., $P_o'^1 = P_o'^2$ = 0.5 pu). The three-phase base power is 10kVA and the line-to-line RMS base voltage is 208V. The following cases are simulated:

1. A micro-grid formation or islanding condition is simulated by disconnecting the circuit breaker (CB) at t = 0.5s.
2. A three-phase-to-ground fault taking place at PCC at t = 0.5s and clears out within 0.05s.
3. An additional load, with apparent power equal to 1.0 + j 1.0 per-unit, is connected in parallel to the *RLC* load and is switched on at t = 0.5s and off at t = 1s.
4. A capacitance, with reactive power equal to 1 per-unit, is connected in parallel to the *RLC* load and is switched on at t = 0.5s and off at t = 1s.

The overall stiffness of the two-DG system is estimated every 0.1s. Figure 3-36 and Figure 3-37 show the frequency response and estimated stiffness during different types of power system disturbances, respectively.

Results from Figure 3-37 shows that the stiffness measure changes from 60.93 to 56.79 dB with an overshoot of -0.83 dB during islanding condition. For the three-phase short circuit fault, $\hat{S}_\omega$ slightly changes to 61.44 dB and then oscillates until it settles back to 60.93 dB at t = 0.8s. For the load and capacitance switching cases, the stiffness measure increases/decreases when additional load/capacitance is switched on, respectively. The value of $\hat{S}_\omega$ is increased to 61.96 dB when the additional load is switched on, while $\hat{S}_\omega$ value decreases to 60.47 dB with a large overshoot of 1.94 dB when the capacitance is switched on. The initial value of $\hat{S}_\omega$ is recovered within 0.2s after the additional load/capacitance is switched off. Therefore, the proposed IDM distinguishes islanding condition from other types of power system disturbances and hence is proven to be robust against different power system disturbances.

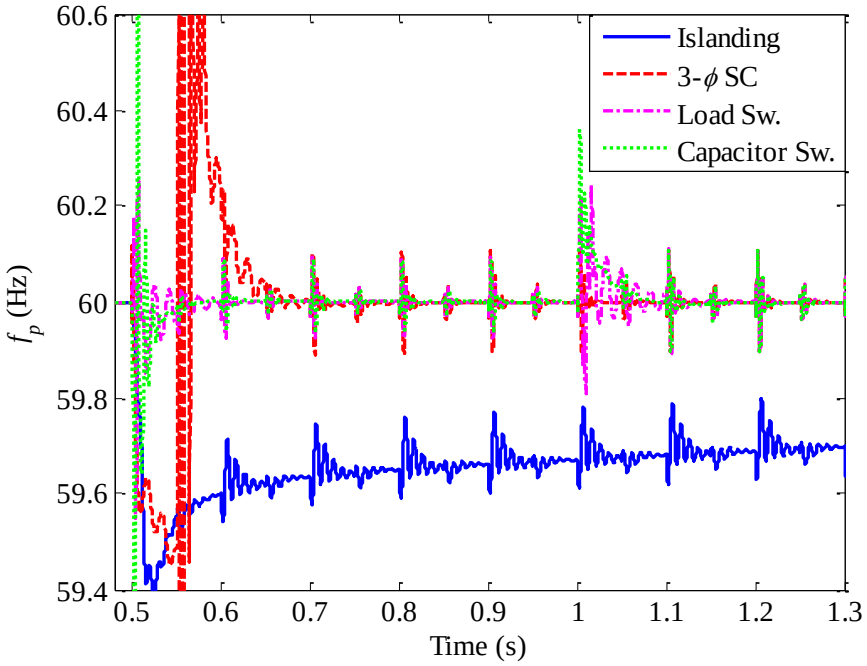

Figure 3-36: Frequency response during different types of power system disturbances.

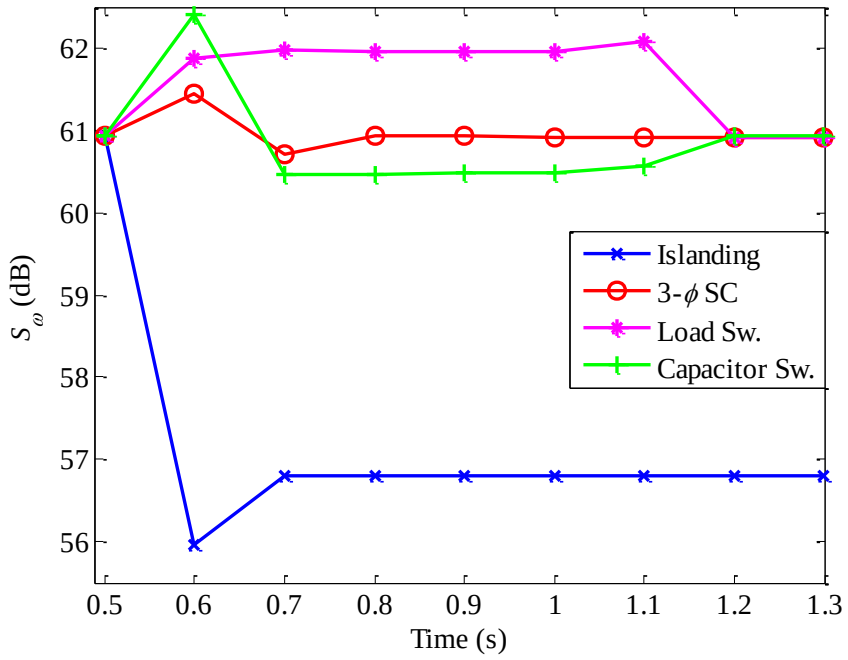

Figure 3-37: $\hat{S}_\omega$ during different types of power system disturbances.

3.2.5 Discussion

From subsection 3.2.4.3, it is important to notice that the amount of power level of the switched capacitance (Q_{Csw}) could significantly degrade the stiffness measure. Also, different values of clearing time (t_{cl}) for the three-phase-to-ground fault could result into significant drop in $\hat{S}_{\omega}$ value since the system stiffness will be corrupted by the ground fault. Figure 3-38 shows the effect of different Q_{Csw} and t_{cl} values on $\hat{S}_{\omega}$. The value of Q_{Csw} is in per-unit system and the load Q_f value is set to 1.

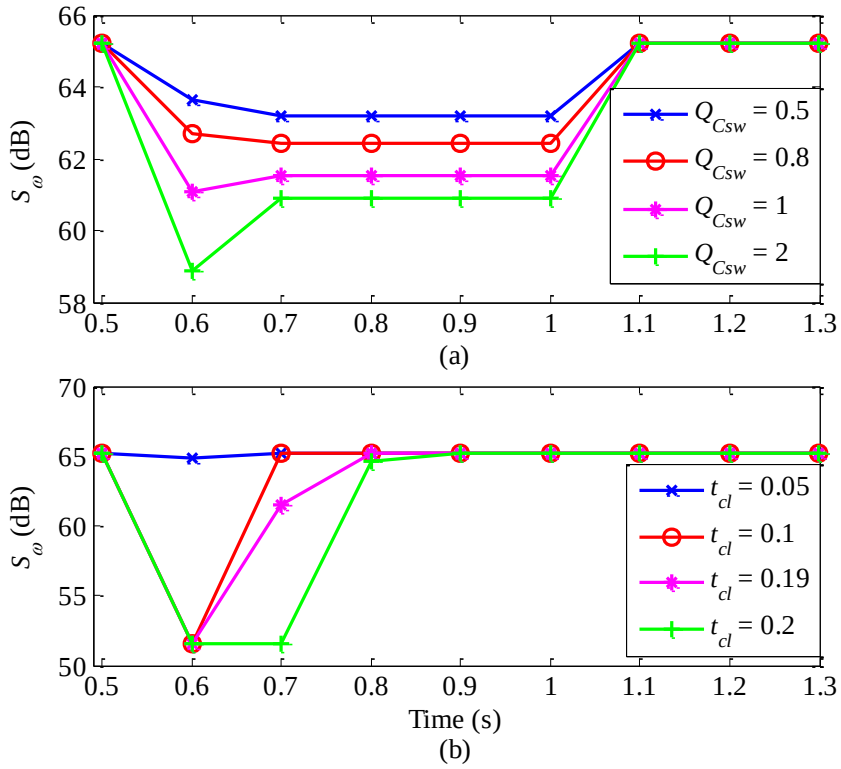

Figure 3-38: Effect of different Q_{Csw} and t_{cl} values on $\hat{S}_{\omega}$. (a) Q_{Csw} changes. (b) t_{cl} changes.

It can be seen from Figure 3-38 that as Q_{Csw} increases, the value of $\hat{S}_{\omega}$ decreases and a S_{TH} value of 59 dB could successfully distinguish islanding condition from capacitance

switching with Q_{Csw} up to 2 pu. However, a large overshoot is noticed for the case Q_{Csw} = 2 pu where $\hat{S}_{\omega}$ changes from 65.21 to 60.88 dB with an overshoot value of 58.89 dB. This value could trigger false islanding condition when we use the condition presented in (3.28). This issue could be resolved by adding a delay to the condition presented in (3.28) where a delay of single measurement cycle (T = 0.1s) could significantly improve the robust performance of the proposed IDM. Hence, the proposed IDM can distinguish islanding from short circuit faults with t_{cl} up to 0.19s. From a protection point of view, protection devices in the DG system are supposed to disconnect or isolate the DG from the rest of the grid when persistent fault is detected. In case islanding operation is not permitted, the proposed IDM will disconnect the DG system for short circuit faults with t_{cl} greater or equal to 0.2s. In case micro-grid operation is permitted and the IDM is required to distinguish islanding condition from persistent faults, the proposed technique could be used in conjunction with other protection schemes such as Over/Under Frequency Protection (OUF). Another way is to modify the proposed IDM in (3.28) as follows:

$$\begin{cases} \hat{S}_{\omega} > S_{TH1}, & \text{Normal operation} \\ S_{TH2} \le \hat{S}_{\omega} \le S_{TH1}, & \text{Islanding is detected} \\ \hat{S}_{\omega} < S_{TH2}, & \text{Persistent Fault} \end{cases} \tag{3.33}$$

where S_{TH1} and S_{TH2} are distinct threshold values that should be designed properly. From previous results, S_{TH1} = 59 dB and S_{TH2} = 53 dB seems to provide good robust performance for single and multi-DG systems.

CHAPTER 4: CONCLUSION

Recently, a lot of work has been conducted to improve efficiency, reliability, safety and sustainability of distribution network. The tremendous increase in the number of integrated Distributed Generations (DGs) has stimulated further research toward upgrading existing grid into the concept of smart grid where information exchange are smartly utilized to improve interaction between consumers and producers as well as enhancing autonomous robust operation and protection behavior. Islanding detection and anti-islanding algorithms have been of great interest to protection engineers in order to improve reliability and safety of grid-connected DGs. In this thesis, a distributed two-level Islanding Detection Algorithm (IDA) is proposed as well as other active techniques to improve islanding detection capability for single and multi-DG systems. Those results were presented in Chapters 2 and 3.

In the first section in Chapter 2, a new Islanding Detection Method (IDM) is developed, and it involves two dynamic estimators based on the system dynamics during islanding occurrence. The dynamic estimators estimate both amplitudes and phase angles of the current injected by the grid at Point of Common Coupling (PCC) in addition to the DG's local bus voltage. Analytical and simulation results show superior performance for the PCC algorithm, especially for high Q_f values due to the increase in grid current amplitude. In addition, the NDZ of the proposed PCC algorithm is very small and it can be approximated by a single line at 60 Hz for all values of Q_f. The time required to detect islanding condition is less than four cycles for all the simulated cases. Moreover, a distributed multi-DG algorithm is proposed for generalized multi-DG structure. The distributed algorithm has the ability to detect islanding both locally and at PCC level. To sum up, the proposed scheme is robust, local and asynchronous, the PCC and

the DGs are the nodes in the meshed communication network to share local information, communication is reduced to be the minimum (in both frequency and bandwidth), and the islanding condition can be distinguished from other types of power system disturbances. However, the performance of the dynamic estimator during frequency variation relies on the tracking capability of PLL which is very limited. Also, there is a lack of analytical proof of robustness and convergence for the RLS estimator. A robust non-linear observer is proposed to address those issues.

The second section of Chapter 2 presented detailed analytical derivation and proof of robustness and convergence for proposed fifth-order robust non-linear observer that estimates amplitude and frequency of a noisy sinusoidal signal. The observer was designed to ensure robustness and to provide better performance for the islanding detection problem. The time required to detect islanding condition at PCC is within four cycles for all implemented cases. The proposed observer showed robust performances against noise, harmonics and disturbances. Analytical and simulation results show that the performance of proposed observer is superior in comparison to observers presented in [59]. Also, the proposed non-linear observer is shown to provide better robust performance against harmonics and noise in comparison to the dynamic estimator presented in section 2.1.

In the first section of Chapter 3, a scheduled perturbation IDM is developed to reduce dependency on SFS gain K to eliminate NDZ. The initial chopping fraction (cf) is increased alternatively to eliminate NDZ, and the highest reduction from regular IDM NDZ is obtained for AFD or SFS with zero gain. The scheduled perturbation technique depends on the idea of combining the advantage of two different IDMs where the overall NDZ is the intersection area between two different NDZs. Two interesting cases are studied extensively. The first case is to

apply scheduling between SFS and OUF (SFS/OUF) IDMs. The second case is to use two SFS (SFS/SFS) with alternating sign of initial chopping fraction. An analytical formula for critical Q_f value is introduced for both regular and scheduled perturbation IDMs. For a single DG system, simulation results show that proper design of scheduled signal duty cycle is the key to yield the proposed theoretical NDZ reduction for both cases. On the other hand, it is shown that synchronization is critical for multi-DG systems and that a maximum delay of 0.33s can be tolerated for a two-DG system. The $\| f_e^2 \|_\infty - K$ and $cf - K$ curves are presented for choosing the parameters toward achieving a certain critical value of Q_f while ensuring that the square error in norm is under a certain bound. The proposed scheduling technique should be useful especially for systems with high DG penetration due to negative impact of SFS gain on stability. However, the proposed scheduled perturbation is limited to DG systems with constant current controllers. Also, for systems with large number of DGs, it might be extremely difficult to synchronize different DGs performances. Hence, a new active technique is proposed for large multi-DG systems.

In the second section of Chapter 3, a new active IDM is proposed for single and multi-DG systems. The proposed technique depends on estimating an overall transient stiffness-measure for the multi-DG system, which is defined in terms of the transfer function infinity-norm. For multi-DG systems, each DG is required to perturb at distinct frequencies from other DGs to avoid spectrum overlapping and hence no communications are needed among the different DGs. The estimated stiffness value is then used to determine the status of the grid where a clear separation between prior- and post-islanding stiffness is obtained. Results show that the proposed technique is scalable and robust against different loading conditions, variation in grid stiffness level, number of connected DGs, and different types of DG controllers.

Furthermore, the proposed technique can distinguish islanding condition from other types of power system disturbances such as three-phase-to-ground fault, capacitance switching, and load variations.

Overall, this thesis investigates the problem of islanding detection where new techniques for detecting islanding condition have been proposed. The concepts of limited-communication, synchronization, and distributed behavior have been utilized in the proposed techniques to enhance the robust and autonomous behavior of multi-DG systems and hence contribute to the future concept of smart grid. The proposed IDMs in this thesis are summarized as follows:

- A dynamic estimator based on RLS algorithm is presented to estimate the amplitudes and phase angles of both the DG bus voltage and the grid current. It is shown that the proposed technique will provide distributed, robust and fast islanding detection capability with negligible NDZ for single and multi-DG systems.
- A robust non-linear observer is presented as an alternative to the RLS algorithm. The proposed observer estimates both the amplitude and frequency of the grid current. Results show that the proposed observer is more robust against noise and harmonics and hence improve the islanding detection capability for the PCC level algorithm.
- To reduce the NDZ for low-gain SFS technique, a scheduled perturbation IDM is proposed. This technique reduces the stability impact of K and hence allowing higher penetration level of DGs into the distribution netwok.
- A transient stiffness-measure for the multi-DG system is developed to detect islanding condition. The proposed technique doesn't require any type of communication among different DGs. It is also shown that the proposed technique is scalable, and robust against different loading conditions and control schemes.

CHAPTER 5: FUTURE WORK AND RECOMMENDATIONS

In this chapter, the limitations of this thesis and obstacles encountered are presented in section 5.1. Additional work and some new directions for future research are given in section 5.2.

5.1 Obstacles and Limitations

Some of the difficulties and obtstacles encountered during this thesis are as follows:

- The current regulations and protection devices set by power companies do not provide a suitable environment to test some of these newly developed IDMs. New standards and regulations shall be imposed by power companies in order to regulate the amount of perturbation that can be injected by DGs for the purpose of detecting an islanding condition. This will regulate the behavior of newly integrated DGs and hence provide a more flexible environment to experiementaly validate new active IDMs.
- Typically, protection engineers try to avoid the use of communication for DGs integraded at distribution level of power networks. This old strategy should be changed to address newly developed safety and reliability considerations as a result of the tremendous increase in the penetration level of DGs in distribution networks. The use of local, low-bandwidth, low-frequency meshed communication networks will enhance reliability and safety of integrated DGs as well as provide autonomous and smart interaction behavior between the DGs and the traditional grid. New standards and regulations should be developed to regulate these limited-communication schemes.

The limitations of this thesis are as follows:

- The specifications of the communication network required for the distributed two-level algorithm proposed in Chapter 2 have not been systematically derived. However, the requirements are expected to be more flexible than the typical meshed communication network used for cooperative control schemes as seen in [46]. This is due to the simplicity of the exchanged information where the only information exchanged is the detection of transition and/or islanding cases between DGs and PCC. The requirement of the communication system in terms of design is that DG should be able to identify the source of the originated signal (whether it is PCC or other DGs). This can be easily done through appending a simple source designation to communication signals. Hence, the required communication system is not complicated and a secure low-frequency low-bandwidth communication topology is sufficient to achieve distributed islanding detection capability for the multi-DG system.
- Only three types of control schemes for DG systems are considered in this thesis and they are: constant current controller, constant power controller, and a simple PMS proposed in [71]. DG units with other advanced control schemes are not investigated. Also, an average model for the inverter is used where the PWM signal generator, the dc source, and the switching power electronic devices are replaced by a controlled voltage or current source. Hence, the effects of inverter switching are not considered. Also, the interactions between the proposed techniques in Chapter 3 with the dc side control (for example, the photovoltaic controller) or the storage system control are not considered.
- The analyses and simulations carried out in this thesis assume balanced three-phase DG systems. Unbalanced loads and unbalanced faults are not considered.

- In the multi-DG system derived in Appendix C, the DGs are assumed to be connected to the same bus. Also, the models in Appendix C are derived for *RLC* loads only and no dynamic loads are included.

5.2 Incremental Work and New Directions for Future Research

In continuation of this work, the following topics are suggested:

- The robust non-linear observer presented in Chapter 2 is used to estimate the amplitude and frequency of grid current only. The proposed observer can be used for estimating amplitude and frequency of DG voltage as well and hence can be used to enhance the robust performance of the DG local algorithm. One of the issues encountered in the DG voltage estimation is the high oscillation in amplitude as a result of using high-gain observer. One way to addresss this problem is to use variable gains that depend on the error where smaller gains are used when the error exceeds a certain threshold.
- For the proposed active techniques in Chapter 3, a parallel *RLC* load has been used to validate the performance of the proposed techniques. In recent studies such as [34] and [35], it is shown that constant *RLC* load do not necessarily constitute the worst loading condition for islanding studies and the load's frequency dependence could significantly influence the performance of SFS IDM. Hence, the performance of proposed techniques in Chapter 3 with frequency and voltage dependent loads can be studied in future work.
- Results from this thesis show that the scheduled perturbation technique is not suitable for DG systems with constant power controller. This is mainly due to the counter effect action between the controller and IDM. Few ideas can be investigated to address this problem. One is to reallocate the phase angle transformation block shown in Figure 3-2

(a) such that the aforementioned negative interference is reduced. Another way is to explore the applicability of this technique on IDMs that perturb voltage such as SVS.

- The effect of scheduled perturbation on small-signal stability for single and multi-DGs cases can be studied. An average small-signal stability model can be developed in a similar way as illustrated in Appendix C. The only difference is that an averaging technique should be applied to both switching models such that an average model with duty cycle variable is obtained. Also, conditions can be imposed on the switching system to ensure stable operation where Eigen-value analysis should be conducted for the switched system.

Also, some new directions that might be considered for future research are as follows:

- An adaptive cooperative technique can be developed for systems with large number of DGs where each DG implements a different IDM. The idea behind this technique is to modify the amount of perturbation injected by each DG such that the overall islanding detection capability and power quality are optimized. Taylor series expansion can be used to synchronize between different IDMs perturbation variables. This technique will require limited information exchange among DGs and is expected to be adaptive, scalable and robust with respect to different load share ratios.
- Since the objective of active IDMs contradict with the objective of DG controllers, the concept of game theory could be used to study these interactions for the multi-DG system. There are many interesting scenarios that can be studied. For example, what will happen to the multi-DG islanding detection capability if one of the DGs is selfish and was trying to maximize its own power output without injecting any perturbation?

- Typically, IDMs are evaluated according to their NDZ. There are other factors that should be considered in the evaluation process such as detection time, price, degradation to DG output power, stability impact, and robust performance against other disturbances. A universal tool should be developed to include all these factors where a grade should be assigned to the IDM under study for each of these factors. This will provide an easy and systematic procedure for protection engineers to follow and hence the right IDM can be chosen.

APPENDIX A:
DERIVATION OF LINEARLY PARAMETERIZED REALIZABLE MODEL IN LAPLACE DOMAIN

From the physical knowledge of the system and by using Kirchhoff Current Law (KCL) and Kirchhoff Voltage Law (KVL) in Figure 2-1, the following differential equations are obtained

$$\begin{cases} \dot{v}_1(t) = -a\, v_1(t) + b[i_s(t) + i_{inv}(t) - i_L(t)] \\ \dot{i}_L(t) = d\, v_1(t) \end{cases} \tag{A.1}$$

where $a = \frac{1}{RC}$, $b = \frac{1}{C}$ and $d = \frac{1}{L}$.

According to the second assumption in subsection 2.1.2, the estimated form of the grid current in the steady state is given by

$$\begin{aligned} i_s(t) &= A_s \sin(\omega_p t + \varphi_s) \\ &= A_s \cos(\varphi_s)\sin(\omega_p t) + A_s \sin(\varphi_s)\cos(\omega_p t) \end{aligned} \tag{A.2}$$

Taking the Laplace transformation of (A.1) yields

$$sV_1 - v_1(0) = -aV_1 + b[I_s + I_{inv} - I_L] \tag{A.3}$$

$$sI_L - i_L(0) = d\, V_1 \tag{A.4}$$

where s denotes the Laplace variable, V_1, I_s, I_L and I_{inv} are the Laplace transform of v_1, i_s, i_L and i_{inv}, respectively. By substituting (A.4) and the Laplace transformation of (A.2) into (A.3) and conveniently rearranging terms, one can obtain the following

$$\begin{aligned} V_1 = {} & \frac{bs}{s^2 + as + bd} A_s \cos(\varphi_s) L\big(\sin(\omega_p t)\big) + \frac{bs}{s^2 + as + bd} A_s \sin(\varphi_s)\, L\big(\cos(\omega_p t)\big) \\ & + \frac{bs}{s^2 + as + bd} I_{inv} + \frac{s}{s^2 + as + bd} v_1(0) - \frac{b}{s^2 + as + bd} i_L(0) \end{aligned} \tag{A.5}$$

where $L(..)$ denotes the Laplace operator. The last two terms in (A.5) denotes signals that do not persist beyond initial transient and hence can be excluded from further analysis for simplicity. The compact representation of the Linearly Parameterized (LP) realizable model is obtained by

$$y = W^T \theta \tag{A.6}$$

where y represent a combination of measured signals, W is a realizable regression vector and θ is an unknown parameter vector. By comparing (A.5) and (A.6), one can define

$$y = V_1 - \frac{bs}{s^2 + as + bd} I_{inv}$$

$$W = \left[\frac{bs}{s^2 + as + bd} L\left(\sin(\omega_p t)\right) \quad \frac{bs}{s^2 + as + bd} L\left(\cos(\omega_p t)\right) \right]^T$$

$$\theta = \left[A_s \cos(\varphi_s) \quad A_s \sin(\varphi_s) \right]^T$$

In case the value of b is small, it might be useful to multiply the regression vector (W) and the combined measured signal (y) by a constant ($\beta_o > 1$) in order to keep it above the noise level and to maintain the persistent excitation characteristic of W. However, in case that the signal y contains measurement noise, a large value of β_o will scale the noise and that will degrade the estimator performance. Therefore, the value of β_o has to be chosen carefully such that it amplifies the vector W as required. Then, the estimated values of grid current amplitude (in per-unit) and phase (in degree) can be calculated as follows:

$$\hat{A}_s = \frac{1}{I_{base}} \sqrt{\hat{\theta}_1^{\,2} + \hat{\theta}_2^{\,2}}, \quad \hat{\varphi}_s = \frac{180}{\pi} \operatorname{atan2}\left(\hat{\theta}_2, \hat{\theta}_1\right).$$

where I_{base} is the single-phase base current.

APPENDIX B:
PROOF OF OBSERVER'S ERROR BOUNDNESS

- Proof of *Lemma* 1

Let us define the following error signals:

$$e_\eta = \hat{\eta}_2 - \eta_2$$
$$e_\theta = \hat{\varphi} - \varphi = \begin{bmatrix} e_{\theta 1} & e_{\theta 2} \end{bmatrix}^T = \begin{bmatrix} \hat{\theta}_1 - \theta_1 & \hat{\varphi}_2 - \varphi_2 \end{bmatrix}^T$$

Then, proposed observer equations in (2.36) can be rewritten as follows:

$$\begin{cases} \dot{e}_\eta = -\alpha e_\eta + e_\theta{}^T \beta_F + \upsilon_F \\ \dot{e}_\theta = -\Gamma \beta_F e_\eta - \sigma \hat{\varphi} - k_a [e_\eta^2 + m_a^2] M \hat{\varphi} \end{cases} \tag{B.1}$$

The Lyapunov function can be defined as:

$$V = \frac{1}{2}\left(e_\eta^2 + e_\theta{}^T \Gamma^{-1} e_\theta\right)$$

Its time derivative is:

$$\begin{aligned} \dot{V} = &-\alpha e_\eta^2 + \upsilon_F e_\eta - \sigma e_\theta{}^T \Gamma^{-1} e_\theta - k_a [e_\eta^2 + m_a^2] e_\theta{}^T \Gamma^{-1} M e_\theta \\ &- \sigma e_\theta{}^T \Gamma^{-1} \varphi - k_a [e_\eta^2 + m_a^2] e_\theta{}^T \Gamma^{-1} M \varphi \end{aligned} \tag{B.2}$$

The upper bound of the filtered disturbance term υ_F can be found by defining the following state matrix:

$$A_C = T \Lambda T^{-1} = \begin{bmatrix} 0 & 1 \\ -B_0 & -B_1 \end{bmatrix}$$

where T is the modal transformation matrix of A_C, $\| e^{A_C t} \| \le c_1 e^{-c_2 t}$, $c_1 = \| T \| \| T^{-1} \|$, $c_2 = -\max\{\mathrm{Re}\, \lambda(A_C)\}$ and $\lambda(A_C)$ is the eigenvectors of matrix A_C.

Since $\delta(t)$ is a bounded disturbance, one can obtain the following upper bounds for sufficiently large t:

$$|\delta(t)| \le \bar{\delta}, \quad |\upsilon| \le \bar{\upsilon}, \quad |\upsilon_F| \le \bar{\upsilon}_F,$$

where $\bar{\upsilon} = \bar{\delta}(A_s + \bar{\delta}/2)$, $\bar{\upsilon}_F = B_0 \bar{\upsilon}(1 + c_1 c_3 / c_2)$, and $c_3 = \sqrt{B_0^2 + B_1^2}$.

Then, equation (B.2) can be bounded as follows:

$$\begin{aligned}\dot{V} \le & -\alpha e_\eta{}^2 + \bar{\upsilon}_F \mid e_\eta \mid -\sigma \gamma_1{}^{-1} e_{\theta 1}{}^2 - \gamma_2{}^{-1}\left(\sigma + k_a[e_\eta^2 + m_a^2]\right) e_{\theta 2}{}^2 \\ & + \sigma \gamma_1{}^{-1} \mid e_{\theta 1} \mid\mid \theta_1 \mid + \gamma_2{}^{-1}\left(\sigma + k_a[e_\eta^2 + m_a^2]\right) \mid e_{\theta 2} \mid \bar{\varphi}_{2\max}\end{aligned} \tag{B.3}$$

According to (B.3), $\dot{V}$ is negative definite outside the following compact set

$$\Omega \overset{\Delta}{=} \left\{ \left[e_\eta \, , e_{\theta 1} \, , e_{\theta 2}\right]^T : \; \alpha e_\eta{}^2 + \frac{\sigma}{\gamma_1} e_{\theta 1}{}^2 + \frac{\sigma + k_a[e_\eta^2 + m_a^2]}{\gamma_2} e_{\theta 2}{}^2 - \frac{\bar{\upsilon}_F{}^2}{\alpha} - \frac{\sigma \theta_1{}^2}{\gamma_1} - \frac{\sigma + k_a[e_\eta^2 + m_a^2]}{\gamma_2} \bar{\varphi}_{2\max}^2 \le 0 \right\} \tag{B.4}$$

It follows from theorem 2.15 and lemma 2.19 (pp.65-72) in [91] that e_η, $e_{\theta 1}$ and $e_{\theta 2}$ are uniformly bounded for all uniformly bounded disturbance $\delta(t)$. Figure B-1 shows the boundary of the compact set Ω where parameters in Table 2-3 are used at A_s = 0.05 p.u., ω = 1 p.u. and $\bar{\delta}$ = 0.001. The robust stability region is given by the complement of the region defined in (B.4) and is denoted by Ω^C. This region is the outside region of the boundary contour in Figure B-1. Hence, equations (B.3) and (B.4) prove the robustness for the proposed observer in the existence of a bounded disturbance $\delta(t)$. Also, it can be seen in Figure B-1 that the projection of frequency estimate and the σ-modification schemes enhance the robustness for the proposed observer.

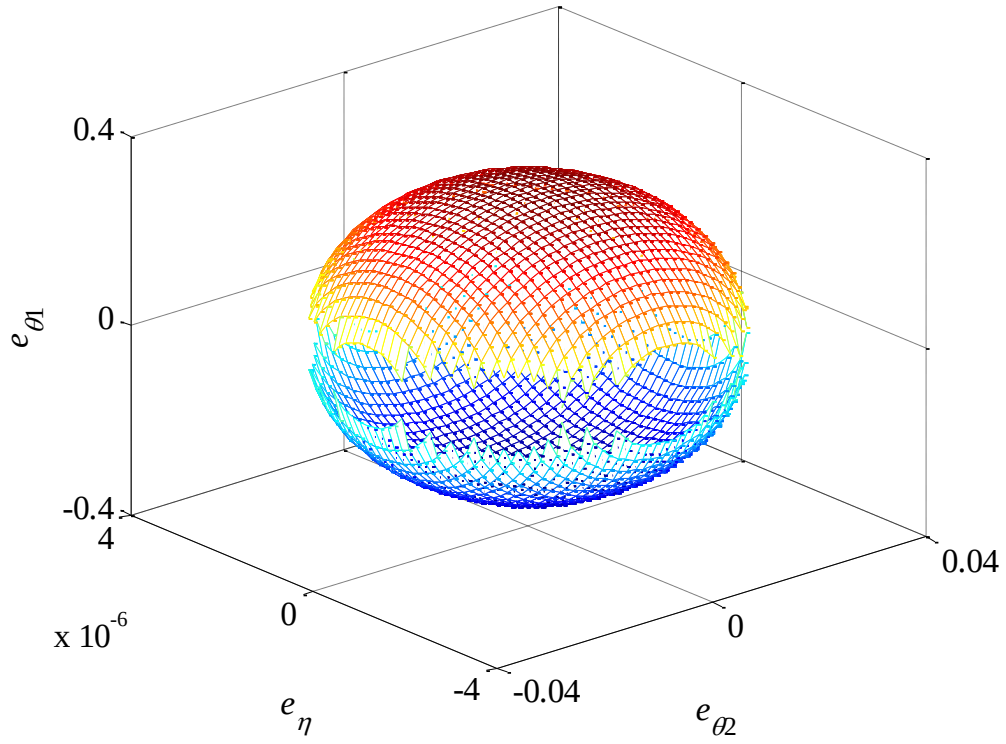

Figure B-1: Residual set of robust stability.

APPENDIX C:
DERIVATION OF SMALL-SIGNAL MODEL FOR SINGLE AND MULTI-DG SYSTEMS

This appendix presents the detailed derivation of the small-signal models for single and multi-DG systems. The DG constant current controller and the SFS IDM are introduced in section C.1. Section C.2 presents the micro-grid power management strategy used to support micro-grid frequency and voltage. The rest of the network is modeled in section C.3. The small-signal models for single- and multi-DG systems with parallel *RLC* load are derived in sections C.4 and C.5, respectively. Finally, the single and multi-DG models are validated through simulation in section C.6.

C.1 Modeling of DG Constant Current Controller and SFS

Figure C-1 shows the details of the current controller, the SFS IDM, and the three-phase PLL blocks used in each DG's control scheme. The current controller block is shown in Figure C-1 (a). i_{dref} and i_{qref} are the *d*- and *q*-axis DG output current references, respectively. A phase angle transformation is applied to obtain new current references i^*_{dref} and i^*_{qref}. The angle θ_f used in transformation is the output of the SFS IDM introduced in Figure C-1 (b). The input frequency to the SFS IDM (ω_p) is measured by a three-phase PLL presented in Figure C-1 (c). Then, the new references are subtracted from measured output currents (i_d and i_q) and applied to proportional-integral (PI) controllers with gains k_{pi} and k_{ii}, respectively. The *d*- and *q*-axis outputs of the current PI controller are u_d and u_q, respectively. Adding $v_d - i_q \omega_p L_f$ term to u_d and $v_q + i_d \omega_p L_f$ term to u_q is known as cross-coupling which is used to match control design equation such that the *dq* currents are decoupled from each other in terms of control equations, and also to substitute for voltage drop caused by DG inductance filter (L_f). Finally, a *dq-abc*

transformation is applied to construct three-phase voltage signals (v_{sa}, v_{sb}, and v_{sc}) which will be used to drive controlled voltage sources as seen in Figure 3-22.

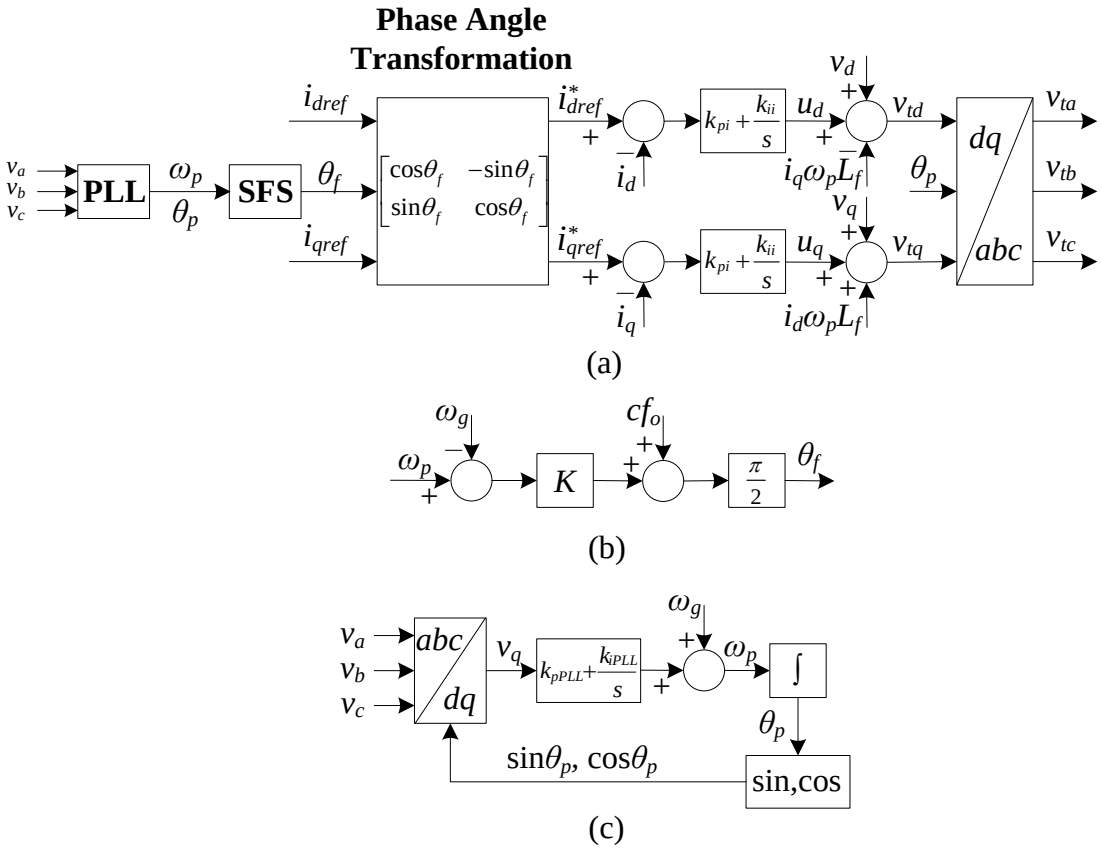

Figure C-1: Block diagrams of controller and islanding detection circuits of single DG system. (a) Constant current controller. (b) SFS IDM. (c) Three-phase PLL.

The *abc-dq* transformation is known as the park transformation [92]. Park transformation is used to convert three-phase AC quantities into two DC quantities to simplify calculations and control design. The relation between *abc* frame and *dq* frame is shown in Figure C-2 [75]. The transformation between *abc* and *dq* frames is given as follows:

$$\begin{bmatrix} v_d \\ v_q \end{bmatrix} = \frac{2}{3}\begin{bmatrix} \cos(\theta_p) & \cos(\theta_p - 2\pi/3) & \cos(\theta_p + 2\pi/3) \\ -\sin(\theta_p) & -\sin(\theta_p - 2\pi/3) & -\sin(\theta_p + 2\pi/3) \end{bmatrix}\begin{bmatrix} v_a \\ v_b \\ v_c \end{bmatrix}, \qquad \text{(C.1)}$$

$$\begin{bmatrix} v_a \\ v_b \\ v_c \end{bmatrix} = \begin{bmatrix} \cos(\theta_p) & -\sin(\theta_p) \\ \cos(\theta_p - 2\pi/3) & -\sin(\theta_p - 2\pi/3) \\ \cos(\theta_p + 2\pi/3) & -\sin(\theta_p + 2\pi/3) \end{bmatrix} \begin{bmatrix} v_d \\ v_q \end{bmatrix}, \tag{C.2}$$

where θ_p is the phase angle of inverter terminal voltage acquired by PLL, v_a, v_b, v_c are the three-phase inverter terminal voltages, and v_d, v_q are the inverter terminal voltages on *dq* frame.

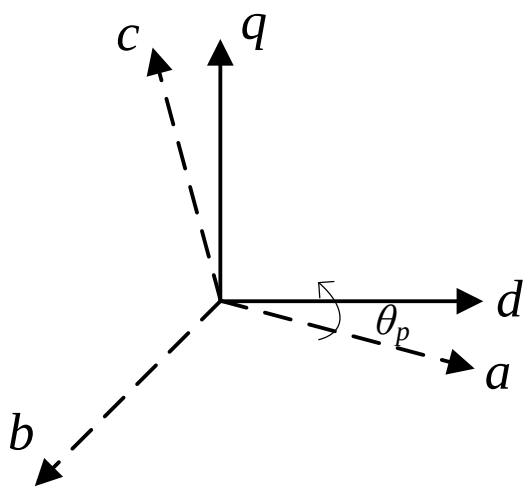

Figure C-2: *abc* frame and *dq* frame.

Let us assume that the three-phase inverter terminal voltage is given as follows:

$$\begin{aligned} v_a &= V\cos(\omega t + \delta_0) \\ v_b &= V\cos(\omega t - 2\pi/3 + \delta_0) \\ v_c &= V\cos(\omega t + 2\pi/3 + \delta_0) \end{aligned} \tag{C.3}$$

where V is the voltage amplitude, and ω is the voltage angular frequency in rad/sec. The initial phase angle δ_0 is a constant that can be determined by the steady-state operation point of the power system. The inverter voltage angle θ in (C.3) can also be expressed as (C.4) if it is assumed that the frequency change is reflected by the change in the voltage phase angle:

$$\theta = \omega_g t + \delta \tag{C.4}$$

Then, the *dq* inverter terminal voltage in (C.1) becomes

$$\begin{aligned} v_d &= V\cos(\theta-\theta_p) = V\cos(\delta-\delta_p) \\ v_q &= V\sin(\theta-\theta_p) = V\sin(\delta-\delta_p) \end{aligned} \tag{C.5}$$

where δ_p is the measured voltage phase angle and it is defined as follows:

$$\delta_p = \theta_p - \omega_g t \tag{C.6}$$

It can be seen from (C.5) that v_q converges to zero when PLL tracks the inverter voltage angle and hence is used as an error signal that is fed into a PI controller as seen in Figure C-1 (c). Then, the tracked voltage frequency by PLL is given as follows:

$$\omega_p = (k_{pPLL} + \frac{k_{iPLL}}{s})v_q + \omega_g \tag{C.7}$$

where s is the Laplace variable and θ_p is the integration of the frequency defined in (C.7). The PLL model can be expressed by the following equations:

$$\begin{aligned} \dot{\omega}_p &= k_{pPLL}\dot{v}_q + k_{iPLL}v_q \\ \dot{\delta}_p &= \omega_p - \omega_g \end{aligned} \tag{C.8}$$

The tracked voltage frequency ω_p is used as an input to the SFS IDM block to obtain the transformation angle θ_f as seen in Figure C-1 (b). The SFS model is represented by the following equation:

$$\theta_f = \frac{\pi}{2}\left(cf_o + K_f(\omega_p - \omega_g)\right) \tag{C.9}$$

where cf_o is the initial chopping fraction and K_f is the SFS gain. It is worth mentioning that the SFS gain defined in (C.9) is different from the one used in section 3.1 and the relation between the two gains is as follows:

$$K_f = \frac{1}{2\pi}K\,.$$

As seen in Figure C-1, the SFS output θ_f is used in a phase angle transformation to obtain new *dq* current references. The transformation is defined as follows:

$$\begin{bmatrix} i_{dref}^* \\ i_{qref}^* \end{bmatrix} = \begin{bmatrix} \cos(\theta_f) & -\sin(\theta_f) \\ \sin(\theta_f) & \cos(\theta_f) \end{bmatrix} \begin{bmatrix} i_{dref} \\ i_{qref} \end{bmatrix}. \tag{C.10}$$

The new references (i_{dref}^* and i_{qref}^*) are then used in the current controller loop. Thus, the phase angle of the reference current is changed by θ_f while its amplitude remains unchanged. For the inverter current control loop, let us define the following states:

$$\begin{aligned} \dot{i}_{ud} &= i_{dref}^* - i_d \\ \dot{i}_{uq} &= i_{qref}^* - i_q \end{aligned} \tag{C.11}$$

Then, the inverter current control can be described by the following:

$$\begin{aligned} v_{td} &= u_d - \omega_p L_f i_q + v_d \\ v_{tq} &= u_q + \omega_p L_f i_d + v_q \end{aligned} \tag{C.12}$$

where

$$\begin{aligned} u_d &= k_{pi}(i_{dref}^* - i_d) + k_{ii} i_{ud} \\ u_q &= k_{pi}(i_{qref}^* - i_q) + k_{ii} i_{uq} \end{aligned} \tag{C.13}$$

The inverter filter circuit equation can be written as follows:

$$\begin{aligned} L_f \dot{i}_d &= v_{td} - v_d + \omega_p L_f i_q \\ L_f \dot{i}_q &= v_{tq} - v_q - \omega_p L_f i_d \end{aligned} \tag{C.14}$$

By substituting (C.12) and (C.13) into (C.14), the following differential equation can be obtained:

$$\begin{aligned} \dot{i}_d &= \frac{1}{L_f}\left(k_{pi}(i_{dref}^* - i_d) + k_{ii} i_{ud}\right) \\ \dot{i}_q &= \frac{1}{L_f}\left(k_{pi}(i_{qref}^* - i_q) + k_{ii} i_{uq}\right) \end{aligned} \tag{C.15}$$

Typically, it is more convenient to perform all calculations in per-unit. Hence, a per-unit system has been adopted according to the following definitions:

$$\begin{aligned} R'_x &= \frac{R_x}{Z_{base}},\ L'_x = \frac{\omega_g L_x}{Z_{base}},\ C'_x = \frac{1}{\omega_g C_x Z_{base}}, \\ v'_x &= \frac{v_x}{V_{base}},\ i'_x = \frac{i_x}{I_{base}},\ P'_x = \frac{P_x}{S_{base}},\ Q'_x = \frac{Q_x}{S_{base}}, \\ \omega'_x &= \frac{\omega_x}{\omega_g},\ I_{base} = \frac{2}{3}\frac{S_{base}}{V_{base}},\ Z_{base} = \frac{V_{base}}{I_{base}}, \end{aligned} \tag{C.16}$$

where S_{base} is the three-phase system base power, and V_{base} is the peak value of the system rated voltage. Using the transformation of variables defined in (C.16), equations (C.10), (C.11), and (C.15) can be rewritten as follows:

$$\begin{aligned} i'^{*}_{dref} &= \cos(\theta_f) i'_{dref} - \sin(\theta_f) i'_{qref} \\ i'^{*}_{qref} &= \sin(\theta_f) i'_{dref} + \cos(\theta_f) i'_{qref} \end{aligned} \tag{C.17}$$

$$\begin{aligned} \dot{i}'_{ud} &= i'^{*}_{dref} - i'_d \\ \dot{i}'_{uq} &= i'^{*}_{qref} - i'_q \end{aligned} \tag{C.18}$$

$$\begin{aligned} \dot{i}'_d &= \frac{\omega_g}{L'_f}\left(k_{pi}(i'^{*}_{dref} - i'_d) + k_{ii} i'_{ud}\right) \\ \dot{i}'_q &= \frac{\omega_g}{L'_f}\left(k_{pi}(i'^{*}_{qref} - i'_q) + k_{ii} i'_{uq}\right) \end{aligned} \tag{C.19}$$

C.2 Modeling of Micro-grid Power Management Strategy

The constant current controller shown in Figure C-1 is typically used for grid-connected inverters. Stand-alone or micro-grid operation is a drawback for the constant current controller due to its inability to provide power management behavior such that both the voltage and the frequency are supported within the micro-grid. In [71], an active/reactive power management strategy is proposed. The proposed strategy includes a frequency-restoration term, and

frequency/voltage droop blocks in addition to the typical power regulator as shown in Figure C-3.

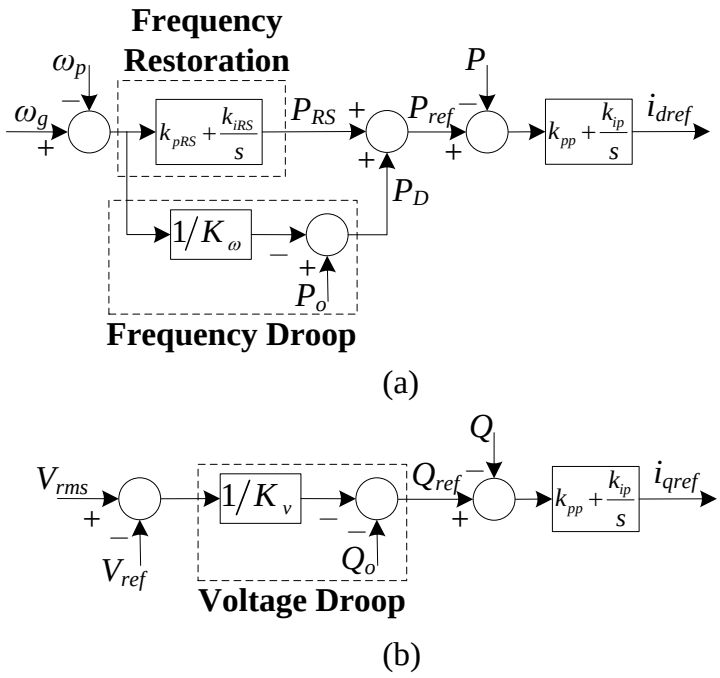

Figure C-3: Block diagrams of micro-grid power management controller. (a) Active power controller. (b) Reactive power controller.

In Figure C-3, the frequency error is applied to a PI controller, with gains k_{pRS} and k_{iRS}, to obtain P_{RS}. P_{RS} is added to P_D to obtain the real power reference of the power regulator block (P_{ref}) where P_D is generated by the frequency droop control. On the other hand, Q_{ref} is generated by the voltage droop control as shown in Figure C-3 (b). Then, the generated power references (P_{ref} and Q_{ref}) are subtracted from the measured power (P and Q) and fed into a PI controller (with gains k_{pp} and k_{ip}) to generate i_{dref} and i_{qref}, respectively, which are used as inputs to the constant current controller shown in Figure C-1 (a). Figure C-4 shows the typical frequency and voltage droop characteristics [74].

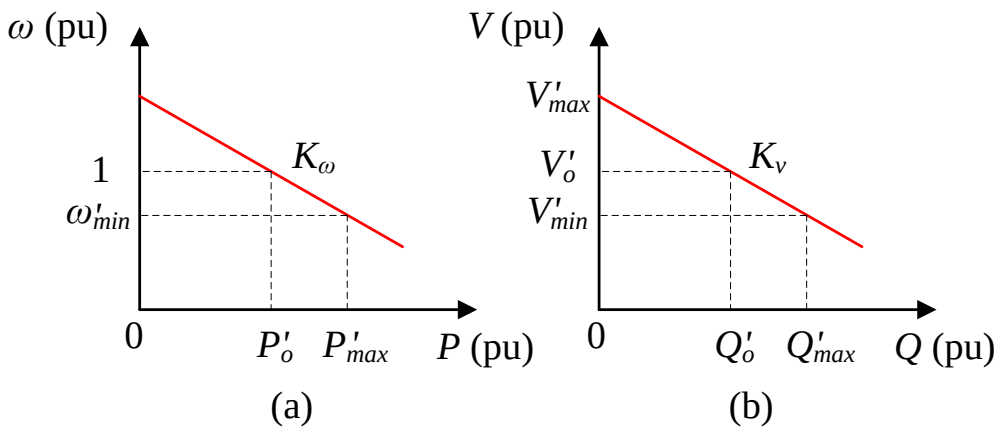

Figure C-4: Frequency and voltage droop characteristics. (a) $\omega - P$ curve. (b) $V - Q$ curve.

The frequency and voltage droop slopes can be calculated as follows:

$$K_\omega = \frac{1-\omega'_{\min}}{P'_o - P'_{\max}}, \quad K_v = \frac{V'_{\max} - V'_{\min}}{-Q'_{\max}}, \tag{C.20}$$

where $V'_{\max}$ and $V'_{\min}$ are the maximum and minimum permissible voltage in per-unit system, respectively, $\omega'_{\min} = 2\pi f_{\min} / \omega_g$ is the normalized minimum frequency allowed for the DG, and P'_o is the initial active power assigned to the DG in per-unit system. $P'_{\max}$ and $Q'_{\max}$ are the maximum active and reactive power of the DG in per-unit system, respectively. In Figure C-3, the per-unit RMS voltage, active, and reactive power are calculated as follows:

$$\begin{aligned} V'_{rms} &= \sqrt{{v'_d}^2 + {v'_q}^2} \\ P' &= v'_d i'_d + v'_q i'_q \\ Q' &= v'_d i'_q - v'_q i'_d \end{aligned} \tag{C.21}$$

It is important to mention that the calculated Q' in (C.21) is the reactive power absorbed by the DG and hence the minus sign, in Figure C-3 (b), is used to generate Q_{ref}. As a result, Q'_o is the initial reactive power injected by the DG at nominal voltage in per-unit system. Then, let us define the following states:

$$\begin{aligned} \dot{p}'_{id} &= P'_{ref} - P' \\ \dot{q}'_{iq} &= Q'_{ref} - Q' \end{aligned} \tag{C.22}$$

The power management controller can be represented by the following equations:

$$\begin{aligned} P'_{ref} &= -\frac{1}{K_\omega \omega_g}(\omega_g - \omega_p) + P'_o - \frac{k_{iRS}}{\omega_g}\delta_p + \frac{k_{pRS}}{\omega_g}(\omega_g - \omega_p) \\ Q'_{ref} &= -\frac{1}{K_v}(V'_{rms} - V'_{ref}) - Q'_o \end{aligned} \tag{C.23}$$

$$\begin{aligned} i'_{dref} &= k_{pp}(P'_{ref} - P') + k_{ip}\, p'_{id} \\ i'_{qref} &= k_{pp}(Q'_{ref} - Q') + k_{ip}\, q'_{iq} \end{aligned} \tag{C.24}$$

where V'_{ref} is set to a value of 1 in the per-unit system and $Q'_o = \frac{1}{K_v}(V'_{ref} - V'_{\max})$.

C.3 Modeling of Parallel *RLC* Load and Grid Representation

The DG control and power management strategy are modeled in sections C.1 and C.2. Figure C-5 shows the three-phase grid-connected inverter-based DG system with parallel *RLC* load [75]. In Figure C-5, R_g and L_g corresponds to the resistance and inductance of distribution line, respectively. The DG system is connected to the traditional grid through a three-phase circuit breaker indicated by CB. The power injected by the DG is $P - jQ$, $P_L + jQ_L$ is the power absorbed by the parallel *RLC* load, and $P_N + jQ_N$ is the power absorbed by the distribution system. The three-phase DG output current is i_a, i_b, i_c, and the DG terminal voltage is v_a, v_b, v_c. The parallel *RLC* load has the following three-phase branch currents: i_{Ra}, i_{Rb}, i_{Rc} (R_L branch), i_{La}, i_{Lb}, i_{Lc} (L_L branch), and i_{Ca}, i_{Cb}, i_{Cc} (C_L branch). i_{Na}, i_{Nb}, i_{Nc} is the three-phase current flown into the distribution network, and v_{sa}, v_{sb}, v_{sc} is the three-phase voltage of the distribution network supply.

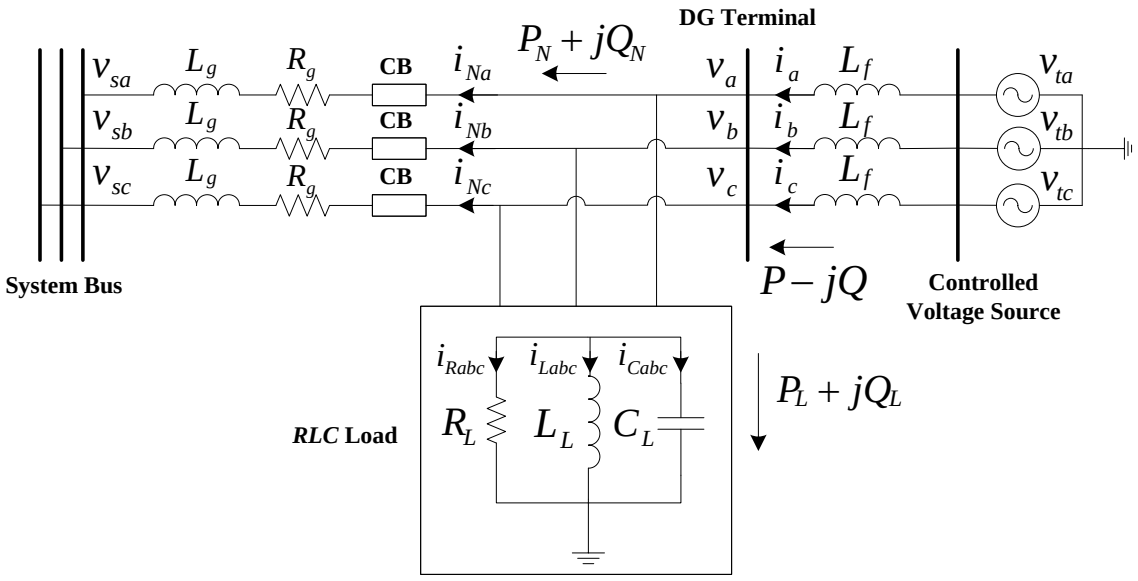

Figure C-5: Schematic diagram of single DG system with *RLC* load.

The *RLC* load and distribution network can be represented by the following equations:

$$\begin{aligned}
\dot{i}_{Na} &= -\frac{R_g}{L_g} i_{Na} + \frac{1}{L_g}(v_a - v_{sa}) \\
\dot{i}_{Nb} &= -\frac{R_g}{L_g} i_{Nb} + \frac{1}{L_g}(v_b - v_{sb}) \\
\dot{i}_{Nc} &= -\frac{R_g}{L_g} i_{Nc} + \frac{1}{L_g}(v_c - v_{sc})
\end{aligned} \tag{C.25}$$

$$\begin{aligned}
\dot{i}_{La} &= \frac{1}{L_L} v_a \\
\dot{i}_{Lb} &= \frac{1}{L_L} v_b \\
\dot{i}_{Lc} &= \frac{1}{L_L} v_c
\end{aligned} \tag{C.26}$$

$$\begin{aligned}
\dot{v}_a &= \frac{1}{C_L} i_{Ca} \\
\dot{v}_b &= \frac{1}{C_L} i_{Cb} \\
\dot{v}_c &= \frac{1}{C_L} i_{Cc}
\end{aligned} \tag{C.27}$$

where

$$\begin{aligned} i_{Ca} &= -v_a / R_L - i_{La} - i_{Na} + i_a \\ i_{Cb} &= -v_b / R_L - i_{Lb} - i_{Nb} + i_b \\ i_{Cc} &= -v_c / R_L - i_{Lc} - i_{Nc} + i_c \end{aligned} \tag{C.28}$$

By applying the *dq* transformation defined in (C.1) to (C.25)-(C.28) and substituting (C.28) into (C.27), the following differential equations are obtained:

$$\begin{aligned} \dot{i}_{Nd} &= -\frac{R_g}{L_g} i_{Nd} + \omega_p i_{Nq} + \frac{1}{L_g}(v_d - v_{sd}) \\ \dot{i}_{Nq} &= -\frac{R_g}{L_g} i_{Nq} - \omega_p i_{Nd} + \frac{1}{L_g}(v_q - v_{sq}) \end{aligned} \tag{C.29}$$

$$\begin{aligned} \dot{i}_{Ld} &= \omega_p i_{Lq} + \frac{1}{L_L} v_d \\ \dot{i}_{Lq} &= -\omega_p i_{Ld} + \frac{1}{L_L} v_q \end{aligned} \tag{C.30}$$

$$\begin{aligned} \dot{v}_d &= -\frac{1}{R_L C_L} v_d + \omega_p v_q + \frac{1}{C_L}(i_d - i_{Ld} - i_{Nd}) \\ \dot{v}_q &= -\frac{1}{R_L C_L} v_q - \omega_p v_d + \frac{1}{C_L}(i_q - i_{Lq} - i_{Nq}) \end{aligned} \tag{C.31}$$

Let us assume that the system bus in Figure C-5 is an infinite bus. Then, the voltage of the distribution network supply is given by:

$$\begin{aligned} v_{sa} &= E\cos(\omega_g t) \\ v_{sb} &= E\cos(\omega_g t - 2\pi/3) \\ v_{sc} &= E\cos(\omega_g t + 2\pi/3) \end{aligned} \tag{C.32}$$

where E is set to be equal to V_{base}. The *dq* voltage of the distribution network supply is calculated as follows:

$$\begin{aligned} v_{sd} &= E\cos\delta_p \\ v_{sq} &= -E\sin\delta_p \end{aligned} \tag{C.33}$$

Then, (C.33) is substituted into (C.29) and the transformation of variable defined in (C.16) is applied to equations (C.29)-(C.31). Hence, (C.29)-(C.31) are rewritten as follows:

$$\begin{aligned} \dot{i}'_{Nd} &= -\frac{\omega_g R'_g}{L'_g} i'_{Nd} + \omega_p i'_{Nq} + \frac{\omega_g}{L'_g}(v'_d - E'\cos\delta_p) \\ \dot{i}'_{Nq} &= -\frac{\omega_g R'_g}{L'_g} i'_{Nq} - \omega_p i'_{Nd} + \frac{\omega_g}{L'_g}(v'_q + E'\sin\delta_p) \end{aligned} \tag{C.34}$$

$$\begin{aligned} \dot{i}'_{Ld} &= \omega_p i'_{Lq} + \frac{\omega_g}{L'_L} v'_d \\ \dot{i}'_{Lq} &= -\omega_p i'_{Ld} + \frac{\omega_g}{L'_L} v'_q \end{aligned} \tag{C.35}$$

$$\begin{aligned} \dot{v}'_d &= -\frac{\omega_g C'_L}{R'_L} v'_d + \omega_p v'_q + \omega_g C'_L (i'_d - i'_{Ld} - i'_{Nd}) \\ \dot{v}'_q &= -\frac{\omega_g C'_L}{R'_L} v'_q - \omega_p v'_d + \omega_g C'_L (i'_q - i'_{Lq} - i'_{Nq}) \end{aligned} \tag{C.36}$$

where E' is equal to 1 in the per-unit system.

C.4 Small-signal Model of Single DG with *RLC* Load

By applying the perturbation and linearization technique, the small-signal model of the single DG system is described by the following equations:

$$\begin{aligned} p\Delta\omega_p &= k_{pPLL} p\Delta v'_q + k_{iPLL}\Delta v'_q \\ p\Delta\delta_p &= \Delta\omega_p \end{aligned} \tag{C.37}$$

$$\Delta\theta_f = \frac{\pi}{2} K_f \Delta\omega_p \tag{C.38}$$

$$\begin{aligned} \Delta i'^{*}_{dref} &= \cos(\theta_{f0})\Delta i'_{dref} - \sin(\theta_{f0})\Delta i'_{qref} - i'_{q0}\Delta\theta_f \\ \Delta i'^{*}_{qref} &= \sin(\theta_{f0})\Delta i'_{dref} + \cos(\theta_{f0})\Delta i'_{qref} + i'_{d0}\Delta\theta_f \end{aligned} \tag{C.39}$$

$$\begin{aligned} p\Delta i'_{ud} &= \Delta i'^{*}_{dref} - \Delta i'_d \\ p\Delta i'_{uq} &= \Delta i'^{*}_{qref} - \Delta i'_q \end{aligned} \tag{C.40}$$

$$
\begin{aligned}
p\Delta i'_d &= \frac{\omega_g}{L'_f}\left(k_{pi}(\Delta i'^{*}_{dref} - \Delta i'_d) + k_{ii}\Delta i'_{ud}\right) \\
p\Delta i'_q &= \frac{\omega_g}{L'_f}\left(k_{pi}(\Delta i'^{*}_{qref} - \Delta i'_q) + k_{ii}\Delta i'_{uq}\right)
\end{aligned}
\tag{C.41}
$$

$$
\begin{aligned}
\Delta V'_{rms} &= \frac{v'_{d0}}{V'_{rms0}}\Delta v'_d + \frac{v'_{q0}}{V'_{rms0}}\Delta v'_q \\
\Delta P' &= i'_{d0}\Delta v'_d + v'_{d0}\Delta i'_d + i'_{q0}\Delta v'_q + v'_{q0}\Delta i'_q \\
\Delta Q' &= i'_{q0}\Delta v'_d + v'_{d0}\Delta i'_q - i'_{d0}\Delta v'_q - v'_{q0}\Delta i'_d
\end{aligned}
\tag{C.42}
$$

$$
\begin{aligned}
p\Delta p'_{id} &= \Delta P'_{ref} - \Delta P' \\
p\Delta q'_{iq} &= \Delta Q'_{ref} - \Delta Q'
\end{aligned}
\tag{C.43}
$$

$$
\begin{aligned}
\Delta P'_{ref} &= \frac{1}{K_\omega \omega_g}\Delta\omega_p + \Delta P'_o - \frac{k_{iRS}}{\omega_g}\Delta\delta_p - \frac{k_{pRS}}{\omega_g}\Delta\omega_p \\
\Delta Q'_{ref} &= -\frac{1}{K_v}\Delta V'_{rms} - \Delta Q'_o
\end{aligned}
\tag{C.44}
$$

$$
\begin{aligned}
\Delta i'_{dref} &= k_{pp}(\Delta P'_{ref} - \Delta P') + k_{ip}\Delta p'_{id} \\
\Delta i'_{qref} &= k_{pp}(\Delta Q'_{ref} - \Delta Q') + k_{ip}\Delta q'_{iq}
\end{aligned}
\tag{C.45}
$$

$$
\begin{aligned}
p\Delta i'_{Nd} &= -\frac{\omega_g R'_g}{L'_g}\Delta i'_{Nd} + \omega_{p0}\Delta i'_{Nq} + i'_{Nq0}\Delta\omega_p + \frac{\omega_g}{L'_g}(\Delta v'_d + E'\sin\delta_0\Delta\delta_p) \\
p\Delta i'_{Nq} &= -\frac{\omega_g R'_g}{L'_g}\Delta i'_{Nq} - \omega_{p0}\Delta i'_{Nd} - i'_{Nd0}\Delta\omega_p + \frac{\omega_g}{L'_g}(\Delta v'_q + E'\cos\delta_0\Delta\delta_p)
\end{aligned}
\tag{C.46}
$$

$$
\begin{aligned}
p\Delta i'_{Ld} &= \omega_{p0}\Delta i'_{Lq} + i'_{Lq0}\Delta\omega_p + \frac{\omega_g}{L'_L}\Delta v'_d \\
p\Delta i'_{Lq} &= -\omega_{p0}\Delta i'_{Ld} - i'_{Ld0}\Delta\omega_p + \frac{\omega_g}{L'_L}\Delta v'_q
\end{aligned}
\tag{C.47}
$$

$$
\begin{aligned}
p\Delta v'_d &= -\frac{\omega_g C'_L}{R'_L}\Delta v'_d + \omega_{p0}\Delta v'_q + v'_{q0}\Delta\omega_p + \omega_g C'_L(\Delta i'_d - \Delta i'_{Ld} - \Delta i'_{Nd}) \\
p\Delta v'_q &= -\frac{\omega_g C'_L}{R'_L}\Delta v'_q - \omega_{p0}\Delta v'_d - v'_{d0}\Delta\omega_p + \omega_g C'_L(\Delta i'_q - \Delta i'_{Lq} - \Delta i'_{Nq})
\end{aligned}
\tag{C.48}
$$

where p is the derivative operator, and variables with subscript $_0$ are the steady-state values. After rearrangement and substitution, the small-signal model becomes:

$$\begin{cases} p\Delta v'_d = -a_{1,1}\Delta v'_d + \omega_{p0}\Delta v'_q + a_{1,3}\Delta i'_d - a_{1,3}\Delta i'_{Nd} - a_{1,3}\Delta i'_{Ld} + v'_{q0}\Delta\omega'_p \\ p\Delta v'_q = -\omega_{p0}\Delta v'_d - a_{1,1}\Delta v'_q + a_{1,3}\Delta i'_q - a_{1,3}\Delta i'_{Nq} - a_{1,3}\Delta i'_{Lq} - v'_{d0}\Delta\omega'_p \end{cases} \tag{C.49}$$

$$\begin{cases} p\Delta i'_d = -a_{3,1}\Delta v'_d + a_{3,2}\Delta v'_q - a_{3,3}\Delta i'_d + a_{3,4}\Delta i'_q + a_{3,9}\Delta i'_{ud} + a_{3,11}\Delta p'_{id} - a_{3,12}\Delta q'_{iq} \\ \qquad - a_{3,13}\Delta\delta_p - a_{3,14}\Delta\omega_p + b_{3,1}\Delta P'_o + b_{3,2}\Delta Q'_o \\ p\Delta i'_q = a_{4,1}\Delta v'_d + a_{4,2}\Delta v'_q - a_{3,4}\Delta i'_d - a_{3,3}\Delta i'_q + a_{3,9}\Delta i'_{uq} + a_{3,12}\Delta p'_{id} + a_{3,11}\Delta q'_{iq} \\ \qquad - a_{4,13}\Delta\delta_p + a_{4,14}\Delta\omega_p + b_{3,2}\Delta P'_o - b_{3,1}\Delta Q'_o \end{cases} \tag{C.50}$$

$$\begin{cases} p\Delta i'_{Nd} = a_{5,1}\Delta v'_d - a_{5,5}\Delta i'_{Nd} + \omega_{p0}\Delta i'_{Nq} + a_{5,13}\Delta\delta_p + i'_{Nq0}\Delta\omega_p \\ p\Delta i'_{Nq} = a_{5,1}\Delta v'_q - \omega_{p0}\Delta i'_{Nd} - a_{5,5}\Delta i'_{Nq} + a_{6,13}\Delta\delta_p - i'_{Nd0}\Delta\omega_p \end{cases} \tag{C.51}$$

$$\begin{cases} p\Delta i'_{Ld} = a_{7,1}\Delta v'_d + \omega_{p0}\Delta i'_{Lq} + i'_{Lq0}\Delta\omega_p \\ p\Delta i'_{Lq} = a_{7,1}\Delta v'_q - \omega_{p0}\Delta i'_{Ld} - i'_{Ld0}\Delta\omega_p \end{cases} \tag{C.52}$$

$$\begin{cases} p\Delta i'_{ud} = -a_{9,1}\Delta v'_d + a_{9,2}\Delta v'_q - a_{9,3}\Delta i'_d + a_{9,4}\Delta i'_q + a_{9,11}\Delta p'_{id} - a_{9,12}\Delta q'_{iq} \\ \qquad - a_{9,13}\Delta\delta_p - a_{9,14}\Delta\omega_p + b_{9,1}\Delta P'_o + b_{9,2}\Delta Q'_o \\ p\Delta i'_{uq} = a_{10,1}\Delta v'_d + a_{10,2}\Delta v'_q - a_{9,4}\Delta i'_d - a_{9,3}\Delta i'_q + a_{9,12}\Delta p'_{id} + a_{9,11}\Delta q'_{iq} \\ \qquad - a_{10,13}\Delta\delta_p + a_{10,14}\Delta\omega_p + b_{9,2}\Delta P'_o - b_{9,1}\Delta Q'_o \end{cases} \tag{C.53}$$

$$\begin{cases} p\Delta p'_{id} = -i'_{d0}\Delta v'_d - i'_{q0}\Delta v'_q - v'_{d0}\Delta i'_d - v'_{q0}\Delta i'_q - a_{11,13}\Delta\delta_p - a_{11,14}\Delta\omega_p + \Delta P'_o \\ p\Delta q'_{iq} = a_{12,1}\Delta v'_d + a_{12,2}\Delta v'_q + v'_{q0}\Delta i'_d - v'_{d0}\Delta i'_q - \Delta Q'_o \end{cases} \tag{C.54}$$

$$\begin{cases} p\Delta\delta_p = \Delta\omega_p \\ p\Delta\omega_p = -a_{14,1}\Delta v'_d - a_{14,2}\Delta v'_q + a_{14,4}\Delta i'_q - a_{14,4}\Delta i'_{Nq} - a_{14,4}\Delta i'_{Lq} - a_{14,14}\Delta\omega_p \end{cases} \tag{C.55}$$

where

$$a_{1,1} = \frac{\omega_g C'_L}{R'_L},\ a_{1,3} = \omega_g C'_L,\ a_{3,1} = \frac{\omega_g}{L'_f}k_{pi}(\cos\theta_{f0}k_{pp}i'_{d0} - \sin\theta_{f0}k_{pp}(i'_{q0} + \frac{v'_{d0}}{V'_{rms0}K_v})),$$

$$a_{3,2} = \frac{\omega_g}{L'_f}k_{pi}(-\cos\theta_{f0}k_{pp}i'_{q0} - \sin\theta_{f0}k_{pp}(i'_{d0} - \frac{v'_{q0}}{V'_{rms0}K_v})),$$

$$a_{3,3} = \frac{\omega_g}{L'_f}k_{pi}(\cos\theta_{f0}k_{pp}v'_{d0} + \sin\theta_{f0}k_{pp}v'_{q0} + 1),\ a_{3,4} = \frac{\omega_g}{L'_f}k_{pi}(-\cos\theta_{f0}k_{pp}v'_{q0} + \sin\theta_{f0}k_{pp}v'_{d0}),$$

$$a_{3,9}=\frac{\omega_g}{L'_f}k_{ii},\ a_{3,11}=\frac{\omega_g}{L'_f}k_{pi}\cos\theta_{f0}k_{ip},\ a_{3,12}=\frac{\omega_g}{L'_f}k_{pi}\sin\theta_{f0}k_{ip},\ a_{3,13}=\frac{1}{L'_f}k_{pi}\cos\theta_{f0}k_{pp}k_{iRS},$$

$$a_{3,14}=\frac{\omega_g}{L'_f}k_{pi}(\frac{\pi}{2}i'_{q0}K_f+\cos\theta_{f0}k_{pp}(k_{pRS}-1/K_\omega)/\omega_g),$$

$$a_{4,1}=\frac{\omega_g}{L'_f}k_{pi}(-\sin\theta_{f0}k_{pp}i'_{d0}-\cos\theta_{f0}k_{pp}(i'_{q0}+\frac{v'_{d0}}{V'_{rms0}K_v})),$$

$$a_{4,2}=\frac{\omega_g}{L'_f}k_{pi}(-\sin\theta_{f0}k_{pp}i'_{q0}+\cos\theta_{f0}k_{pp}(i'_{d0}-\frac{v'_{q0}}{V'_{rms0}K_v})),\ a_{4,13}=\frac{1}{L'_f}k_{pi}\sin\theta_{f0}k_{pp}k_{iRS},$$

$$a_{4,14}=\frac{\omega_g}{L'_f}k_{pi}(\frac{\pi}{2}i'_{d0}K_f-\sin\theta_{f0}k_{pp}(k_{pRS}-1/K_\omega)/\omega_g),$$

$$a_{5,1}=\frac{\omega_g}{L'_g},\ a_{5,5}=\frac{\omega_g R'_g}{L'_g},\ a_{5,13}=\frac{\omega_g}{L'_g}E'\sin\delta_0,\ a_{6,13}=\frac{\omega_g}{L'_g}E'\cos\delta_0,\ a_{7,1}=\frac{\omega_g}{L'_L},$$

$$a_{9,l}=\frac{L'_f}{\omega_g k_{pi}}a_{3,l},\ a_{10,m}=\frac{L'_f}{\omega_g k_{pi}}a_{4,m},\ l=1,2,3,4,11,12,13,14,\ m=1,2,13,14,$$

$$a_{11,13}=\frac{k_{iRS}}{\omega_g},\ a_{11,14}=\frac{1}{\omega_g}(k_{pRS}-\frac{1}{K_\omega}),\ a_{12,1}=-i'_{q0}-\frac{v'_{d0}}{V'_{rms0}K_v},\ a_{12,2}=i'_{d0}-\frac{v'_{q0}}{V'_{rms0}K_v},$$

$$a_{14,1}=k_{pPLL}\omega_{p0},\ a_{14,2}=k_{pPLL}\frac{\omega_g C'_L}{R'_L}-k_{iPLL},\ a_{14,4}=k_{pPLL}\omega_g C'_L,\ a_{14,14}=k_{pPLL}v'_{d0},$$

$$b_{3,1}=\frac{\omega_g}{L'_f}k_{pi}\cos\theta_{f0}k_{pp},\ b_{3,2}=\frac{\omega_g}{L'_f}k_{pi}\sin\theta_{f0}k_{pp},\ b_{9,1}=\cos\theta_{f0}k_{pp},\ b_{9,2}=\sin\theta_{f0}k_{pp}.$$

Then, the complete small-signal model can be represented as follows:

$$p\Delta\mathbf{x}=\mathbf{A}\Delta\mathbf{x}+\mathbf{B}\Delta\mathbf{u}, \tag{C.56}$$

where

$$\Delta\mathbf{x}=\begin{bmatrix}\Delta v'_d & \Delta v'_q & \Delta i'_d & \Delta i'_q & \Delta i'_{Nd} & \Delta i'_{Nq} & \Delta i'_{Ld} & \Delta i'_{Lq} & \Delta i'_{ud} & \Delta i'_{uq} & \Delta p'_{id} & \Delta q'_{iq} & \Delta\delta_p & \Delta\omega_p\end{bmatrix}^T,$$

$$\Delta\mathbf{u}=\begin{bmatrix}\Delta P'_o & \Delta Q'_o\end{bmatrix}^T,$$

$$\mathbf{A}=\begin{bmatrix}\mathbf{A}_1 & \mathbf{A}_2\\ \mathbf{A}_3 & \mathbf{A}_4\end{bmatrix},$$

$$\mathbf{A}_1 = \begin{bmatrix} -a_{1,1} & \omega_{p0} & a_{1,3} & 0 & -a_{1,3} & 0 \\ -\omega_{p0} & -a_{1,1} & 0 & a_{1,3} & 0 & -a_{1,3} \\ -a_{3,1} & a_{3,2} & -a_{3,3} & a_{3,4} & 0 & 0 \\ a_{4,1} & a_{4,2} & -a_{3,4} & -a_{3,3} & 0 & 0 \\ a_{5,1} & 0 & 0 & 0 & -a_{5,5} & \omega_{p0} \\ 0 & a_{5,1} & 0 & 0 & -\omega_{p0} & -a_{5,5} \end{bmatrix},$$

$$\mathbf{A}_2 = \begin{bmatrix} -a_{1,3} & 0 & 0 & 0 & 0 & 0 & 0 & v'_{q0} \\ 0 & -a_{1,3} & 0 & 0 & 0 & 0 & 0 & -v'_{d0} \\ 0 & 0 & a_{3,9} & 0 & a_{3,11} & -a_{3,12} & -a_{3,13} & -a_{3,14} \\ 0 & 0 & 0 & a_{3,9} & a_{3,12} & a_{3,11} & -a_{4,13} & a_{4,14} \\ 0 & 0 & 0 & 0 & 0 & 0 & a_{5,13} & i'_{Nq0} \\ 0 & 0 & 0 & 0 & 0 & 0 & a_{6,13} & -i'_{Nd0} \end{bmatrix},$$

$$\mathbf{A}_3 = \begin{bmatrix} a_{7,1} & 0 & 0 & 0 & 0 & 0 \\ 0 & a_{7,1} & 0 & 0 & 0 & 0 \\ -a_{9,1} & a_{9,2} & -a_{9,3} & a_{9,4} & 0 & 0 \\ a_{10,1} & a_{10,2} & -a_{9,4} & -a_{9,3} & 0 & 0 \\ -i'_{d0} & -i'_{q0} & -v'_{d0} & -v'_{q0} & 0 & 0 \\ a_{12,1} & a_{12,2} & v'_{q0} & -v'_{d0} & 0 & 0 \\ 0 & 0 & 0 & 0 & 0 & 0 \\ -a_{14,1} & -a_{14,2} & 0 & a_{14,4} & 0 & -a_{14,4} \end{bmatrix},$$

$$\mathbf{A}_4 = \begin{bmatrix} 0 & \omega_{p0} & 0 & 0 & 0 & 0 & 0 & i'_{Lq0} \\ -\omega_{p0} & 0 & 0 & 0 & 0 & 0 & 0 & -i'_{Ld0} \\ 0 & 0 & 0 & 0 & a_{9,11} & -a_{9,12} & -a_{9,13} & -a_{9,14} \\ 0 & 0 & 0 & 0 & a_{9,12} & a_{9,11} & -a_{10,13} & a_{10,14} \\ 0 & 0 & 0 & 0 & 0 & 0 & -a_{11,13} & -a_{11,14} \\ 0 & 0 & 0 & 0 & 0 & 0 & 0 & 0 \\ 0 & 0 & 0 & 0 & 0 & 0 & 0 & 1 \\ 0 & -a_{14,4} & 0 & 0 & 0 & 0 & 0 & -a_{14,14} \end{bmatrix},$$

$$\mathbf{B} = \begin{bmatrix} 0 & 0 & b_{3,1} & b_{3,2} & 0 & 0 & 0 & 0 & b_{9,1} & b_{9,2} & 1 & 0 & 0 & 0 \\ 0 & 0 & b_{3,2} & -b_{3,1} & 0 & 0 & 0 & 0 & b_{9,2} & -b_{9,1} & 0 & -1 & 0 & 0 \end{bmatrix}^T.$$

The steady-state values of the state variables in the model are calculated as follows:

$$\begin{aligned}
&\theta_{f0} = \frac{\pi}{2} cf_o, \;\; v'_{d0} = V'_0, \;\; v'_{q0} = 0, \;\; V'_{rms0} = \sqrt{{v'_{d0}}^2 + {v'_{q0}}^2}, \\
&\omega_{p0} = \omega_g, \;\; P'_{ref0} = P'_o, \;\; Q'_{ref0} = -\frac{1}{K_v}(V'_{rms0} - V'_{\max}), \\
&i'_{d0} = \frac{P'_{ref0}}{V'_0}, \;\; i'_{q0} = \frac{Q'_{ref0}}{V'_0}, \;\; i'_{Ld0} = \frac{\omega_g v'_{q0}}{\omega_{p0} L'_L}, \;\; i'_{Lq0} = \frac{-\omega_g v'_{d0}}{\omega_{p0} L'_L}, \\
&i'_{Nd0} = i'_{d0} - \frac{v'_{d0}}{R'_L} - i'_{Ld0} + \frac{\omega_{p0} v'_{q0}}{\omega_g C'_L}, \;\; i'_{Nd0} = i'_{q0} - \frac{v'_{q0}}{R'_L} - i'_{Lq0} - \frac{\omega_{p0} v'_{d0}}{\omega_g C'_L}
\end{aligned} \tag{C.57}$$

The values of V'_0 and δ_0 in (C.57) are obtained by solving the steady-state power flow equation of the equivalent circuit shown in Figure C-6.

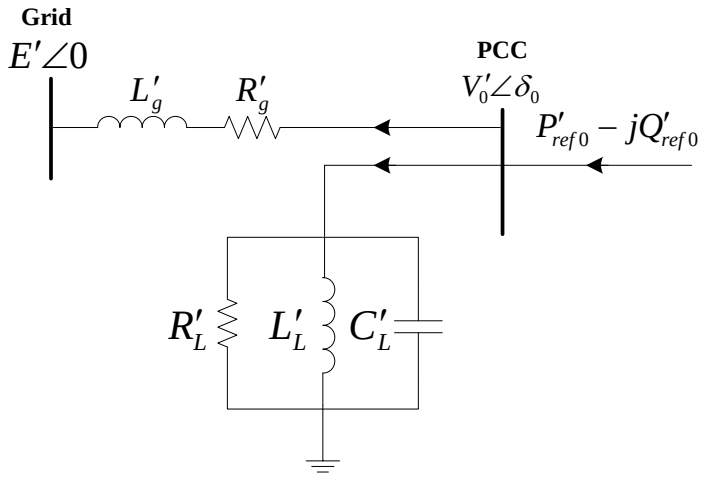

Figure C-6: Equivalent steady-state circuit of single DG system with *RLC* load.

The power flow equation is given as follows:

$$P'_{ref0} - jQ'_{ref0} = V'\angle\delta_0 \left(\frac{V'\angle\delta_0 - E'\angle 0}{R'_g + jL'_g} + \frac{V'\angle\delta_0}{Z'_L} \right)^*, \tag{C.58}$$

where superscript * designates conjugate in phasor expression, and

$$Z'_L = \frac{R'_L L'_L C'_L}{L'_L C'_L + jR'_L L'_L - jR'_L C'_L}.$$

A single DG system with constant power controller is considered as a special case scenario of the model defined by (C.56) where $k_{pRS} = k_{iRS} = 0$ and $K_\omega = K_v = -\infty$. The steady-state values in the constant power controller case is similar to (C.57) except that $Q'_{ref\,0} = -Q'_o$. When islanding condition takes place, the new state space equation is similar to (C.56) except that $\Delta i'_{Nd}$ and $\Delta i'_{Nq}$ states are removed.

C.5 Small-signal Model of Multi-DG with *RLC* Load

The model derived in section C.4 can be generalized to a multi-DG system. To simplify the model, the PLL controller gains, used at each DG system, are assumed to be the same (i.e., $k_{pPLL} = k^i_{pPLL}$ and $k_{iPLL} = k^i_{iPLL}$ for $i = 1,2,\cdots,N$). Hence, the total number of state variables in the overall system is reduced to $6N+8$. Accordingly, the small-signal model of the multi-DG system is described as follows:

$$\begin{aligned} p\Delta\omega_p &= k_{pPLL}\, p\Delta v'_q + k_{iPLL}\Delta v'_q \\ p\Delta\delta_p &= \Delta\omega_p \end{aligned} \tag{C.59}$$

$$\Delta\boldsymbol{\theta}_f = \frac{\pi}{2}\mathbf{K}_f \mathbf{1}\Delta\omega_p \tag{C.60}$$

$$\begin{aligned} \Delta\mathbf{i}'^{*}_{dref} &= \mathbf{cos}\boldsymbol{\theta}_{f0}\Delta\mathbf{i}'_{dref} - \mathbf{sin}\boldsymbol{\theta}_{f0}\Delta\mathbf{i}'_{qref} - \mathbf{i}'_{q0}\Delta\boldsymbol{\theta}_f \\ \Delta\mathbf{i}'^{*}_{qref} &= \mathbf{sin}\boldsymbol{\theta}_{f0}\Delta\mathbf{i}'_{dref} + \mathbf{cos}\boldsymbol{\theta}_{f0}\Delta\mathbf{i}'_{qref} + \mathbf{i}'_{d0}\Delta\boldsymbol{\theta}_f \end{aligned} \tag{C.61}$$

$$\begin{aligned} p\Delta\mathbf{i}'_{ud} &= \Delta\mathbf{i}'^{*}_{dref} - \Delta\mathbf{i}'_d \\ p\Delta\mathbf{i}'_{uq} &= \Delta\mathbf{i}'^{*}_{qref} - \Delta\mathbf{i}'_q \end{aligned} \tag{C.62}$$

$$\begin{aligned} p\Delta\mathbf{i}'_d &= \omega_g \mathbf{L}'^{-1}_f\left(\mathbf{k}_{pi}(\Delta\mathbf{i}'^{*}_{dref} - \Delta\mathbf{i}'_d) + \mathbf{k}_{ii}\Delta\mathbf{i}'_{ud}\right) \\ p\Delta\mathbf{i}'_q &= \omega_g \mathbf{L}'^{-1}_f\left(\mathbf{k}_{pi}(\Delta\mathbf{i}'^{*}_{qref} - \Delta\mathbf{i}'_q) + \mathbf{k}_{ii}\Delta\mathbf{i}'_{uq}\right) \end{aligned} \tag{C.63}$$

$$
\begin{aligned}
\Delta V'_{rms} &= V'^{-1}_{rms0} v'_{d0} \Delta v'_d + V'^{-1}_{rms0} v'_{q0} \Delta v'_q \\
\Delta \mathbf{P}' &= \mathbf{i}'_{d0} \mathbf{1} \Delta v'_d + v'_{d0} \Delta \mathbf{i}'_d + \mathbf{i}'_{q0} \mathbf{1} \Delta v'_q + v'_{q0} \Delta \mathbf{i}'_q \\
\Delta \mathbf{Q}' &= \mathbf{i}'_{q0} \mathbf{1} \Delta v'_d + v'_{d0} \Delta \mathbf{i}'_q - \mathbf{i}'_{d0} \mathbf{1} \Delta v'_q - v'_{q0} \Delta \mathbf{i}'_d
\end{aligned}
\tag{C.64}
$$

$$
\begin{aligned}
p\Delta \mathbf{p}'_{id} &= \Delta \mathbf{P}'_{ref} - \Delta \mathbf{P}' \\
p\Delta \mathbf{q}'_{iq} &= \Delta \mathbf{Q}'_{ref} - \Delta \mathbf{Q}'
\end{aligned}
\tag{C.65}
$$

$$
\begin{aligned}
\Delta \mathbf{P}'_{ref} &= \mathbf{K}_\omega^{-1} \mathbf{1} \omega_g^{-1} \Delta \omega_p + \Delta \mathbf{P}'_o - \mathbf{k}_{iRS} \mathbf{1} \omega_g^{-1} \Delta \delta_p - \mathbf{k}_{pRS} \mathbf{1} \omega_g^{-1} \Delta \omega_p \\
\Delta \mathbf{Q}'_{ref} &= -\mathbf{K}_v^{-1} \mathbf{1} \Delta V'_{rms} - \Delta \mathbf{Q}'_o
\end{aligned}
\tag{C.66}
$$

$$
\begin{aligned}
\Delta \mathbf{i}'_{dref} &= \mathbf{k}_{pp} (\Delta \mathbf{P}'_{ref} - \Delta \mathbf{P}') + \mathbf{k}_{ip} \Delta \mathbf{p}'_{id} \\
\Delta \mathbf{i}'_{qref} &= \mathbf{k}_{pp} (\Delta \mathbf{Q}'_{ref} - \Delta \mathbf{Q}') + \mathbf{k}_{ip} \Delta \mathbf{q}'_{iq}
\end{aligned}
\tag{C.67}
$$

$$
\begin{aligned}
p\Delta i'_{Nd} &= -\omega_g L'^{-1}_g R'_g \Delta i'_{Nd} + \omega_{p0} \Delta i'_{Nq} + i'_{Nq0} \Delta \omega_p + \omega_g L'^{-1}_g (\Delta v'_d + E' \sin \delta_0 \Delta \delta_p) \\
p\Delta i'_{Nq} &= -\omega_g L'^{-1}_g R'_g \Delta i'_{Nq} - \omega_{p0} \Delta i'_{Nd} - i'_{Nd0} \Delta \omega_p + \omega_g L'^{-1}_g (\Delta v'_q + E' \cos \delta_0 \Delta \delta_p)
\end{aligned}
\tag{C.68}
$$

$$
\begin{aligned}
p\Delta i'_{Ld} &= \omega_{p0} \Delta i'_{Lq} + i'_{Lq0} \Delta \omega_p + \omega_g L'^{-1}_L \Delta v'_d \\
p\Delta i'_{Lq} &= -\omega_{p0} \Delta i'_{Ld} - i'_{Ld0} \Delta \omega_p + \omega_g L'^{-1}_L \Delta v'_q
\end{aligned}
\tag{C.69}
$$

$$
\begin{aligned}
p\Delta v'_d &= -\omega_g C'_L R'^{-1}_L \Delta v'_d + \omega_{p0} \Delta v'_q + v'_{q0} \Delta \omega_p + \omega_g C'_L (\Delta i'_d - \Delta i'_{Ld} - \Delta i'_{Nd}) \\
p\Delta v'_q &= -\omega_g C'_L R'^{-1}_L \Delta v'_q - \omega_{p0} \Delta v'_d - v'_{d0} \Delta \omega_p + \omega_g C'_L (\Delta i'_q - \Delta i'_{Lq} - \Delta i'_{Nq})
\end{aligned}
\tag{C.70}
$$

where $\mathbf{1} = \begin{bmatrix} 1 & \cdots & 1 \end{bmatrix}^T \in \Re^{N \times 1}$ is the unity vector that consists of N elements of one, and the small-signal variables highlighted in bold are vectors where each vector is composed of N elements. For example, the current controller reference vectors have the following definitions:

$$
\begin{aligned}
\Delta \mathbf{i}'_{dref} &= \begin{bmatrix} \Delta i'^1_{dref} & \Delta i'^2_{dref} & \cdots & \Delta i'^N_{dref} \end{bmatrix}^T, \\
\Delta \mathbf{i}'_{qref} &= \begin{bmatrix} \Delta i'^1_{qref} & \Delta i'^2_{qref} & \cdots & \Delta i'^N_{qref} \end{bmatrix}^T,
\end{aligned}
$$

Additionally, the diagonal matrices $\mathbf{i}'_{d0}$, $\mathbf{i}'_{q0}$, $\mathbf{cos\theta}_{f0}$, $\mathbf{sin\theta}_{f0}$, $\mathbf{k}_{pi}$, $\mathbf{k}_{ii}$, $\mathbf{k}_{pp}$, $\mathbf{k}_{ip}$, $\mathbf{k}_{pRS}$, $\mathbf{k}_{iRS}$, $\mathbf{K}_f$, $\mathbf{K}_\omega$, $\mathbf{K}_v$, and $\mathbf{L}'_f$ have the following definitions: $\mathbf{i}'_{d0} = \text{diag}\{i'^i_{d0}\}$, $\mathbf{i}'_{q0} = \text{diag}\{i'^i_{q0}\}$, $\mathbf{cos\theta}_{f0} = \text{diag}\{\cos \theta^i_{f0}\}$, $\mathbf{sin\theta}_{f0} = \text{diag}\{\sin \theta^i_{f0}\}$, $\mathbf{k}_{pi} = \text{diag}\{k^i_{pi}\}$, $\mathbf{k}_{ii} = \text{diag}\{k^i_{ii}\}$,

$\mathbf{k}_{pp} = \text{diag}\{k_{pp}^i\}$, $\mathbf{k}_{ip} = \text{diag}\{k_{ip}^i\}$, $\mathbf{k}_{pRS} = \text{diag}\{k_{pRS}^i\}$, $\mathbf{k}_{iRS} = \text{diag}\{k_{iRS}^i\}$, $\mathbf{K}_f = \text{diag}\{K_f^i\}$, $\mathbf{K}_\omega = \text{diag}\{K_\omega^i\}$, $\mathbf{K}_v = \text{diag}\{K_v^i\}$, and $\mathbf{L}_f = \text{diag}\{L_f^i\}$ with $i = 1,2,\ldots,N$. After rearrangement and substitution, the multi-DG small-signal model becomes:

$$\begin{cases} p\Delta v_d' = -a_{1,1}\Delta v_d' + \omega_{p0}\Delta v_q' + a_{1,3}\mathbf{1}^T\Delta\mathbf{i}_d' - a_{1,3}\Delta i_{Nd}' - a_{1,3}\Delta i_{Ld}' + v_{q0}'\Delta\omega_p' \\ p\Delta v_q' = -\omega_{p0}\Delta v_d' - a_{1,1}\Delta v_q' + a_{1,3}\mathbf{1}^T\Delta\mathbf{i}_q' - a_{1,3}\Delta i_{Nq}' - a_{1,3}\Delta i_{Lq}' - v_{d0}'\Delta\omega_p' \end{cases} \quad \text{(C.71)}$$

$$\begin{cases} p\Delta\mathbf{i}_d' = -\mathbf{a}_{3,1}\Delta v_d' + \mathbf{a}_{3,2}\Delta v_q' - \mathbf{a}_{3,3}\Delta\mathbf{i}_d' + \mathbf{a}_{3,4}\Delta\mathbf{i}_q' + \mathbf{a}_{3,9}\Delta\mathbf{i}_{ud}' + \mathbf{a}_{3,11}\Delta\mathbf{p}_{id}' - \mathbf{a}_{3,12}\Delta\mathbf{q}_{iq}' \\ \qquad - \mathbf{a}_{3,13}\Delta\delta_p - \mathbf{a}_{3,14}\Delta\omega_p + \mathbf{b}_{3,1}\Delta\mathbf{P}_o' + \mathbf{b}_{3,2}\Delta\mathbf{Q}_o' \\ p\Delta\mathbf{i}_q' = \mathbf{a}_{4,1}\Delta v_d' + \mathbf{a}_{4,2}\Delta v_q' - \mathbf{a}_{3,4}\Delta\mathbf{i}_d' - \mathbf{a}_{3,3}\Delta\mathbf{i}_q' + \mathbf{a}_{3,9}\Delta\mathbf{i}_{uq}' + \mathbf{a}_{3,12}\Delta\mathbf{p}_{id}' + \mathbf{a}_{3,11}\Delta\mathbf{q}_{iq}' \\ \qquad - \mathbf{a}_{4,13}\Delta\delta_p + \mathbf{a}_{4,14}\Delta\omega_p + \mathbf{b}_{3,2}\Delta\mathbf{P}_o' - \mathbf{b}_{3,1}\Delta\mathbf{Q}_o' \end{cases} \quad \text{(C.72)}$$

$$\begin{cases} p\Delta i_{Nd}' = a_{5,1}\Delta v_d' - a_{5,5}\Delta i_{Nd}' + \omega_{p0}\Delta i_{Nq}' + a_{5,13}\Delta\delta_p + i_{Nq0}'\Delta\omega_p \\ p\Delta i_{Nq}' = a_{5,1}\Delta v_q' - \omega_{p0}\Delta i_{Nd}' - a_{5,5}\Delta i_{Nq}' + a_{6,13}\Delta\delta_p - i_{Nd0}'\Delta\omega_p \end{cases} \quad \text{(C.73)}$$

$$\begin{cases} p\Delta i_{Ld}' = a_{7,1}\Delta v_d' + \omega_{p0}\Delta i_{Lq}' + i_{Lq0}'\Delta\omega_p \\ p\Delta i_{Lq}' = a_{7,1}\Delta v_q' - \omega_{p0}\Delta i_{Ld}' - i_{Ld0}'\Delta\omega_p \end{cases} \quad \text{(C.74)}$$

$$\begin{cases} p\Delta\mathbf{i}_{ud}' = -\mathbf{a}_{9,1}\Delta v_d' + \mathbf{a}_{9,2}\Delta v_q' - \mathbf{a}_{9,3}\Delta\mathbf{i}_d' + \mathbf{a}_{9,4}\Delta\mathbf{i}_q' + \mathbf{a}_{9,11}\Delta\mathbf{p}_{id}' - \mathbf{a}_{9,12}\Delta\mathbf{q}_{iq}' \\ \qquad - \mathbf{a}_{9,13}\Delta\delta_p - \mathbf{a}_{9,14}\Delta\omega_p + \mathbf{b}_{9,1}\Delta\mathbf{P}_o' + \mathbf{b}_{9,2}\Delta\mathbf{Q}_o' \\ p\Delta\mathbf{i}_{uq}' = \mathbf{a}_{10,1}\Delta v_d' + \mathbf{a}_{10,2}\Delta v_q' - \mathbf{a}_{9,4}\Delta\mathbf{i}_d' - \mathbf{a}_{9,3}\Delta\mathbf{i}_q' + \mathbf{a}_{9,12}\Delta\mathbf{p}_{id}' + \mathbf{a}_{9,11}\Delta\mathbf{q}_{iq}' \\ \qquad - \mathbf{a}_{10,13}\Delta\delta_p + \mathbf{a}_{10,14}\Delta\omega_p + \mathbf{b}_{9,2}\Delta\mathbf{P}_o' - \mathbf{b}_{9,1}\Delta\mathbf{Q}_o' \end{cases} \quad \text{(C.75)}$$

$$\begin{cases} p\Delta\mathbf{p}_{id}' = -\mathbf{i}_{d0}'\mathbf{1}\Delta v_d' - \mathbf{i}_{q0}'\mathbf{1}\Delta v_q' - v_{d0}'\mathbf{I}\Delta\mathbf{i}_d' - v_{q0}'\mathbf{I}\Delta\mathbf{i}_q' - \mathbf{a}_{11,13}\Delta\delta_p - \mathbf{a}_{11,14}\Delta\omega_p + \Delta\mathbf{P}_o' \\ p\Delta\mathbf{q}_{iq}' = \mathbf{a}_{12,1}\Delta v_d' + \mathbf{a}_{12,2}\Delta v_q' + v_{q0}'\mathbf{I}\Delta\mathbf{i}_d' - v_{d0}'\mathbf{I}\Delta\mathbf{i}_q' - \Delta\mathbf{Q}_o' \end{cases} \quad \text{(C.76)}$$

$$\begin{cases} p\Delta\delta_p = \Delta\omega_p \\ p\Delta\omega_p = -a_{14,1}\Delta v_d' - a_{14,2}\Delta v_q' + a_{14,4}\mathbf{1}^T\Delta\mathbf{i}_q' - a_{14,4}\Delta i_{Nq}' - a_{14,4}\Delta i_{Lq}' - a_{14,14}\Delta\omega_p \end{cases} \quad \text{(C.77)}$$

where

$a_{1,1} = \omega_g C_L' R_L'^{-1}$, $a_{1,3} = \omega_g C_L'$, $\mathbf{a}_{3,1} = \omega_g \mathbf{L}_f'^{-1}\mathbf{k}_{pi}(\cos\boldsymbol{\theta}_{f0}\mathbf{k}_{pp}\mathbf{i}_{d0}'\mathbf{1} - \sin\boldsymbol{\theta}_{f0}\mathbf{k}_{pp}(\mathbf{i}_{q0}' + \mathbf{K}_v^{-1}V_{rms0}'^{-1}v_{d0}')\mathbf{1})$,
$\mathbf{a}_{3,2} = \omega_g \mathbf{L}_f'^{-1}\mathbf{k}_{pi}(-\cos\boldsymbol{\theta}_{f0}\mathbf{k}_{pp}\mathbf{i}_{q0}'\mathbf{1} - \sin\boldsymbol{\theta}_{f0}\mathbf{k}_{pp}(\mathbf{i}_{d0}' - \mathbf{K}_v^{-1}V_{rms0}'^{-1}v_{q0}')\mathbf{1})$,
$\mathbf{a}_{3,3} = \omega_g \mathbf{L}_f'^{-1}\mathbf{k}_{pi}(\cos\boldsymbol{\theta}_{f0}\mathbf{k}_{pp}v_{d0}' + \sin\boldsymbol{\theta}_{f0}\mathbf{k}_{pp}v_{q0}' + \mathbf{I})$, $\mathbf{a}_{3,4} = \omega_g \mathbf{L}_f'^{-1}\mathbf{k}_{pi}(-\cos\boldsymbol{\theta}_{f0}\mathbf{k}_{pp}v_{q0}' + \sin\boldsymbol{\theta}_{f0}\mathbf{k}_{pp}v_{d0}')$,

$$\mathbf{a}_{3,9}=\omega_g\mathbf{L}_f'^{-1}\mathbf{k}_{ii},\ \mathbf{a}_{3,11}=\omega_g\mathbf{L}_f'^{-1}\mathbf{k}_{pi}\mathbf{cos\theta}_{f0}\mathbf{k}_{ip},\ \mathbf{a}_{3,12}=\omega_g\mathbf{L}_f'^{-1}\mathbf{k}_{pi}\mathbf{sin\theta}_{f0}\mathbf{k}_{ip},\ \mathbf{a}_{3,13}=\mathbf{L}_f'^{-1}\mathbf{k}_{pi}\mathbf{cos\theta}_{f0}\mathbf{k}_{pp}\mathbf{k}_{iRS}\mathbf{1},$$

$$\mathbf{a}_{3,14}=\omega_g\mathbf{L}_f'^{-1}\mathbf{k}_{pi}(\frac{\pi}{2}\mathbf{i}'_{q0}\mathbf{K}_f\mathbf{1}+\mathbf{cos\theta}_{f0}\mathbf{k}_{pp}(\mathbf{k}_{pRS}-\mathbf{K}_\omega^{-1})\mathbf{1}\omega_g^{-1}),$$

$$\mathbf{a}_{4,1}=\omega_g\mathbf{L}_f'^{-1}\mathbf{k}_{pi}(-\mathbf{sin\theta}_{f0}\mathbf{k}_{pp}\mathbf{i}'_{d0}\mathbf{1}-\mathbf{cos\theta}_{f0}\mathbf{k}_{pp}(\mathbf{i}'_{q0}+\mathbf{K}_v^{-1}V'^{-1}_{rms0}v'_{d0})\mathbf{1}),$$

$$\mathbf{a}_{4,2}=\omega_g\mathbf{L}_f'^{-1}\mathbf{k}_{pi}(-\mathbf{sin\theta}_{f0}\mathbf{k}_{pp}\mathbf{i}'_{q0}\mathbf{1}+\mathbf{cos\theta}_{f0}\mathbf{k}_{pp}(\mathbf{i}'_{d0}-\mathbf{K}_v^{-1}V'^{-1}_{rms0}v'_{q0})\mathbf{1}),\ \mathbf{a}_{4,13}=\mathbf{L}_f'^{-1}\mathbf{k}_{pi}\mathbf{sin\theta}_{f0}\mathbf{k}_{pp}\mathbf{k}_{iRS}\mathbf{1},$$

$$\mathbf{a}_{4,14}=\omega_g\mathbf{L}_f'^{-1}\mathbf{k}_{pi}(\frac{\pi}{2}\mathbf{i}'_{d0}\mathbf{K}_f\mathbf{1}-\mathbf{sin\theta}_{f0}\mathbf{k}_{pp}(\mathbf{k}_{pRS}-\mathbf{K}_\omega^{-1})\mathbf{1}\omega_g^{-1}),$$

$$a_{5,1}=\omega_g L_g'^{-1},\ a_{5,5}=\omega_g R'_g L_g'^{-1},\ a_{5,13}=\omega_g L_g'^{-1}E'\sin\delta_0,\ a_{6,13}=\omega_g L_g'^{-1}E'\cos\delta_0,\ a_{7,1}=\omega_g L_L'^{-1},$$

$$\mathbf{a}_{9,l}=\omega_g^{-1}\mathbf{k}_{pi}^{-1}\mathbf{L}'_f\mathbf{a}_{3,l},\ \mathbf{a}_{10,m}=\omega_g^{-1}\mathbf{k}_{pi}^{-1}\mathbf{L}'_f\mathbf{a}_{4,m},\ l=1,2,3,4,11,12,13,14,\ m=1,2,13,14,$$

$$\mathbf{a}_{11,13}=\omega_g^{-1}\mathbf{k}_{iRS}\mathbf{1},\ \mathbf{a}_{11,14}=\omega_g^{-1}(\mathbf{k}_{pRS}-\mathbf{K}_\omega^{-1})\mathbf{1},\ \mathbf{a}_{12,1}=-(\mathbf{i}'_{q0}+\mathbf{K}_v^{-1}V'^{-1}_{rms0}v'_{d0})\mathbf{1},\ \mathbf{a}_{12,2}=(\mathbf{i}'_{d0}-\mathbf{K}_v^{-1}V'^{-1}_{rms0}v'_{q0})\mathbf{1},$$

$$a_{14,1}=k_{pPLL}\omega_{p0},\ a_{14,2}=k_{pPLL}\omega_g C'_L R_L'^{-1}-k_{iPLL},\ a_{14,4}=k_{pPLL}\omega_g C'_L,\ a_{14,14}=k_{pPLL}v'_{d0},$$

$$\mathbf{b}_{3,1}=\omega_g\mathbf{L}_f'^{-1}\mathbf{k}_{pi}\mathbf{cos\theta}_{f0}\mathbf{k}_{pp},\ \mathbf{b}_{3,2}=\omega_g\mathbf{L}_f'^{-1}\mathbf{k}_{pi}\mathbf{sin\theta}_{f0}\mathbf{k}_{pp},\ \mathbf{b}_{9,1}=\mathbf{cos\theta}_{f0}\mathbf{k}_{pp},\ \mathbf{b}_{9,2}=\mathbf{sin\theta}_{f0}\mathbf{k}_{pp},$$

And

$\mathbf{I}$ is the $N\times N$ identity matrix, $\mathbf{0}=\begin{bmatrix}0 & \cdots & 0\end{bmatrix}^T\in\Re^{N\times 1}$ is a zero vector that consists of N elements of zeros, and $\mathbf{0}_N=\mathbf{0}\mathbf{0}^T$ is a zero matrix that consists of $N\times N$ elements of zeros.

Then, the complete multi-DG small-signal model can be represented as follows:

$$p\Delta\mathbf{x}=\mathbf{A}\Delta\mathbf{x}+\mathbf{B}\Delta\mathbf{u}, \tag{C.78}$$

where

$$\Delta\mathbf{x}=\begin{bmatrix}\Delta v'_d & \Delta v'_q & \Delta\mathbf{i}'^T_d & \Delta\mathbf{i}'^T_q & \Delta i'_{Nd} & \Delta i'_{Nq} & \Delta i'_{Ld} & \Delta i'_{Lq} & \Delta\mathbf{i}'^T_{ud} & \Delta\mathbf{i}'^T_{uq} & \Delta\mathbf{p}'^T_{id} & \Delta\mathbf{q}'^T_{iq} & \Delta\delta_p & \Delta\omega_p\end{bmatrix}^T,$$

$$\Delta\mathbf{u}=\begin{bmatrix}\Delta\mathbf{P}'^T_o & \Delta\mathbf{Q}'^T_o\end{bmatrix}^T,$$

$$\mathbf{A}=\begin{bmatrix}\mathbf{A}_1 & \mathbf{A}_2\\ \mathbf{A}_3 & \mathbf{A}_4\end{bmatrix}\in\Re^{(6N+8)\times(6N+8)},$$

$$\mathbf{A}_1 = \begin{bmatrix} -a_{1,1} & \omega_{p0} & a_{1,3}\mathbf{1}^T & \mathbf{0}^T & -a_{1,3} & 0 \\ -\omega_{p0} & -a_{1,1} & \mathbf{0}^T & a_{1,3}\mathbf{1}^T & 0 & -a_{1,3} \\ -\mathbf{a}_{3,1} & \mathbf{a}_{3,2} & -\mathbf{a}_{3,3} & \mathbf{a}_{3,4} & \mathbf{0} & \mathbf{0} \\ \mathbf{a}_{4,1} & \mathbf{a}_{4,2} & -\mathbf{a}_{3,4} & -\mathbf{a}_{3,3} & \mathbf{0} & \mathbf{0} \\ a_{5,1} & 0 & \mathbf{0}^T & \mathbf{0}^T & -a_{5,5} & \omega_{p0} \\ 0 & a_{5,1} & \mathbf{0}^T & \mathbf{0}^T & -\omega_{p0} & -a_{5,5} \end{bmatrix} \in \Re^{(2N+4)\times(2N+4)},$$

$$\mathbf{A}_2 = \begin{bmatrix} -a_{1,3} & 0 & \mathbf{0}^T & \mathbf{0}^T & \mathbf{0}^T & \mathbf{0}^T & 0 & v'_{q0} \\ 0 & -a_{1,3} & \mathbf{0}^T & \mathbf{0}^T & \mathbf{0}^T & \mathbf{0}^T & 0 & -v'_{d0} \\ \mathbf{0} & \mathbf{0} & \mathbf{a}_{3,9} & \mathbf{0}_N & \mathbf{a}_{3,11} & -\mathbf{a}_{3,12} & -\mathbf{a}_{3,13} & -\mathbf{a}_{3,14} \\ \mathbf{0} & \mathbf{0} & \mathbf{0}_N & \mathbf{a}_{3,9} & \mathbf{a}_{3,12} & \mathbf{a}_{3,11} & -\mathbf{a}_{4,13} & \mathbf{a}_{4,14} \\ 0 & 0 & \mathbf{0}^T & \mathbf{0}^T & \mathbf{0}^T & \mathbf{0}^T & a_{5,13} & i'_{Nq0} \\ 0 & 0 & \mathbf{0}^T & \mathbf{0}^T & \mathbf{0}^T & \mathbf{0}^T & a_{6,13} & -i'_{Nd0} \end{bmatrix} \in \Re^{(2N+4)\times(4N+4)},$$

$$\mathbf{A}_3 = \begin{bmatrix} a_{7,1} & 0 & \mathbf{0}^T & \mathbf{0}^T & 0 & 0 \\ 0 & a_{7,1} & \mathbf{0}^T & \mathbf{0}^T & 0 & 0 \\ -\mathbf{a}_{9,1} & \mathbf{a}_{9,2} & -\mathbf{a}_{9,3} & \mathbf{a}_{9,4} & \mathbf{0} & \mathbf{0} \\ \mathbf{a}_{10,1} & \mathbf{a}_{10,2} & -\mathbf{a}_{9,4} & -\mathbf{a}_{9,3} & \mathbf{0} & \mathbf{0} \\ -\mathbf{i}'_{d0}\mathbf{1} & -\mathbf{i}'_{q0}\mathbf{1} & -v'_{d0}\mathbf{I} & -v'_{q0}\mathbf{I} & \mathbf{0} & \mathbf{0} \\ \mathbf{a}_{12,1} & \mathbf{a}_{12,2} & v'_{q0}\mathbf{I} & -v'_{d0}\mathbf{I} & \mathbf{0} & \mathbf{0} \\ 0 & 0 & \mathbf{0}^T & \mathbf{0}^T & 0 & 0 \\ -a_{14,1} & -a_{14,2} & \mathbf{0}^T & a_{14,4}\mathbf{1}^T & 0 & -a_{14,4} \end{bmatrix} \in \Re^{(4N+4)\times(2N+4)},$$

$$\mathbf{A}_4 = \begin{bmatrix} 0 & \omega_{p0} & \mathbf{0}^T & \mathbf{0}^T & \mathbf{0}^T & \mathbf{0}^T & 0 & i'_{Lq0} \\ -\omega_{p0} & 0 & \mathbf{0}^T & \mathbf{0}^T & \mathbf{0}^T & \mathbf{0}^T & 0 & -i'_{Ld0} \\ \mathbf{0} & \mathbf{0} & \mathbf{0}_N & \mathbf{0}_N & \mathbf{a}_{9,11} & -\mathbf{a}_{9,12} & -\mathbf{a}_{9,13} & -\mathbf{a}_{9,14} \\ \mathbf{0} & \mathbf{0} & \mathbf{0}_N & \mathbf{0}_N & \mathbf{a}_{9,12} & \mathbf{a}_{9,11} & -\mathbf{a}_{10,13} & \mathbf{a}_{10,14} \\ \mathbf{0} & \mathbf{0} & \mathbf{0}_N & \mathbf{0}_N & \mathbf{0}_N & \mathbf{0}_N & -\mathbf{a}_{11,13} & -\mathbf{a}_{11,14} \\ \mathbf{0} & \mathbf{0} & \mathbf{0}_N & \mathbf{0}_N & \mathbf{0}_N & \mathbf{0}_N & \mathbf{0} & \mathbf{0} \\ 0 & 0 & \mathbf{0}^T & \mathbf{0}^T & \mathbf{0}^T & \mathbf{0}^T & 0 & 1 \\ 0 & -a_{14,4} & \mathbf{0}^T & \mathbf{0}^T & \mathbf{0}^T & \mathbf{0}^T & 0 & -a_{14,14} \end{bmatrix} \in \Re^{(4N+4)\times(4N+4)},$$

$$\mathbf{B} = \begin{bmatrix} \mathbf{0} & \mathbf{0} & \mathbf{b}_{3,1} & \mathbf{b}_{3,2} & \mathbf{0} & \mathbf{0} & \mathbf{0} & \mathbf{0} & \mathbf{b}_{9,1} & \mathbf{b}_{9,2} & \mathbf{I} & \mathbf{0}_N & \mathbf{0} & \mathbf{0} \\ \mathbf{0} & \mathbf{0} & \mathbf{b}_{3,2} & -\mathbf{b}_{3,1} & \mathbf{0} & \mathbf{0} & \mathbf{0} & \mathbf{0} & \mathbf{b}_{9,2} & -\mathbf{b}_{9,1} & \mathbf{0}_N & -\mathbf{I} & \mathbf{0} & \mathbf{0} \end{bmatrix}^T \in \Re^{(6N+8)\times(2N)}.$$

C.6 Validation of Single and Multi-DGs Models

The average model for single and multi-DG system are set up in MATLAB/Simulink. Results from the small-signal models are compared with the average Simulink model to verify their accuracy. Table C-1 shows the parameters used for the single DG model. The parameters provided in Table C-1 corresponds to P_L = 10 kW, Q_f = 2.5, f_o = 60 Hz, Z_g = 0.2 Ω, and X_g / R_g = 1.5.

Table C-1
Simulation Parameters for Single-DG Small-Signal Model

Parameters	*Value*	*Parameters*	*Value*
E	170 V	k_{pi}	0.5
V_{base}	170 V	k_{ii}	50
S_{base}	10 kVA	k_{pp}	0.5
f_g	60 Hz	k_{ip}	50
R_g	0.1109 Ω	k_{pRS}	0.5
L_g	0.4414 mH	k_{iRS}	5
L_f	1 mH	k_{pPLL}	50
R_L	4.32 Ω	k_{iPLL}	500
L_L	4.5837 mH	$V'_{\min}$	0.88 pu
C_L	1.5351 mF	$V'_{\max}$	1.1 pu
cf_o	0	V'_{ref}	1 pu
K_f	0	$P'_{\max}$	1.2 pu
$f_{\min}$	59.3 Hz	$Q'_{\max}$	0.2 pu

For a single DG system, the initial active power P'_o is changed from 1 pu to $1+0.5\cos(200\pi t+10^o)$ at t = 0.15s. The same input is applied to the single DG system after islanding as well. Variations on ω_p and v_d responses are shown in Figure C-7 for both the

small-signal model and the Simulink average model before and after islanding. It can be seen from Figure C-7 that the small-signal model provides a good estimation for the single DG system under study.

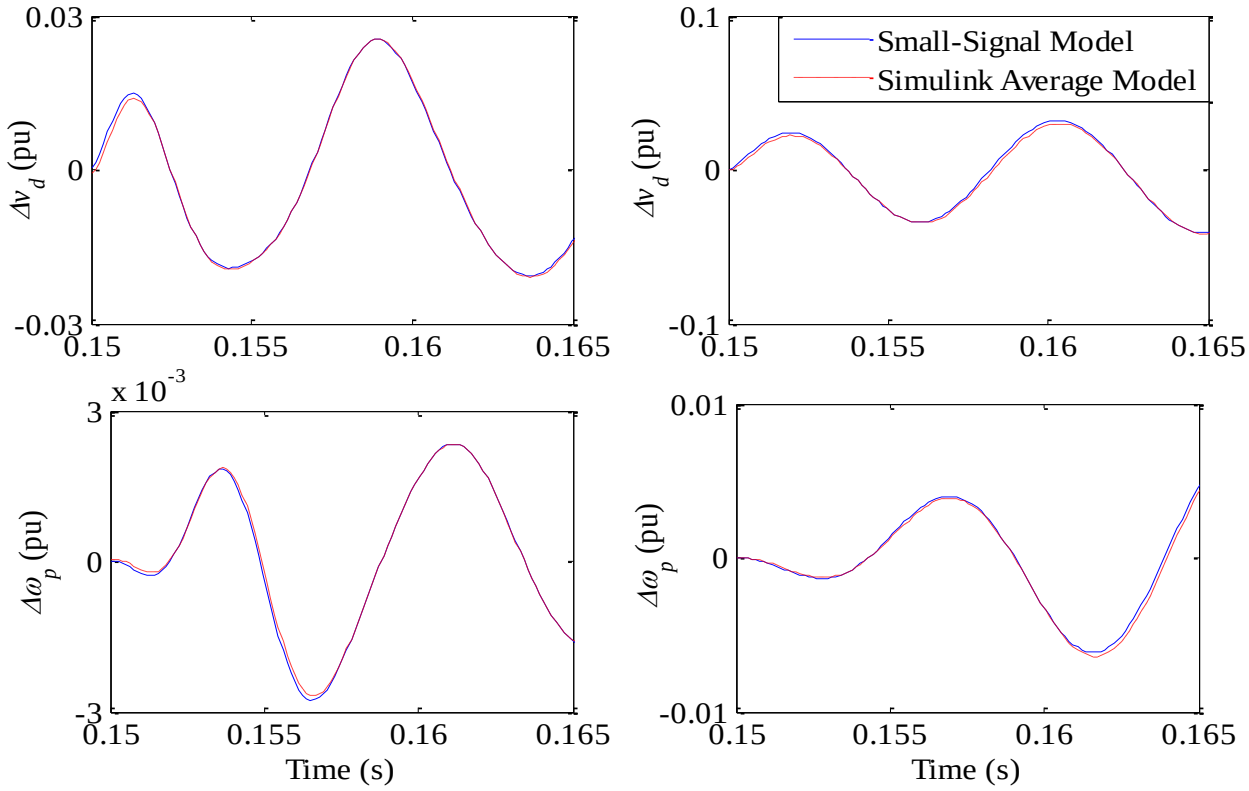

Figure C-7: Validation of a single DG small-signal model. (left: before islanding, right: after islanding).

In order to validate the multi-DG small-signal model presented in section C.5, a two-DG system is considered. Table C-2 shows the parameters used for the two-DG model.

Table C-2
Simulation Parameters for a Multi-DG Small-Signal Model

Parameters	*Value*	*Parameters*	*Value*
E	170 V	k_{pPLL}	50
V_{base}	170 V	k_{iPLL}	500
S_{base}	10 kVA	k_{pi}^{i}	0.5
f_g	60 Hz	k_{ii}^{i}	50
R_g	0.1109 Ω	k_{pp}^{1}, k_{pp}^{2}	0.5, 2
L_g	0.4414 mH	k_{ip}^{i}	50
R_L	4.32 Ω	k_{pRS}^{i}	0.5
L_L	4.5837 mH	k_{iRS}^{i}	5
C_L	1.5351 mF	$V_{\min}^{\prime i}$	0.88 pu
L_f^i	1 mH	$V_{\max}^{\prime i}$	1.1 pu
cf_o^i	0	$V_{ref}^{\prime i}$	1 pu
K_f^i	0	$P_{\max}^{\prime 1}$, $P_{\max}^{\prime 2}$	0.6, 0.7 pu
$f_{\min}^{i}$ ($i=1,2$)	59.3 Hz	$Q_{\max}^{\prime 1}$, $Q_{\max}^{\prime 2}$ ($i=1,2$)	0.1, 0.2 pu

The initial active power for DG1 ($P_o^{\prime 1}$) is changed from 0.5 pu to $0.5+0.5\cos(200\pi t+10^o)$ at t = 0.15s. On the other hand, the initial active power for DG2 ($P_o^{\prime 2}$) is changed from 0.5 pu to $0.5+0.7\cos(240\pi t+20^o)$ at t = 0.15s. Similarly, the same procedure is applied to the two-DG system after islanding. Variations on ω_p and v_d responses for the two-DG system are shown in Figure C-8. It can be seen from Figure C-8 that the derived multi-DG small-signal model provides a good estimation for the two DG system under study. Hence, the small-signal model for the two-DG system is validated and this result can be generalized to the general *N*-DG system.

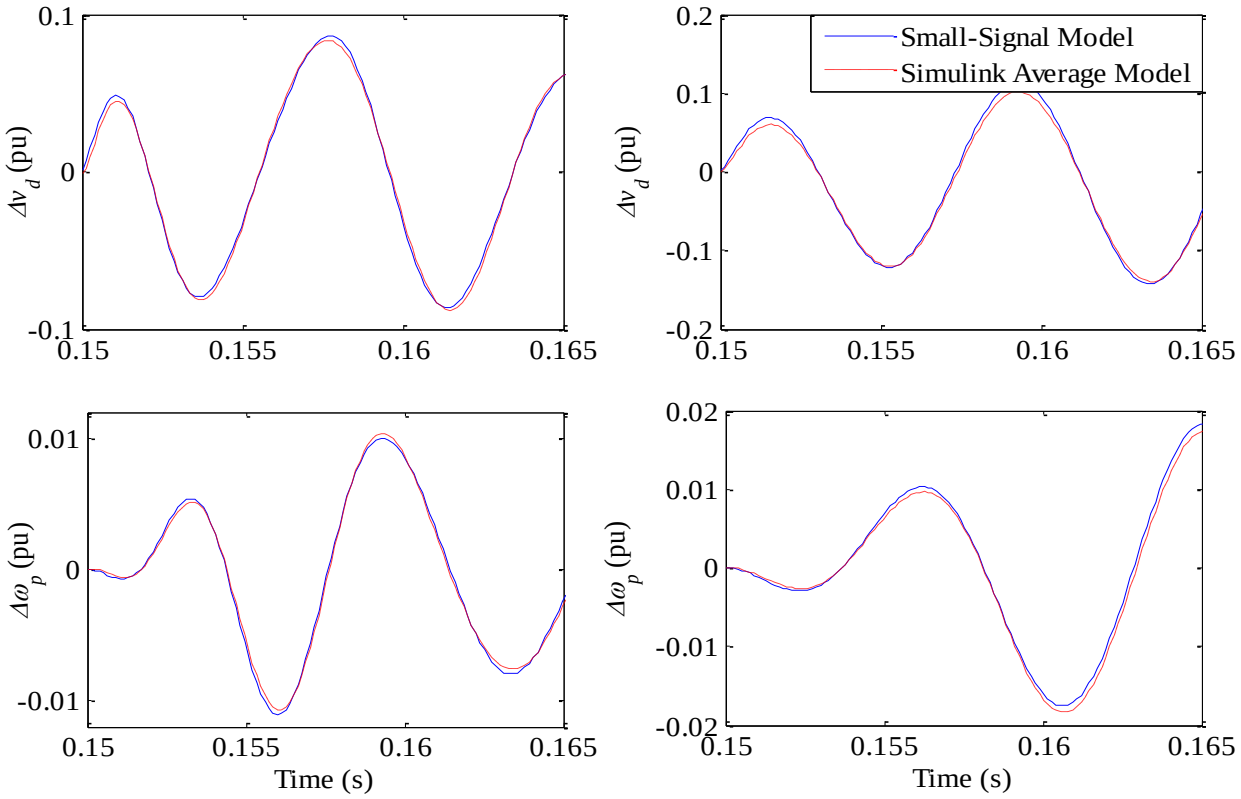

Figure C-8: Validation of a two-DG small-signal model. (left: before islanding, right: after islanding).

PUBLICATIONS RESULTING FROM THIS WORK

1. M. Al Hosani, Z. Qu, and H. Zeineldin, "Development of Current Dynamic Estimator for Islanding Detection of Inverter Based Distributed Generation," *2010 International Conference on Power System Technology (POWERCON)*, pp. 1-8, 24-28 October 2010.

2. M. Al Hosani, and Z. Qu, "Robust Non-Linear Observer for Islanding Detection of Inverter Based Distributed Generation," *Proceedings of the 2012 Australian Control Conference*, pp. 41-47, 15-16 November 2012.

3. M. Al Hosani, Z. Qu, and H. Zeineldin, "Development of Dynamic Estimators for Islanding Detection of Inverter Based Distributed Generation," *IEEE Transactions on Power Delivery*, submitted on February 22, 2012; revised on December 27, 2012, June 19, 2013, and on September 23, 2013.

4. M. Al Hosani, Z. Qu, and H. Zeineldin, "Scheduled Perturbation to Reduce Non-Detection Zone for Low Gain Sandia Frequency Shift Method," *IET Generation, Transmission and Distribution*, submitted on May 04, 2013.

5. M. Al Hosani, and Z. Qu, "Robust Non-Linear Observer for Islanding Detection of Inverter Based Distributed Generation," *IEEE Transactions on Instrumentation and Measurement*, to be submitted.

6. M. Al Hosani, and Z. Qu, "Transient Stiffness-Measure for Islanding Detection of Multi-DG Systems," *IEEE Transactions on Power Delivery*, to be submitted.

LIST OF REFERENCES

[1] U.S. Department of Energy (2012) [online]. Available: http://energy.gov/oe/technology-development/smart-grid.

[2] M. Thiele (2011) Smart Grid & The Cloud: Why are they linked [online] Available: http://www.infowars.com/smart-grid-the-cloud-why-are-they-linked.

[3] *IEEE Recommended Practice for Utility Interface of Photovoltaic (PV) Systems*, IEEE Standard 929–2000, April 2000.

[4] *Inverters, Converters, and Controllers for Use in Independent Power Systems*, UL Std. 1741, 2002.

[5] *IEEE Standard for Interconnecting Distributed Resources With Electric Power Systems*, IEEE Std. 1547-2003, July 2003.

[6] *IEEE Application Guide for IEEE Std. 1547, IEEE Standard for Interconnecting Distributed Resources With Electric Power Systems*, IEEE Std. 1547.2-2008, April 2009.

[7] Testing Procedure of Islanding Prevention Measures for Utility Interactive Photovoltaic Inverters, IEC 62116, 2008.

[8] B. Verhoeven *et al.* (1998) Utility Aspects of Grid Connected Photovoltaic Power Systems. International Energy Agency Photovoltaic Power Systems, IEA PVPS T5-01: 1998. [Online]. Available: www.iea-pvps.org.

[9] M. E. Ropp, "Design Issues for Grid-Connected Photovoltaic Systems," Ph.D. dissertation, Georgia Institute of Technology, Atlanta, GA, 1998.

[10] C. Whitaker, J. Newmiller, M. Ropp and B. Norris, "Distributed Photovoltaic Systems Design and Technology Requirements", Sandia National Laboratories report SAND2008-0946 P, February 2008.

[11] W. Xu, K. Mauch and S. Martel, "An Assessment of Distributed Generation Islanding Detection Methods and Issues for Canada," Natural Resources Canada CANMET Energy Technology Centre Report 2004-074 (TR) 411-INVERT, July 2004.

[12] M. E. Ropp, M. Begovic, and A. Rohatgi, "Prevention of islanding in grid-connected photovoltaic systems," Progress in Photovoltaics: Research and Applications, vol. 7, pp. 39–59, 1999.

[13] Z. Ye, R. Walling, L. Garces, R. Zhou, L. Li, and T. Wang, "Study and development of anti-islanding control for grid-connected inverters," Nat. Renewable Energy Lab., Golden, CO, Tech. Rep. NREL/SR-560-36243, May 2004.

[14] M. Ropp, “Suggested Guidelines for Assessment of DG Unintentional Islanding Risk,” Sandia National Laboratories, Nat. Renewable Energy Lab., Albuquerque, New Mexico, Rep. SAND2012-1365, Feb. 2012.

[15] W. Bower and M. Ropp, “Evaluation of Islanding Detection Methods for Photovoltaic Utility-Interactive Power Systems,” Rep. IEA-PVPS T5-09:2002, March 2002.

[16] Beltran H., Gimeno F., Seguí-Chilet S. and Torrelo J. M. (2006). Review of the Islanding Phenomenon Problem for Connection of Renewable Energy Systems [online]. Available: www.icrepq.com/icrepq06/201-BELTRAN.pdf

[17] B. Yu, M. Matsui and G. Yu, “A review of current anti-islanding methods for photovoltaic power system,” *Solar Energy*, Vol. 84, No.5, pp. 745-754, May 2010.

[18] A. Massoud, K. Ahmed, S. Finney, and B. Williams, "Harmonic distortion-based island detection technique for inverter-based distributed generation," *IET Renewable Power Generation*, vol.3, no.4, pp.493-507, Dec. 2009.

[19] G. Petrone, G. Spagnuolo, R. Teodorescu, M. Veerachary, and M. Vitelli, "Reliability Issues in Photovoltaic Power Processing Systems," *IEEE Transactions on Industrial Electronics*, vol.55, no.7, pp.2569-2580, July 2008.

[20] F. De Mango, M. Liserre, and A. D. Aquila, “Overview of anti-islanding algorithms for PV systems Part I: Passive methods,” in *Proc. 12th Int. Power Electron. Motion Control Conf.*, pp. 1878–1883, Sep. 2006.

[21] S. Samantaray, A. Samui, and B. Babu, "Time-frequency transform-based islanding detection in distributed generation," *IET Renewable Power Generation*, vol.5, no.6, pp.431-438, Nov. 2011.

[22] M. Liserre, A. Pigazo, A. Aquila, and V. Moreno, "An Anti-Islanding Method for Single-Phase Inverters Based on a Grid Voltage Sensorless Control," *IEEE Transactions on Industrial Electronics*, vol.53, no.5, pp.1418-1426, Oct. 2006.

[23] F. De Mango, M. Liserre, and A. D. Aquila, “Overview of anti-islanding algorithms for PV systems Part II: Active methods,” in *Proc. 12th Int. Power Electron. Motion Control Conf.*, pp. 1884–1889, Sep. 2006.

[24] F. Liu, Y. Kang, Y. Zhang, S. Duan, and X. Lin, "Improved SMS islanding detection method for grid-connected converters," *IET Renewable Power Generation*, vol.4, no.1, pp.36-42, Jan. 2010.

[25] H. Zeineldin, E. El-Saadany, and M. Salama, “Islanding detection of inverter-based distributed generation,” *IEE Proceedings-Generation, Transmission and Distribution*, vol. 153, no.6, pp. 644-652, Nov. 2006.

[26] H. Karimi, A. Yazdani, and R. Iravani, “Negative sequence current injection for fast islanding detection of a distributed resource unit,” *IEEE Transactions on Power Electronics*, vol. 23, no. 1, pp. 298-307, Jan. 2008.

[27] G. Gonzalez and R. Iravani, “Current injection for active islanding detection of electronically-interfaced distributed resources,” *IEEE Transactions on Power Delivery*, vol. 21, no. 3, pp. 1698-1705, Jul. 2006.

[28] M. Ropp, M. Begovic and A. Rohatgi, "Analysis and performance assessment of the active frequency drift method of islanding prevention," *IEEE Transactions on Energy Conversion*, vol.14, no.3, pp.810-816, Sep 1999.

[29] M. Ropp, M. Begovic, A. Rohatgi, G. A. Kern, R. H. Bonn, and S. Gonzalez, “Determining the relative effectiveness of islanding detection methods using phase criteria and nondetection zones,” *IEEE Trans. on Energy Conversion*, vol. 15, no. 3, pp. 290–296, Sep. 2000.

[30] L. Lopes and H. Sun, “Performance assessment of active frequency drifting islanding detection methods,” *IEEE Trans. on Energy Conv.*, vol. 21, no. 1, pp. 171-180, March 2006.

[31] Y. Zhang and L.A.C. Lopes, "Design and Compliance of Frequency Drifting Islanding Detection Methods with the IEEE Standard 1547.1," *Canadian Conference on Electrical and Computer Engineering, CCECE 2007*, vol., no., pp.1574-1577, 22-26 April 2007.

[32] J. Vieira, W. Freitas, W. Xu and A. Morelato, "An Investigation on the Nondetection Zones of Synchronous Distributed Generation Anti-Islanding Protection," *IEEE Transactions on Power Delivery*, vol.23, no.2, pp.593-600, April 2008.

[33] B. Bahrani, H. Karimi, and R. Iravani, "Nondetection Zone Assessment of an Active Islanding Detection Method and its Experimental Evaluation," *IEEE Transactions on Power Delivery*, vol.26, no.2, pp.517-525, April 2011.

[34] H. Zeineldin, and J. Kirtley, “Performance of the OVP/UVP and OFP/UFP method with voltage and frequency dependent loads,” *IEEE Transactions on Power Delivery*, vol. 24, no. 2, pp. 772-778, Apr. 2009.

[35] H. Zeineldin, and M. Salama, "Impact of load frequency dependence on the NDZ and performance of the SFS islanding detection method," *IEEE Transactions on Industrial Electronics*, vol.58, no.1, pp.139-146, Jan. 2011.

[36] H. Wang, F. Liu, Y. Kang, J. Chen, and X. Wei, "Experimental Investigation on Non Detection Zones of Active Frequency Drift Method for Anti-islanding," *33rd Annual Conference of the IEEE Industrial Electronics Society*, pp.1708-1713, 5-8 Nov. 2007.

[37] Z. Ye, A. Kolwalkar, Y. Zhang, P. Du, and R.Walling, “Evaluation of anti-islanding schemes based on nondetection zone concept,” *IEEE Trans. on Power Electron.*, vol. 19, no. 5, pp. 1171–1176, Sep. 2004.

[38] X. Wang, W. Freitas and W. Xu, "Dynamic Non-Detection Zones of Positive Feedback Anti-Islanding Methods for Inverter-Based Distributed Generators," *IEEE Transactions on Power Delivery*, vol.26, no.2, pp.1145-1155, April 2011.

[39] H. Zeineldin, E. El-Saadany and M. Salama, "Impact of DG interface control on islanding detection and nondetection zones," *IEEE Transactions on Power Delivery*, vol.21, no.3, pp.1515-1523, July 2006.

[40] X. Wang, W. Freitas, W. Xu and V. Dinavahi, "Impact of DG Interface Controls on the Sandia Frequency Shift Anti-islanding Method," *IEEE Transactions on Energy Conversion*, vol.22, no.3, pp.792-794, Sept. 2007.

[41] V. Menon, and M. Nehrir, "A hybrid islanding detection technique using voltage unbalance and frequency set point," *IEEE Transactions on Power Systems*, vol. 22, no. 1, pp. 442-448, Feb. 2007.

[42] P. Mahat, Z. Chen, and B. Jensen, "A hybrid islanding detection technique using average rate of voltage change and real power shift," *IEEE Transactions on Power Delivery*, vol. 24, no. 2, pp. 764-771, Apr. 2009.

[43] A. Pigazo, M. Liserre, R. Mastromauro, V. Moreno, and A. Aquila, "Wavelet-based islanding detection in grid-connected PV systems," *IEEE Transactions on Industrial Electronics*, vol. 59, no. 11, pp. 4445-4455, Nov. 2009.

[44] K. M. Vu (2007). *Optimal discrete control theory: the rational function structure model.* [online]. Available: http://www.aulactechnologies.com.

[45] H. Zeineldin and S. Kennedy, "Sandia Frequency-Shift Parameter Selection to Eliminate Nondetection Zones," *IEEE Transactions on Power Delivery*, vol.24, no.1, pp.486-487, Jan. 2009.

[46] H. Xin, Z. Qu, J. Seuss, and A. Maknouninejad, "A Self-Organizing Strategy for Power Flow Control of Photovoltaic Generators in a Distribution Network," *IEEE Transactions on Power Systems*, vol.26, no.3, pp.1462-1473, Aug. 2011.

[47] Kersting W.H., "Radial distribution test feeders," *IEEE Power Engineering Society Winter Meeting, 2001*, vol.2, no., pp.908-912 vol.2, 2001.

[48] V. Moreno, M. Liserre, A. Pigazo, and A. Dell'Aquila, "A comparative analysis of real-time algorithms for power signal decomposition in multiple synchronous reference frames," *IEEE Transactions on Power Electronics*, vol. 22, no. 4, pp. 1280–1289, July 2007.

[49] P. Stoica, Li Hongbin and Li Jian, "Amplitude estimation of sinusoidal signals: survey, new results, and an application," *IEEE Trans. Sign. Proces.*, vol.48, no.2, pp.338-352, Feb. 2000.

[50] A. Routray, A. Pradhan, and K. Rao, "A novel Kalman filter for frequency estimation of distorted signals in power systems," *IEEE Trans. Instrum. & Meas.*, vol.51, no.3, pp.469-479, Jun. 2002.

[51] X. Chen, "Identification of a sinusoidal signal," *SICE 2004 Annual Conf.*, vol.1, pp. 89-92, 4-6 Aug. 2004.

[52] L. Hsu, R. Ortega, and G. Damm, "A globally convergent frequency estimator," *IEEE Trans. Autom. Contr.*, vol.44, no.4, pp.698-713, Apr. 1999.

[53] M. Mojiri, and A. Bakhshai, "An adaptive notch filter for frequency estimation of a periodic signal," *IEEE Trans. Autom. Contr.*, vol.49, no.2, pp. 314- 318, Feb. 2004.

[54] M. Mojiri, M. Karimi-Ghartemani, and A. Bakhshai, "Estimation of Power System Frequency Using an Adaptive Notch Filter," *IEEE Trans. Instrum. & Meas.*, vol.56, no.6, pp.2470-2477, Dec. 2007.

[55] X. Xia, "Global frequency estimation using adaptive identifiers," *IEEE Trans. Autom. Contr.*, vol. 47, no. 7, pp. 1188–1193, Jul. 2002.

[56] G. Obregon-Pulido, B. Castillo-Toledo, and A. Loukianov, "A globally convergent estimator for n-frequencies," *IEEE Trans. Autom. Contr.*, vol. 47, no. 5, pp. 857–863, May 2002.

[57] R. Marino and P. Tomei, "Global estimation of n unknown frequencies," *IEEE Trans. Autom. Contr.*, vol. 47, no. 8, pp. 1324–1328, Aug. 2002.

[58] S. Sastry and M. Bodson, *Adaptive Control-Stability, Convergence and Robustness.* Upper Saddle River, NJ: Printice-Hall, 1989.

[59] M. Hou, "Amplitude and frequency estimator of a sinusoid," *IEEE Trans. Autom. Contr.*, vol.50, no.6, pp. 855- 858, June 2005.

[60] M. Hou, "Estimation of sinusoidal frequencies and amplitudes using adaptive identifier and observer," *IEEE Trans. Autom. Contr.*, vol. 52, no. 3, pp. 493–499, Mar. 2007.

[61] K. S. Narendra and A. M. Annaswamy, *Stable Adaptive Systems*, Dover Publications, Inc., 1989.

[62] Z. Qu, "Cooperative control of networked nonlinear systems," *the 49th IEEE Conf. on Decis. and Contr. (CDC)*, pp.3200-3207, 15-17 Dec. 2010.

[63] X. Wang and W. Freitas, "Impact of Positive-Feedback Anti-Islanding Methods on Small-Signal Stability of Inverter-Based Distributed Generation," *IEEE Transactions on Energy Conversion*, vol.23, no.3, pp.923-931, Sept. 2008.

[64] L. Lopes and Y. Zhang, "Islanding Detection Assessment of Multi-Inverter Systems with Active Frequency Drifting Methods," *IEEE Transactions on Power Delivery*, vol.23, no.1, pp.480-486, Jan. 2008.

[65] H. Zeineldin and S. Conti, "Sandia frequency shift parameter selection for multi-inverter systems to eliminate non-detection zone," *Renewable Power Generation, IET* , vol.5, no.2, pp.175-183, March 2011.

[66] X. Wang, W. Freitas, V. Dinavahi and W. Xu, "Investigation of Positive Feedback Anti-Islanding Control for Multiple Inverter-Based Distributed Generators," *IEEE Transactions on Power Systems*, vol.24, no.2, pp.785-795, May 2009.

[67] E. Estebanez, V. Moreno, A. Pigazo, M. Liserre and A. Aquila, "Performance Evaluation of Active Islanding-Detection Algorithms in Distributed-Generation Photovoltaic Systems: Two Inverters Case," *IEEE Transactions on Industrial Electronics*, vol.58, no.4, pp.1185-1193, April 2011.

[68] R. Bhandari, S. González, and M. Ropp, "Investigation of two anti-islanding methods in the multi-inverter case," *IEEE Power and Energy Society General Meeting - Conversion and Delivery of Electrical Energy in the 21st Century*, pp. 1–7, July 2008.

[69] M. Xue, F. Liu, Y. Kang, and Y. Zhang, "Investigation of active islanding detection methods in multiple grid-connected converters," *IEEE 6th International Power Electronics and Motion Control Conference*, pp. 2151–2154, May 2009.

[70] F. Liu, Y. Zhang, M. Xue, X. Lin, and Y. Kang, "Investigation and evaluation of active frequency drifting methods in multiple grid-connected inverters," *IET Power Electronics*, vol.5, no.4, pp.485-492, Apr. 2012.

[71] F. Katiraei, and M. Iravani, "Power Management Strategies for a Microgrid With Multiple Distributed Generation Units," *IEEE Transactions on Power Systems*, vol.21, no.4, pp.1821-1831, Nov. 2006.

[72] F. Katiraei, M. Iravani, and P. Lehn, "Small-signal dynamic model of a micro-grid including conventional and electronically interfaced distributed resources," *IET Generation, Transmission & Distribution*, vol.1, no.3, pp.369-378, May 2007.

[73] F. Gao, and M. Iravani, "A Control Strategy for a Distributed Generation Unit in Grid-Connected and Autonomous Modes of Operation," *IEEE Transactions on Power Delivery*, vol.23, no.2, pp.850-859, April 2008.

[74] F. Katiraei, "Dynamic analysis and control of distributed energy resources in a micro-grid," Ph.D. dissertation, University of Toronto, Toronto, ON, 2005.

[75] X. Wang, "Investigation of positive feedback anti-islanding scheme for inverter-based distributed generation," Ph.D. dissertation, University of Alberta, Edmonton, AB, 2008.

[76] H. Zeineldin, E. El-Saadany, and M. Salama, "Distributed Generation Micro-Grid Operation: Control and Protection," *Power Systems Conference: Advanced Metering, Protection, Control, Communication, and Distributed Resources*, pp.105-111, 14-17 March 2006.

[77] H. Zeineldin, E. El-Saadany, and M. Salama, "Intentional islanding of distributed generation," *IEEE Power Engineering Society General Meeting*, pp.1496-1502 Vol. 2, 12-16 June 2005.

[78] I. Balaguer, Q. Lei, S. Yang, U. Supatti, and F. Peng, "Control for Grid-Connected and Intentional Islanding Operations of Distributed Power Generation," *IEEE Transactions on Industrial Electronics*, vol.58, no.1, pp.147-157, Jan. 2011.

[79] Y. Mohamed, and E. El-Saadany, "Adaptive Decentralized Droop Controller to Preserve Power Sharing Stability of Paralleled Inverters in Distributed Generation Microgrids," *IEEE Transactions on Power Electronics*, vol.23, no.6, pp.2806-2816, Nov. 2008.

[80] Y. Li, and C. Kao, "An Accurate Power Control Strategy for Power-Electronics-Interfaced Distributed Generation Units Operating in a Low-Voltage Multibus Microgrid," *IEEE Transactions on Power Electronics*, vol.24, no.12, pp.2977-2988, Dec. 2009.

[81] J. Guerrero, L. Vicuna, J. Matas, M. Castilla, and J. Miret, "A wireless controller to enhance dynamic performance of parallel inverters in distributed generation systems," *IEEE Transactions on Power Electronics*, vol.19, no.5, pp.1205-1213, Sept. 2004.

[82] J. Guerrero, J. Matas, L. Vicuna, M. Castilla, and J. Miret, "Decentralized Control for Parallel Operation of Distributed Generation Inverters Using Resistive Output Impedance," *IEEE Transactions on Industrial Electronics*, vol.54, no.2, pp.994-1004, April 2007.

[83] J. Guerrero, J. Vasquez, J. Matas, M. Castilla, and L. Vicuna, "Control Strategy for Flexible Microgrid Based on Parallel Line-Interactive UPS Systems," *IEEE Transactions on Industrial Electronics*, vol.56, no.3, pp.726-736, March 2009.

[84] M. Marwali, and A. Keyhani, "Control of distributed generation systems-Part I: Voltages and currents control," *IEEE Transactions on Power Electronics*, vol.19, no.6, pp.1541-1550, Nov. 2004.

[85] M. Marwali, J. Jung, and A. Keyhani, "Control of distributed generation systems - Part II: Load sharing control," *IEEE Transactions on Power Electronics*, vol.19, no.6, pp.1551-1561, Nov. 2004.

[86] F. Blaabjerg, R. Teodorescu, M. Liserre, and A. Timbus, "Overview of Control and Grid Synchronization for Distributed Power Generation Systems," *IEEE Transactions on Industrial Electronics*, vol.53, no.5, pp.1398-1409, Oct. 2006.

[87] A. Timbus, M. Liserre, R. Teodorescu, P. Rodriguez, and F. Blaabjerg, "Evaluation of Current Controllers for Distributed Power Generation Systems," *IEEE Transactions on Power Electronics*, vol.24, no.3, pp.654-664, March 2009.

[88] M. Chandorkar, D. Divan, and R. Adapa, "Control of parallel connected inverters in standalone AC supply systems," *IEEE Transactions on Industry Applications*, vol.29, no.1, pp.136-143, Jan/Feb 1993.

[89] J. Guerrero, L. Vicuna, J. Matas, M. Castilla, and J. Miret, "Output Impedance Design of Parallel-Connected UPS Inverters With Wireless Load-Sharing Control," *IEEE Transactions on Industrial Electronics*, vol.52, no.4, pp.1126-1135, Aug. 2005.

[90] R. Qi, F. Coakley, and B. Evans, "Practical consideration for bandpass sampling," *Electronics Letters*, vol.32, no.20, pp.1861-1862, Sep. 1996.

[91] Z. Qu, *Robust Control of Nonlinear Uncertain Systems*, New York: Wiley Interscience, 1998.

[92] C. Schauder, and H. Mehta, "Vector analysis and control of advanced static VAR compensators," *IEE Proceedings Generation, Transmission and Distribution*, vol.140, no.4, pp.299-306, July 1993.